



HAL
open science

Etude des électrodes sur batterie zinc-air

Minhui Gong

► **To cite this version:**

Minhui Gong. Etude des électrodes sur batterie zinc-air. Matériaux. Université Paris sciences et lettres, 2021. Français. NNT : 2021UPSLC024 . tel-03956352

HAL Id: tel-03956352

<https://pastel.hal.science/tel-03956352>

Submitted on 25 Jan 2023

HAL is a multi-disciplinary open access archive for the deposit and dissemination of scientific research documents, whether they are published or not. The documents may come from teaching and research institutions in France or abroad, or from public or private research centers.

L'archive ouverte pluridisciplinaire **HAL**, est destinée au dépôt et à la diffusion de documents scientifiques de niveau recherche, publiés ou non, émanant des établissements d'enseignement et de recherche français ou étrangers, des laboratoires publics ou privés.



THÈSE DE DOCTORAT
DE L'UNIVERSITÉ PSL

Préparée à Chimie ParisTech

Electrodes Investigation on Zinc-Air Battery

Soutenue par

Minhui Gong

Le 27 Mai 2021

Ecole doctorale n° 397

**Physique et Chimie des
Matériaux**

Spécialité

**Physique et Chimie des
Matériaux**

Composition du jury :

Sophie, CASSAIGNON Professeure, Sorbonne Université	<i>Présidente</i>
Emmanuel, BAUDRIN Professeur, Université de Picardie Jules Verne	<i>Rapporteur</i>
Florence, GENESTE Directrice de recherche CNRS, Université de Rennes	<i>Rapporteur</i>
Silvia, GUTIERREZ Professeure, Université de Guanajuato	<i>Examineur</i>
Virginie, LAIR Maitre de conférences, Chimie ParisTech	<i>Examineur</i>
Philippe, BARBOUX Professeur, Chimie ParisTech	<i>Directeur de thèse</i>

Acknowledgement

14/07/2018 is the first day when I stepped on the land of Paris. The next day France won the World Cup, quite a momentary time.

Then I joined in the group. The group is filled of joy and care, everyone is dynamic and kind. I really like this atmosphere for working. A pity is that I cannot communicate with them totally in French, while they are always glad to have me in the conversation.

For the research life, under the wise supervising from Philippe, I obtained a lot of scientific knowledge as well as logical thinking. Every time discussion with him is a treasure for me. Either a fundamental knowledge that I lacked is clearly introduced, or logical reasoning is intrigued via questioning step by step, again and again. He made me believe that repeating has great power and is always the most effective way for grasping knowledge or methods deeply in mind. His patience and wisdom encourage me a lot. Dom also shares all she could to guide me in the experiment conducting and background interpreting as well as providing ideas. I was welcomed every time if I had something to discuss or ask. Her detailed interpretation always makes things clearer and understandable. Her warm personality also brings much joy in research.

The lovely colleagues including postdocs, PhD students, master interns coming and going gave me endless warm and touch, Emmanuel, Gonzalo, Nadia, Caroline, Romain, Marc, Teddy, Lucia, Sandrine, Alexandre, etc. always lighted me in the lab life by their energy and humor, also with their assistance for the lab issues. I am not a talkative person, and maybe we have not much conversation, but I still want to declare that the days spend and work with them were, are and will be always a great treasure in my life.

Finally, thanks to Chinese Scholarship Council (CSC) for the financial support for 3 years. I would like also to show my great gratitude for the last half year's financial support from Philippe and Campus France.

Content

Acknowledgement.....	1
Content.....	3
Résumé français	5
General introduction	15
Chapter 1 Role of battery in energy storage systems	17
1.1. Energy storage systems	17
1.2. Battery technology	20
1.2.1. Conventional batteries.....	22
1.2.2. Metal-air batteries	24
1.3. Zinc-air battery.....	27
1.3.1. Basic components of zinc-air battery	29
1.3.2. Challenges of zinc-air battery.....	31
1.3.3. Proper solutions to the above problems	38
1.3.4. Zinc-air flow battery.....	42
1.4. Conclusion	47
Chapter 2 Zinc electrode	49
2.1. Bibliographic study on zinc electrode.....	49
2.1.1. Zinc electrode in zinc-based batteries	49
2.1.2. Studies on zinc dendrite growth	50
2.2. Experimental study	64
2.2.1. Experimental conditions.....	64
2.2.2. Cyclic voltammetry study on zinc dissolution and deposition.....	68
2.2.3. Static case of rechargeable zinc electrode.....	71
2.2.4. Flow case of rechargeable zinc electrode.....	78
2.3. Conclusion	89

Chapter 3	Catalyst synthesis and characterization	91
3.1.	ORR catalysis mechanism	91
3.2.	Catalysts for ORR and OER	94
3.2.1.	Noble metal catalysts	94
3.2.2.	Carbon-based metal-free catalysts	97
3.2.3.	Metal/carbon hybrid catalysts	98
3.2.4.	Transition metal catalysts	100
3.2.5.	Bi-functional catalysts	112
3.2.6.	Conclusion on the literature survey	116
3.3.	ORR or OER catalytic characterization	117
3.4.	Synthesis methods for perovskite oxides	121
3.5.	Experimental study	124
3.5.1.	$\text{La}_{1-x}\text{Sr}_x\text{MnO}_3$ (LSMO) synthesis	124
3.5.2.	Physical characterization of $\text{La}_{1-x}\text{Sr}_x\text{MnO}_3$	125
3.5.3.	Electrochemical characterization of $\text{La}_{1-x}\text{Sr}_x\text{MnO}_3$	131
3.5.4.	Conclusion	155
3.6.	Air electrode and zinc-air battery assembly	155
3.6.1.	PTFE used as the binder used in air electrode	157
3.6.2.	PVDF-HFP used as the binder in air electrode	158
3.7.	Zinc-air battery assembly	159
3.7.1.	Air electrode formulation with PTFE as the binder	160
3.7.2.	Air electrode formulation with PVDF-HFP as the binder	162
3.7.3.	Zinc-air battery setup	163
3.8.	Conclusion	165
Chapter 4	Overall conclusion and perspective	167
4.1.	Overall conclusion	167
4.2.	Perspectives	169

Résumé français

Introduction : Pourquoi travailler sur des batteries zinc- air ?

La demande d'énergie et la pollution de l'environnement sont progressivement devenues des problèmes urgents dans le monde. L'accent est mis sur les ressources énergétiques renouvelables et le système de stockage d'énergie électrique. Pour adapter les périodes de forte production à celles de forte consommation, il est nécessaire de stocker l'énergie électrique produite sous d'autres formes d'énergie (par exemple, gravitationnelle, adiabatique, mécanique, chimique, thermique, magnétique, etc.). Le stockage électrochimique est cependant la technologie la plus largement adoptée et aussi la plus ancienne.

Même si le stockage de l'énergie électrique ne peut pas éliminer tous les problèmes, il peut jouer un rôle essentiel dans l'amélioration de la fiabilité et de l'utilisation du réseau. Les systèmes électrochimiques ont l'avantage structurel de pouvoir être construits et installés n'importe où par contraste avec les autres systèmes qui sont moins faciles à implémenter sous toute tailles et dans tous les emplacements (air comprimé, hydroélectricité). Les systèmes de stockage électrochimique peuvent générer de l'énergie avec une plage allant de quelques watts à plusieurs méga-watts. L'efficacité varie de 60% à 90% selon le mode de fonctionnement et le type de batterie.

Les batteries traditionnelles comme les batteries au plomb ont une longue histoire de plus de 150 ans. La batterie au lithium-ion est beaucoup plus jeune avec seulement 30 ans depuis son apparition mais elle est devenue rapidement le système le plus fiable en termes de nombre de cycles et c'est le système le moins cher en termes de €/kWh. Ces systèmes représentent la plus grande partie du marché des batteries rechargeables commerciales. Cependant leur prix arrive au plancher défini par le coût des éléments chimiques et ces batteries, fonctionnant avec des liquides organiques inflammables, peuvent devenir dangereuses lorsqu'on les dimensionne pour de l'énergie stationnaire. Il faut également adapter librement la quantité d'énergie stockée (en Wh) et la puissance de la batterie (en W). Diminuer le coût par kWh et par cycle, augmenter la sécurité, trouver un meilleur équilibre entre le coût d'investissement initial et d'utilisation (CAPEX/ OPEX) nécessite de rechercher de nouveaux systèmes. Les batteries métal-air et les batteries à flux pourraient être un moyen d'équilibrer les deux aspects, ce qui signifie en même temps réduire le coût et augmenter les performances.

Les batteries métal-air (métal = Zn, Al, Mg) sont prometteuses car elles utilisent des éléments relativement peu coûteux et permettent une très bonne densité d'énergie (en Wh/m³). Parmi ces systèmes, nous avons sélectionné les batteries zinc-air qui semblent le plus avancées dans le niveau de technologie.

Mais ces batteries nécessitent des améliorations car elles ont des problèmes de mauvaise réversibilité, un mauvais rendement électrochimique et surtout un vieillissement rapide. En effet, bien que les piles zinc-air aient été largement étudiées et développées pendant près d'un siècle, divers défis accompagnent leur développement sous forme de batteries rechargeables. La difficulté concerne aussi la mise à l'échelle qui devrait prendre en compte de nombreux paramètres, par exemple le coût, l'efficacité, la sécurité, etc.

Les problèmes impliqués dans le vieillissement de ces batteries résident principalement dans l'électrode de zinc. Il s'agit de de façon générale de problèmes de non-uniformité pendant le dépôt-dissolution qui sont liés à trois phénomènes à savoir le blocage de la réaction pendant la dissolution par la passivation de la surface (décharge) et le dépôt irrégulier du zinc (la croissance de dendrites) et le dégagement parasite d'hydrogène pendant la recharge.

Pendant la décharge, la passivation se produit lorsque la décharge normale est limitée par la formation d'un film isolant sur la surface de l'électrode. La passivation se produit lorsque les ions zincates atteignent leur concentration de saturation près de la surface de l'électrode et précipitent. Ensuite, ils peuvent former des films compacts de sels de zinc, d'oxyde ou d'hydroxyde de zinc qui recouvrent la surface de l'électrode, bloquant les sites réactifs et résistant au processus de décharge efficace.

Les dendrites sont définies comme l'arborisation formée par de fins cristaux. Morphologiquement, les dendrites sont des protubérances métalliques acérées et en forme d'aiguilles. Le dégagement d'hydrogène résulte intrinsèquement d'un potentiel de réduction plus élevé de la réaction de dégagement d'hydrogène (-0,86 V) que celui de réduction du Zn(OH)₄²⁻ / Zn (-1,2 V). Il est thermodynamiquement favorisé mais retardé pour des raisons cinétiques. Il s'agit d'une réaction secondaire dans les batteries zinc-air.

Pour les problèmes ci-dessus concernant la dissolution et le dépôt du zinc, il existe différentes approches pour y faire face comprenant des additifs dans l'électrolyte ou dans l'électrode, des revêtements sur l'électrode, la modification des conditions hydrodynamiques, le changement du mode de charge-décharge, etc. Les dendrites sont souvent liées à des gradients de concentration dans l'électrolyte ou à un trop fort appauvrissement en zinc à la surface des électrodes. Les dendrites peuvent générer des courts circuits dangereux dans la batterie ou en cassant, se déconnecter du circuit électrique et provoquer la perte de matière active dans la batterie.

Les additifs inorganiques ou des molécules organiques peuvent servir à diminuer le taux de transfert de masse des ions zinc et modifier le rapport entre réaction- diffusion. Les additifs organiques sont souvent des tensioactifs amphiphiles. Ils peuvent être divisés en trois groupes en fonction de leurs caractéristiques ioniques. Leur fonction est de s'adsorber sur l'électrode de zinc, en outre, de diminuer son contact avec l'eau, par lequel la passivation et la corrosion de l'anode pourraient être supprimées. Les additifs organiques dans l'électrode sont généralement des polymères, qui agissent normalement comme liant dans les électrodes de zinc, offrant la structure stable. Cependant nous n'avons pas exploré cette piste.

La circulation de l'électrolyte dans une batterie à flux pourrait éliminer les problèmes de gradients de concentration en renouvelant la solution à l'interface électrolyte-électrode. L'électrolyte qui s'écoule améliore le transfert de masse de l'électrolyte, ce qui est avantageux pour supprimer la croissance des dendrites. D'autre part, l'électrolyte qui s'écoule peut aussi entraîner les ions zincates formés pendant la décharge et éviter la passivation. Il peut aussi éliminer l'hydrogène formé sur l'électrode de zinc ou l'oxygène dégagé sur l'électrode à air pendant la recharge de la batterie, ce qui empêcherait les bulles de gaz de bloquer les réactions et de réduire la zone réactive.

La batterie à flux peut donc présenter de multiples avantages qui compenseraient le coût énergétique de la pompe de circulation. De plus, d'un point de vue pratique, la batterie à flux pourrait permettre d'augmenter la puissance d'une même surface d'électrode et diminuer le coût initial d'une batterie (plus petite mais plus puissante).

Dans notre travail expérimental nous nous sommes donc concentrés sur deux parties :

- L'effet de la circulation d'un électrolyte sur la croissance dendritique du zinc et la génération d'hydrogène
- La fabrication de catalyseurs oxydes pour la réaction de réduction de l'oxygène pendant la décharge d'une batterie.

Nous avons également cherché à mettre en action une électrode à air complète avec des empilements de couches hydrophiles et hydrophobes mais, faute de temps, cela n'a pu rester qu'une ébauche de travail offrant une perspective pour la suite de ce travail.

Etude des électrodes de zinc pendant le dépôt (recharge de la batterie)

La littérature sur le dépôt électrochimique du zinc et les phénomènes de croissance dendritique est abondante. Il est souvent difficile de comprendre quel paramètre joue sur la croissance dendritique (conditions électrochimiques, temps de charge et apparitions de gradients etc). Il est aussi difficile de comprendre l'intrication entre irrégularité du dépôt et dégagement d'hydrogène car les deux

phénomènes sont fortement liés. La littérature académique travaille très souvent dans un mode où l'on contrôle la réaction par le potentiel. Pour nous approcher d'un fonctionnement réel de l'emploi d'une batterie nous avons plutôt employé le contrôle par courant, c'est-à-dire le mode galvanostatique. Nous n'avons travaillé que dans des solutions alcalines parce que les ions zincates sont très solubles. Ceci élimine en grande partie les phénomènes de passivation.

Pour les études de croissance dendritique, nous avons élaboré deux configurations de laboratoire. Dans le premier système, nous avons utilisé une géométrie confinée pour éliminer toute convection et pour que la réaction soit contrôlée uniquement par la diffusion (configuration 1, Figure 0-1). Dans le second système au contraire, nous avons travaillé sous convection forcée avec un flux d'électrolyte (configuration 2, Figure 0-2). Les deux montages sont tous deux constitués de deux pièces de zinc servant d'électrodes symétriques.

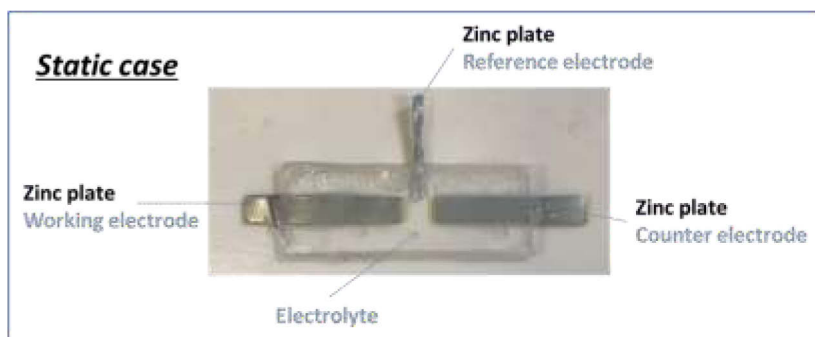


Figure 0-1 : Configuration 1 pour le cas statique

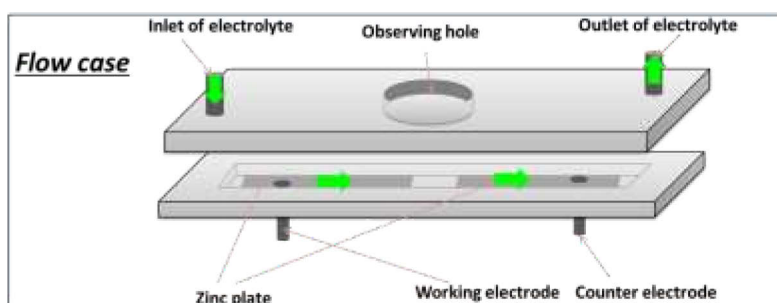


Figure 0-2 : Configuration 2 pour le cas d'écoulement

Avec le montage 1, les variables considérées sont la densité de courant variant de 1 à 40 mA cm⁻², la présence de LiOH ou non dans l'électrolyte, la concentration des ions zincate dans la solution KOH de 0,1 M à 0,7 M, et le temps qui a varié sur plusieurs heures. On obtient les résultats et les conclusions suivantes:

Pour une même quantité de charge passée dans l'échantillon (soit $Q = I.t$ en coulomb), la densité de courant plus élevée donne des dépôts de zinc plus dispersés. Avec une densité de courant de 1 mA cm⁻², les dépôts sont compacts avec peu de changement de forme de surface. À 10 mA cm⁻², il y a

apparition de dendrites avec des formes encore arrondies mais à 40 mA cm^{-2} les dépôts sont très dispersés avec des pointes plus acérées.

Les dendrites n'apparaissent pas immédiatement mais au bout d'un délai. Une concentration plus faible de zincate dans l'électrolyte donne plus rapidement des dépôts dendritiques. Ceci prouve que les dendrites apparaissent bien suite à un épuisement des ions Zn à l'interface électrode - électrolyte. La variation du potentiel au cours de l'expérience de chronopotentiométrie est le résultat des effets de polarisation, du dégagement d'hydrogène et du dépôt non uniforme. Le dégagement d'hydrogène est plus fort quand il y a une densité de courant plus faible et dans un électrolyte avec une concentration de zincate plus faible.

La présence de LiOH dans l'électrolyte n'apporte pas d'effet clair sur le dépôt de zinc, comme indiqué sur la Figure 0-3 et la Figure 0-4.

La circulation de l'électrolyte favorise évidemment la suppression de la croissance des dendrites. Une densité de courant plus élevée peut-être appliquée avec un électrolyte en flux. Le dégagement de l'hydrogène est plus facile en circulation. Finalement on peut constater que le dégagement d'hydrogène est plus fort dans les conditions où il y a moins de dendrites.

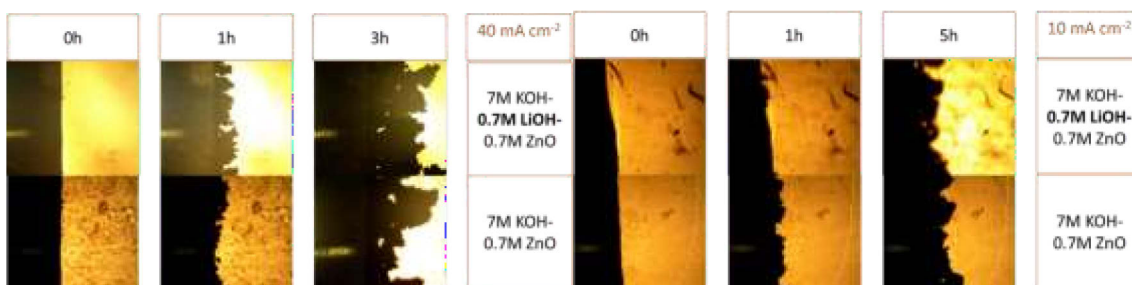


Figure 0-3 : Evolution du dépôt de zinc à 10 mA cm^{-2} dans les électrolytes avec ou sans LiOH

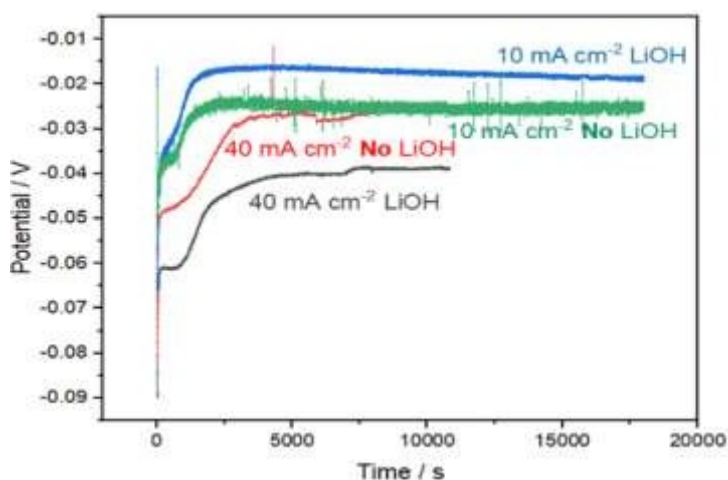


Figure 0-4 : Variation du potentiel avec processus de dépôt à 10 mA cm^{-2} et 40 mA cm^{-2} dans les électrolytes avec ou sans LiOH

Avec plusieurs cycles de dépôt-dissolution, l'électrode de zinc devient de plus en plus irrégulière. La croissance des dépôts et leur dissolution est pourtant linéaire avec le temps sous charge galvanostatique comme sous décharge.

Etude de formulation de catalyseurs pour une électrode à air

Du côté de l'électrode à air, les principaux défis sont d'augmenter l'activité catalytique et l'assemblage électrode. Il faut générer une interface triple gaz- électrolyte- conducteur avec 1) l'arrivée du gaz oxygène au travers d'un système poreux mais qui ne doit pas être noyé par l'électrolyte et 2) permettre le départ des ions formés dans l'électrolyte et 3) assurer la collecte des charges électriques dans le solide.

La génération d'oxygène pendant la recharge c'est-à-dire la réaction d'évolution de l'oxygène (OER) est assez bien connue parce qu'elle est documentée dans les problèmes d'électrolyse de l'eau. On cherche encore de bons catalyseurs pour la réaction inverse de réduction de l'oxygène (ORR). Dans les batteries zinc-air primaires commerciales et les piles à combustible zinc-air rechargeables, le Pt / C et le MnO₂ sont les catalyseurs les plus utilisés pour la réaction de réduction de l'oxygène. Le catalyseur à base de Pt pose le problème d'une faible stabilité dans l'électrolyte alcalin concentré ; l'activité catalytique du MnO₂ est relativement faible.

Les métaux nobles pour la catalyse ORR et OER sont encore en développement ainsi que la détermination de leurs mécanismes catalytiques. Les effets de taille accompagnés d'effets structurels des perspectives micro et macro font l'objet de recherches approfondies et largement approfondies. Un pool de catalyseurs à base de métaux nobles est conçu et synthétisé selon des effets électroniques spécifiques.

Les oxydes de métaux de transitions sont une alternative plus stable en milieu basique et surtout moins coûteuse. Mais il est difficile de contrôler l'état d'oxydation et la stœchiométrie d'oxydes simples tels que les oxydes de cobalt ou de manganèse lors de leur synthèse et lors de leurs propriétés électrochimiques. La conductivité électronique est également importante pour optimiser des échanges électrochimiques. Ces oxydes simples ont une conductivité essentiellement basée sur leur non-stœchiométrie qui peut évoluer pendant les réactions chimiques et ils ne donnent pas de résultats reproductibles en électrocatalyse

Les états électroniques et la conductivité des oxydes multiples semblent plus faciles à contrôler. Leur conductivité est facile à stabiliser par des substitutions chimiques dans des sites cristallographiques bien déterminés. Les oxydes de pérovskite de formule ABO₃ sont en particulier largement étudiés en tant que catalyseurs d'oxygène dans l'électrode à air. A titre d'exemple, dans la

structure ABO_3 , on peut faire une substitution aliovalente dans le site A (Sr^{2+} pour La^{3+}), ce qui peut modifier le remplissage des orbitales d du cation B sans créer de désordre dans le site B. Cela transformera facilement le matériau d'isolant en métal. Ces métaux offrent une alternative bon marché aux métaux précieux et leur surface contenant des oxydes est bien adaptée pour adsorber l'oxygène. Dans la littérature, les matériaux les plus étudiés et peut-être les plus prometteurs sont $LaMnO_3$, $LaCoO_3$, et $LaNiO_3$. Surtout, le manganèse ($3d^4$, haut spin $t_{2g}^3 e_g^1$) et le nickel ($3d^7$ bas spin, $t_{2g}^6 e_g^1$) sont intéressants car bon marché (par rapport au cobalt) et ils donnent facilement de bonnes phases conductrices lors du dopage (manganèse dans $La_{1-x}Sr_xMnO_3$, LSMO) ou même sans dopage (nickel dans $LaNiO_3$).

Nous avons donc entrepris une étude de ces pérovskites dans le but de coupler une étude cristallographique et microstructurale avec les propriétés d'électrocatalyse.

Notre synthèse de pérovskites de nickel avec une surface spécifique élevée par des techniques de solution n'a pas été aussi réussie et reproductible car nous ne pouvions pas obtenir de matériaux monophasés. Nous nous sommes donc concentrés plus particulièrement sur le système LSMO. De plus, sa synthèse est bien connue, de sorte que l'on peut utiliser des poudres reproductibles pour étudier la formulation d'encres et l'assemblage d'électrodes.

L'oxyde mixte de lanthane et de manganèse dopé au strontium a été synthétisé par deux méthodes différentes : un processus de solution de citrate polymère et un processus de coprécipitation de carbonate. Après synthèse et caractérisation des poudres, des études électrochimiques ont été menées avec une électrode à disque rotatif. Nous nous sommes concentrés sur l'effet de substitution du strontium dans le système $La_{1-x}Sr_xMnO_3$ car, en conclusion de l'étude de la littérature, son activité est correcte et le manganèse est bon marché et non toxique.

Nous avons adapté une méthode de synthèse par voie citrate. Dans notre travail, des acétates au lieu de nitrates ont été utilisés pour éviter l'explosion causée par la réaction très exothermique des nitrates avec des matières organiques lors de la calcination à haute température. Le mélange avec de l'acide citrique donne une résine polymérique après chauffage à $150^\circ C$. Les ions sont intimement mélangés à l'échelle moléculaire et retenus de façon homogène par les liaisons avec les citrates.

Nous avons également utilisé une méthode alternative de synthèse par coprécipitation de solution de nitrates de La, Sr Mn avec de l'hydrogénocarbonate d'ammonium en excès. Dans les deux méthodes (citrate, carbonate), les poudres obtenues par séchage à basse température, ont été homogénéisées par broyage et calcinées 4 h dans une atmosphère d'oxygène à $500^\circ C$, $700^\circ C$, $900^\circ C$ et $1100^\circ C$. Les effets de la substitution du strontium, la température de calcination, le processus de synthèse et l'atmosphère de calcination ont été comparés et discutés en détail.

La calcination à 500 ° C donne des matériaux oxydes amorphes à la fois dans le processus de coprécipitation ou dans le processus de solution de citrate. Le fait qu'un matériau amorphe soit obtenu au lieu d'oxydes simples cristallisés indique un bon mélange des différents éléments par la chimie en solution qui empêche la séparation de phase et la cristallisation d'oxydes simples. La méthode au citrate donne la pérovskite pure à partir de 700 ° C alors que pour le procédé de coprécipitation au carbonate, le matériau obtenu à 700 ° C est toujours un système multiphasé. Dans ce cas, la pérovskite n'apparaît comme phase majoritaire qu'au-dessus de 900 ° C. Les phases obtenues à 700°C par la voie citrate présentent une surface spécifique relativement élevée de 20-30 m²/g. Ceci est un bon résultat compte tenu de la densité du composé LSMO.

Nous avons dû beaucoup travailler la formulation d'électrodes pour obtenir des résultats reproductibles en électrochimie. Pour effectuer les mesures, une suspension contenant du catalyseur, du carbone et du liant est déposée par goutte à la pointe de l'électrode tournante. Une fois le solvant évaporé, une couche catalytique est formée et fixée sur l'électrode en carbone vitreux. Le rôle principal du matériau carboné mélangé au catalyseur est d'améliorer la conductivité et de disperser le catalyseur, tout en ayant également un effet catalytique sur l'ORR.

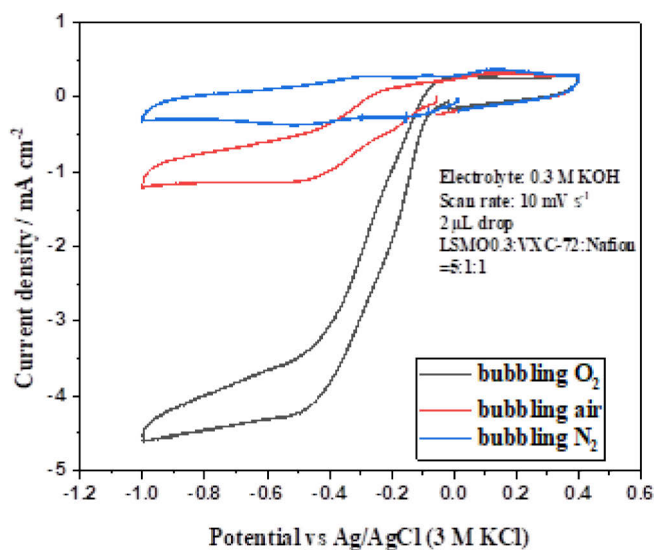


Figure 0-5 : Courbes de voltampérométrie cyclique d'un échantillon de LSMO avec différentes concentrations d'oxygène.

Nous avons donc successivement optimisé les rapports catalyseur/carbone/liant polymère. Nous avons aussi optimisé l'épaisseur de l'électrode en jouant sur la taille des gouttes déposées sur

l'électrode tournante en carbone vitreux. Les expériences ont été effectuées dans un électrolyte dilué de concentration 0,3 M KOH.

Pour l'optimisation de la formulation de l'encre, une sélection appropriée du matériau de carbone, de la composition du matériau, du volume de goutte sur le disque peut être décidée. Trop de catalyseur ou de matériau carboné augmente l'effet capacitif qui gêne l'observation du phénomène de réduction de l'oxygène.

Le premier cycle de balayage en potentiel effectué sur des encres LSMO est toujours différent des scans suivants en raison de l'état d'origine de l'électrode. La vitesse de balayage de 10 mV s⁻¹ et la manière de normaliser la densité de courant ont été rationalisées.

Pour les catalyseurs synthétisés à partir de différents procédés, ceux calcinés dans l'oxygène présentent une activité ORR plus élevée que ceux calcinés dans l'air. Ceci est probablement lié à une composition en oxygène plus élevée qui donne une meilleure conductivité électronique. La voie citrate ayant permis obtenir des structures mieux cristallisées avec moins d'impuretés donne également de meilleures performances pour l'activité ORR. La température de calcination génère une différence évidente dans la surface. La calcination à 800 - 900 ° C apparaît comme un bon compromis entre une bonne activité liée à une bonne cristallinité et une bonne surface spécifique.

Pour l'effet du dopage, le dopage au strontium avec un rapport atomique de 0,3 au lanthane (c'est-à-dire La_{0.7}Sr_{0.3}MnO₃) montre la meilleure activité catalytique même si l'effet n'est pas très important.

Toutes ces études de formulations réalisées pour l'électrode à disque rotatif et l'optimisation des études analytiques ont pu être utilisées pour la formulation de véritables assemblages d'électrodes à air que nous avons montré dans la partie finale de notre travail.

Deux procédés de formulation de l'électrode à air ont été présentés. Ils diffèrent par l'utilisation du liant polymère hydrophobe. Nous avons utilisé des dispersions aqueuses de polytetrafluoroéthylène (CF₂-CF₂)_n (PTFE en dispersion 60% dans l'eau désionisée, Sigma-Aldrich) selon une méthode couramment employée pour la fabrication des batteries Zn-air. Mais nous avons aussi testé une méthode utilisant du polyvinylidène difluorure (CH₂-CF₂)_n (le PVDF-HFP, Sigma-Aldrich, Mw moyen ~ 455000) qui est couramment utilisé comme liant dans la technologie des batteries lithium-ion. Le rapport carbone/catalyseur/liant détermine le degré d'hydrophobie des membranes. Différentes quantités de liants ont été utilisées pour réaliser des couches hydrophiles (couche catalytique permettant l'accès de l'électrolyte) et hydrophobes (gaz diffusion layer poreux permettant l'accès du gaz mais repoussant l'électrolyte).

Une batterie entière a été montée et sa performance de charge-décharge a été effectuée. Par rapport à la littérature, notre utilisation de PVDF-HFP est originale et a permis de monter une

faisabilité d'une batterie complète basée sur une telle technologie. Notre batterie a fonctionné sur quelques cycles avec cependant une forte différence entre le potentiel de charge (1,9 V) et de décharge (1,4V). La réalisation d'autres batteries complètes en vraie géométrie d'application réelle n'a pas pu être effectuée faute de temps mais il est vrai qu'elle relève plus de travaux d'ingénierie que de recherche fondamentale.

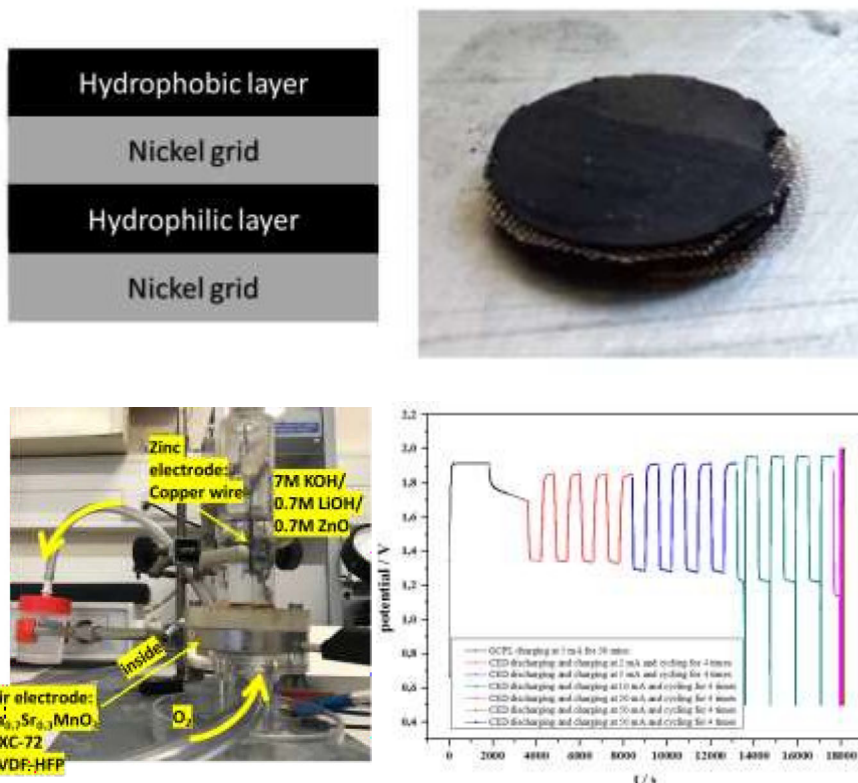


Figure 0-6 : Schéma et photographie de notre assemblage d'électrode à air. Photographie d'une batterie Zn-O₂ complète, cycles de charge- décharge à différents courants.

En conclusion de ce travail notre apport aura consisté à développer des formulation d'électrodes permettant d'obtenir des expériences répétables et de comparer des catalyseurs pour la réaction de réduction de l'oxygène. La projection de ces formulations vers la réalisation d'électrodes complètes de batteries Zinc-air a également pu être démontrée.

General introduction

Energy storage is becoming an alternative for sustainable development in the world, of which battery technology is a feasible approach. Many new batteries are showing up to replace or assist conventional batteries applied for energy storage, especially the metal-air batteries due to their availability, reversibility, and sustainability. Zinc-air battery is superior owing to the steady chemical-physical properties, the abundant deposit of zinc and the high theoretical energy density. This work will focus on the zinc-air full battery fabrication. Flowing electrolyte is adopted to suppress dendrite growth and enhance the overall performance of the whole battery. Based on the above, this work will expand to three parts.

In **chapter 1**, the importance of the zinc-air flow battery will be highlighted. The very initial background of zinc-air battery and its role in the energy storage systems will be emphasized. Further the challenges and new developments will also be mentioned. Our goal is therefore to give a little contribution to its development and commercialization.

In **chapter 2**, the detailed issues related to zinc electrode will be introduced including the detrimental aspects and the corresponding solutions. The study about zinc electrodeposition will also be investigated. The effect of flowing electrolyte and the interference with hydrogen evolution will be discussed.

In **chapter 3**, the catalyst for oxygen reduction reaction (ORR), oxygen evolution reaction (OER), and their catalytic mechanism will be reviewed. The ORR catalyst perovskite oxides will be detailed in this scope including the synthesis and kinetic studies. Different synthesis methods will be compared to synthesize the same perovskite $\text{La}_{1-x}\text{Sr}_x\text{MnO}_3$ (LSMO). The systematic work about a series of catalysts will be expanded from the characterization to electrocatalysis kinetic analysis using cyclic voltammetry (CV). A normalization alternative for providing the reliability of comparative metric of catalytic activity for ORR will be put forwards. Last a trial for the air electrode formulation and full zinc-air flow battery processing will be presented. Two types of air electrode formulation will be tried, and the composition of the electrode will be optimized. A cycling test will be presented.

Chapter 1 **Role of battery in energy storage systems**

1.1. Energy storage systems

Energy demanding and environmental pollution have emerged gradually to be urgent issues worldwide. The deposit of traditional fossil fuel is predicted to be exhausted in 50 years and its combustion generates severe atmosphere contamination. Global energy structure will be followed to change or adjust soon with its running out, especially in the countries, which are depending a lot on the traditional fuels to satisfy the energy demand. The worldwide demand of electricity will double in 2050 [1]. Efforts to find new energy resources and renewable energy alternatives are crucial and enormous. Renewable energy like hydro, solar, wind energy, etc. is applied to address the problem. Renewable energy has been deemed as very important strategy in the global blueprint. Figure 1-1 shows the growth of renewable energy capacity in different regions or countries [2]. Despite the emphasis on renewable energy resources, energy storage system is also required to avoid waste from unbalanced renewable energy distribution and the half-load situation. Storage of electricity energy cannot sustain, so conversion into other forms of energy (e.g., gravitational, adiabatic, mechanical, chemical, thermal, magnetic, etc.) is necessary and their application is effective [3]. Energy storage technologies are also kept refreshed in pace with renewable energy resources application. The reliable energy storage system is depicted in Figure 1-2.

Renewable capacity growth by country/region, 2018-2024

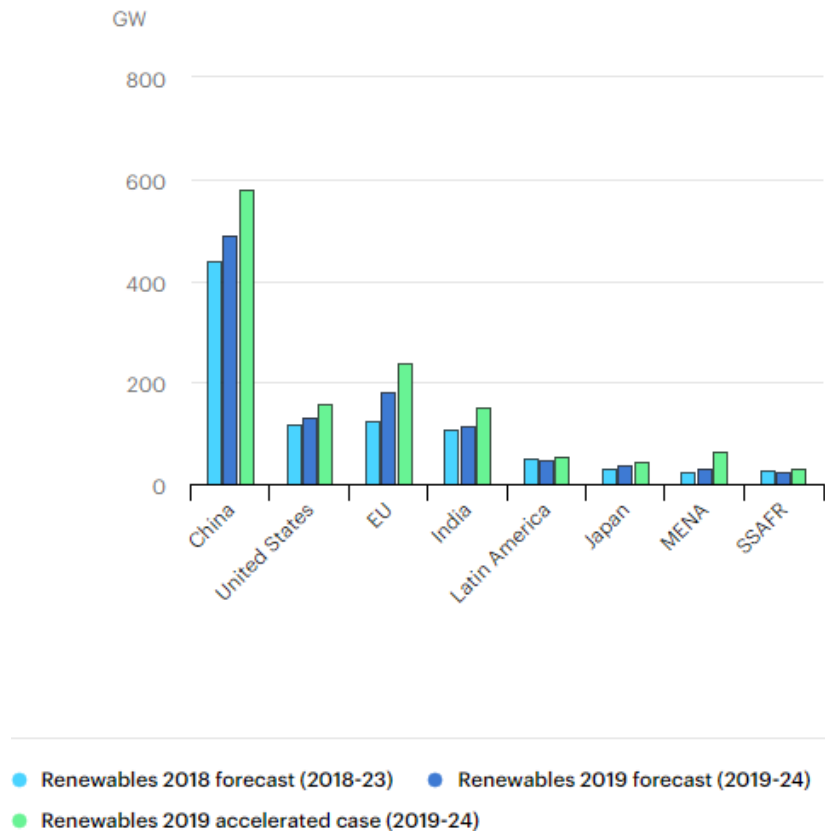


Figure 1-1 : Renewable capacity growth by country/region, 2018-2024 [2]

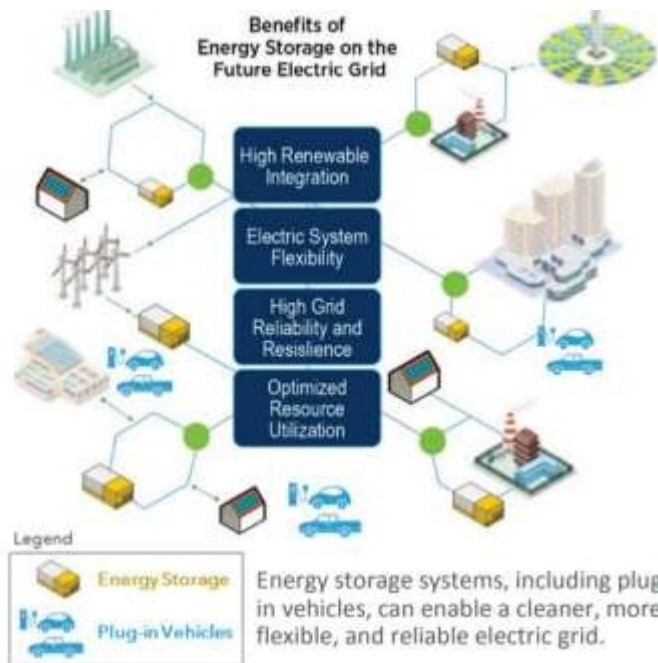


Figure 1-2 : Schematic of reliable energy storage system [4]

Renewable energies, despite their advantages of being clean and unlimited, they face the difficulty of integrating into power grid, especially in adjusting the different demands in different periods, because their utilization depends on some uncontrollable elements like weather condition and climate change. Some unsuited situations would happen that the net supply cannot satisfy the midday's demand, while much energy generated remains unused and wasted in the morning and evening. To ameliorate the energy efficiency and economic benefits, hybrid energy systems which realize combination of different energy sources, seek a way to complement the situation. Energy storage systems (ESS) are highlighted in the role of improving the integration of renewable energy resources into the power grid because they can manage flexible load shift.

The common ESS are generally categorized into 6 types according to the involved energy type. Currently, mechanical energy storage includes pumped hydro storage (PHS), compressed air energy storage (CAES) and flywheel energy storage (FES). PHS utilizes the gravity potential energy of water to supply electricity. Fallen water carrying high energy rotates the turbines to fulfill electricity demands. Its storage capacity depends on the height of the waterfall and the volume of the water. The conversion efficiency can be 65%-80% [5]. CAES stores compressed air with the electricity during off-peak hours and the air with high pressure activates turbines to generate electricity during peak hours. The energy efficiency is estimated to be around 70% [5]. FES transfers the kinetic energy into electricity. Thermal energy storage involves conversion between heat energy and electricity. Two types of heat, sensible and latent heat are used. The former undergoes temperature change, while the latter has also phase change. Electromagnetic storage system contains supercapacitors and superconducting magnetic energy storage (SMES). Supercapacitor shares the properties of capacitor and battery, except that no chemical reactions are involved. They can achieve 95% of energy efficiency while the main defect is self-discharge and very low energy density [5]. Superconducting magnetic energy storage operates at extreme low temperature around $-270\text{ }^{\circ}\text{C}$ and completes electricity (DC current) and magnetic energy conversion. The efficiency is superior, and response is quite quick, but it is a costly technology. The main characteristic of chemical energy storage is utilizing hydrogen, natural gas, or other combustible gas as medium for energy conversion. Hydrogen is often synthesized from water electrolysis. Hydrogen can also be reacted into natural gas. When energy is required, the medium will be oxidized further to supply electricity. Electrochemical reactions only occur in obtaining hydrogen but not direct for electricity, which is different from the electrochemical storage system that only secondary batteries are referred. The detailed types of energy storage systems are listed in Figure 1-3.

Finally, electrochemical energy storage is probably not the best method considering the energy conversion efficiency or the cost per stored kWh. But in the state of the art, it proves to be the most

versatile method that can be installed anywhere with systems of any size. Of course, this will be the topic of the next chapters.

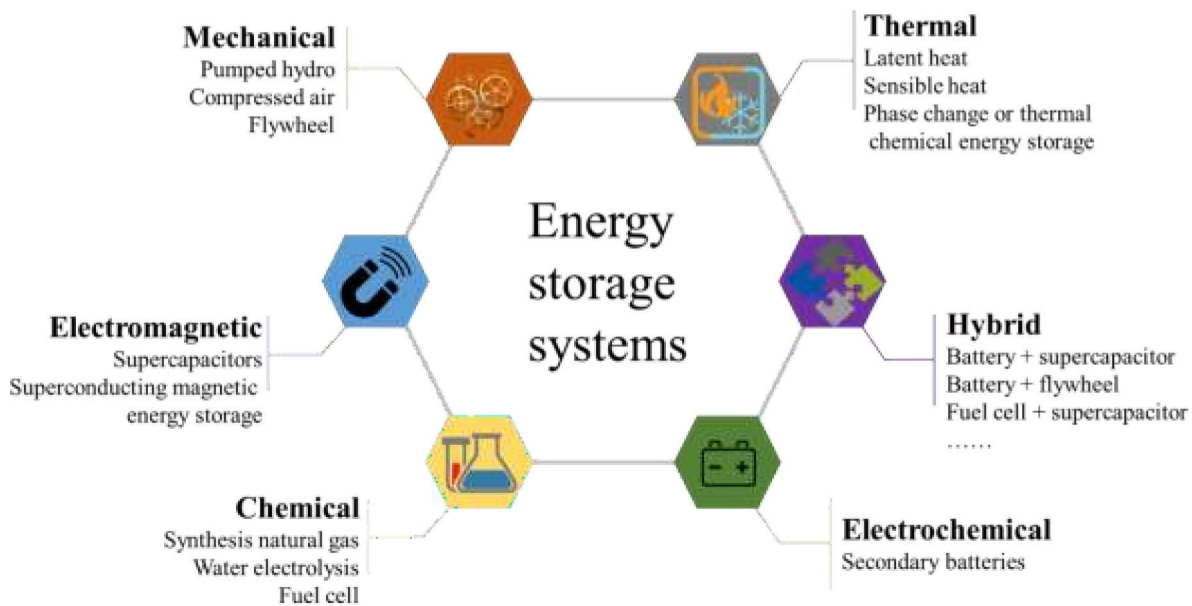


Figure 1-3 : Constitutes of energy storage systems

1.2. Battery technology

Battery energy storage system is the most widely adopted and earliest technology. In addition to the chemical energy conversion system, the batteries-based energy storage systems also consist of the battery management system (BMS), the power conditioning system (PCS), and the energy management system (EMS), which are schematically shown as Figure 1-4 [6]. The BMS is responsible for monitoring the operational performance of the batteries, including the voltage, whether they are over-discharged, the temperature etc. The PCS most aims to deliver a voltage of the proper level and characteristics to achieve proper function of load equipment, especially the inversion function that enable the conversion between AC and DC electric energy. The EMS gathers several components including supervisory control and data acquisition system, automatic generation control system, state estimator system, security analysis system, economic dispatch control system, and dispatcher training system together to ensure the comprehensive cooperation [7].

Even though electrical energy storage cannot wipe out all the issues, it can play a vital role in improving the grid reliability and utilization. They have the structural advantage to be constructed and installed conveniently in the grid energy storage systems [6]. They can generate power with the range of few Watts to several Mega-Watts. The efficiency varies from 60% to 90% depending on their operation and type of battery [8]. Batteries are composed of serial-parallel assembled cells, where-in

conversion between chemical energy and electrical energy is the main motion for energy storage [1]. Surplus energy can be stored for later use during this conversion, a process with charging and discharging. The targeted voltage and current that the grid offer can be obtained by adjusting the quantities and arrangement of cells. The response is sensitive, and the operation is controllable. It will show more cost advantage with the development of battery technology [9].

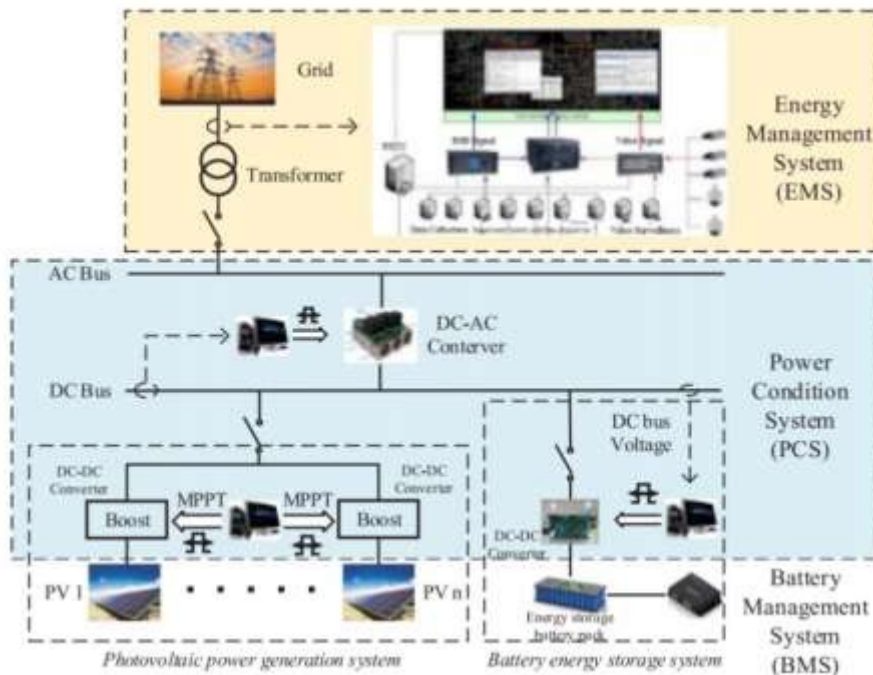


Figure 1-4 : Schematic of batteries-based energy storage systems [6]

Due to its outstanding advantages, battery energy storage system (BESS) plays a vital role in all the ESS. Figure 1-5 shows the structures of four different ESSs integrating BESS. This categorization is based on the BESS sizing criteria that from (a) to (d), the size becomes bigger. There have been many grid-level battery energy storage systems around the world, either under operation or contracted state [6]. With the rapid cost drop of battery technology owing to the fast development of electric vehicles, BESS shows more and more superiority. The installed capacity of battery storage is comparable with the open-cycle gas turbines in India by 2020. If the cost of battery becomes very cheap, it is estimated that the share of battery energy will dominate the renewable energy storage systems [10].

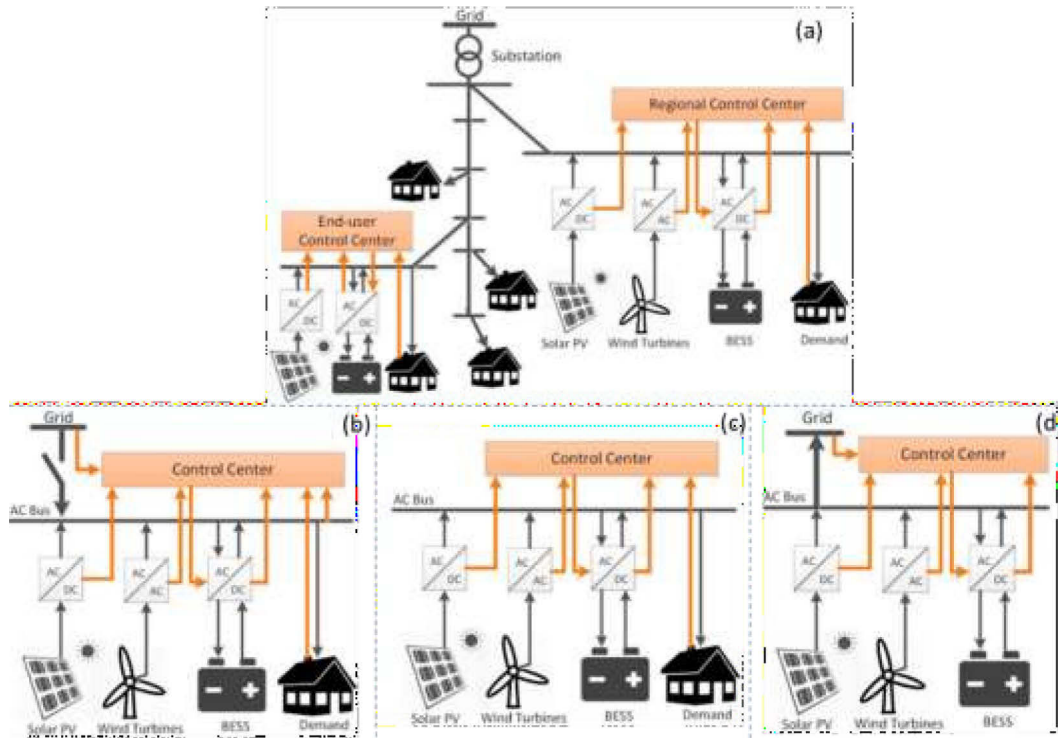


Figure 1-5 : The structures of four categories of energy storage system: (a)distributed renewable energy system (b) microgrid (c) standalone hybrid renewable energy system (d) renewable energy power plant [11]

1.2.1. Conventional batteries

Figure 1-6 presents the proportions of the mixed energy storage technologies during 2011-2016 [12]. Traditional batteries like lead acid battery have a long history of more than 150 years. Lithium-ion battery is much younger with only 30 years since appearance. They account for most proportion in the commercial rechargeable battery market. The positive electrode material of lead acid battery is lead dioxide and the negative material is spongy lead, with a micro-porous separator saturated by the electrolyte of aqueous sulfuric acid. The standard voltage can reach to 2.05 V and can obtain the specific energy density of near $50 \text{ Wh}\cdot\text{kg}^{-1}$ [13]. In the early XXI century, the lead battery outweighed in the aspects of cost and sustainability, because the shell of the lead-acid batteries are easy to be recycled with low energy input [13]. But in areas of energy density and durability, it is in the shadow of lithium-ion batteries. Indeed, lithium ion batteries have higher applied energy density ($300 - 500 \text{ Wh}\cdot\text{kg}^{-1}$), nearly 8 times that of lead acid battery, and storage efficiency of nearly 100% [14]. Noteworthy is that the lifespan of lithium-ion batteries is much longer (5000 cycles in stationary applications), which makes it on roads to power equipment application [1]. The price of a lithium-ion battery became very low is now $150 \text{ \$ kWh}^{-1}$ (in 2019) half that of a lead acid battery and it can make at least 5 to 10 times more cycles. This explains that it is the battery widely used in the present times.

Other commercial batteries, like sodium-sulfur battery firstly discovered in 1983 and commercialized since 2002 in Japan [8], sodium-nickel chloride battery applied in electronic vehicles

but not in power grid, nickel-cadmium battery, and flow battery, though not as widely applied as the above two because of rigid operation condition like high temperature, or expensive cost, or environmental pollution, they show outstanding durability. The flow batteries can be traced back to 1960s. After a decade, there appeared numerous types e.g., Fe/Cr, V/Br, Br/polysulfide, Zn/Ce, Zn/Br, and all-vanadium redox flow batteries. Because the circulated aqueous electrolyte has the limited concentration of 8 M, the energy density of flow batteries is less than $25 \text{ Wh}\cdot\text{kg}^{-1}$ [1].

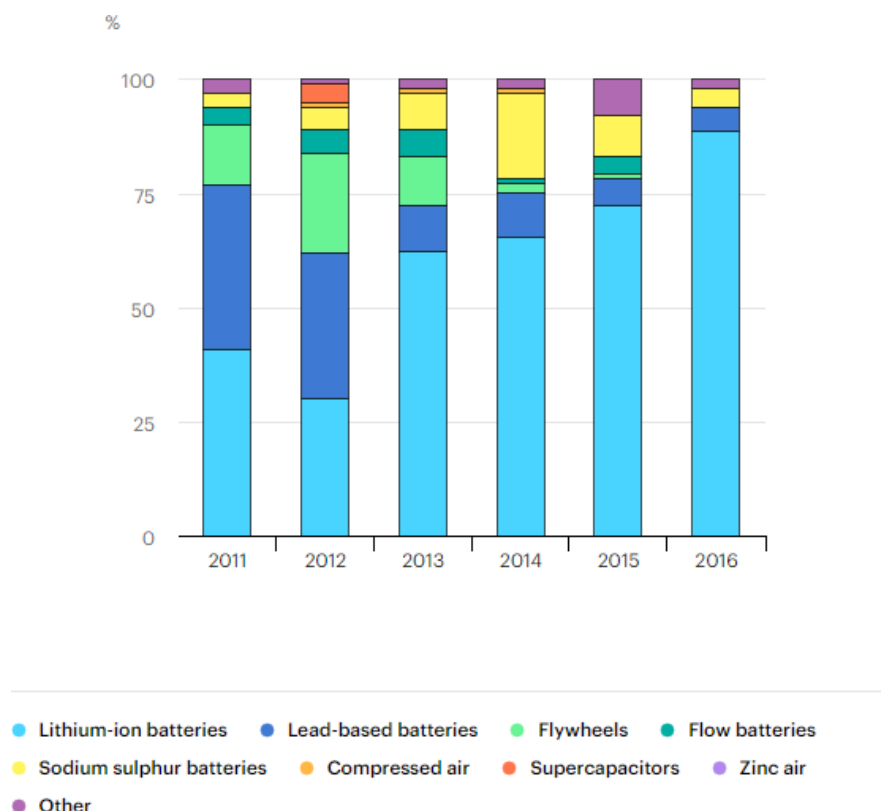


Figure 1-6 : Technology mix in storage installations excluding pumped hydro, 2011-2016 [12]

It is hard to find the trade-off between the technological performance and market interest within the commercial batteries mentioned above. Metal-air batteries and flow batteries have sought a way to balance the two aspects, which means to decrease the cost and increase the performance at the same time. Recent works have shown that the cost for electrochemical energy storage should be less than $20 \text{ \$ kWh}^{-1}$ (with at least 20000 cycles) to make renewable electricity less expensive than nuclear electricity which, in the state of art is the cheapest mode of electricity production [15]. However, the less expensive batteries in the state of art are lithium-ion batteries with a cost around $150 \text{ \$ kWh}^{-1}$ in 2019. Some strong effort is thus necessary to invent the battery able to store electricity at such low cost.

1.2.2. Metal-air batteries

Demanding for clean energy stimulates the prosperous development of electric vehicles (EV). High specific energy (unit of Wh kg⁻¹) and high specific power (unit of W kg⁻¹) are required to ensure long driven miles and high acceleration rate for hill climbing capacity, respectively [16]. The most widely used conventional rechargeable battery lead acid batteries are very limited by their low energy density. Nowadays the most popular batteries are lithium-ion batteries. Compared to gasoline as the fuel to generate power with a practical energy density of 1700 Wh kg⁻¹ [17], lithium-ion batteries have a maximum energy density of up to 300 Wh kg⁻¹ by far, which is way lower than that of gasoline.

Metal-air batteries have received much attention because of their theoretical high energy density and low cost. Since an earlier age in 1878, zinc-air battery had been realized in lab research by Leclanché. Continuous studies are implemented to improve the electrochemical performance to accomplish commercial applications. The first air electrode was commercialized in the 1930s patented by Heise and Schumacher [18], after which aluminum-air, magnesium-air, iron-air were invented in 1960s. Following the appearance of lithium-ion battery in 1980, lithium-air was firstly put forward in 1996. When it came to XXI century, sodium-air and potassium-air also joined the lab-research world [19]. The schematic of metal-air battery is shown in Figure 1-7. Commonly, it has a liquid-gas-solid (catalyst) interface in the air electrode. The first main group element-based metal-air batteries often use an aprotic electrolyte (made of any organic liquid able to solvate corresponding metal salts); the others use alkaline or saline aqueous electrolytes.

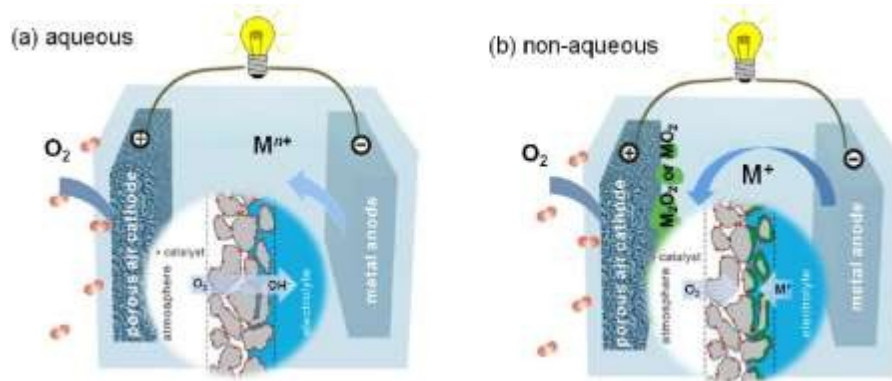


Figure 1-7 : Schematic of metal-air battery with (a) aqueous and (b) non aqueous electrolyte [20]

Lithium-air battery, magnesium-air battery, aluminum-air battery, and zinc-air battery are widely researched in the lab, they also gradually take a place in the commercial application, especially in the electronic vehicle industry and smart power grid. The characteristic data of metal-oxygen cells is listed in Table 1-1. The specific capacity or specific energy are calculated in the basis of metal anode, while in practical cases, added the mass of electrolyte with different compositions and current

collectors, membrane of separator, and package materials, the real specific capacity or energy should be reduced by 20-30% [21].

Table 1-1 : Characteristic data of metal-oxygen cells [22]

Metal anode	Theoretical specific capacity of metal/(Ah·kg ⁻¹)	Theoretical cell voltage with O ₂ electrode/(V)	Practical operating voltage/(V)	Theoretical specific energy of metal oxygen couple/(Wh·kg ⁻¹)
Li	3861	3.3	2.4	12741
Mg	2205	3.1	1.4	6837
Al	2980	2.7	1.6	8046
Zn	820	1.6	1.1	1312
Fe	960	1.3	1.0	1248
Cd	478	1.2	0.9	572

Lithium-air battery was proposed early, but it attracted little attention because of its inherent instability while contact with air and hydrous electrolyte. According to the electrolyte applied, the lithium-air batteries have four types: aprotic/non-aqueous, aqueous, hybrid aprotic-aqueous, and solid. The aprotic electrolyte contains lithium salts like LiPF₆, LiAsF₆, LiSO₃CF₃ in organic solvent such as organic carbonates, ethers, and esters, which is from the reference of lithium-ion batteries [23-25]. The aqueous type is lithium salts dissolved in water, where an artificial solid electrolytic interface (SEI) is required [26] to protect from the direct reaction of lithium with water. Different from aqueous electrolytes, a protecting SEI is spontaneously formed in aprotic electrolytes [27]. The hybrid electrolytes are used to avoid cathode clogging and moisture problems, aprotic electrolyte is in contact with anode [28-30]. Solid electrolyte is often a polymer, a ceramic, or a glass, which ensures high thermal stability and rechargeability [31, 32].

Compared to lithium-air batteries, the zinc-air batteries show less potential decay when discharging at a constant current density of 50-100 mA·cm⁻² [33]. Zinc metal is also a common metal already used in secondary batteries, like zinc-bromide, zinc-cerium, and zinc ferro-ferricyanide batteries [34]. Aqueous and solid electrolytes are commonly used in zinc-air batteries, of which alkaline aqueous electrolyte is the most widely applied, while aprotic electrolyte is seldom utilized in zinc-air batteries [35]. There are various anode forms, porous zinc, zinc foil, filamentous zinc, zinc alloy etc. [36, 37]. Magnesium-air battery though has high theoretical voltage and energy density comparable to lithium-air battery; it faces the difficulty in undergoing reduction reaction effectively, which would result in self-charging and low coulombic efficiency [38]. Magnesium plate is used as

anode conventionally, and there are many drawbacks such as thermal instability from self-discharge, formation of passivating film from dissolution and deposition cycles [17], modified magnesium nanoparticles and magnesium alloys are reported to be more rechargeable and have longer cycle life [39-41]. Electrolyte for magnesium-air battery is often acidic or neutral, e.g. NaCl, KHCO₃, NH₄NO₃, NaNO₃, NaNO₂, Na₂SO₄, MgCl₂, MgBr₂, and Mg(ClO₄)₂ [42].

Aluminum-air battery and zinc-air battery have also attracted much attention for their theoretical specific energy, as high as 8100 Wh·kg⁻¹ and 1300 Wh·kg⁻¹, respectively, though the rechargeable aluminum-air battery is much harder to obtain than the zinc-air battery because aluminum easily reacts with oxygen and forms hydrated aluminum oxide [43]. Either salt solution or alkaline solution can be the choices of electrolyte for aluminum-air batteries [44]. Efforts are also made on aluminum alloys and gelled electrolytes to improve the battery performance [17]. Zinc is stable and active to be reduced. It is tougher than the other metals to stand in highly corrosive electrolytes. Zinc-air battery could exhibit 6-9 times energy efficiency that of aluminum-air battery [45, 46]. Iron-air batteries have high possibility to be rechargeable, while they face the problem of rather low energy density of only 60-80 Wh kg⁻¹ even though their cyclability (> 1000 cycles) is agreeable [20].

Overall, zinc-air battery is the most promising metal-air battery technology though requires a further improvement. Besides, zinc-air batteries have a cost efficiency that would reach the goal of 20 \$ kWh⁻¹, much cheaper than Li-ion batteries [19].

Table 1-2 : Components of common metal-air batteries

Battery type	Anode	Cathode	Electrolyte	State-of-art battery performance
Lithium-air	Lithium metal	Carbon supported (with or without catalyst)	-aprotic electrolyte -aqueous electrolyte -hybrid electrolyte -solid electrolyte	Co ₃ O ₄ /GR composite acting as bi-functional catalyst, operating for 80 h, a round-trip efficiency of 83% [30]
Magnesium-air	-magnesium metal -magnesium alloy	-with aqueous electrolyte carbon material, catalyst, and hydrophobic	-aqueous electrolyte neutral salt solution acidic solution -solid electrolyte	SmMn ₂ O _{5-δ} nanocrystal 101 mW cm ⁻² , 1770 mAh g ⁻¹ with durability (~115 h) [47]
Aluminum-air	-aluminum metal		-aqueous electrolyte	Peak power density up to 545 mW cm ⁻² ,

	-aluminum alloy	polymer material -with solid electrolyte	neutral salt solution alkaline solution -solid electrolyte	energy efficiency of 42.6% with a flow alkaline electrolyte [48]
Zinc-air	-zinc metal -zinc alloy -other metals if electrolyte contains zincate ions [49]		-aqueous alkaline electrolyte -solid electrolyte	109.6 mW cm ⁻² using Co-Nx-C bi-functional catalyst [50]

1.3. Zinc-air battery

Zinc-air battery has been involved in long-time development, which can be dated back to 1878. It is also a starting point for all the batteries working with air electrode. The first commercial primary zinc-air batteries were fabricated in 1932. A 20 wt. % NaOH aqueous electrolyte was used, and the current density was 7 - 10 mA cm⁻², this value increased by tenfold in 1960s. In 1995, zinc-air batteries started to be applied in EV.

Larger scale application of zinc-air battery is undergoing, especially in microgrid. The initial rechargeable zinc-air batteries, technically speaking, are fuel cells, which introduce zinc slurry from time to time, and zinc is recovered outside of battery. Efforts on more robust rechargeable zinc-air batteries have never stopped. Companies such as EnZinc (formal CarV3), EDF, EOS Energy Storage, ZAF Energy Systems, NantEnergy (formal Fluidic Energy), ZnR Batteries (EDF filial) have made many progresses in designing and manufacturing rechargeable zinc-based/air batteries [34].

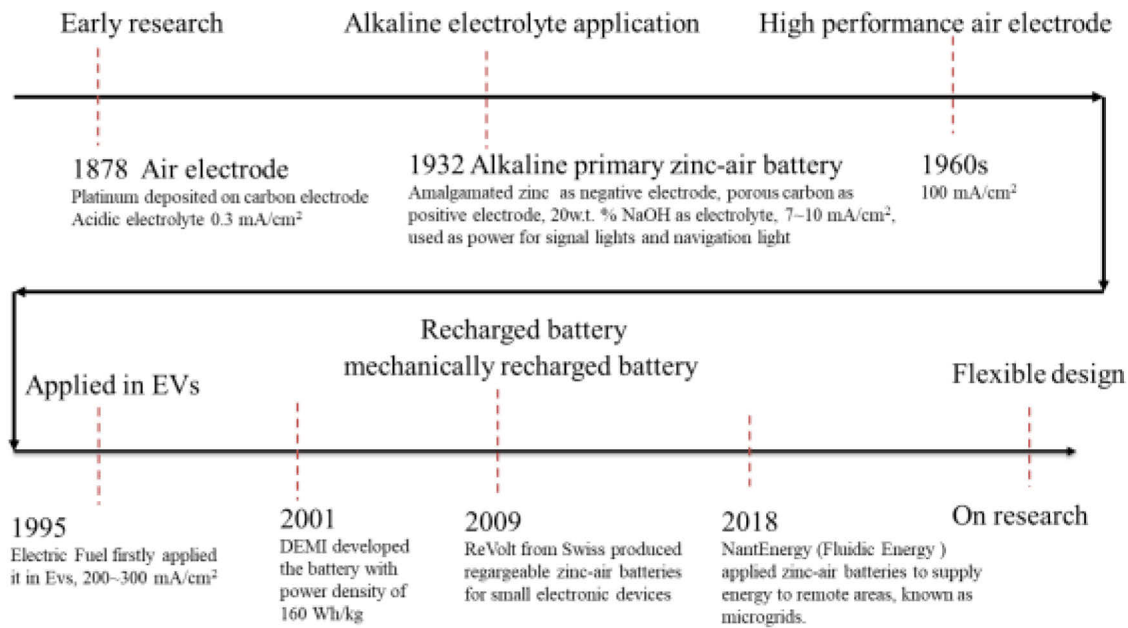
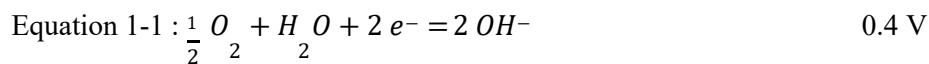


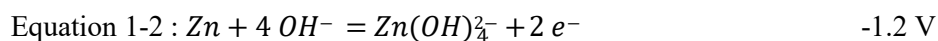
Figure 1-8 : Timeline of development of zinc-air battery

Zinc air battery mainly has four parts, namely a zinc electrode (negative electrode and anode while discharging), an air electrode (positive electrode and cathode while discharging), an electrolyte and a separator. The oxidation state of zinc is various and depends on the pH of the electrolyte. When the pH is low, the products could be Zn^{2+} and when the pH is high, the products could be $Zn(OH)_y^{2-y}$ at $pH = 9.3-12.3$ (normally, $y = 0-4$) and $Zn(OH)_4^{2-}$ at $pH > 13$ [51, 52]. Alkaline electrolyte has been widely used, though a few neutral aqueous electrolytes and some new types of solid-state electrolyte or ionic liquid electrolyte are also applicable in zinc-air battery system from the consideration of inhibiting formation of inactive carbonates, reducing zinc dendrite growth, enhancing the mechanical strength etc.[53-57]. LiOH, NaOH, KOH are three common electrolytes used in both labresearch and industrial applications. Hydroxide ions are the mediums for electron transfers, which can be seen from the two electrode reactions as below:

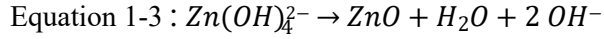
Air electrode reaction during discharge:



Zinc electrode reaction during discharge:



When the battery is discharging, zinc releases electrons then combines with hydroxide ions to form zincate ions. If zincate ions reach their saturation solubility, they decompose to zinc oxide, water, and hydroxide ion.



Oxygen in air accepts the electrons conducted from the exterior cycle and reacts with water to produce hydroxide ion. Hydroxide ions would migrate from the electrode where they are generated to the other electrode through the interior electrolyte. The schematic is depicted in Figure 1-9.

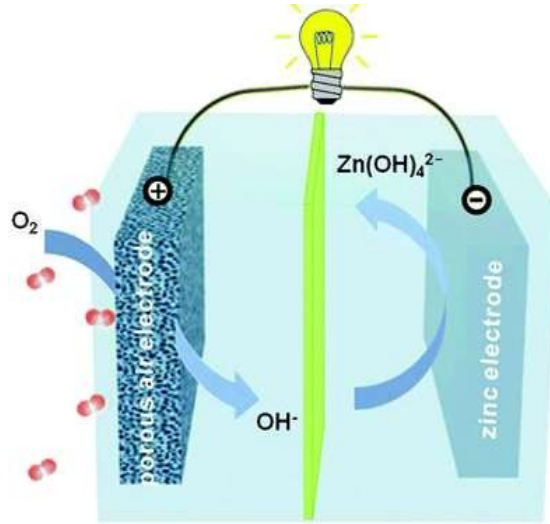


Figure 1-9 : Principle of zinc-air battery [58]

1.3.1. Basic components of zinc-air battery

1.3.1.1. The separator

The separator permits migration of hydroxide ions but hinders the crossing of zincate ions, because zincate ions may precipitate as zinc oxide on the active sites of catalyst on air electrode, which would bring about impairment to catalyst [57]. Besides, the separator plays the main role to physically separate the two electrodes from contacting with each other in avoidance of short-circuit. They are often ion permeable membranes which are expensive because of their fine structures, accounting for 40% of the whole capital cost in a battery system. Considering the cost efficiency, membrane-less batteries are preferred. The separator could be removed under the condition that the active materials of both electrodes co-exist in the electrolyte with minimum loss from self-discharge.

In certain circumstances, zinc-based flow batteries can be designed into a membrane-less configuration as long as that the reactions involve pure solid state transformations, or limited dissolution of the reaction products [59]. As the work of P. K. Leung [60] who proposed a battery installing zinc and para-benzoquinone as the active materials of two electrodes.

1.3.1.2. Electrolyte

The Pourbaix diagram of Zinc is shown in Figure 1-10. The solubility of zinc is high in acidic pH as well as in basic pH. Over the whole range of pH, the hydrogen evolution may also occur. No surface oxide is steady in the purple zone in Figure 1-10 between two dashed red lines characteristic of the water stability zone. Although oxide films may appear in this pH range, they are porous and not passivating, namely not steady. When pH is around 8-11, as shown in the yellow zone, oxide and hydroxide are the stable forms. In this range, the solubility of zinc also strongly decreases. It again increases above pH = 13, since oxide and hydroxide can be dissolved in this strong alkaline environment to form Zn(OH)_4^{2-} or Zn(OH)_3^- , and the solubility increases again with pH [34,61].

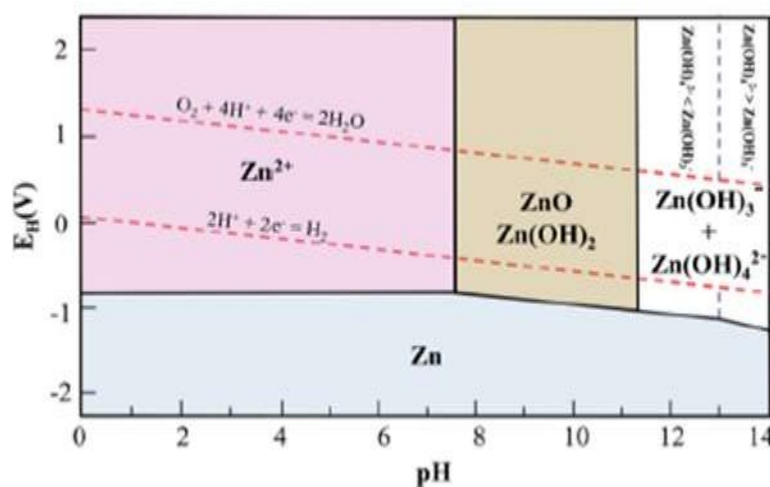


Figure 1-10 : Pourbaix diagram of zinc in alkaline electrolyte at 25°C [52]

Therefore, except few examples of acidic electrolytes, which were proposed to restrain carbonate precipitation on the cathode and zinc dendrite formation on the anode. While it has the sacrifice of severe corrosive problems because the transition metals especially Mn, Co, Fe are unstable in the acidic chemical conditions [62], alkaline electrolytes are mostly used in the zinc-air batteries. NaOH and KOH solutions are quite often the choices, of which KOH is preferable in terms of the activity of both zinc and air electrodes because it has lower viscosity, higher ionic conductivity (the ionic conductivity of K^+ is $73.51 \text{ S}\cdot\text{cm}^2 \text{ mol}^{-1}$, Na^+ is $50.11 \text{ S}\cdot\text{cm}^2 \text{ mol}^{-1}$, and Li^+ is $38.71 \text{ S}\cdot\text{cm}^2 \text{ mol}^{-1}$) and higher oxygen diffusion coefficient. The solution with KOH concentration of 6-7 M (26-30 wt.%) is evidenced to provide highest conductivity of around 640 mS cm^{-1} at 25°C [63]. 9 M (37 wt.%) KOH is also frequently adopted in preference of low corrosion gassing [46]. There appear some new forms of electrolytes like solid and gel alkaline electrolyte for the sake of avoiding leakage or evaporation of water [64-66]. The properties and performance of KOH in perspective to its mass ratio are shown in Figure 1-11. Compared to NaOH and KOH, LiOH is less reported as electrolyte in the zinc-air batteries because of the lower solubility of LiOH and higher price as compared to KOH.

However, in the rechargeable nickel zinc batteries, LiOH can be added as an additive in the KOH alkaline electrolyte. It is reported that Li^+ can suppress the oxygen evolution in convenience of NiOOH recharge [66]. The presence of LiOH is also believed to be helpful for zinc electrode, from the aspect of stabilizing supersaturated zincate ions, and therefore depress the passivation effects [67].

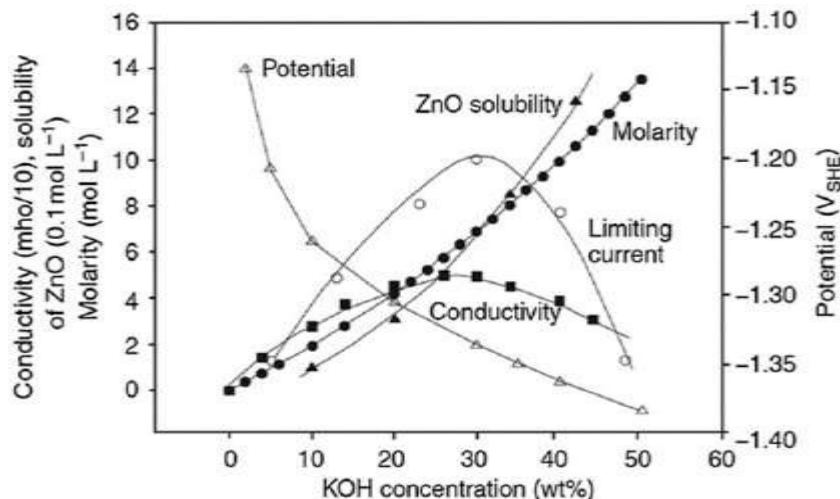


Figure 1-11 : Performance and properties of alkaline electrolytes as function of KOH concentration [52]

1.3.1.3. Catalysts and positive electrode

In the commercialized primary zinc-air batteries, Pt is the active catalyst for oxygen reduction reaction (ORR). While in strong alkaline electrolytes, hydroxide species are prone to cover on the Pt surface, which suppresses its catalytic activity [68]. Transition metals are widely utilized as ORR catalysts, some of them are reported to have better activity or stability than the reference Pt [69]. From the standpoint of rechargeable zinc-air battery, the inverse reaction of ORR, oxygen evolution reaction (OER) is also quite important to realize. Bi-functional oxygen electrocatalysts are pursued to fulfill the realization. Transition metal-based or metal-free bi-functional catalysts are synthesized. Catalysts with superior ORR and OER catalytic performance respectively are combined in one electrode, acting for their part in the charge-discharge cycles separately. Besides, the battery structure is another alternative. Two-electrode structure or tri-electrodes ensures ORR and OER occurs at different electrodes, which avoids the problem of catalyst destabilization and peeling off by evolved oxygen.

In the following chapters 2 and 3, more will be focused on the zinc electrode and the different catalysts for Oxygen reduction (ORR) and discuss the mechanisms. In most applications nickel has been used as the cheapest compromise for OER (recharge of the battery) between cost and efficiency.

1.3.2. Challenges of zinc-air battery

Though zinc-air batteries have been broadly and deeply researched and developed for near a century, they are applied within a small scale for now. The application reaches only in the regime of

primary battery, such as hearing aids and electronic devices [70]. Various challenges surround its development into rechargeable batteries. The impedance is not about the possibility but the scaling-up which should take multifarious parameters e.g., cost, efficiency, safety etc. into consideration. Though hard situation for scaling, there were many sporadic real exemplifications of electronic vehicles driven by zinc-air batteries, as well as smart grid based on battery energy storage. EOS Energy Storage had established the storage grid scaled by 1 MW/4 MWh zinc-air battery with a cost of 160 US\$ kWh⁻¹. Fluidic Energy has fulfilled 6 years' reliable operation of the zinc-air battery storage system, with two times longer life span than lead acid battery and less energy cost. Except for the achieved accomplishment, more and more enterprises join to work on a carbon-free smart grid [71]. The improvement in durability and efficiency of zinc-air batteries develops not only from the advancement of the two electrodes, but also focusing on the design of the cell structure [46]. The tapered-end structure has been proved both experimentally and computationally to eliminate clogging problems [72].

1.3.2.1. Dissolution of zincate ions

Concerning secondary battery application, reversible dissolution-redeposition of the zinc electrode is required. If there is a consensus on the final dissolution product Zn(OH)₄²⁻, discrepancy still lies in zinc anodic dissolution mechanism as presented in Figure 1-12. The differences relates to the dissolved products, the intermediates, the absorption, and the states of solvation [52].

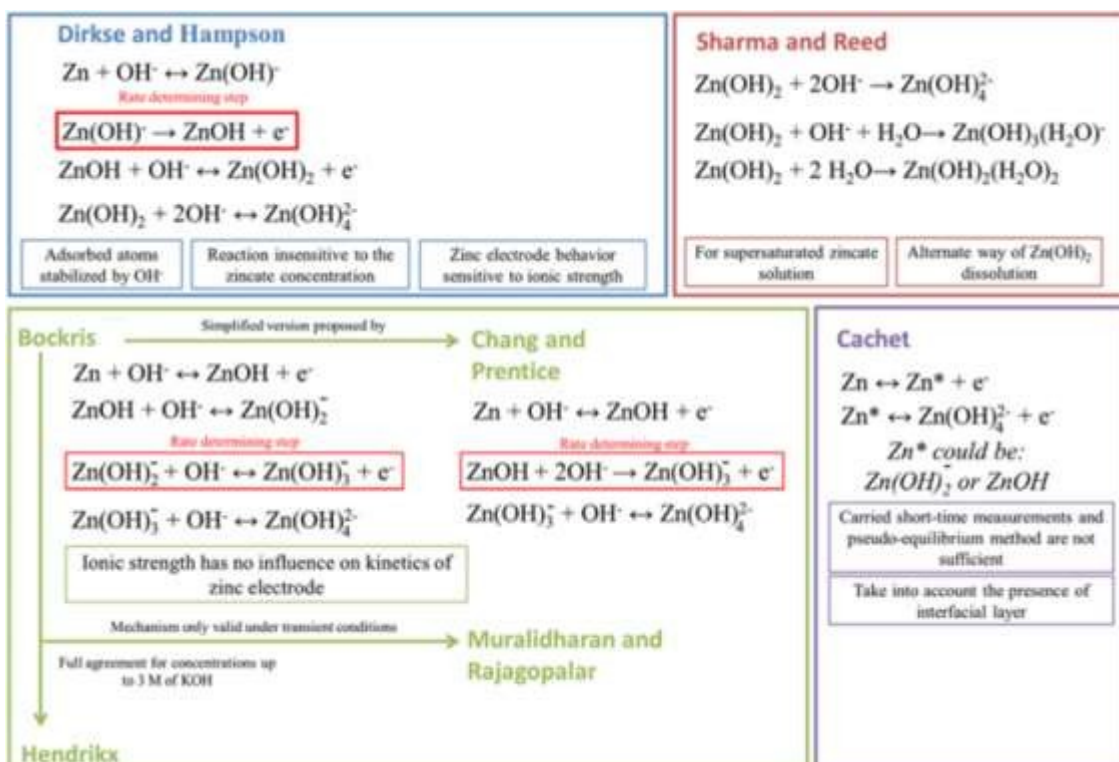


Figure 1-12 : Proposed mechanisms for zinc dissolution [52]

Considering different measuring techniques (galvanostatic method, potentiostatic method, single-pulse, double-pulse etc.), experimental conditions (different zinc electrode, setup etc.) in different articles, some discrepancies exist in the value of exchange current, the relationship between the exchange current density and the electrolyte composition, especially the zincate, thus resulting in different reaction orders and mechanisms. Dirkse and Hampson [73-75] adopted different methods obtained accordingly that the exchange current density is independent on zincate concentration in KOH electrolyte, though with distinct values of exchange current densities. Contrary to Dirkse and Hampson, Bockris et al. [76], Hendrikx et al. [77] and Muralidharan et al. [78] insisted that concentration of zincate is relative to the exchange current density, and obtaining different reaction orders from that of Dirkse and Hampson. Chang and Prentice [79, 80] put forward a similar mechanism to that of Bockris, while they deemed one rate-determining step (from ZnOH directly to $\text{Zn}(\text{OH})_3^-$) which in Bockris' mechanism was divided into two steps (ZnOH firstly formed to $\text{Zn}(\text{OH})_2^-$, then to $\text{Zn}(\text{OH})_3^-$), was rate-determining. The relative experiments were conducted under different conditions, and the related assumptions were also different, none of them could dominate the reality. While in general, the relationship between OH^- concentration and exchange current density is in accordance, i.e., the more OH^- , the higher exchange current density, except that there is a summit value at OH^- concentration of 7 - 8 M indicated by Dirkse and Hampson. Later, Mokaddem et al. [81] evidenced the formation of zinc hydroxide film on the surface from experiment which is a rejection to Bockris' mechanism because in Bockris' mechanism, $\text{Zn}(\text{OH})_2^-$ was transformed to soluble $\text{Zn}(\text{OH})_3^-$. The different reaction orders obtained between them also indicate the divergence though consistency is reached to the point that Tafel slope was reported to be almost independent of electrolyte composition in both cases [82] shown in Figure 1-13. Sharma and Reed [83] suggested that in anodic supersaturated zincate alkaline electrolyte, OH^- and H_2O served as ligands to form soluble zincates $\text{Zn}(\text{OH})_2(\text{H}_2\text{O})_2$, $\text{Zn}(\text{OH})_3(\text{H}_2\text{O})^-$ apart from $\text{Zn}(\text{OH})_4^{2-}$. Cachet et al. [84-86] emphasized an interfacial layer interpretation and indicated that there were at least four adsorbates during zinc deposition and dissolution, they proposed a general mechanism including the two most important reactions which involved electron transfer, which were not the only existent processes.

Overall, the zinc anodic dissolution is quite a complex process, depending on the electrode and electrolyte nature, and involves various intermediates including adsorbates on electrodes or solutes in electrolyte.

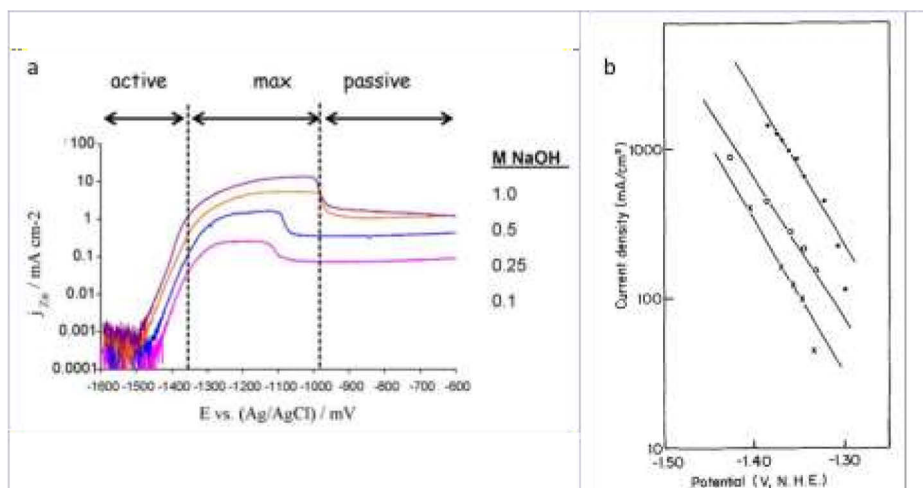


Figure 1-13 : Tafel behavior of zinc dissolution (a) in different concentrations of NaOH electrolyte (active part) [81]; (b) in different zincate concentrations, solid black circle, 0.5 M, hollow circle, 0.082 M, cross, 0.051 M [76]

Zinc dissolution process is a process that industrial application is one step ahead to lab mechanism research. Nevertheless, the mechanism study is still not clear though much insight has been shed on this topic. Aiming to have a better understanding and acknowledge about the intrinsic nature of zinc dissolution and deposition and further serves for better application conditions e.g., electrolyte composition selection or additive adoption, the relative mechanisms are referred above. In this work, experimental conditions would be more approachable to the industrialized battery, the corresponding electrochemical performance concerning zinc deposition and dissolution will also be discussed.

1.3.2.2. Non-uniform dissolution and redeposition dendrites

Apart from the kinetic mechanism study, zinc dendrite growth during zinc deposition is another research focus because zinc dendrites growth resists the industrial development of zinc-based batteries. The electrochemical reaction from zincate ion (2^+) to zinc metal (0) is easily realized, but nonuniform potential or current distribution along the electrode results in nonuniform zinc deposition. The non-uniformity issues around zinc electrode are related to four phenomena, i.e., dendrite growth, shape change, passivation, and hydrogen evolution. Its schematic is shown as Figure 1-14.

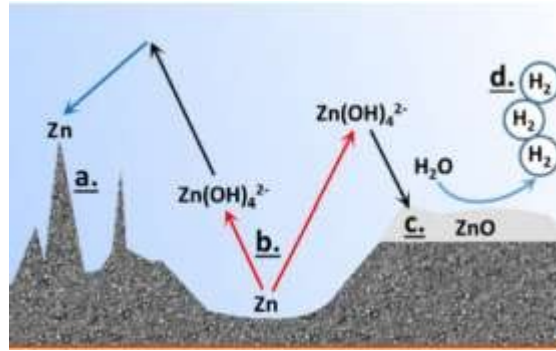


Figure 1-14 : Schematic representation of performance-limiting phenomena that may occur on the zinc electrode: a) dendrite growth, b) shape change, c) passivation, and d) hydrogen evolution [38]

Dendrites are mineralogical defined as the arborization formed by fine crystals. Morphologically, dendrites are sharp and needle-like metallic protrusions [38]. Macroscopically, it is widely accepted that dendrite is caused from high solubility of zincate ions in KOH electrolyte [34]. There are many statements from researchers during last 50 years supported by their simulation and experimental work about the cause and mechanism for zinc dendrites growth [87-89]. While the most acceptable conclusion is that zinc dendrite growth is associated to diffusion-limited mechanisms [38, 87, 90].

The research on the mechanism of dendrite formation includes:

- 1) exploring the main parameters affecting the time initiation of formation, the propagation rate, etc.
- 2) model establishing to quantify the relationship between the main parameters.
- 3) experimental and numerical testifying of nucleation kinetics [88, 91].

Shape change is caused by uneven current distribution within the zinc electrode, generated from uneven reaction zone and convective flow of the electrolyte. It is a general phenomenon including dendrites. Indeed, the dendrite formation starts from the random nucleation induced by impurities or dislocation, which would generate a nonuniform current distribution. In turn, the heterogeneous current density facilitates the protrusion growing, until the radius of curvature of its tip decreases to a value comparable to one percent of the diffusion layer thickness; meanwhile the protrusion grows across the linear diffusion layer to undergo spherical diffusion. Under this condition, the plate-like precursor would change into sword-like dendrites. Not all the precursors would grow into dendrites because the current is mostly drawn away by the dendrite first appeared, leaving the rest unable to achieve the condition of tip radius of curvature. Nevertheless, it may cause more severe problem piercing the electrodes and whereby cause short-circuit of the battery due to fast dendrite growth [88, 89, 91].

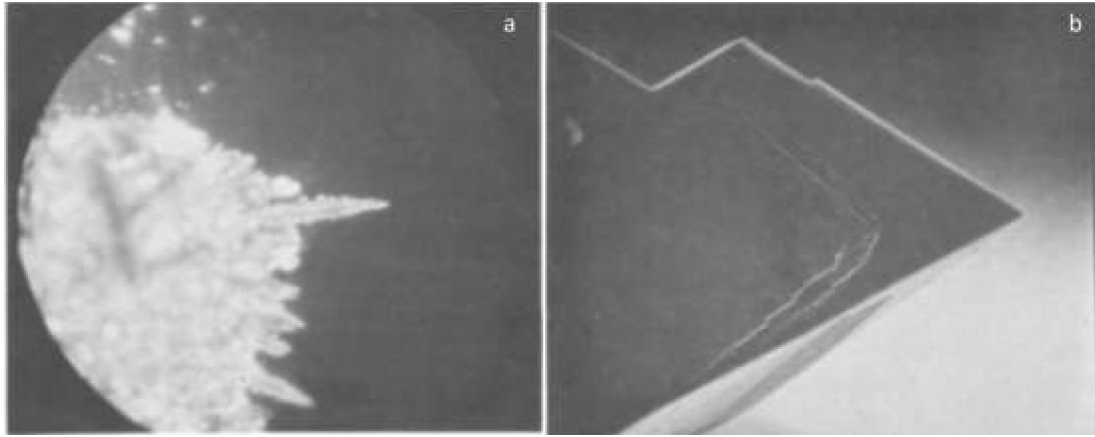


Figure 1-15 : (a) The typical pictures of zinc dendrites 75× magnification; (b) tip of one dendrite 850× magnification [89]

1.3.2.3. Passivation during discharge

Passivation occurs when normal discharge is limited by the formation of an insulating film on the electrode surface, it is termed as passivation. Passivation will occur when the zincate ions reach their saturation concentration near the surface of electrode. Then, they can form compact zinc salts, oxide or zinc hydroxide films which coat the surface of the electrode, blocking the reactive sites and resisting the effective discharging process [82, 92]. Normally, zinc oxide is the main passivating film in electrolyte with high KOH concentration [92]. Once passivation gets severe, zinc cannot be deposited, and the recharging can be limited. Huber [93], Hull [94] etc. made noticeable efforts studying zinc passivation in an early age, with the aid of optical instruments and spectroscopic methods. The research is always accompanied by mechanism study of zinc dissolution in alkaline electrolyte. Zinc oxide was mostly detected as the passivating film, and the black color of the passivating film was deemed to a non-stoichiometry Zn/O in the layer of zinc oxide (ZnO_{1-x}).

The main parameters that influence zinc passivation include pH of electrolyte, composition in the electrolyte, hydrogen evolution, temperature, convection, and interruption [82, 95]. Generally, there are two types of zinc oxide formed on the zinc surface. They are reported to obey different models. Nevertheless, many authors propose different types of reactions that can be classified in two major classes [81].

- Type I is from normal zinc dissolution-precipitation model, that zinc is dissolved to form $Zn(OH)_4^{2-}$, with the saturation of $Zn(OH)_4^{2-}$, ZnO is precipitated. It is porous and it still allows OH^- diffusion although it decreases its diffusion rate towards the electrode surface.



- Type II is deemed to be formed via nucleation and growth model and/or via adsorption model. Nucleation and growth model proposes that zinc reacts directly with OH⁻ to form ZnO, and adsorption model indicates that certain adsorbed species rejects protons and form ZnO [61, 96, 97]. It is compact and responsible for the local passivation.



So, the differences would be between a uniform deposition of porous zinc oxide or the local deposition of a dense zinc oxide.

The interfacial pH is a critical factor for forming the two types of ZnO. The slow-down of the transportation of OH⁻ towards the electrode surface by type I porous ZnO may result in a decrease of interfacial pH, and form type II dense ZnO [61]. Type II ZnO could also form directly under the condition of low pH and saturated zincate ions [34], which is consistent to the hypothesis in [81] that passivating oxide may be formed from phase transition of type I to type II or it may be formed independently. Though passivation is detrimental to zinc anode, it is only a small amount and appears only in a certain potential range [81]. ZnO formation decreases the porosity of the commercial porous zinc electrode because of its higher volume than that of zinc, based on which, it is needed an initial zinc electrode with a porosity of 37% theoretically (Zn paste). While in reality, the required porosity is twice, because the thickness of the electrode also induces the ZnO formation due to resistance of the diffusion of hydroxide ions [98].

1.3.2.4. Hydrogen evolution

Passivating ZnO film on the electrode not only makes a barrier to the contact of active zinc with electrolyte, but also decreases the potential for hydrogen evolution, therefore makes easier the hydrogen evolution on the surface of the ZnO film [99]. While ZnO as an additive in the alkaline electrolyte (forming zincate ions), can suppress hydrogen evolution and does not encourage electrode passivation, while it must be noted that a low concentration with a mole ratio of additive to KOH being around 1 : 1000 should be kept [100]. On the other hand, high ZnO concentration in the alkaline electrolyte is advantageous to suppress zinc dendrite formation.

Hydrogen evolution results intrinsically from higher reduction potential of hydrogen evolution reaction (-0.86 V) than that of Zn(OH)₄²⁻/Zn (-1.2 V). It is thermodynamically favored, while it is a side reaction in zinc-air batteries. Because of the above detrimental effects, the utilization efficiency of zinc material is less than 60%. Based on the above, the good way to restrict the hydrogen evolution during discharging is to increase the overpotential of hydrogen evolution reaction. Though hydrogen evolution occurs during all the pH range according to Pourbaix diagram of zinc, it is not the dominant cationic reaction when pH is between 4 - 12 in the case of zinc corrosion, instead, oxygen reduction

becomes dominant [101]. When external current is applied on the electric circuit of zinc-air battery, the hydrogen evolution may also occur on zinc electrode during charging, which decreases the coulombic efficiency of charging process. If the passivating oxide film forms on the electrode, OH⁻ diffusion to the surface is retarded, pH decreasing would be the reason that hydrogen evolution is easier to occur, corresponding to the decrease of overpotential of hydrogen evolution reaction, as mentioned above [99]. Overall, the above problems occur during the processes of discharge-charge cycles of zinc-based alkaline rechargeable batteries that include active materials diffusion from the bulk electrolyte to the surface of electrode, then adsorption on the surface, later reaction (zinc dissolution and deposition) during which there is sometimes formation of new phases, so nucleation and growth is also accompanied. Besides, there may be side reactions and side products, schematically presented in Figure 1-16.

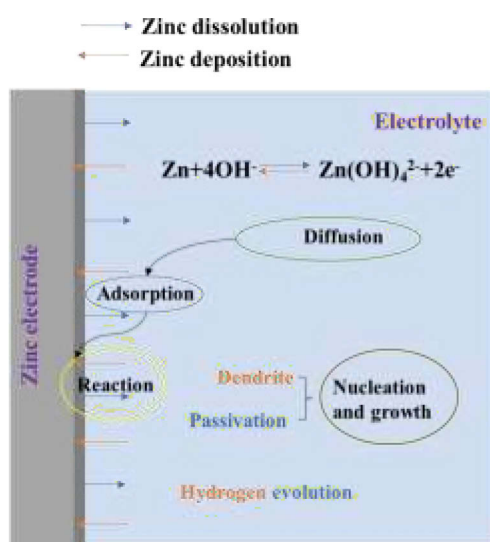


Figure 1-16 : Processes that involved in zinc-based alkaline rechargeable batteries

Considering the utilization of aqueous alkaline electrolyte, water leakage, evaporation, and electrolyte carbonation with atmospheric carbon dioxide are also minor problems compared to the above [102].

1.3.3. Proper solutions to the above problems

For the above problems concerning the zinc dissolution and deposition, there are various approaches to tackle it including additives in the electrolyte or in the electrode, coatings on the electrode, modification of the hydrodynamic conditions, changing the charge-discharge mode, etc. All of them are aimed to modify the kinetics of zinc dissolution or deposition, specifically in the aspect of the diffusion.

1.3.3.1. Additives to reduce dendrites or H₂ evolution

The methods used to depress one of the problems may cause drawbacks to another one, whereas it is also the case that one method can solve several of the problems concurrently. Especially, the way to avoid zinc dendrite growth from the perspective of increasing hydroxide concentration is also good for preventing zinc passivation; while increasing the surface area of zinc anode is good for inhibition of passivation, while intensifying anode corrosion [103]. The mechanism and the methods to depress the zinc dendrites growth have been widely researched. Jens-Christian Riede [104] proposed a critical concentration of zinc ions on the electrode surface, only below which, the zinc dendrites can be totally avoided, whereas obtaining this critical concentration is not controllable. Additives in the electrolyte or electrode could inhibit or suppress zinc dissolution, further, to reduce the possibility of dendrite growth. These additives can be categorized into organic and inorganic chemicals.

The inorganic additives share a priority of their reductive ability due to the metallic ions which would be reduced to act as the substrate of the electrodeposition of zinc and the electro-conductor of the electrode; the organic molecules serve to decrease mass transfer rate of zinc ions [105-107]. The inorganic additives often meet the requirements of being soluble in the electrolyte and having higher standard potential than zinc [108]. But the side effect that they will increase the polarization potential is a compromise, which would generate low coulombic efficiency [59].

Examples of inorganic additives limit the dissolution of zinc (Zn^{2+}), by forming less soluble products, e.g., $Ca(OH)_2$ addition in the electrode engenders the formation of $Ca(OH)_2 \cdot 2Zn(OH)_2 \cdot 2H_2O$ which is insoluble in the electrolyte [67]. Al_2O_3 coated on zinc particles anode is investigated to have a good effect on retarding hydrogen evolution and zinc corrosion by acting as a solid electrolyte with relatively good ionic conductivity to prevent the contact between aqueous electrolyte with zinc particles [109].

The organic additives are often some surfactants which are amphiphilic. They can be divided into three groups according to their ionic characteristics [103]. Their function is to adsorb on the zinc electrode, further, to decrease its contact with water, via which the anode passivation and corrosion could be suppressed. Electrode additive is a less effective way to suppress the shape change or dendrites growth on zinc electrode.

The organic additives in the electrode are usually polymers, which normally act as the binder in zinc electrodes, offering the stable structure. Commonly seen organic additives are cellulose, Polyethylene glycol, CTAB, SDS, PEG-8000, and thiourea etc. [110]. The cycle life of the zinc-based secondary cells can be significantly improved with the binder.

Some additives have several functions. Cadmium plated on the zinc electrode have a combined function of suppressing dendrite growth and hydrogen evolution [111]. The commonly reported additives in the alkaline electrolyte of zinc-based batteries are listed in Table 1-3.

Table 1-3 : Some reported additives used in alkaline zinc secondary batteries

Additive	Anode form	Bulk	Function	Ref.
Polyethylenimine	Zinc wire	Electrolyte	Suppressing dendrite growth	[107]
Dodecyltrimethylammonium bromide (DTAB)	Planar zinc	Electrolyte	Suppressing Passivation and corrosion	[112]
Poly(oxyethylene)nonylphenyl and pluronic F-127 (P127)	Gelled zinc slurry	Electrolyte	Suppressing Passivation and corrosion	[113]
Ethylene diamine tetraacetic acid (EDTA)	Zn-Ni alloys film	Electrolyte	Prevention of dendrite formation	[114]
Sodium dodecyl benzene sulfonate (SDBS)	Gelled zinc slurry	Electrolyte	Suppressing passivation	[95]
Sodium dodecyl sulfate (SDS)	Zinc sheets	Electrolyte	Suppressing Passivation and corrosion	[115]
Triethanolamine	Zinc paste anode	Electrolyte	Formation of complex and reduction of the solubility of zincate ions	[116]
Tartaric acid	Vitreous carbon	Electrolyte	Inhibition of zinc dendritic deposits	[117]
Bismuth and lead alloyed	Zinc alloy powder	Electrode	Suppression hydrogen evolution	[118]
Ethanol	Pristine graphite felts electrode	Electrolyte	Suppressing zinc dendrite by decreasing exchange current density of zinc anode	[119]
Ethanol	Zinc granules	Electrolyte	Hinderance of passivation	[119, 120]
Bismuth ion and tetrabutylammonium bromide	Planar zinc electrode	Electrolyte	Inhibition of zinc dendrite growth	[121]

Na ₂ WO ₄ and lead	Deposited zinc electrode	Electrolyte	Inhibition of dendrite growth	[108, 122]
Aluminum oxide (Al ₂ O ₃)	Al ₂ O ₃ coated on zinc particles	Electrode	Inhibition of hydrogen evolution	[109]
I ³⁻	Graphite felt electrode	Membrane	Consuming zinc dendrite	[123]
Bismuth and calcium	Pasted zinc electrode	Electrode	Formation of conducting matrix to reduce the solubility	[124]
Barium hydroxide	Pasted zinc electrode	Electrolyte	Formation of complex and reduction of zinc dendrite growth	[125]
LiOH	-	Electrolyte	Stabilization of zincate ions and suppressing passivation	[67]
Sn	Carbon felt	Electrode	Suppressing both zinc dendrite growth and hydrogen evolution	[126]
(NH ₄) ₂ CS	Porous zinc electrode	Electrolyte	Suppression of passivation	[100]
HgO and TiO ₂	Porous zinc electrode	Electrolyte	Inhibition of dendritic deposition	[127]

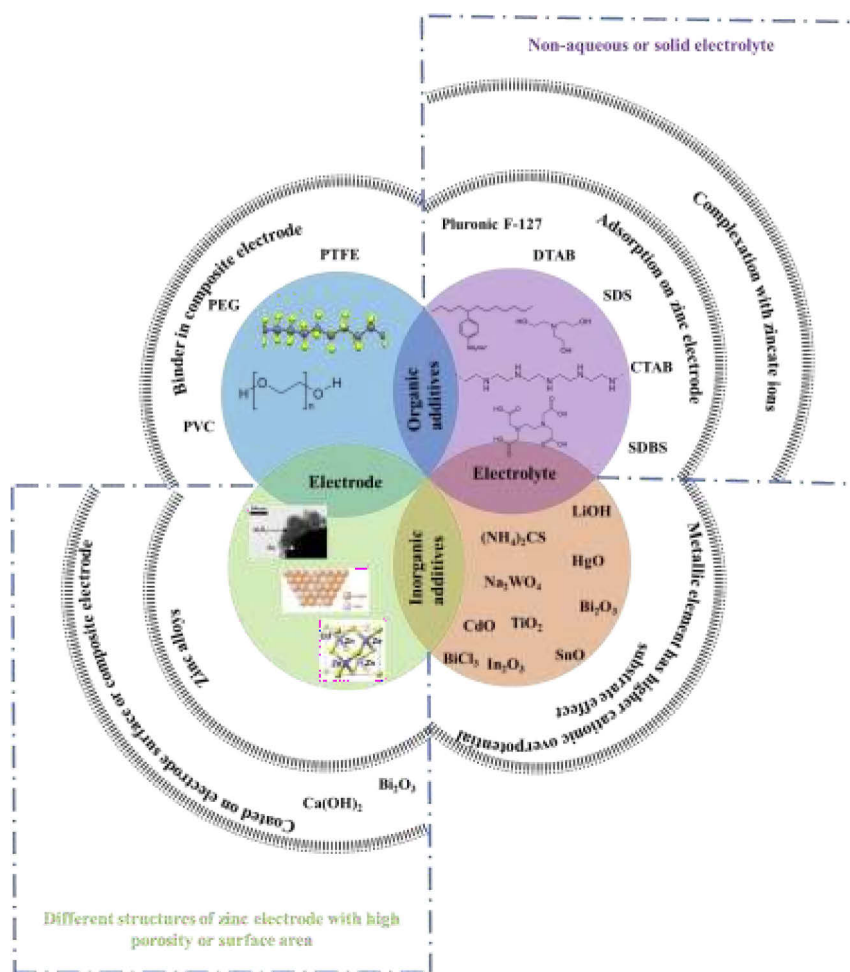


Figure 1-17 : Methods to improve zinc electrode performance by organic or inorganic additives in electrode or electrolyte, or newly fabrication of electrode or electrolyte

Additives in electrolyte or zinc electrode either play a role of adsorbents separating electrolyte and electrode, or reacting (complexation) with the zinc ions, avoiding their saturation, or increasing the anode overpotential. Additives and their functions in zinc-based batteries are schematically shown in Figure 1-17. Sometimes the same additive in electrolyte or electrode has the same effect on zinc dissolution and deposition process, like lead, bismuth; while some additives in electrode or in electrolyte give an inverse effect [128].

1.3.4. Zinc-air flow battery

Besides additives, flowing electrolyte is a special measure that has multiple advantages to zinc-based batteries. Flowing electrolyte enhances the mass transfer of the electrolyte, which is advantageous to suppress dendrite growth. On the other hand, flowing electrolyte can remove the gas evolved on the air electrode, which prevents gas bubbles or the gas from adsorbing on the electrode

and decreasing the reactive area. Besides, from a practical view, flow battery is feasible to scale up power or capacity by simply refreshing the electrolyte.

1.3.4.1. Effect of flow on dendrites hydrogen evolution and passivation

Flow is reported to have a good effect on suppressing the formation of passivating films and zinc dendrites [103].

Zinc dendrite suppression: Electrolyte flow in zinc-based batteries reduces the zinc dendrite growth rate or even eliminates it, therefore it enhances the cyclability, though in some cases zinc dendrite cannot be totally inhibited [119, 123, 126, 129-132]. Dendrite growth is a non-equilibrium deposition process, as is believed that the morphology of crystals is dependent on the ‘distance’ from the thermodynamic equilibrium shown as Figure 1-18, and flowing electrolyte is an effective way to make the system closer to thermodynamic equilibrium by changing diffusion control to convection control [130, 133].

Hydrogen evolution can be also suppressed by flowing electrolyte because the flowing electrolyte can avoid the situation concentration gradients near the electrode surface which causes hydrogen evolution rather than zinc deposition [49, 134].

Besides, flowing electrolyte has also been proposed in zinc-organic hybrid flow batteries for the convenience of increasing cell voltage by flowing two different electrolytes separately, especially with non-aqueous electrolytes [119, 135, 136].

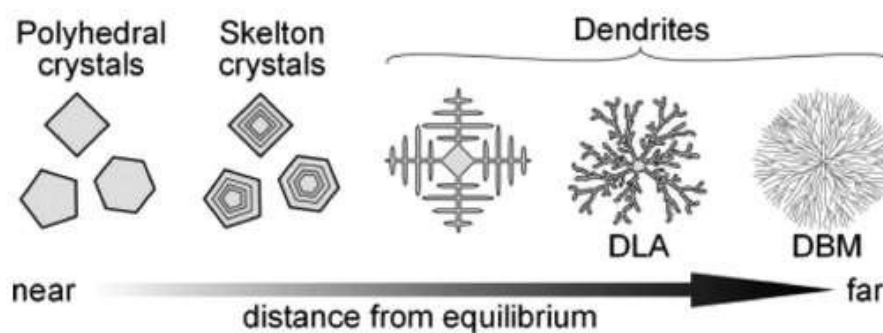


Figure 1-18 : Schematic illustration of a correlation between the distance of the formation conditions from the equilibrium and the morphologies of formed crystals [133]

1.3.4.2. From zinc-air to redox flow batteries

From the common view, flow batteries have the attractive characteristics of high safety, high energy efficiency, long cycle life, and environmental friendliness [137]. Besides, it allows membrane-less structure fabrication, therefore it can be cost-effective [131]. Flow may also allow to transport species to an external tank of reactants which may also allow to store a large capacity of energy whereas the surface area of the electrode determines the power of the cell. So, power (W) and energy

(Wh) can be easily decoupled. Though flowing electrolyte cannot be totally inhibited the dendritic growth in actual cases with cycles going on, it could limit it to a great extent.

Rechargeable zinc-air flow batteries have two different operation modes. The more practical one is the combination of zinc-air flow primary battery and zinc electrolyzer system which is also known as zinc-air fuel cell, compartmenting the discharge and charge processes in two different cells. The fresh zinc is provided as fuel when discharging, and its regeneration is realized in another electrolyzer system. The flowing electrolyte with the discharged products can be introduced into the electrolyzer where zinc is deposited. This mode is also termed as mechanical recharge. The other mode is electrical recharge where both charging and discharging processes are fulfilled in one cell. The main problems are the deterioration of air electrode caused by the evolved oxygen, and dendrite growth. The mechanical rechargeable zinc-air batteries have been pilot demonstrated and applied in small scale regional energy storage [138]. The electrical ones remain in laboratory development enormously due to its great potential in operational flexibility and cost efficiency. In the electrical recharge batteries, two- or three-electrodes are the main configurations. Three-electrodes configuration separates oxygen reduction reaction (ORR) during discharge and oxygen evolution reaction (OER) during charge on two separate electrodes, while zinc electrode is shared during both.

From the literature we observe that flow battery has the effect to limit the dendritic growth [139], to increasing the cyclability but also it makes the negative (zinc) electrode simpler. It can be a simple foil or plate instead of a porous paste since zincate ions are not supposed to precipitate locally since they are carried away by the flow [140]. They usually highlighted with significant cyclability [141]. Not many applicable zinc-air flow batteries are realized with high performance, the limited papers or patents are presented here, the overall cycling performance and technique details are shown in Figure 1-19 and Table 1-4. All these data suggest that a flowing zinc – air battery cell can be built with a reasonable current density of 50 mA cm^{-2} and a corresponding power of 50 mW cm^{-2} .

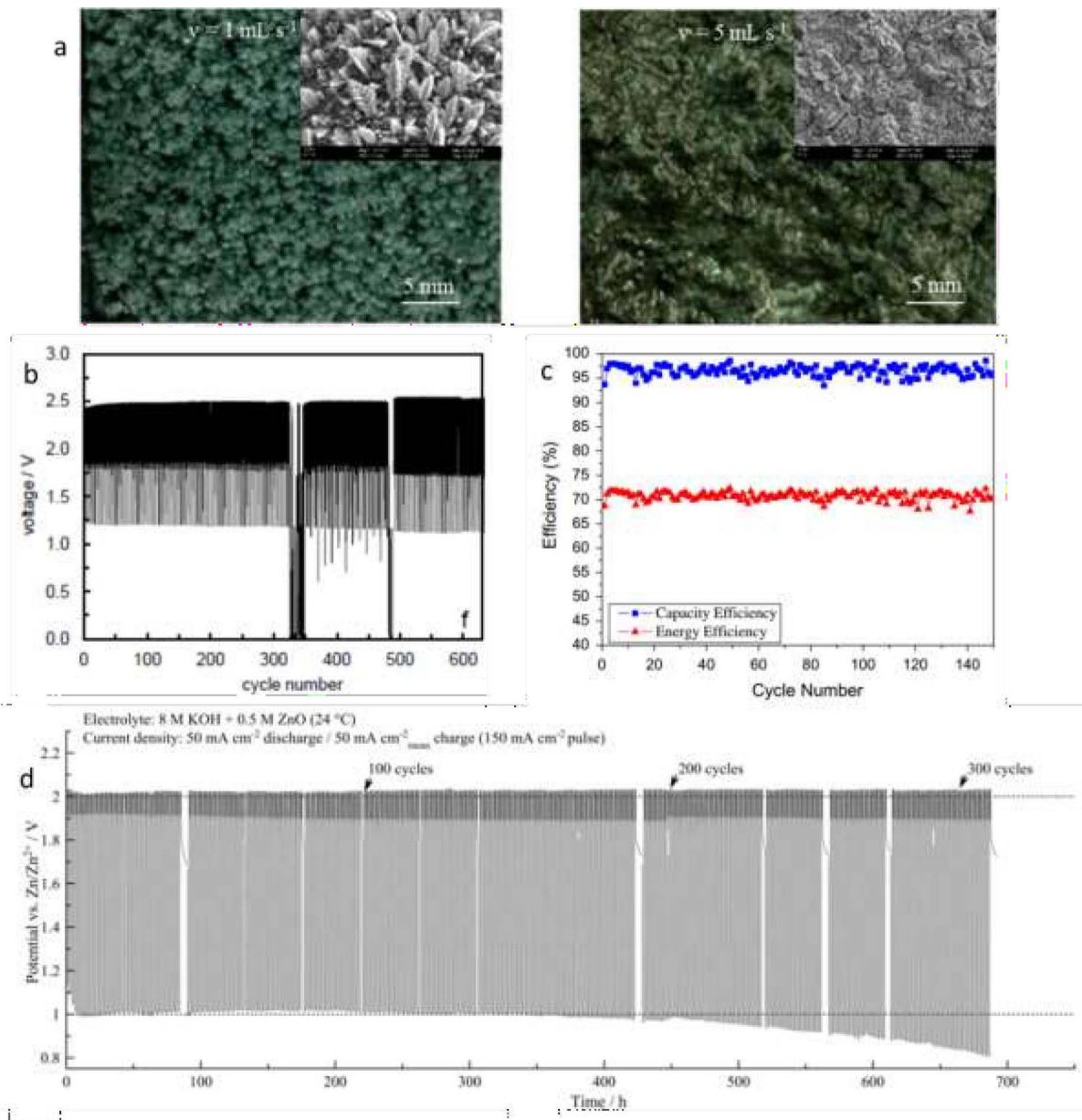
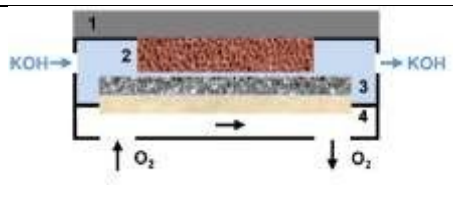
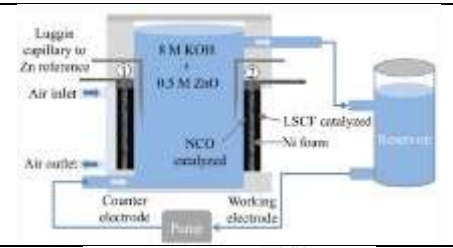
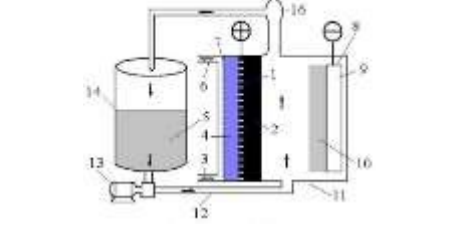
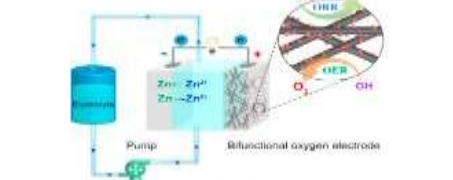
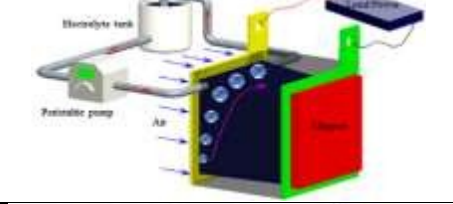
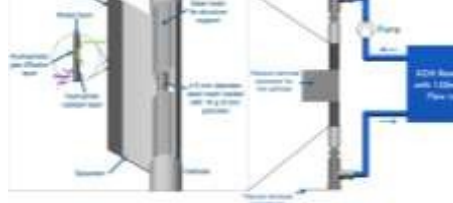


Figure 1-19 : (a) The morphology of zinc electrode after the cycling of the battery at different flow rates [139]; (b) (c) (d) cycling performance of zinc-air flow battery [140, 141]

Table 1-4 : Some reported zinc-air flow batteries

Main components in air electrodes	Zinc electrode	Electrolyte composition	Flow rate	Schematic presentation	Ref
Oxygen depolarized cathode for ORR and a nickel foam for OER	Copper foam	30 wt.% KOH electrolyte with 2 wt.% ZnO	0.4 L min ⁻¹		[141]
NiCo ₂ O ₄ for OER La _{0.6} Sr _{0.4} Co _{0.2} Fe _{0.8} O ₃ for ORR	Rota-Hull cathode cylinder	8 M KOH with 0.2 - 0.5 M ZnO	6 or 8 cm s ⁻¹		[142]
β-Ni(OH) ₂ for OER, MnO ₂ for ORR	Copper	7 M KOH- 0.7 M LiOH -0.7 M ZnO	450 mL h ⁻¹		[140]
NiS _x -FeO _y particles on sulfur doped carbon fiber paper	Zinc foil	8 M KOH and 0.5 M ZnO	-		[143]
Fe-based catalyst for ORR, Ni mesh for OER	-	7 M KOH and 0.6 M ZnO	5 mL s ⁻¹		[139]
MnO ₂ as ORR catalyst and nickel foam as current collector	Zinc granules coated on stainless steel mesh cylinder	7 M KOH with SDS (0-8 mM) or P127 (0-1000 ppm)	150 mL min ⁻¹		[128]

1.4. Conclusion

A comprehensive and systematic introduction of zinc-air battery has been done in this chapter. The importance and challenges of zinc-air battery are emphasized. Both academic and industrial developments about zinc-air battery are also mentioned in detail. From the above, we grasp the following main points.

- Renewable sources of energy and energy storage systems are necessary to be integrated into the power grid or supplement other electricity demands to reduce carbon emissions.
- Battery technology as one of the energy storage systems serves well for obtaining the above objective. Compared to the conventional batteries, zinc-air battery takes advantages of its low cost, high theoretical energy density, high safety and few demonstrated cases.
- However, there are some problems related to the aging of the battery (poor cycling) and the low reversibility at the oxygen electrode with a large difference of potential between charge and discharge. This results in poor energy storage efficiency.
- Non-uniform zinc deposition and the catalyst in air electrode as well as the formulation of air electrode are the most important problems to solve.
- Additives in the electrolyte or electrode, coatings on the electrode, the modification of hydrodynamic condition or discharge-charge mode could somewhat solve the problems.
- Among the proposed solutions, flowing electrolyte outweighs due to its multiple functions, e.g., suppression the zinc dendrite growth, removal of the adsorbed oxygen evolving during charging.

Since the most important difficulties are associated to dendrite formation at the zinc electrode and oxygen reduction at the positive electrode, we are going to focus on all these problems in the experimental chapters. Thus, this thesis is ambitious to fabricate an effective zinc-air flow battery. Each part of the battery will be emphasized and discussed in detail, namely, the electrochemical aspects of zinc electrode, electrolyte, air electrode.

In chapter 2 we are going to study the effect of flow on the dendritic growth at the zinc electrode. Low-cost catalysts in air electrode for oxygen reduction with good electrochemical performance will be introduced in the chapter 3. Cyclic voltammetry experiments on DRE have been imposed to measure the corresponding catalytic activity, and the reproductivity of this method will be verified, which is a vital and fundamental part of both the thesis and the related catalysts characterization.

The air electrode with applicable size is further formulated to fulfill the ambitious

flow battery assembly. The formulation route effect will also be introduced. Its electrochemical performance will be presented.

Chapter 2 Zinc electrode

2.1. Bibliographic study on zinc electrode

While primary zinc electrode batteries are widely distributed commercially, secondary zinc electrode batteries have only been sporadically put into market. This can be explained by the properties of high solubility and electrochemical kinetics of the zinc electrode. Much research has been focused on the mechanism of zinc dissolution and deposition, and the accompanied phenomena of passivation and hydrogen evolution are also discussed vastly in the literature [33, 59, 82]. We report in this chapter most of the conclusions obtained from literature on the dendritic growth in terms of mechanisms, kinetics, interferences, and possible solutions, before studying the main parameters controlling the dendrite growth in our specific conditions of flowing electrolyte.

2.1.1. Zinc electrode in zinc-based batteries

Due to the multiple existing zinc-based batteries, various zinc electrodes have been developed to fit with the electrolyte, the positive electrode, and the cell configuration to a certain extent. We can thus find porous Zn electrode formulated with polymer, zinc plate, zinc alloys or Zn-KOH slurry etc. The electrode could also be fabricated in different ways, for example by pasting, precipitation, powder compression, electrodeposition, sintering, etc. [144].

However, in both academic and industrial domains, the zinc-based alkaline batteries are using quite similar zinc electrodes. Materials composing zinc electrode in zinc-based batteries are mainly zinc or zinc oxide particles or their mixtures with certain ratio. The shape of the powders is reported to have different battery performance [144]. The polymer binder material is also important to fabricate zinc electrode, the commonly used binder is PTFE (polytetrafluoroethylene, also known as Teflon) with different specifications. Porosity and pore distribution of zinc electrode is important to the electrode performance. An optimum porosity was identified to be 64% [145], and for polymer-bonded zinc electrodes, porosities of 60-75% are commonly seen. Common ways to generate pores in the electrode is to pre-put something easy to evaporate at higher temperature, e.g., C_4H_{10} [144]; easy to be reacted into gas, e.g.,

NH_4NO_3 [140], $(\text{NH}_4)_2\text{CO}_3$ [146]; or easy to be extracted by some solvents, e.g., DBP (Dibutyl phthalate).

Turney et al. [146] made a systematic work on the Zn-Mn rechargeable battery, emphasizing the performance of zinc electrode. They studied zinc electrodes, specifically modified to show increasing wettability, or permeability, or reducing the hydrogen evolution reaction (HER), etc. It was found that the failure of the battery could result from zinc dendrite growth and accompanied short-circuit, or from zinc passivation which reduced the porosity of the electrode and resisted the permeation of active species, or hydrogen evolution and the accompanied ZnO formation.

2.1.2. Studies on zinc dendrite growth

2.1.2.1. The dendrite issues

Dendritic deposit may cause a short circuit between electrodes or a loss of capacity of the battery when the loose dendrites disconnect from the electrode [38, 147]. To solve the problem, a better knowledge of zinc electrodeposition is unavoidable. The studies related to zinc electrodeposition are focused on two groups of studies: on one side the study which considers the electrochemical reaction on the surface of electrode, the crystallization of zinc onto the substrate; on the other side the study of the morphology of the deposits related to concentration gradients in the cell [88].

For now, the known variables influencing zinc deposition are overpotential, current density, charge mode (electrochemistry) [89, 147, 148]; composition in the alkaline electrolyte, hydrodynamics (electrolyte) [149, 150]; anode substrate (electrode) [49, 151, 152]; cycles, time and temperature.

The uncontroversial conclusions are that pulse charge mode can reduce dendrite growth; that the deposit crystallization is relative to the substrate; and that the electrolyte flow can suppress shape change or the dendritic growth by refreshing the electrolyte and avoiding concentration gradients.

2.1.2.2. The controversy about dendrites origins

The study on the mechanism of zinc electrodeposition was concentrated in the middle of XX century. The studies focused on the morphology of zinc deposits, the growth mechanism of deposits, the controlling variables for morphology, etc. A great number of insightful and well-designed work has been done, while there is always no identical conclusion between them,

which indirectly indicates that the zinc electrodeposition is a process very complete, and the avoidance of zinc dendrite growth is kind of empirical.

On the one hand, when working under galvanostatic conditions, Naybour et al. [153] reported three different morphologies of zinc electrodeposition at different current densities using zinc single crystals with different orientations of the hexagonal zinc lattice (0001) (10-10) (11-20) as cathode substrate. The zinc deposits were dendritic at current density of 100 mA cm^{-2} , they were layer and granular at 20 mA cm^{-2} , and at 4 mA cm^{-2} the morphology was mossy as seen in Figure 2-1.

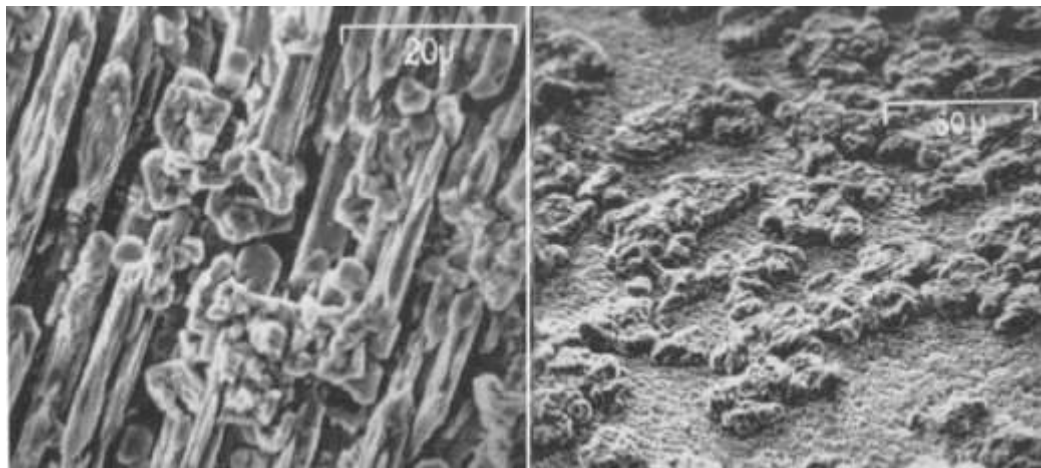


Figure 2-1 : Layer morphology deposited at 20 mA cm^{-2} (left) and mossy at 4 mA cm^{-2} (right) [153]

Wang et al. [149] confirmed these morphologies later with a very systematic work about zinc electrodeposition. They studied the surface conditions of the electrode, the different substrates, the electrolyte compositions, and the temperatures.

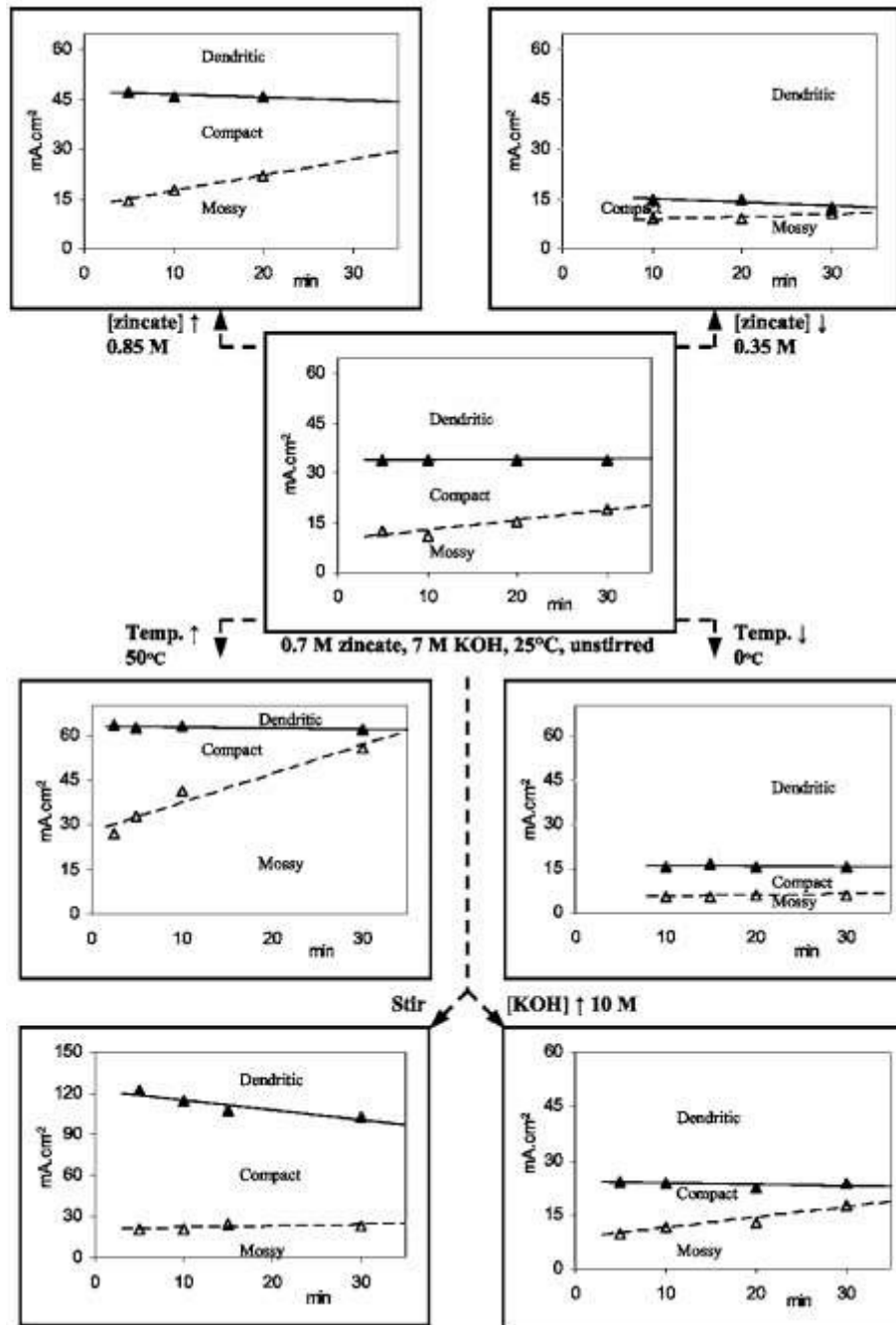


Figure 2-2 : Morphology diagram of zinc deposits [149]

They observed the same morphologies as Naybour (Figure 2-3), and related them with the conditions during kinetic studies (Figure 2-2) and with different growth mechanisms:

- The mossy, the layer-like, and spongy (more likely the layer-like) deposits were grown under activation control.

- The growth of boulder or heavy spongy (large boulder agglomerates and highly branched dendrites) were under mixed mechanisms both activation and diffusion control.
- The dendritic deposits were formed under diffusion control.

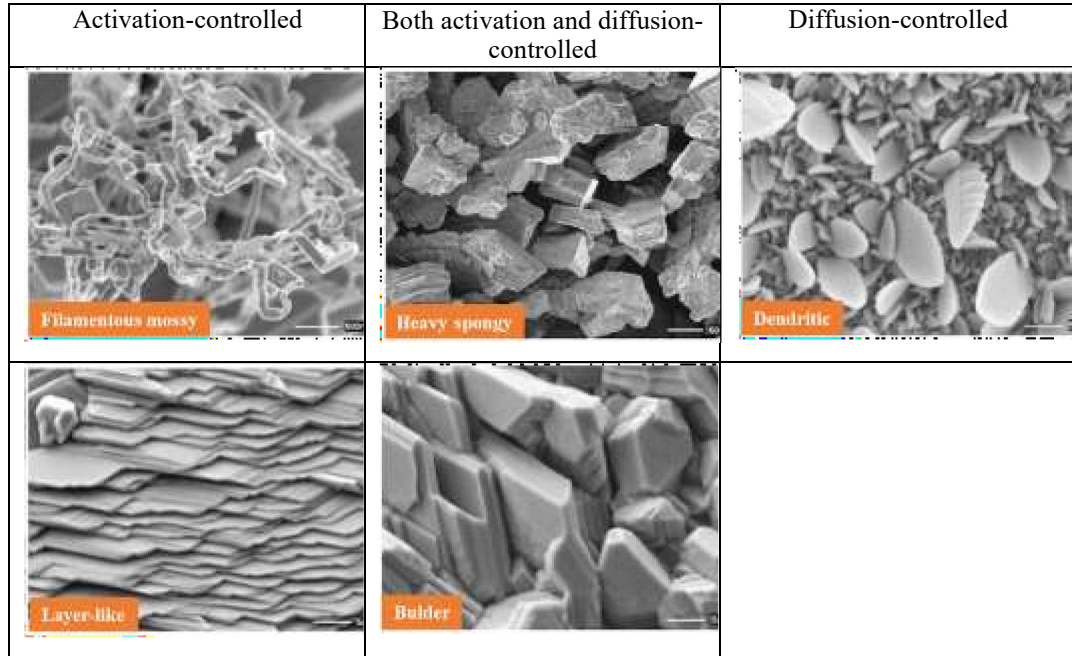


Figure 2-3 : Different morphologies of electrodeposited zinc in work of [149]

Both claimed the current density to be a critical parameter determining dendrite initiation and growth.

Going further into the control mechanisms, Naybour et al. claimed that the orientations of the zinc substrate had an influence on the dendrite growth only in the early growth stage: there were fewer growth sites on the basal planes; while there was no big difference once the dendrites developed, and the dendrite growth direction was indicated to be (11-20), which was also supported by Justinijanovic et al. [154] and the compact morphology was found to grow in the direction of (0001). With this study, they proposed that the dendrite growth occurred when the current is limited by zincate diffusion. Such conclusion is also brought by Wang et al. which experimental results demonstrated that activation control was not responsible for dendrites growth because after dendrites had been initiated, and activation-controlled condition was then imposed, there was only mossy deposits but no dendrites.

Arouete et al. [147] adopted constant currents below and above the so-called critical current to study the type of control of zinc electrodeposition on the zinc foil electrode, emphasizing the effect of pulse charge on more compact zinc deposits, namely increase of deposits adherence. The critical current density marked the transition from activation control to

mass transport control which was dependent on temperature. Mossy deposits occur under activation control and dendritic deposits were deemed to be formed when the electron reaction was controlled by mass transfer. The pulse charging mode could suppress dendrite growth by sparing time for transport of zincate ions towards the electrode and overcome the diffusion control. The main controllable factors are the pulsed current density, the time duration of on- and off-states and ratio of on- and off-times.

On the other hand, under potentiostatic conditions, different conclusions can be given, first proposed by Diggle et al. [89]. They found the morphologies of deposited zinc were related to the overpotential. When the overpotential was lower than 85 mV, the morphology was spongy; and above 140 mV, the deposits became mixed spongy and dendritic; between the two overpotentials, there were dendritic deposits. A critical overpotential for dendrite initiation was proposed to be 75-85 mV. If such specific value of critical overpotential could be further discussed, the works of Bockris et al. [88], Justinijanovic et al. [154] and then Moshtev et al. [91] confirmed that overpotential rather than current density was more likely the controlling parameter of the morphology of deposits.

Diggle et al. also applied a screw dislocation model to present the dendrite initiation and growth, and a basic model extended according to Tafel equation. Based on the models and experiments, they concluded that dendrite initiation was the result of pyramidal growth due to rotation of a screw dislocation under bulk diffusion control. At some optimum value of radius of curvature, the dendrite growth rate became the highest and constant, thus the length of the dendrite would grow linearly with time. They concluded that dendrite growth was under activation control. Their experiments showed that the time required for the appearance of dendrites decreased and the rate of propagation increased as the zincate concentration increased.

Some years later, Justinijanovic et al. [154] observed that dendrites were grown from nuclei of the high index plane, which required a critical overpotential for probability of nucleation of the corresponding type for dendrite growth. They thus proposed a new mechanism of 1-D nucleation for dendrite growth and claimed its preference to screw-dislocation mechanism due to the fast growth, the compact deposits were indicated to obey the growth mechanism of screw-dislocation. The reverse dissolution of the deposits was conducted using anodic currents, and the result are shown in Figure 2-4(b), the dramatic drop of current after some time was thought to originate from the initial faster dissolution of the dispersed deposits as compared to the compact ones.

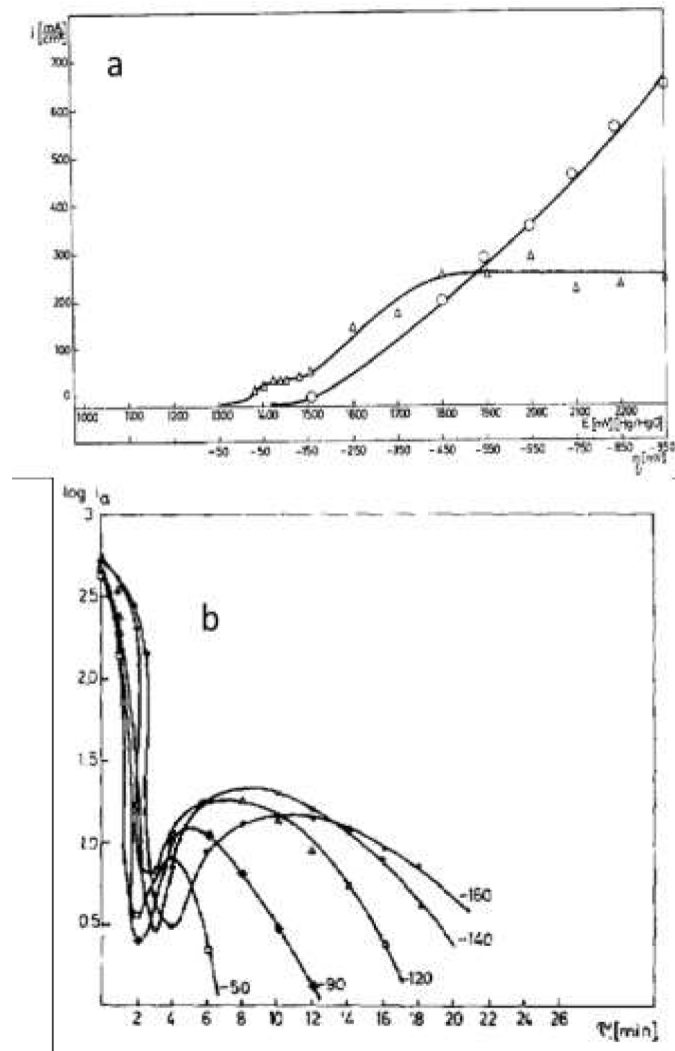


Figure 2-4 : (a) Average current density as a function of potential and of overpotential for zinc deposition (Δ) and hydrogen evolution (O) from alkaline zincate solutions; (b) Current density of anodic dissolution of zinc deposit as a function of time [154]

Bockris et al. [88] also followed the same model of nucleation of dendrite on high-index planes to explain their observations. They applied electrodes with different substrate orientations to study the morphology of the zinc deposits at very beginning of the electrodeposition (only in a timescale of several minutes). They claimed that the morphologies of the zinc deposits were independent on the orientation of the substrate, while the growth rate of the deposits was influenced by the orientations. At each substrate, the morphology was layer-like at overpotential of 50 mV in a mode of epitaxial growth. It was boulder-like at 100 mV, most of the boulders were epitaxial with the substrate while there were others not epitaxial but originated from nucleation. Dendrites could appear subsequently after a period for initiation among the boulder-like deposits, which was supposed to be the precursor of dendrites, the initiation time could be as long as 50 min. The reasonable low proportion of boulders evolved

into dendrites might be resulted from the proof that dendrites only grown from the nuclei on high index planes [154]. At overpotential of 200 mV, dendrites dominated. Overpotential rather than current density was proved more likely as the controlling parameter of the morphology of deposits. Two different zincate concentrations of 0.1 M and 0.02 M were used to study their influence on morphology change, and the results showed the same morphology at the same overpotential in these two electrolytes. Its effect on the dendrite growth was not explored.

Later, Moshtev et al. [91] applied a RDE (rotating disk electrode) to study the kinetics of zinc electrodeposition. They showed a typical potentiostatic current-time (I-t) graph as Figure 2-5(a). There were three regions in the graph, region marked with 'a' might be a result of reduction of oxide film or desorption of some species on the electrode surface. The constant current in region 'b' was deemed the limiting current, and in region 'c' current was linear dependence of time. The intercept of the two regions was marked the transition time τ which decreased with increase of either the rotating rate of electrode or overpotential applied. Experiments showed that the transition time corresponded the visible appearance of sword-like or fern-like dendrites. And the even height of the dendrite was found to be equal to the thickness of diffusion layer, which may also explain the dendrite initiation due to the transfer of linear diffusion to spherical diffusion in Diggle's work. The τC_0 (C_0 : the concentration of zincate ions) varied insignificantly with C_0 and decreased with the increase of the overpotential, unvaried under the constant overpotential and RDE rotating rate. Thus, under the same overpotential and rotating rate, the time for sword-like dendrites growth decreased with the increase of zincate concentration as Figure 2-5(b) shows.

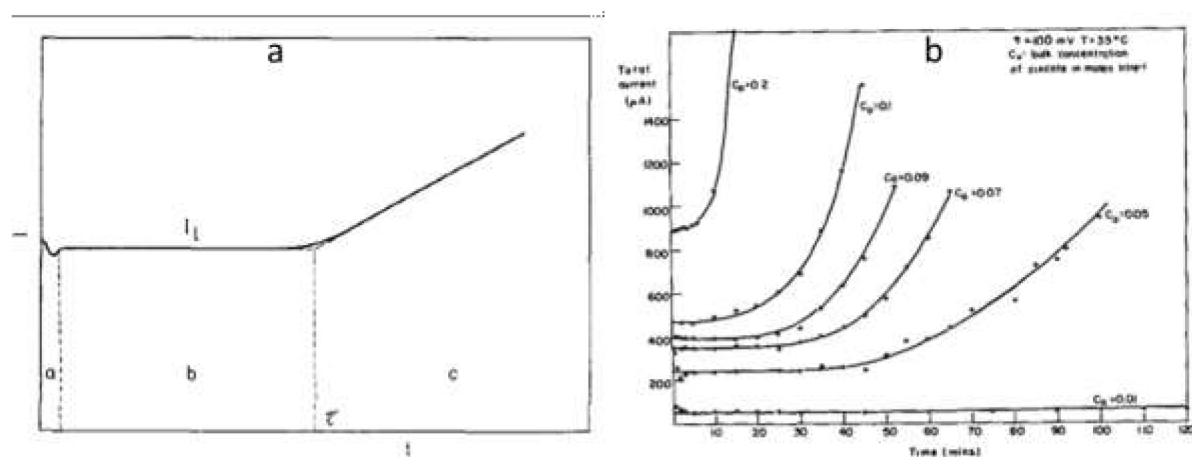


Figure 2-5 : (a) Typical potentiostatic I-t curve on the RDE [91]; (b) Total current-time relationship as a function of zincate concentration [89]

The related studies on zinc electrodeposition are listed in Table 2-1, the conditions of the electrodes and electrolytes, the corresponding growth model, and the general conclusions are included for easy comparison.

Table 2-1 : The proposed mechanisms of zinc electrodeposition in references

Conditions	Model	Morphology	Conclusion	Ref
Electrode: single zinc crystal with different orientations Electrolyte: 5 M KOH saturated with ZnO; Galvanostatic control	-	Dendritic at 100 mA cm ⁻² ; layer and granule at 20 mA cm ⁻² ; mossy at 4 mA cm ⁻²	1. The density of dendrites was about the same (~10 ⁶ cm ⁻²) for all substrate orientations; 2. Dendrites grown in the direction of (11-20)	[153]
Electrode: Pt sphere electrode Electrolyte: 10% w/w solution of KOH, 0.01 and 0.2 M ZnO; Potentiostatic control	Kinetic model: extended to the Tafel region of overpotential; Growth model: Screw-dislocation	Dendritic at -85- -140 mV; Spongy and dendritic at < -140 mV; spongy at > -85 mV	1. There was a critical overpotential for dendrite initiation; 2. Dendrite initiation was attained until the required radius of curvature giving rise to spherical flux to the propagating tip; 3. Dendrite growth was linear with time under activation control	[89]
Electrodes: zinc sheet, electrolyte: 43% KOH solution 1.13 M zincate; Galvanostatic control	-	Smooth, black and porous mossy, and dendritic	1. Mossy deposits could turn to be smooth using pulsed current charging; 2. Pulsed current could decrease dendrite growth because of the dendrite growth was under diffusion control	[147]
Electrode: polycrystalline zinc electrodes known orientation;	Nucleation and epitaxial	Layer-like, boulder, dendritic	1. Overpotential was found to be the critical variable; 2. At low overpotential (50 mV) there was epitaxial	[88]

Electrolyte: 2 M KOH and 0.1 M or 0.02 M zincate; Potentiostatic control			growth, at 100 mV, there were boulders with epitaxial and a few not, with nucleation; 3. Dendrite would grow from the boulders	
Electrode: steel substrate; Electrolyte: 0.5 M zincate and 6 M KOH; Potentiostatic control	Epitaxial and 1-D nucleation	Compact and dispersed deposits	1. Dendrite grown from nuclei of higher indices (10-10) and (11-20); 2. Much faster growth on the (10-10) or (11-20) plane than on the (0001) plan could be explained by the mechanism of unidimensional nucleation	[154]
Electrode: RDE (zinc 3mm in diameter); Electrolyte: 0.34 M zincate and 8 M KOH; Potentiostatic control		Only focused on dendrite growth at overpotential of -150 mV, plate-like precursors to sword-like dendrites	1. The growth rate of zinc dendrite precursors is constant within the diffusion layer; 2. An equation concerning zincate concentration and the time of appearance of dendrites was derived	[91]
Electrode: single crystals; Electrolyte: 7 M KOH solution saturated with 0.7 M ZnO; Galvanostatic control	Nucleation and epitaxial	Mossy, layer-like, boulder, heavy spongy, dendritic	1. There were two types of deposits, either under single-factor control, or two-factors; 2. At low overpotential the growth was epitaxial, at high overpotential, it was from nucleation; 3. No universal critical overpotential for a specific deposit morphology existed	[149]

2.1.2.3. The interference with hydrogen evolution

Hydrogen evolution occurs during both discharge and charge processes while the potential remains below the hydrogen reduction threshold. It is usually called self-discharge or corrosion during anodic polarization or at open circuit potential (rest). It is generally detrimental to the performance of battery, with only a little gain from stirring [155]. As observed by Justinijanovic et al. [154], hydrogen evolution occurs concomitantly with dendritic growth during deposition, and is proportional to overpotential above a critical value, as shown in Figure 2-4(a). Some works thus attribute the dendritic growth to hydrogen evolution or consider that they interfere with each other. So, a study on dendrite growth should also consider hydrogen evolution.

Experimental works to quantitatively measure this hydrogen evolution and separate it from the cathodic polarization and/or static chemical corrosion face technical issues. When measuring the rate of hydrogen evolution by recording the electrolyte volume change in a pipette in a static condition without any electrochemical polarization, P. Dirkse et al. [156], they obtained the results that static zinc corrosion decreases with zincate ion concentration in alkaline aqueous electrolyte and increases with temperature, giving rise to different corrosive products. The drawback of this experiment was that the dissolved hydrogen made the apparent hydrogen volume less than its expected value [157]. With a similar aim, R. E. F. Einerhand [158] applied a RRDE (rotating ring disk electrode) technique to measure the hydrogen evolution from the zinc deposition and separated it from the corrosion of zinc. They also pointed the limitations of this analysis when there were hydrogen bubbles not dissolving in the electrolyte. This work is very elegant, but the question remains unsolved: once there is dendrite growth on the electrode, whether it would affect the hydrogen evolution and vice versa. The dedicate measurements and analysis of hydrogen evolution during cathodic polarization or static corrosion in the zinc based alkaline electrolyte have been fulfilled, but the relationship between dendrite growth and hydrogen evolution is not deeply revealed.

Additives in the zinc anode or in the aqueous alkaline electrolyte are useful for suppressing hydrogen evolution and/or dendrite growth in zinc-air battery [99, 107, 159]. Because the rate of hydrogen evolution is greatly dependent on the overpotential of hydrogen on zinc electrode, many additives in the electrolyte play the role to decrease the potential of hydrogen evolution (the absolute value of overpotential is increased but in fact the hydrogen reduction potential becomes more negative) [151].

In the early trials, mercury was found effective to improve performance of zinc deposition by suppressing hydrogen evolution, but it is highly toxic and not environmentally

friendly [67]. So, other non-toxic additives have been tested to replace it, especially some organic additives. The common mechanism of the additives is to adsorb on the electrode by π -bond combination preventing further dendrite growth or increasing the hydrogen reduction overpotential.

2.1.2.4. The effect of liquid convection or flow towards the electrode surface

Flow effect is widely applied and discussed in full zinc-based batteries.

Naybour et al. [150] investigated the effect of flowing electrolyte on the morphology of zinc deposits in alkaline electrolyte containing zincate ions. They concluded that a flow, either laminar or turbulent, greatly modifies the morphology of zinc deposits. Flat and smooth deposits were systematically obtained under high Reynold's numbers and intermediate current density around 40 mA cm^{-2} . A phase diagram of current density-Reynold's number-morphology (Figure 2-6) was proposed to take the hydrodynamic conditions into consideration.

Wang et al. [87, 160] used a phase-field model to simulate the zinc deposition in electrode-electrolyte surface composed of the steel electrode in the alkaline zincate electrolyte. This model revealed that the dendrite tip should present a higher electric potential and higher concentration of zincate ions around it. Flowing electrolyte and pulsed charging experimentally proved to suppress zincate dendrite effectively. This further indicated that the dendrite growth was diffusion controlled. Hydrogen evolution was not mentioned neither in the model simulation nor in the experimental observation.

Ito et al. [161] proposed as an indicator the ratio of current density to limiting current density. The limiting current density is defined as below:

$$\text{Equation 2-1 : } i_{lim} = \frac{nFD C_0}{d_e} S_h$$

$$\text{Equation 2-2 : } S_h = 1.85 R_e^{1/3} S_c^{1/3} (d_e/L)^{1/2}$$

where i_{lim} is the limiting current density, n is the number of electrons in the reaction, F is Faraday's constant, D is the diffusion constant, C_0 is the bulk zinc concentration, S_h is Sherwood number, R_e is Reynolds number, S_c is Schmidt number, d_e is the hydraulic diameter, L is the plate length in the streamwise direction.

The flow effect was taken into consideration, to emphasize the morphology transition of zinc deposits in alkaline electrolyte. They only observed three morphologies within all the deposition experimental conditions: mossy, compact and intermediate with the co-existence of

mossy and compact. This is different with other experiments such as by Wang et al. [149], but this is probably due to the different deposition conditions especially the flowing electrolyte.

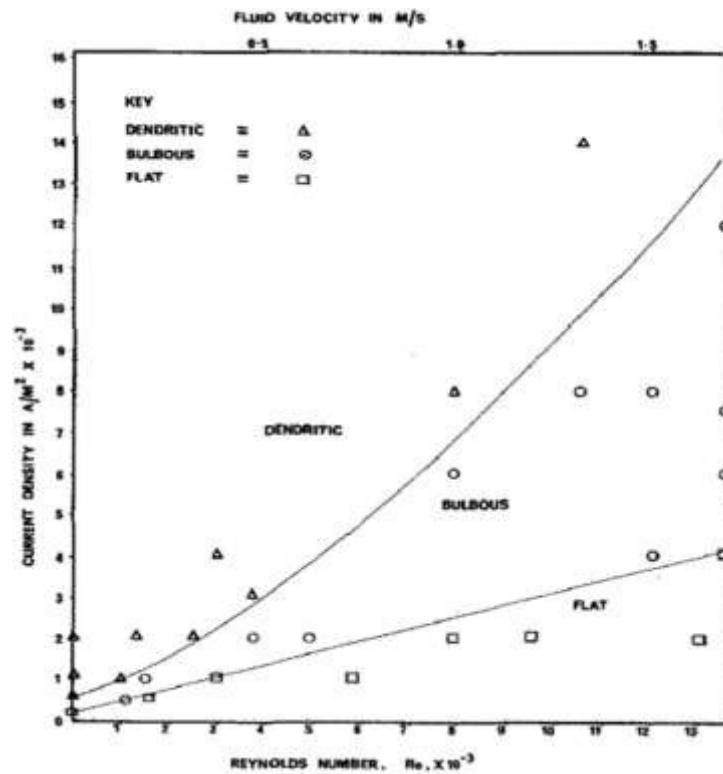
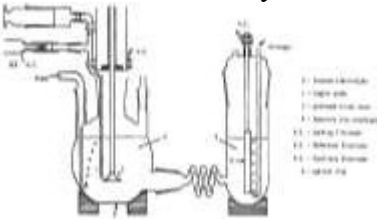
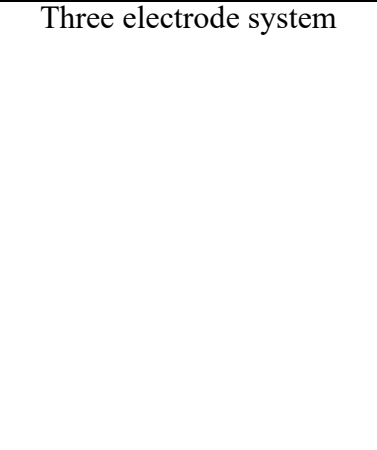


Figure 2-6 : Phase diagram of current- Reynold's number [150]

Hyeon Sun Yang et al. [162] found a critical flow rate that ensures optimal performance of zinc-bromine redox battery from the perspective of both electrodes; the circulating rate had an influence on the kinetic of electrochemical reactions on bromine electrode, which further affected the zinc dissolution and deposition onto the zinc electrode, therefore a critical flow rate induced good mixing of the positive electrolyte and a decrease of dendritic growth. The effect of flowing electrolyte on gas evolution was quantitatively evaluated in a zinc-nickel oxide battery [130]. Recently there is much modeling work on the quantification about dendrite growth.

Table 2-2 : Hydrogen evolution study during zinc deposition in alkaline zincate electrolyte

Electrode	Electrolyte	Setup	Conclusion	Reference
RDE	3 M KOH with zincate concentrations of 0.01-0.08 M	Three electrode system 	Hydrogen evolution is preferable for electrodes charging at high current density; at low overall current density, the hydrogen evolution provides condition for dendrite growth	[163]
RRDE	1-7 M KOH, 0.01-0.2 M zincate	Three electrode system 	Hydrogen production increases with decrease of KOH and zincate concentration; In zinc secondary batteries, hydrogen is produced mainly through zinc electrode corrosion	[164]
Carbon composite plate	8 M KOH containing various concentrations of ZnO	Three electrode system 	Hydrogen evolved enhances the mass transport near the electrode surface, affecting the morphology transition of zinc deposit	[165]

2.1.2.5. Zinc-based rechargeable batteries with improved performance of zinc electrode

Although the earlier explorations of zinc deposition and dissolution mechanisms were performed in a fundamental way, the recent works are more oriented towards practical battery examples especially for the application to zinc-nickel and zinc-air batteries.

Zhang et al. [49] conducted three experiments concerning zinc electrode and zinc-nickel battery. Firstly, they studied the effect of substrates on their cyclic voltammograms in highly concentrated alkaline zincate electrolyte (1 M ZnO in 10 M KOH), and concluded that the

cadmium electroplated on copper was the best among copper, lead and cadmium in the perspectives of simplicity of reactions on the substrate and the adherence of deposited zinc on the substrate. Then they used cadmium as the electrode to study the difference between the zinc deposition in stationary and flowing electrolyte. The results showed that the flowing electrolyte suppressed enormously the dendrite growth. Lastly, the charge-discharge cycles at the current density of 10 mA cm^{-2} were performed with a full zinc-nickel single flow battery ($70 \times 70 \text{ cm}^2$ electrodes). The battery achieved no deterioration over 220 charge-discharge cycles and high average coulombic and energy efficiency of about 98% and 88%, respectively.

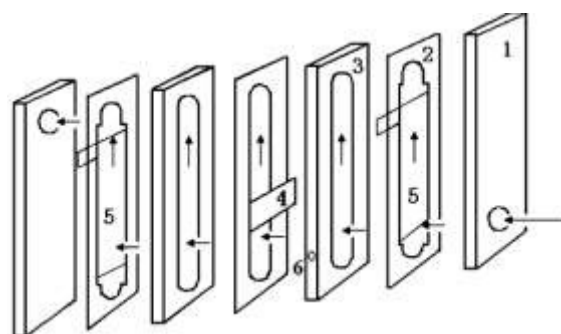


Figure 2-7 : Schematic diagram of the experimental device for zinc deposition in flowing electrolytes; 1: Perspex end plate; 2: rubber gasket; 3: flow passage; 4: WE; 5: CE; 6: hole for RE by Zhang et al. [49]

Ito et al. [130] fabricated a larger zinc-nickel oxide flow battery with a zinc electrode with a width of 13 mm and length of 1000 mm, which was plated onto copper. The flow battery configuration and the charged zinc electrode is shown in Figure 2-8. Sintered nickel oxide plate was the positive electrode. The flow velocity and the charge/discharge rate were varied in a range of $1.6 - 25.7 \text{ cm s}^{-1}$ and $C/4 - 1.5C$ ($10 - 60 \text{ mA cm}^{-2}$). Generally, electrolyte flowing at higher velocity attributed to a better battery performance, with at least 85% of coulombic efficiency and 80% of capacity efficiency. However, the dendrites always appeared even with high flow velocity. The morphology changed little with the increase of velocity, but the battery exhibited better performance. The authors explained that the dendrites grew along the direction of the electrolyte flow. So, the distance between dendrites and the positive electrode was lengthened, and the flow therefore suppressed the short-circuits, maintaining a good electrochemical performance.

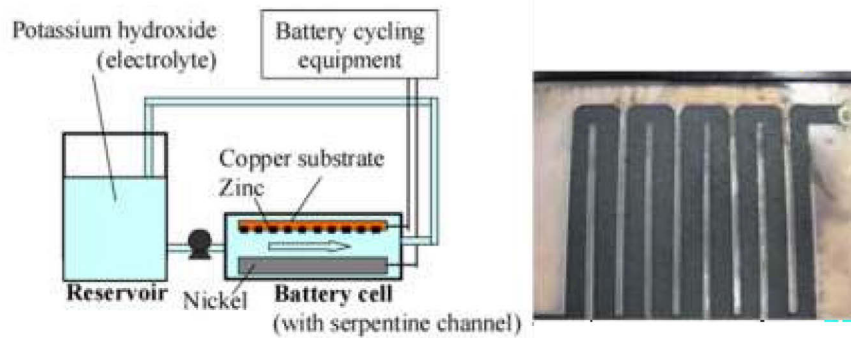


Figure 2-8 : Setup of the zinc-nickel flow battery (left) and the zinc electrode (right) [130]

Schmitt et al. [166] presented a 2D-model for shape change of zinc-air secondary battery emphasizing. They associated the mechanisms of zinc passivation and revealed that redissolution during discharging had an important effect on the battery cycle-life. They also concluded that a low current charge was better for obtaining more cycles. Besides, thicker anodes and higher operating temperature also contributed to longer cycle-life.

2.2. Experimental study

Whereas potentiostatic condition for zinc deposition study is widely chosen for the study of mechanism and fundamental thermodynamics considerations, in application, galvanostatic condition is more often performed (a fixed charge time or a fixed current density are defined). So, in this work, galvanostatic control will be preferred. We chose to work in alkaline electrolyte, concentrated KOH solutions for stability of the zinc electrode, but will try to improve its performance. More specifically, we want to understand the effect of LiOH and ZnO in concentrated KOH electrolyte on the performance of zinc electrode. The goal of this experimental part is to study the appearance of dendrites and evolution of hydrogen in such conditions.

2.2.1. Experimental conditions

Cyclic voltammetry (CV) experiments are conducted firstly using an electrolytic cell with five entries. Prior to each experiment, the electrode is first polished with emery paper. The cyclic voltammograms vary from different cell conditions. Taking an example of the substrate, the initiation of zinc deposition onto a copper substrate would result in formation of Zn-Cu alloy, a monolayer of underpotential deposited zinc, and bulk deposits, while deposition on cadmium, only bulk zinc deposition occurs [49]. Considering the availability of copper, we use it as the substrate.

For the electrochemical studies, a copper wire is used as the working electrode (WE), platinum wire is the counter electrode (CE) and the Ag/AgCl (3 M KCl) is the reference electrode (RE). It is protected from the corrosion of KOH by a porous extension filed with saturated KCl. The three electrodes are installed through the three entries on the cover of the electrochemical cell, the other two entries are sealed by two plastic corks. The electrolyte contains 7 M KOH-0.7 M ZnO-0.7 M LiOH. The cyclic voltammetry experiment is accomplished using a Bio-Logic VSP-2 potentiostat. The potential ranges from -1.8 V to -0.6 V, and different scan rates are applied from 10 mV s⁻¹ to 100 mV s⁻¹.

The electrolytes with different ZnO concentrations are prepared. Because ZnO is not very easy to be dissolved in KOH solutions. To make it dissolve a little faster, a much more concentrated KOH solution is obtained, and ZnO is added in this KOH solution little by little. Quantically, if 500 mL 7 M KOH-0.7 M ZnO-0.7 M LiOH is needed, 196.385 g KOH (MW 56.11 g mol⁻¹ from Fisher Chemical) is dissolved in 200 mL deionized water. 28.483 g ZnO (MW 81.38 g mol⁻¹ from Fisher Chemical) is four-time added. It takes around 1 - 2 hours for dissolving.

For the dendritic growth studies, two laboratory-made setups have been used to investigate the diffusion-controlled situation (setup 1) and the convection-controlled situation under electrolyte flow (setup 2), respectively. The setup 1 and setup 2 both consist of two pieces of zinc plates serving as symmetrical electrodes.

Static conditions, no convection: The shell of setup 1 is composed of two pieces of microscope slides, which are sealed completely to study only the static conditions without flowing electrolyte. This design was done after the work of C. Brissot et al. [167]. The zinc plates are cut and polished by an emery paper, then rinsed with ethanol and distilled water. Two longer borders and two surfaces between the slides of the zinc plates are glued with corrosion-resistant epoxy, so are the side boundaries of the slides. The electrolyte is injected between the slides with a syringe. Because the setup 1 is totally sealed, it can be used only once under each deposition condition. Only the edge of the zinc plates is exposed to the electrolyte and to the electrochemical reactions. So, the dimensions of the exposed electrode are a length of around 8 mm, and a thickness of 0.26 mm, highlighted in yellow line seen in Figure 2-9.

With setup 1, the variables considered are current density from 1 to 40 mA cm⁻², the presence of LiOH or not in the electrolyte, the concentration of the zincate ions in the KOH solution from 0.1 M to 0.7 M, and time varied in hours.

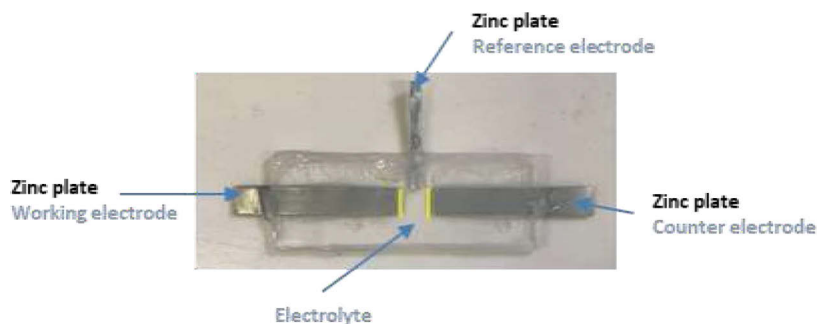


Figure 2-9 : The photo of the setup 1 (static conditions with reference electrode)

Convection cell, flowing state: The electrode of cell in setup 2 is similar but the lateral dimension is 2 cm, so the area of the exposed electrode is $20 \times 0.26 \text{ mm}^2$ as shown in Figure 2-10. The electrolyte is circulated by a pump (REGLO-CPF Digital). The sizes of the space where the electrolyte flows in the cell are as following: height of 1 cm, width of 2.5 cm, and length of 10 cm.

The zinc plates are fixed on two screws inside the cell shell, leaving one cross surface uncovered by epoxy, the other parts including the screws are covered completely. The screws tip outside the cell are connected to the potentiostat. There is a rubber to ensure the good tightness between the two shells of the setup. The electrolyte is pumped in and out from two gas nozzles, respectively. Two tubes are connected to the electrolyte and the setup. The electrolyte container is closed by a supplementary cover, and the tubes are through two size-equivalent holes on the cover.

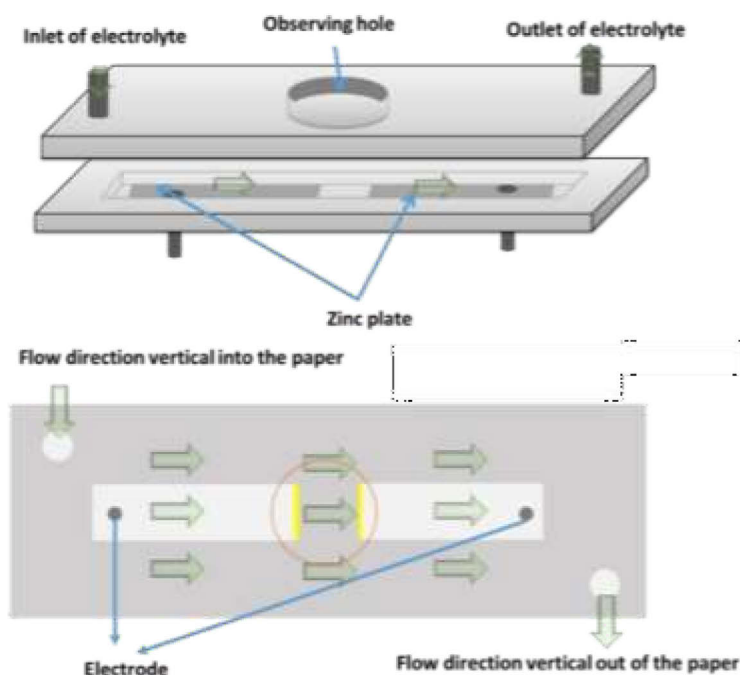


Figure 2-10 : The schematic of the setup 2

The investigation of the two setups will be classified into two cases, and it will be detailed separately below. With setup 2, the variables in the experiment are the current density of 40 mA cm⁻² and 100 mA cm⁻², and the flow or static electrolyte. The experimental details are introduced below sequentially. The flow rate is set at 7.5 mL s⁻¹. Thus, the linear flow rate of the electrolyte is 1.5 cm s⁻¹.

All the experiments have been done at room temperature. A constant current is imposed to the electrodes for zinc deposition and dissolution by a potentiostat (Bio-Logic), and there is a microscope (AmScope) with a camera to in-situ record the evolution process. All the pictures are amplified with a magnification of 20×.

The electrolyte has the composition of 7 M KOH-0.7 M ZnO-0.7 M LiOH. This electrolyte was originally utilized in reference [140]. The role of LiOH is obscure and we will try to verify it later. From literature, the LiOH addition in the alkaline zincate electrolyte is mostly seen in zinc-nickel rechargeable batteries. It can suppress O₂ evolution to augment NiOOH rechargeability [66] and can stabilize supersaturated zincate solutions to prevent zinc passivation [67]. Besides, the absence of supporting electrolyte was studied theoretically to have effect of slowing down the instability of zinc deposition [168]. Therefore, the role of LiOH as additive in the electrolyte will also be highlighted in this work. On the other hand, it is widely accepted as mentioned above in the small literature review that the dendrite growth is under diffusion control, flowing electrolyte is adopted to suppress dendrite growth.

Experiments performed under static conditions with setup 1 are listed in Table 2-3.

Table 2-3 : Parameters of the electrodes and the corresponding deposition conditions

Item	Length/mm	Current density/(mA cm ⁻²)	Electrolyte compositions	Time/h
S#1	7.90	1	7 M KOH-0.7 M ZnO-0.7 M LiOH	20
S#2	8.06	10	7 M KOH-0.7 M ZnO-0.7 M LiOH	10
S#3	7.35	40	7 M KOH-0.7 M ZnO-0.7 M LiOH	3
S#4	7.96	1	7 M KOH-0.1 M ZnO-0.7 M LiOH	20
S#5	7.38	10	7 M KOH-0.1 M ZnO-0.7 M LiOH	10

S#6	8.35	40	7 M KOH-0.1 M ZnO-0.7 M LiOH	1.75
S#7	6.15	1	7 M KOH-0.4 M ZnO-0.7 M LiOH	20
S#8	6.92	10	7 M KOH-0.4 M ZnO-0.7 M LiOH	5
S#9	7.66	40	7 M KOH-0.4 M ZnO-0.7 M LiOH	3
S#10	6.75	1	7 M KOH-0.7 M ZnO	20
S#11	6.40	10	7 M KOH-0.7 M ZnO	5
S#12	6.50	40	7M KOH-0.7M ZnO	3

Zinc is deposited on the working electrode in all the experiments. The three electrodes are all zinc plates, which are connected to the potentiostat.

2.2.2. Cyclic voltammetry study on zinc dissolution and deposition

Cyclic voltammetry study is conducted to locate the potential for deposition and dissolution of zinc. Because at beginning, the copper is bare and clean, cathodic scan for zinc deposition should be firstly adopted. A relatively large range of potential range between -2.5 V and 1.5 V (vs Ag/AgCl) is tried to identify the electrolyte window and locate the potential range for zinc deposition and dissolution. Electrolytes with LiOH and without LiOH are both tested as shown in Figure 2-11. The water oxidation (oxygen evolution reaction, OER, starts at 0.75 V whereas at a potential lower than -1.8 V we start observing the hydrogen evolution.

The deposition–dissolution reaction of zinc is found to occur at an equilibrium potential of around -1.6 V (vs Ag/AgCl).

The corresponding current-time curve for Figure 2-11 is presented in Figure 2-12. The integration of current to time gives the charge with the inserted calculator in the EC-lab software. The results show that the charges passed through cathodic scans are more than those through anodic scans, so the charges passed through cathodic scan include those from hydrogen evolution, namely the cathodic limit of electrolyte window is located.

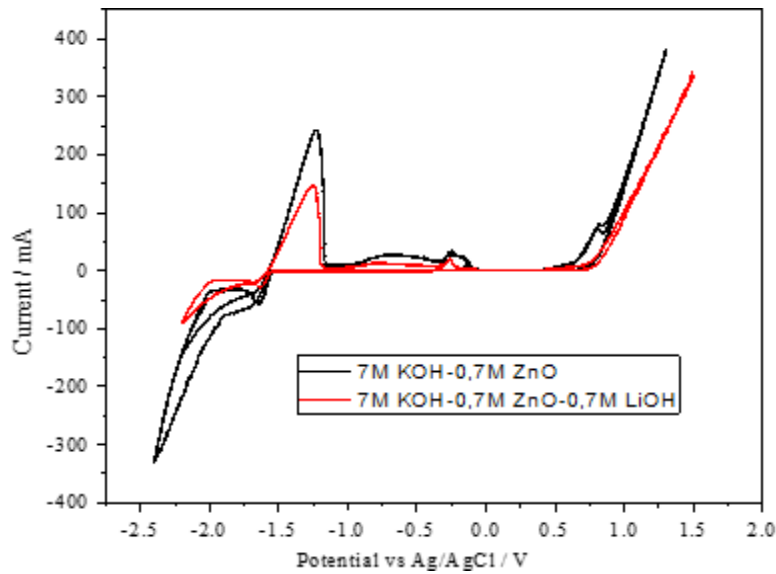


Figure 2-11 : Potential window of two electrolytes with and without LiOH

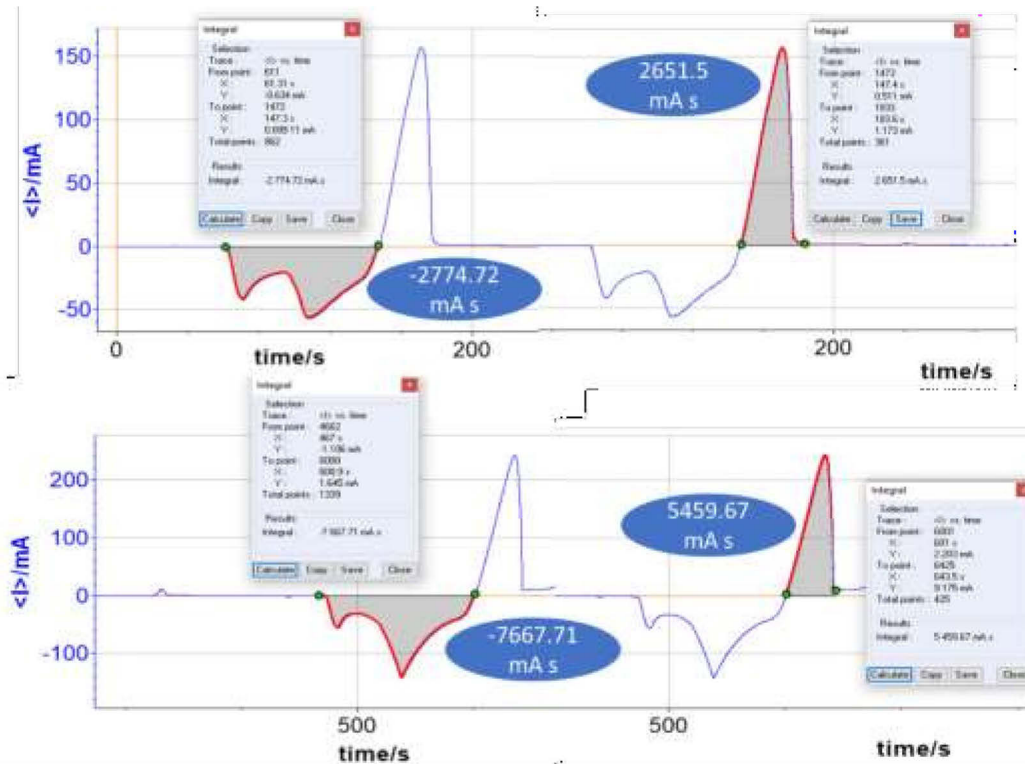


Figure 2-12 : Integration of the current with time during a full cycle scan in electrolyte 7 M KOH-0.7 M LiOH-0.7 M ZnO (top) and 7 M KOH-0.7 M ZnO (bottom)

The zinc deposition and dissolution sequence were further studied in the window from -0.6 V vs RE to -1.8 V vs RE, and firstly also via cathodic scan. The copper electrode is polished and rinsed before putting into the electrolyte. Figure 2-13 shows the cyclic voltammogram of zinc deposition and dissolution at several different potential scan rates, the insertion is a part range of potential, for the convenience to compare with the other work as in Figure 2-14 [49].

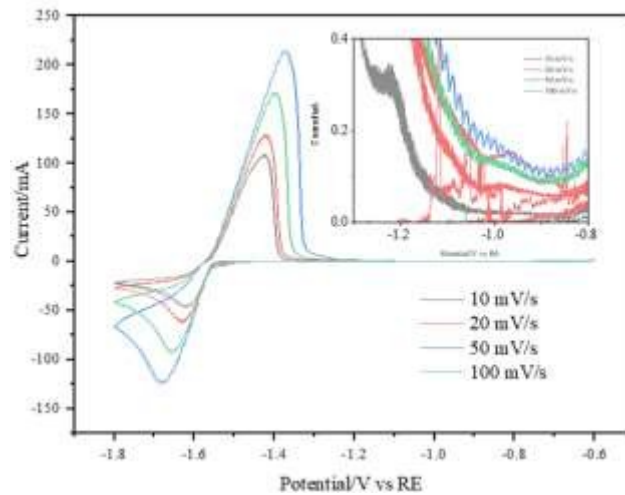


Figure 2-13 : Cyclic voltammogram for electrolyte with 7 M KOH-0.7 M ZnO-0.7 M LiOH at copper electrode under different scan rates. Reference electrode RE is Ag/AgCl

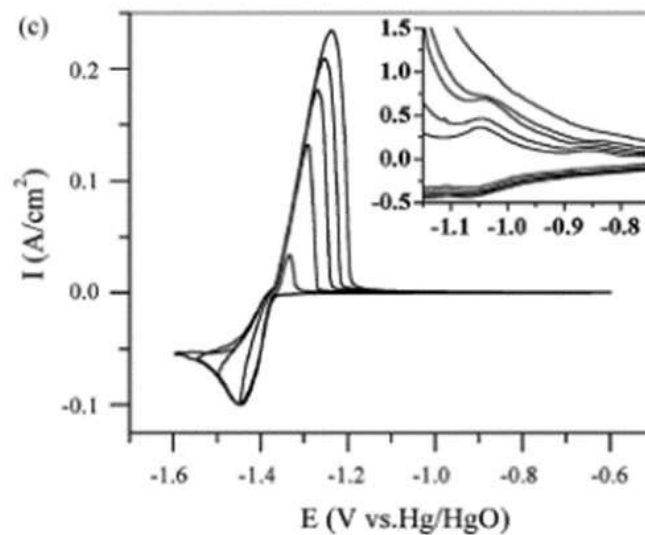


Figure 2-14 : Cyclic voltametric curve for potassium zincates solution at copper electrode [49]

Figure 2-13 shows the cyclic voltametric curve for electrolyte with 7 M KOH-0.7 M ZnO-0.7 M LiOH at copper electrode under different scan rates. According to Li Zhang’s work [49], the potentials for the bulk zinc deposition and dissolution are -1.45 V and -1.32 V vs Hg/HgO. And in our work, the corresponding potentials are -1.61 V and -1.41 V vs Ag/AgCl (3 M KCl), respectively. Except the one of bulk zinc dissolution at -1.32 V, there are other two anodic peaks at -1.05 V and -0.86 V where the dissolution of Cu-Zn alloy and underpotential deposited zinc occurs respectively [162]. In our result, there presents only one at -1.21 V. It should be the dissolution of Cu-Zn alloy. We do not observe a monolayer of deposited zinc at underpotential nor its dissolution.

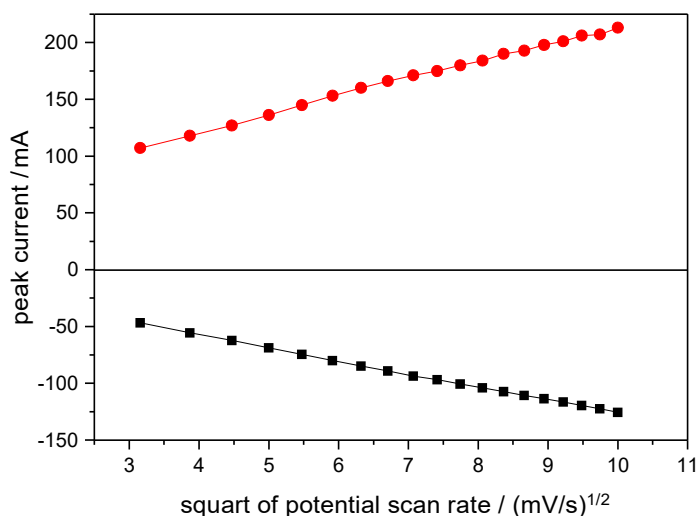


Figure 2-15 : Relation between peak current and potential scan rate

According to Randles-Sevcik equation shown below, linear plot of peak current to square root of potential scan rate provides evidence for a chemically reversible redox process controlled by diffusion. As shown in Figure 2-15, peak current indeed relates quite linearly to the square root of scan rate, which confirms that the zinc deposition and dissolution are reversible reactions controlled by diffusion kinetics.

$$\text{Equation 2-3 : } i_p = 0.4463nFAC\left(\frac{nFvD}{RT}\right)^{1/2}$$

Where i_p is the peak current (A), n is the number of electrons transferred, F is the Faradaic constant ($C \text{ mol}^{-1}$), A is the electrode surface area (cm^2), D is the diffusion coefficient ($\text{cm}^2 \text{ s}^{-1}$), C is the concentration (mol cm^{-3}), R is the gas constant ($\text{J K}^{-1} \text{ mol}^{-1}$), and T is temperature (K).

2.2.3. Static case of rechargeable zinc electrode

As introduced above, static case of zinc electrode is studied in the homemade symmetry cell fabricated by two pieces of microscope slides and two wider zinc plates serving as working and counter electrodes and one thinner zinc plate as reference electrode. Different current densities of 1, 10, 40 mA cm^{-2} are imposed on the cell, electrolytes with different compositions are also infused in the cell for acknowledge of the effect of LiOH and zincate ions in the electrolyte on the zinc dissolution and deposition while discharge and charge.

2.2.3.1. Effect of current density in static conditions with cell 1

The zinc deposition has been conducted at different constant current densities in the electrolyte with the same composition 7 M KOH-0.7 M ZnO-0.7 M LiOH. The evolution of the zinc deposition at different current densities is shown in Figure 2-16. The corresponding potential-time curves are shown in Figure 2-17.

From Figure 2-16, we observe that dendrites appear in all cases. Of course, for a same time they do not grow as large at low current as that at high current. There does not seem to exist a delay time before the dendrites start to grow. They appear in the very early beginning. The roughness of the surface is higher when the current density is increased, and the deposit is more porous and looser. Comparing the pictures of the deposits after 4 hours at 10 mA cm^{-2} with that after 1 hour at 40 mA cm^{-2} in perspective of same coulombic charge passed in the cell, it shows that the deposit is more porous and dendritic at 40 mA cm^{-2} , as seen in the part marked with red rectangle.

From Figure 2-17, we observe that the overpotentials are negative which is expected for a reduction reaction. The overpotential at 40 mA cm^{-2} is the most negative as also can be expected. Their absolute value decreases with time and this may be associated to the increase of the electrochemical reaction area due to the irregular growth of dendrites.

From Figure 2-16, we also observe that the highest hydrogen evolution occurs at the lowest current of 1 mA cm^{-2} . No hydrogen bubbles are observed at 40 mA cm^{-2} and the behavior at 10 mA cm^{-2} is intermediate. This may be explained by the fact that a lower potential increases the reduction rate of zincate as compared to the kinetics of evolution of hydrogen. Indeed, for the 10 mA cm^{-2} , the initial potential is rather negative at the beginning, and no hydrogen evolves. When it becomes less negative, hydrogen bubbles appear after 10 hours.

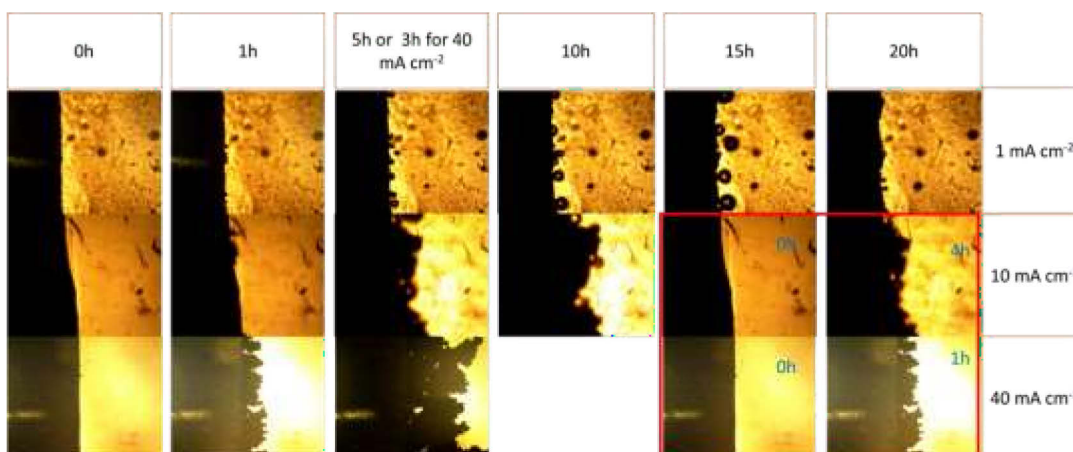


Figure 2-16 : Evolution of zinc deposition under different current densities (static conditions of cell 1). The inset in the bottom right compares the pictures at 10 mA cm^{-2} -4 hours with 40 mA cm^{-2} -1 hour

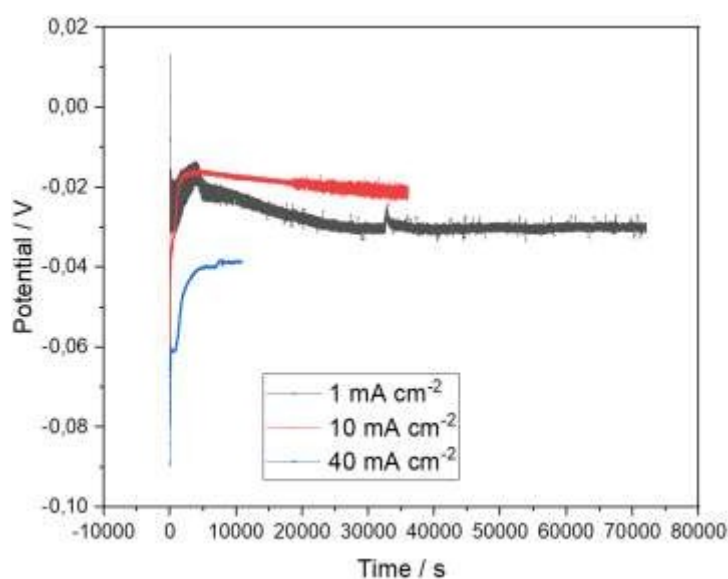


Figure 2-17 : Potential change with deposition process at different current densities in setup 1

Potential: According to Butler–Volmer equation and the theory on limited reaction kinetics, higher current density is supposed to end up with a higher overpotential. During reduction this means that a more negative potential is expected at higher current densities. This is indeed the case for the initial potentials where potential at 40 mA cm^{-2} is more negative than 10 mA cm^{-2} and 1 mA cm^{-2} .

But the potentials all increase rapidly at the beginning to reach a constant value. The increase of potential is faster for the smaller current densities and slower at 40 mA cm^{-2} (Figure 2-17). This potential increase is thought to be relative to the balance between **hydrogen evolution reaction** that makes bubble and decrease the reaction area, **zinc deposition** that is rough and increases the surface area, and the **zinc self-oxidation** in KOH that transforms the

solid surface from metallic zinc to zinc oxide. At high current densities, the deposited zinc increases the deposition area, and it does not have time to passivate (oxidize). This may explain why the permanent potential at 10 mA cm^{-2} is less negative (deposition of Zn onto Zn) than for 1 mA cm^{-2} (deposition of Zn onto oxidized Zn). Also, as will be discussed below, hydrogen evolution at 1 mA cm^{-2} is larger than at higher current densities (10 and 40 mA cm^{-2}); Hydrogen bubbles decrease the deposition area and modify the local current densities.

Hydrogen evolution: At the current density of 1 mA cm^{-2} , there is hydrogen evolution at the very beginning. This is indicated by both the fluctuation of the potential-time curve and the picture captured in-situ. At the current density of 10 mA cm^{-2} , there is no hydrogen evolution during the first 3 hours which can be also seen from Figure 2-16 where the transparent bubble in the view at 5 hours first appeared at around 3 hours. At 40 mA cm^{-2} , there is little visible hydrogen evolution during all the experiment.

The hydrogen evolution seems to be associated to fluctuations of potentials (noise in the curves) in Figure 2-17. At 1 mA cm^{-2} the curve is always noisy, whereas at 10 mA cm^{-2} the potential starts fluctuating after 3 hours, just when hydrogen evolution can be observed. At 40 mA cm^{-2} , there are no hydrogen and no fluctuation of potential. The curve is very smooth.

Zinc Deposition: At 1 mA cm^{-2} , the deposits grow relatively evenly along the electrode surface and they are quite compact. At 10 mA cm^{-2} , zinc is deposited faster (of course) and more roughly, especially in the beginning, while in the later period when the whole surface is covered, the deposits grow less selectively with a similar deposition rate along the whole surface under view. At 40 mA cm^{-2} , the deposits are quite dispersed and there are pointed or sword-like dendrites. The pointed parts or protruding parts grow faster and contact to the near ones, leaving several interstices between them.

After the current is off, the majority of deposits contract evidently by themselves in the first 40 minutes, while the deposits on the protrusions continue extending after 2 hours of current-off, or the very loosely grown deposits are moved by the aid of desorption of a few bubbles and the accompanied disturbing, as shown in Figure 2-18. This movement does not happen in the case at 1 or 10 mA cm^{-2} . This is mostly attributed to the much more compact and smoother deposits obtained at 1 and 10 mA cm^{-2} than that at 40 mA cm^{-2} .

Concerning the deposits at 1 mA cm^{-2} , the change of surface area would be small because they grow slowly. But there are a lot of hydrogen bubbles evolved all the time which block the active surface of electrode.

Conclusion: high current densities yield dendritic growth whereas low current densities yield hydrogen bubbles.

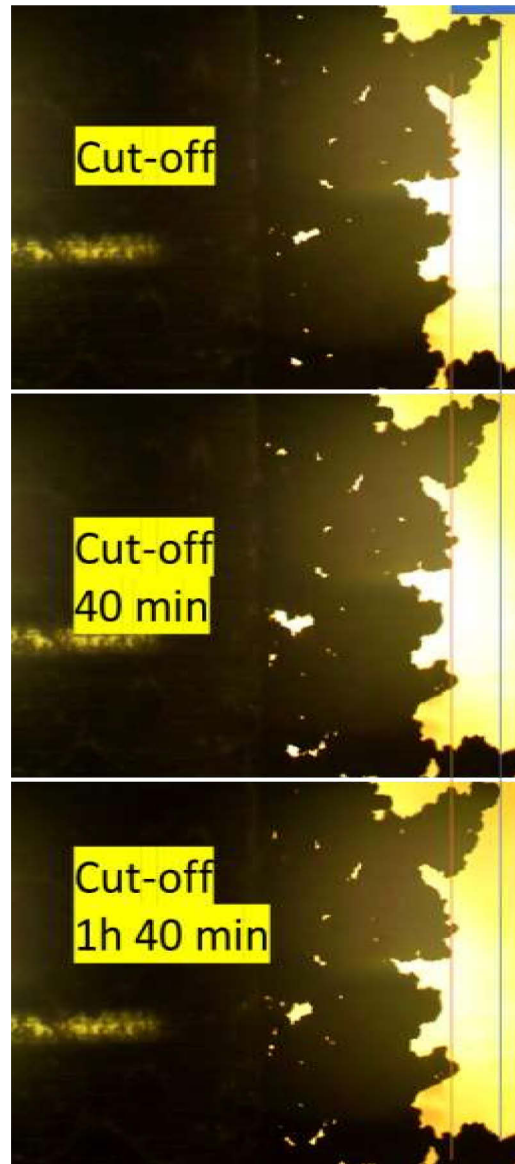


Figure 2-18 : After cut-off, the change of the deposits

2.2.3.2. Effect of zincate concentration in the electrolyte

We have studied the effect of the zincate concentration using three different concentrations of 0.1 M, 0.4 M, and 0.7 M ZnO in the electrolyte. The deposition processes have been conducted at a constant current density of 10 mA cm^{-2} . The results are shown in Figure 2-19 for the pictures and in Figure 2-20 for the potential-time curves.

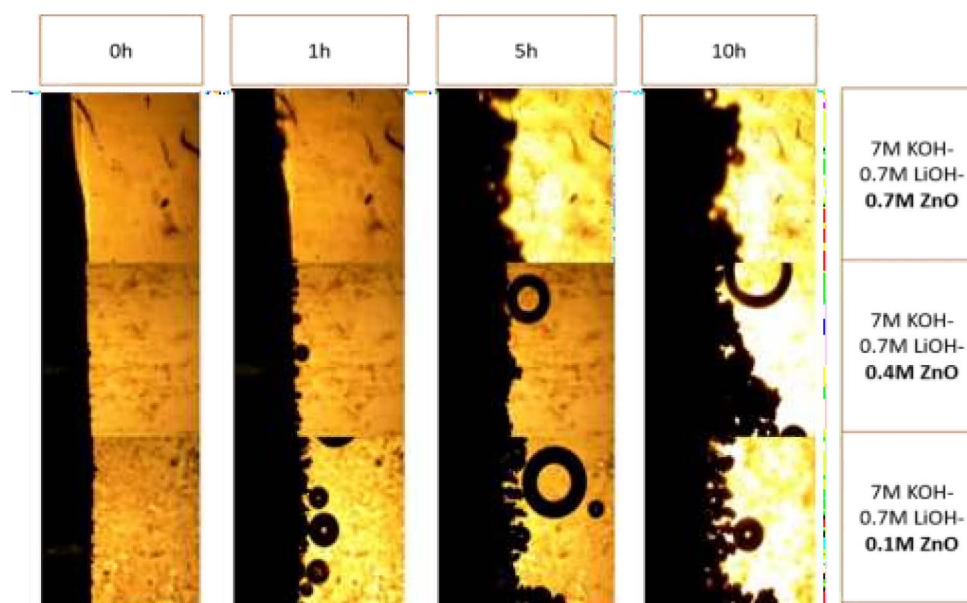


Figure 2-19 : Evolution of zinc deposition at 10 mA cm^{-2} in electrolytes with different concentrations of zincate ions

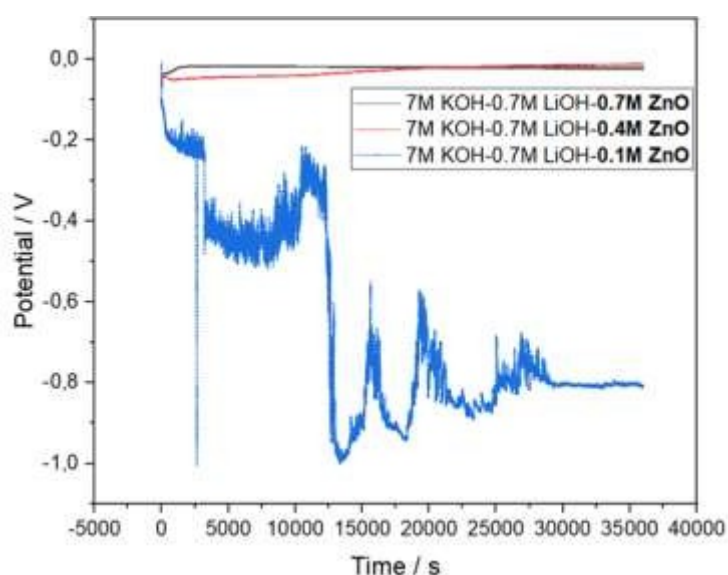


Figure 2-20 : Potential change with deposition process at 10 mA cm^{-2} in electrolytes with different concentrations of zincate ions

The major observations are as follows:

The hydrogen evolution is faster, and the hydrogen bubbles are much larger in the electrolyte with less zincate concentration as shown in Figure 2-19. They appear from the very beginning for 0.1 M ZnO and only after a delay with 0.4 M and 0.7 M zincate.

Potentials obtained from deposition in electrolyte with 0.4 M and 0.7 M zincate are similar, while the curve of potential is observed at a much more negative potential, is very noisy and shows big fluctuations when the zincate concentration is low (0.1 M) as presented in Figure

2-20. This fluctuation is probably associated to the formation of large bubbles that hinder the electrochemical reaction on the electrode surface.

Conclusion: *The deposit is much more dendritic, and the hydrogen evolves more in electrolyte with lower concentration of zincate ions. There may be a critical concentration of the zincate ions, below which hydrogen evolves very fast, and the potential curve becomes fluctuated.*

2.2.3.3. Effect of LiOH in the electrolyte

We have studied the effect of LiOH by comparing two electrolytes of 7 M KOH-0.7 M LiOH-0.7 M ZnO with 7 M KOH-0.7 M ZnO at two different current densities of 40 mA cm⁻² and 10 mA cm⁻² as shown in Figure 2-21 and Figure 2-22.

At 10 mA cm⁻², there is no hydrogen evolution in electrolyte without LiOH during the whole period of deposition for 5 hours. While in electrolyte with LiOH, there appears hydrogen bubbles in the late period of deposition. At 40 mA cm⁻², the situation is contrary, hydrogen evolution occurs in the electrolyte without LiOH, but not in the electrolyte with LiOH, and it only occurs in the beginning of deposition.

The morphology of the deposits in both electrolytes at the same current density are similar. Potential is always higher in the case with hydrogen evolution, i.e., deposition in the electrolyte with LiOH at 10 mA cm⁻² and without LiOH at 40 mA cm⁻² show higher potential presented in Figure 2-23.

Conclusion: *Overall, the effect of LiOH in the electrolyte is not clear in the aspects of hydrogen evolution or dendrite growth, because in different deposition conditions, the results are different and not regular.*

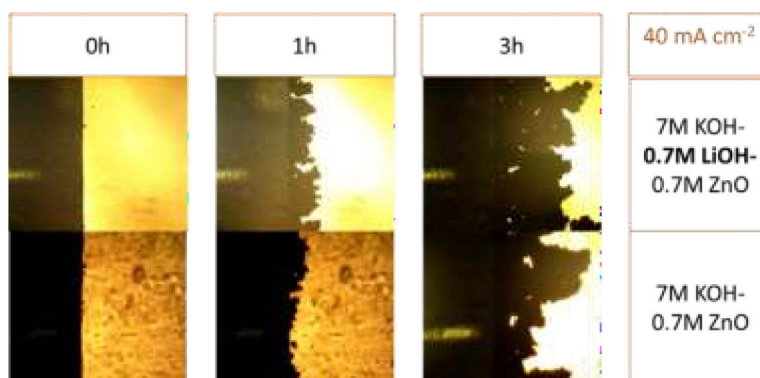


Figure 2-21 : Evolution of zinc deposition at 40 mA cm⁻² in electrolytes with or without LiOH

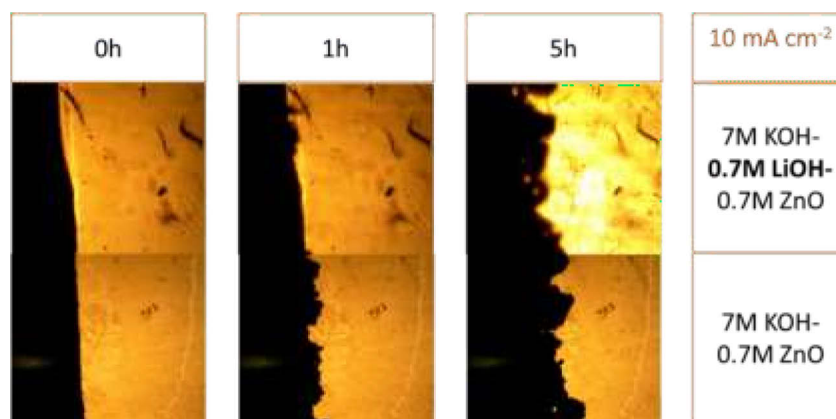


Figure 2-22 : Evolution of zinc deposition at 10 mA cm⁻² in electrolytes with or without LiOH

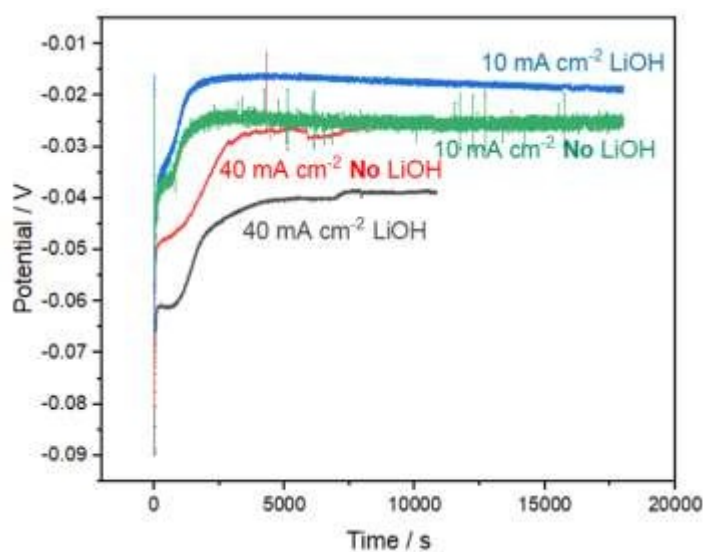


Figure 2-23 : Potential change with deposition process at 10 mA cm⁻² and 40 mA cm⁻² in electrolytes with or without LiOH

2.2.4. Flow case of rechargeable zinc electrode

The following studies have been performed with flowing conditions (using setup 2). We will observe that much higher current densities are allowed for zinc deposition in the flow experiments.

2.2.4.1. Effect of electrolyte flow

The effect of the electrolyte flow has been studied for zinc deposition at a fixed current density of 100 mA cm⁻². Experiments were carried out without flow (static) or with a flow rate of 7.5 mL s⁻¹ which corresponds to a linear flow rate of 1.5 cm s⁻¹. Experiments were limited to 3 hours because the deposits stretch very quickly in the static electrolyte to cover the whole sight from the microscope as shown in Figure 2-24.

Hydrogen evolution: At the beginning (first 20 mins of deposition), there is a small quantity of hydrogen evolution in the flowing electrolyte, and it disappears later. In static electrolyte, hydrogen evolution is not observed during the whole deposition.

Zinc deposition: in the first 30 mins when the zincate concentration is possibly concentrated enough for deposition in both experiments, the evolution of the electrode surface in both cases does not show any difference, except that there are more small protruding tips in the case of static electrolyte. After 30 min, deposits grow much faster in volume in the static electrolyte than in flowing electrolyte. Their morphology is also a little sharper in static than in flowing electrolyte, though not totally sharp during this period.

Potential: The potential is more negative in the static electrolyte than in the flow electrolyte as presented in Figure 2-25. This probably corresponds to diffusion impedance (decrease of the zinc concentration) though the electrochemical polarization could be lower owing to the higher surface area generated from more dispersed deposits in static electrolyte. During the experiment in the flowing electrolyte, there is little gas bubble which is introduced from the tube to the cell which can explain the blur pictures shown in Figure 2-24, accompanied by a sudden jump of potential in Figure 2-25. The gas bubble could be squeezed out from the cell with flowing continuation.

During the potential increase part in the beginning of the potential-time curves, the increase slope for the case of flowing electrolyte is higher than that of static electrolyte, due to the hydrogen evolution. Then they both undergo steady deposition with unchanged potential.

Conclusion: *The results also confirm the static experiments which indicate that the growth of dendrites may increase the surface area, favoring zinc deposition against hydrogen evolution and that lower voltages favor zinc deposition too.*

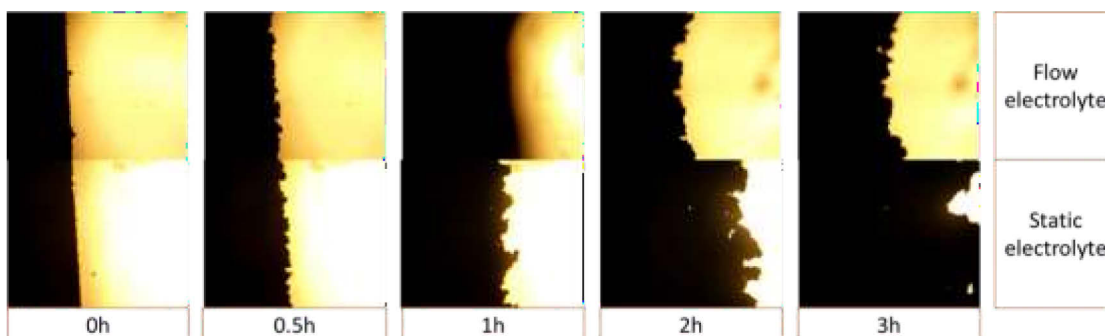


Figure 2-24 : Evolution of zinc deposition under a current density of 100 mA cm^{-2} in static and flowing electrolyte

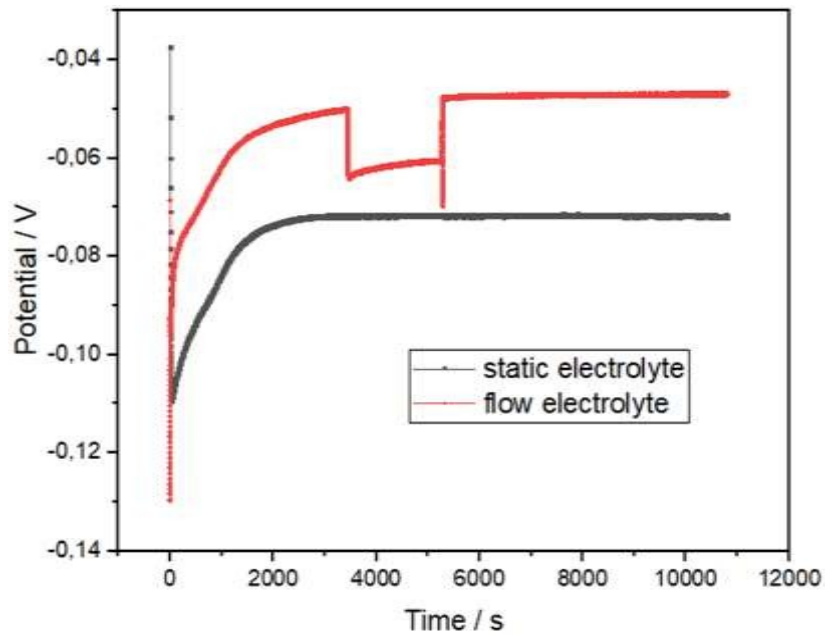


Figure 2-25 : Potential change with deposition process at different flow conditions

2.2.4.2. Effect of the current density in flow conditions

The experiments were carried out with a constant flow of 7.5 mL s^{-1} corresponding to a flow speed of 1.5 cm s^{-1} . Considering the effect of current density, zinc deposition was conducted at three different current densities $40, 100$ and 200 mA cm^{-2} . Pictures taken during deposition are shown in Figure 2-26. The corresponding changes of potential between the two electrodes with time are shown in Figure 2-27.

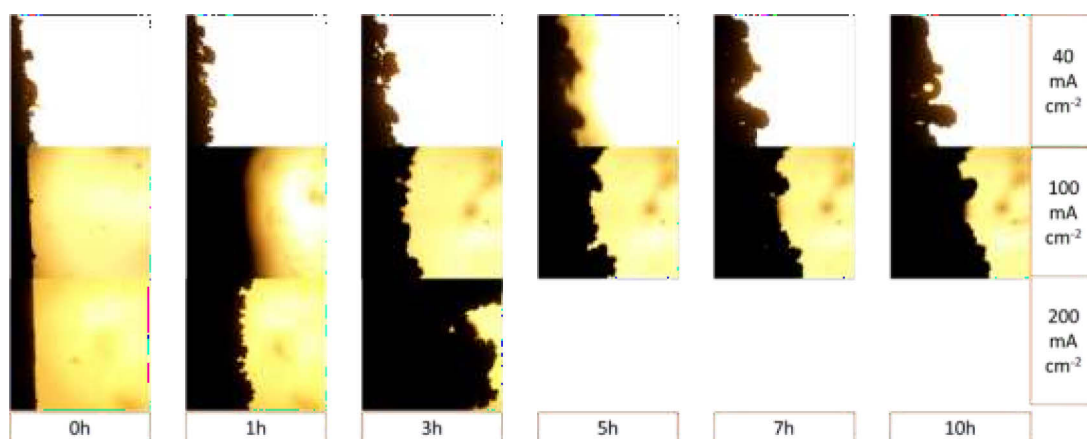


Figure 2-26 : Evolution of zinc deposition under electrolyte flow with time for different current densities. Remark: Please note that the electrode used during the deposition under 40 mA cm^{-2} has already been used in the static case after deposition and it has been recovered by dissolution for 3.5h. Under this condition, the surface of the electrode before deposition is a little rough due to the deposit left after deposition and dissolution in the last experiment.

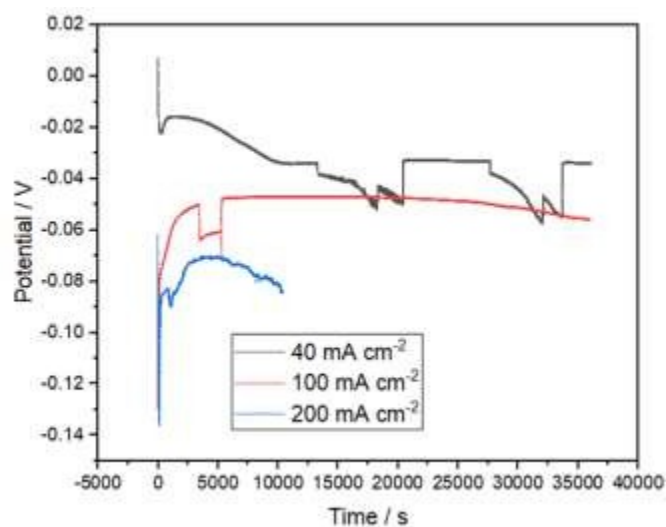


Figure 2-27 : Potential change with deposition process at different current densities in setup 2. Jumps in the curves may be associated to the release of big bubbles

At higher current densities, the deposits grow faster, as expected. There is no hydrogen evolution during deposition at 200 mA cm^{-2} while at 40 mA cm^{-2} , hydrogen evolution never ceases in the whole process of deposition.

The decrease of potential in the first ~ 3 hours of deposition at 40 mA cm^{-2} is possibly due to the blocking of the electrode area by the adsorbed hydrogen on the initial electrode. During this period, zinc deposits grow selectively at some places where no bubble is adsorbed, and they grow relatively faster because of increased local current density.

At 100 mA and 200 mA cm^{-2} , the potential first increases and this may be due to the larger interface area offered by the growth of dendrites.

But for 200 mA cm^{-2} the potential has a decrease in the final part of deposition, this may be caused by the increased thickness of the dendritic zone and a worse access of the solution to the interface with the depletion of zincate ions in this porous layer. During the potential increase stage (first hour) deposits grow relatively slowly and synchronously along the whole electrode. Then instabilities appear with zones showing faster growth than other. It can be also seen that one dendrite grows into several from former branches and tips. Generally, the surface moves simultaneously. Then after the first hour, the new deposits tend to insert inside the deposits already grown and densify them, which decreases the surface area. This may explain the potential decrease (i.e., more negative potential corresponding to larger overpotential for the reduction of zinc).

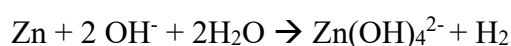
Conclusion: *These results again confirm the results in static conditions. The lower current gives a higher hydrogen evolution and a lower overvoltage (higher potentials, less negative). At high current densities (in flow condition) large dendrites are formed in a first step. Then they are filled.*

2.2.4.3. Deposition-dissolution cycle

After deposition at 100 mA cm⁻² for 10 hours, the current direction is reverse for dissolution during another 10 hours. Figure 2-28 gives the morphology evolution during deposition-dissolution cycles, and Figure 2-29 presents the corresponding potential change with time. We should remind that the starting electrode are zinc plates. So, they may also be dissolved during the oxidation step.

Comparing the first picture before deposition and the last picture after dissolution, we can detect that the initial zinc plate has been slightly dissolved after one cycle of deposition-dissolution. This is expected because the parasitic hydrogen evolution causes the coulombic loss during deposition, so the deposited zinc is not enough for the dissolution sequence during the same time. Since the electrode is also zinc, the dissolution will also dissolve part of the electrode. This can be seen because the dissolution goes deeper than the initial surface (to its left on the figure).

Also, we observe that some deposits remain on the initial zinc. It may be because the contact between the deposits and the electrode is quite loose and they are disconnected. After dissolution for 5 hours, there appears a bubble. The current is oxidizing so it cannot be electrochemical generation of hydrogen. The potential during dissolution is low so it cannot be oxygen either. We made two hypotheses: the gas may be the hydrogen generated during the deposition cycle, but which remained adsorbed or trapped in the porous deposits. When the deposits are dissolved, the hydrogen goes out, as in the case of reference [162]. Another possibility maybe the direct evolution of hydrogen by reaction of water with the fresh zinc surface generated by the dissolution:



This zincate formation could induce zinc oxide film afterwards.

From Figure 2-29, after 5 hours of dissolution, the overpotential increases. Based on this, there is most likely a zinc oxide film formed, accompanied with hydrogen evolution, which increases the electronic impedance and hence increases the overpotential during dissolution.

Conclusion: We can observe that the rugosity obtained during deposition will be amplified during the deposition. This explains that “dendritic growth” may be increasing upon cycling the electrodes.

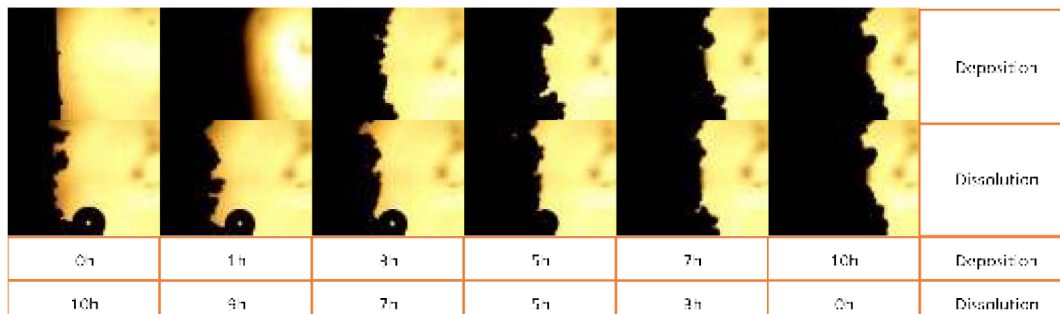


Figure 2-28 : Evolution of zinc deposition and dissolution under current density of 100 mA cm^{-2} in flowing electrolyte

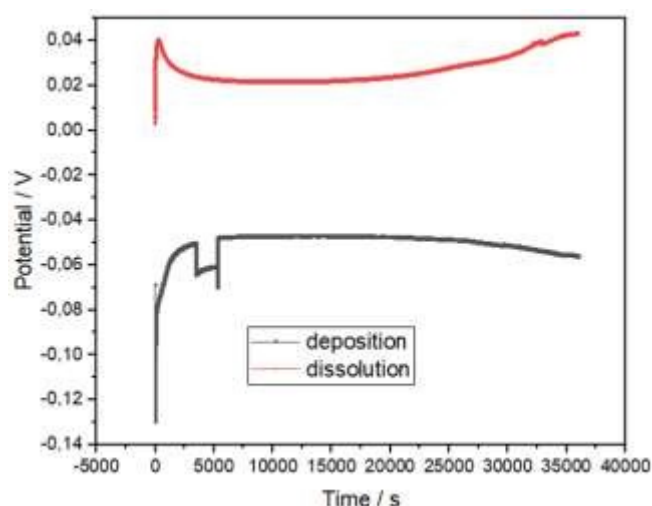


Figure 2-29 : Potential change with deposition and dissolution process at 100 mA cm^{-2} in flow electrolyte

2.2.4.4. Cyclability

We have studied the effect of four consecutive cycles on a zinc electrode. The conditions are a current density of 100 mA cm^{-2} in a flowing electrolyte of velocity 1.5 cm s^{-1} . Cycle periodicity was 3 h of charge and discharge. Both starting electrodes are zinc plates. The results are shown in Figure 2-30 and Figure 2-31.

During the first two cycles, the deposition and dissolution are both similar at the same designated time, which means at beginning, the electrode is quite reversible. While with more cycles, e.g., for the third and the fourth cycles, the deposits start to grow so loosely that intervals are evidently seen between the deposits during both deposition and dissolution.

As is discussed in the last experiment, the initial zinc would be corroded after deposition-dissolution cycle with remaining deposits on the surface. Dissolution always results in a rougher surface of electrode.

Mention should be referred that at beginning of each cycle of deposition, there is no visible hydrogen evolution, and after the second cycle of deposition, the hydrogen evolved during the dissolution step remains present in the system. After the last cycle of dissolution when the electronic circuit is open, hydrogen continues to evolve, which probably shows it is generated by a direct chemical reaction (no galvanic chemistry involved).

For the potential change during the cycles, the dissolution half-cycles show similar trend. Interpretation is complicated because we used a two-electrode system where the two zinc plates alternatively serve as a working electrode and a counter electrode/reference electrode, respectively.

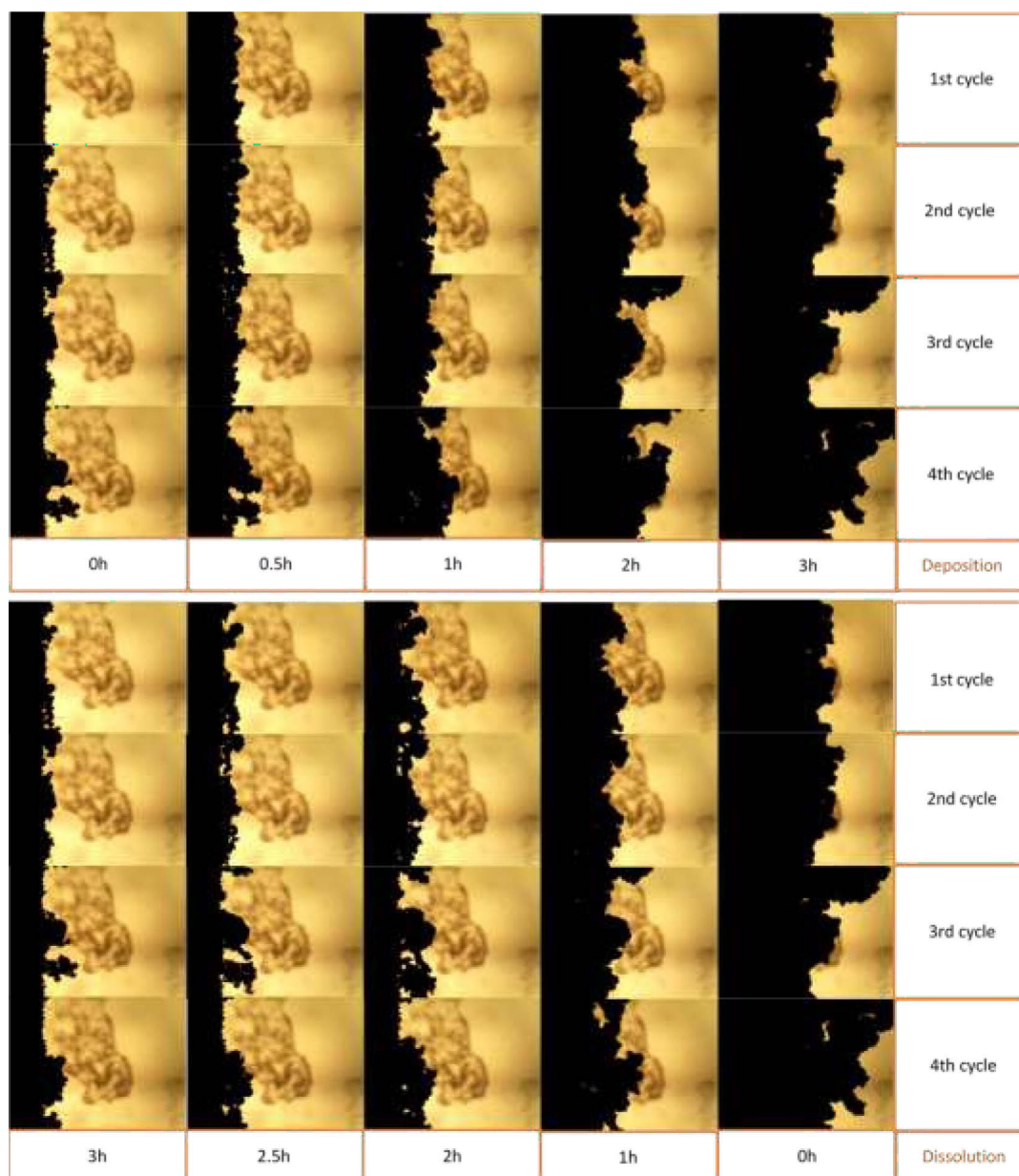


Figure 2-30 : Four cycles of deposition and dissolution at 100 mA cm^{-2} in flowing electrolyte. Before the experiment, the electrode was aged as follows; Aging conditions: After 20 hours of deposition and dissolution in flowing electrolyte and another 20 hours in static electrolyte, the electrodes keep still and undergo another four cycles of deposition-dissolution, each cycle for 6 hours, each 3 hours for deposition or dissolution

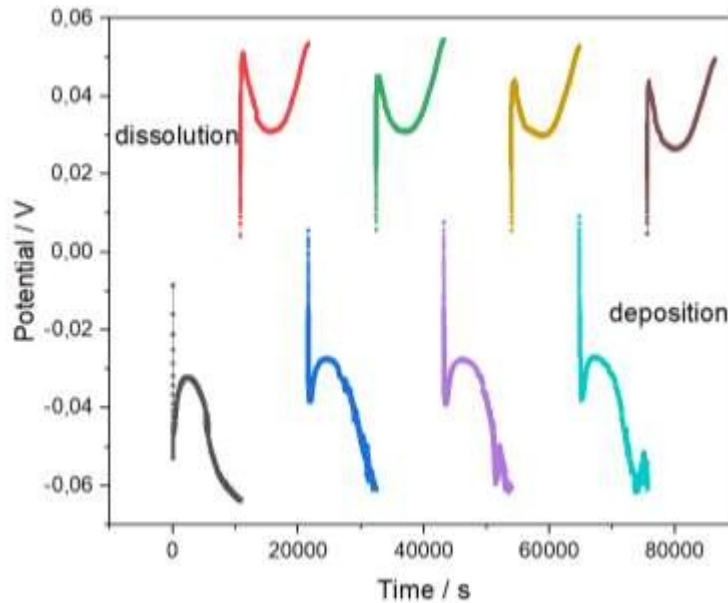


Figure 2-31 : Potential change of the four cycles of deposition and dissolution process at 100 mA cm^{-2} in flow electrolyte

2.2.4.5. Cycle test with copper substrate

To avoid the dissolution of the initial zinc electrode, we have replaced the zinc plate with a copper plate as the working electrode to conduct deposition-dissolution cycles. The counter/reference electrode is still a zinc plate. The cycle test on a copper substrate is also done with the same experimental parameters: a current density of 100 mA cm^{-2} is used during both deposition and dissolution, and flow rate of 1.5 cm s^{-1} . The electrolyte and the setup are kept the same with former experiments. For each deposition, the time is still set for 3 hours. But, instead of setting a time-scale limit during dissolution, we imposed a potential limit of 1 V on the electrodes during dissolution to avoid oxidizing and dissolving copper and meanwhile make sure that deposited zinc has been totally dissolved. In this case, 5 cycles of deposition-dissolution have been conducted.

At the beginning of the first cycle, there appear small bubbles along the surface of the copper substrate. A few of the small bubbles become bigger and deposition is also accompanied with a slow growth rate within this short period of time.

Around 20 min later, some instability appears, and deposits start growing much quicker than the others and dendritic growth appears. Hydrogen evolution is not observed anymore.

The dissolution appears reversible. Dendrites disappear and a smooth substrate is observed after the dissolution finishes and the potential reaches 1 V. There are still few deposits on the copper substrate along with small bubbles. The following cycles are similar to the first one.

The potential change is quite fluctuated during all cycles of deposition. While during dissolution, the potential is rather steady. This may be related to the reaction occurring on the zinc plate, namely reference electrode.

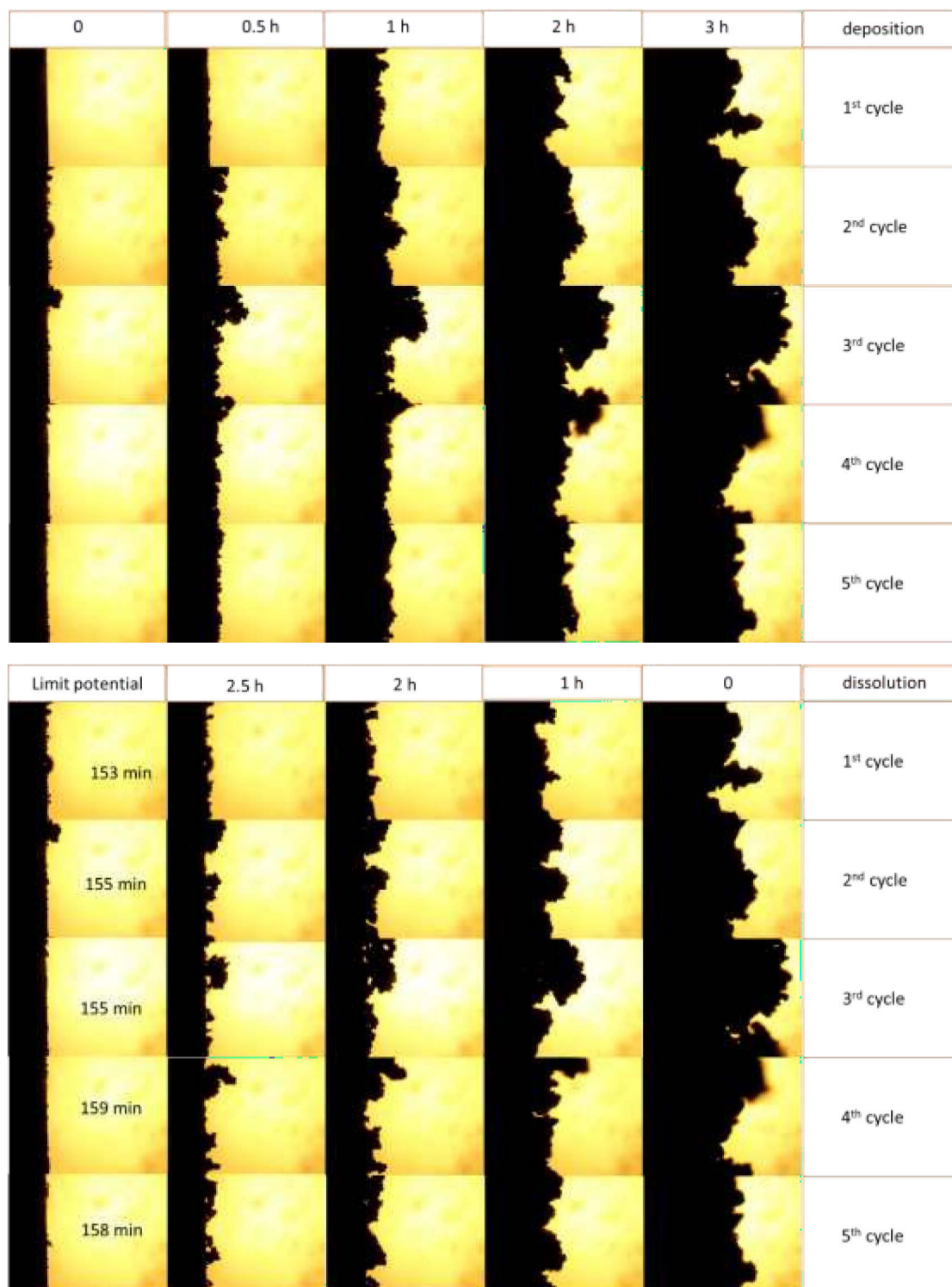


Figure 2-32 : Five cycles of deposition and dissolution onto copper at 100 mA cm^{-2} in flow electrolyte.

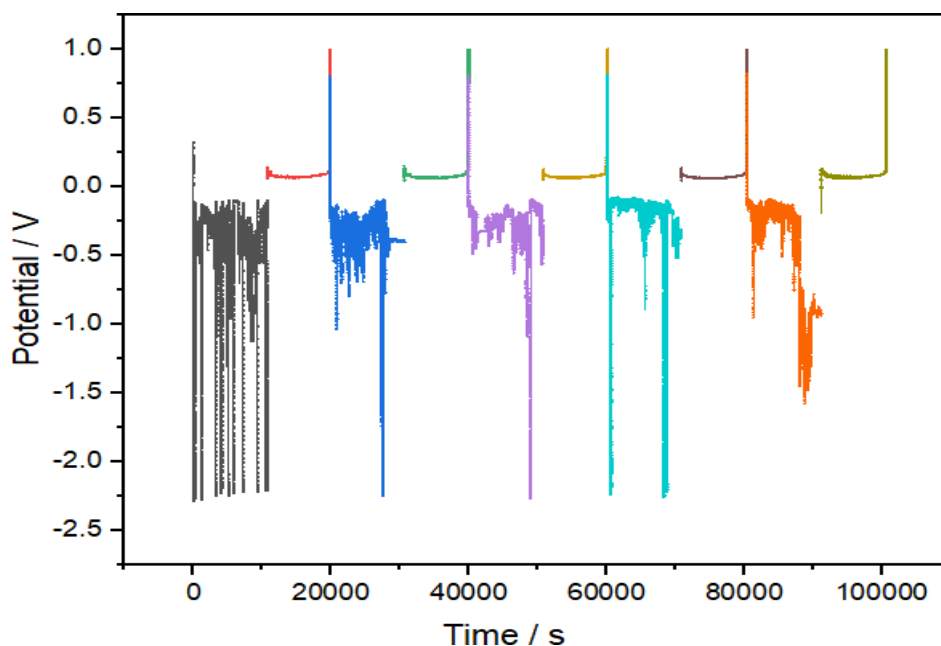


Figure 2-33 : Potential change of the five cycles of deposition and dissolution process on copper substrate at 100 mA cm^{-2} in flow electrolyte

2.2.4.6. Growth rate of deposits

Even though the pictures captured by the camera are not the full view of the electrode because they give a 2D image of a 3D process, they can generally represent the evolution of deposits. We have measured the area of the deposits to have a rough quantification of the growth rate.

The pictures captured are turned into black and white images, then the black deposits are selected out, and the ratio of its area to the whole image area is related using the Matlab2019a. Thereafter, the change trend of this area ratio with time is depicted. Because the pictures are 2D projection of the shadow projected by the zinc electrode and the deposits, the area could not reflect the mass of the deposits especially when the deposits are porous or dispersed. Considering the current is kept the same, the mass of deposits should be linear with time assuming that coulombic efficiency is 100% during deposition or dissolution. Based on this, if the area ratio changes faster in one cycle, it may indicate that in this cycle, the deposits are more porous and dispersed.

The pictures recorded from the cycle experiment every one hour in Figure 2-30 have been treated and the corresponding change of deposits area ratio is shown in Figure 2-34. We observe that the growth area of zinc deposits is generally linear with time, and in each cycle, the area change is faster during deposition than dissolution as shown by the linear slope obtained from fitting. This is in accordance with the fact that there remain deposits on the electrode.

Within the same period, the area ratios during deposition and dissolution are not the same, and area ratio of dissolution is always smaller, this is because the dissolution would prefer firstly occurring in the edges of the electrode rather the middle part as discussed above. As a result, the area change is slower in the later period than in the beginning of dissolution. The area ratio of the zinc electrode remains nearly the same after each cycle of deposition-dissolution despite that the electrode becomes rougher and rougher. The rate of area change generally increases with the cycles. This increase means the deposits are more dispersed upon cycling.

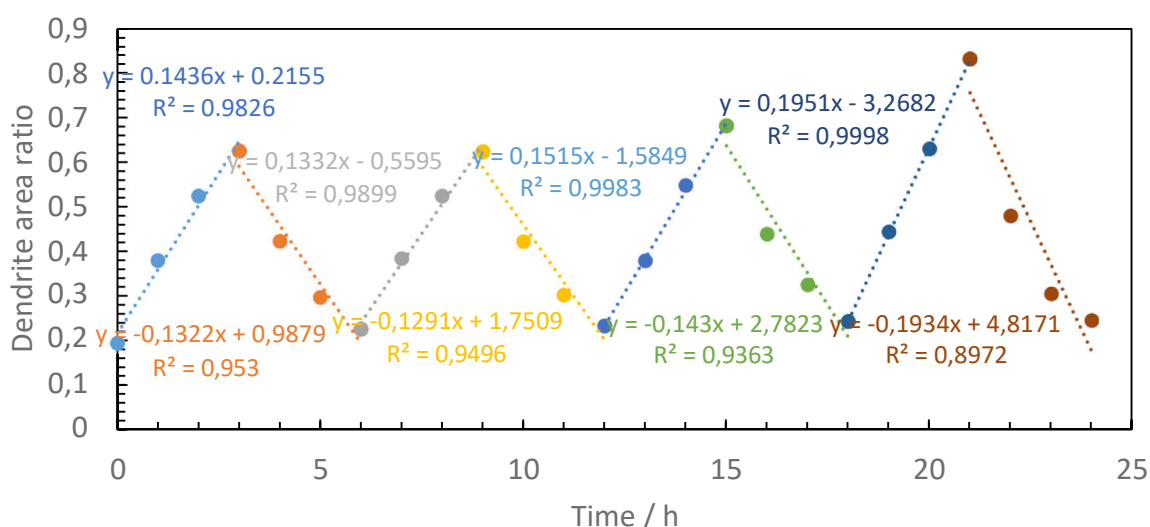


Figure 2-34 : The evolving of dendrite area ratio for the four cycles of zinc deposition and dissolution at 100 mA cm⁻² in flow electrolyte as in Figure 2-30

2.3. Conclusion

Three setups have been used to study the zinc electrode and the relative conclusions are as follows:

- 1) Three-electrodes system in an electrochemical cell
 - Zinc dissolution and deposition are diffusion-controlled reactions.
 - No evident difference is generated from the presence of LiOH between the electrolytes of 7 M KOH-0.7 M ZnO-0.7 M LiOH and 7 M KOH-0.7 M ZnO, in term of cyclic voltammogram within potential window of the electrolytes.
- 2) Static geometry

- For a same amount of charge, the higher current density gives more dispersed zinc deposits. At 1 mA cm^{-2} , the deposits are compact with little surface shape change. At 10 and 40 mA cm^{-2} , there are evident blunt-sword dendrites, and at 40 mA cm^{-2} the deposits are more dispersed with sharper tips.
- The lower zincate concentration in the electrolyte gives more dendritic zinc deposits with sharp sword-like shape.
- The potential change with time in the chronopotentiometry experiment is a result from the effects of evolved hydrogen adsorption and the non-uniform deposition.
- In term of galvanostatic zinc deposition and microscopic observation, LiOH in the electrolyte does not bring a clear effect on zinc deposition.
- Hydrogen evolution is easier at lower current density and in electrolyte with lower zincate concentration.

3) Flowing electrolyte

- Flowing electrolyte evidently promotes the suppression of dendrite growth. Higher current density can be applied with flowing electrolyte.
- Hydrogen evolution is easier to occur in flowing electrolyte.
- With more deposition-dissolution cycles going on, zinc plate becomes rougher and rougher.
- The growth of deposits and their dissolution is linear with time under galvanostatic charge and discharge. Specifically, dissolution rate is higher in the beginning of discharge than in the later period.

Chapter 3 Catalyst synthesis and characterization

3.1. ORR catalysis mechanism

Generally accepted is that there are two pathways for oxygen reduction reaction in aqueous solution. One is four-electron pathway, where oxygen is directly reduced to OH⁻ in alkaline media, which is preferably for ORR catalytic activity; the other is two-electron pathway where HO₂⁻ is formed firstly in a first step, then it is reduced to OH⁻ in a second step; in acidic media, OH⁻ and HO₂⁻ are replaced by H₂O and H₂O₂, respectively [169]. Table 3-1 presents the ORR pathways and the corresponding standard reaction potentials in aqueous electrolytes.

Table 3-1 : ORR pathways and reaction potential in aqueous electrolytes [170]

Electrolyte	Reaction pathway	Standard reaction potential (V vs. NHE)
Alkaline electrolyte	Four-electron pathway	
	$O_2 + 2 H_2O + 4 e^- = 4 OH^-$	+0.401
	Two-electron pathway	
	$O_2 + H_2O + 2 e^- = HO_2^- + OH^-$	-0.065
	$HO_2^- + H_2O + 2 e^- = 3 OH^-$	+0.867
Acidic electrolyte	Four-electron pathway	
	$O_2 + 4 H^+ + 4 e^- = 2 H_2O$	+1.229
	Two-electron pathway	
	$O_2 + 2 H^+ + 2 e^- = H_2O_2$	+0.67
	$H_2O_2 + 2 H^+ + 2 e^- = 2 H_2O$	+1.77

For the kinetics of ORR catalysis, it is more complicated regarding the complex intermediate reactions and products with different catalysts and electrolytes. Only concerning the oxygen species, it is classified into two different mechanisms: associative or dissociative mechanisms in both alkaline and acidic electrolyte. Their difference lies in the adsorption forms of oxygen.

In the associative mechanism, ORR begins from associative adsorption of the O₂ molecule whereas, in the dissociative mechanism, O₂ adsorbed on free sites directly dissociates into two O_(ads). Table 3-2 lists the general oxygen species evolution during ORR in alkaline and acidic electrolyte in two pathways. The peroxide way occurs at the third step in associative mechanism, and at the second step in dissociative mechanism, respectively [169].

Table 3-2 : ORR mechanisms in alkaline and acidic electrolyte

Mechanism	Alkaline electrolyte	
	Hydroxide as final product	Peroxide as final product
Associative mechanism	(1) $O_2 + * \rightarrow O_{2(ads)}$	(1) $O_2 + * \rightarrow O_{2(ads)}$
	(2) $O_{2(ads)} + H_2O + e^- \rightarrow OOH_{(ads)} + OH^-$	(2) $O_{2(ads)} + H_2O + e^- \rightarrow OOH_{(ads)} + OH^-$
	(3) $OOH_{(ads)} + e^- \rightarrow O_{(ads)} + OH^-$	(3) $OOH_{(ads)} + e^- \rightarrow OOH^- + *$
	(4) $O_{(ads)} + H_2O + e^- \rightarrow OH_{(ads)} + OH^-$	
	(5) $OH_{(ads)} + e^- \rightarrow OH^- + *$	
Dissociative mechanism	(1) $1/2 O_2 + * \rightarrow O_{(ads)}$	(1) $1/2 O_2 + * \rightarrow O_{(ads)}$
	(2) $O_{(ads)} + H_2O + e^- \rightarrow OH_{(ads)} + OH^-$	(2) $O_{(ads)} + OH^- \rightarrow OOH^- + *$
	(3) $OH_{(ads)} + e^- \rightarrow OH^- + *$	
Mechanism	Acidic electrolyte	
	Hydroxide as final product	Peroxide as final product
Associative mechanism	(1) $O_2 + * \rightarrow O_{2(ads)}$	(1) $O_2 + * \rightarrow O_{2(ads)}$
	(2) $O_{2(ads)} + H^+ + e^- \rightarrow OOH_{(ads)}$	(2) $O_{2(ads)} + H^+ + e^- \rightarrow OOH_{(ads)}$
	(3) $OOH_{(ads)} + H^+ + e^- \rightarrow O_{(ads)} + H_2O$	(3) $OOH_{(ads)} + H^+ + e^- \rightarrow H_2O_2 + *$
	(4) $O_{(ads)} + H^+ + e^- \rightarrow OH_{(ads)}$	
	(5) $OH_{(ads)} + H^+ + e^- \rightarrow H_2O + *$	
Dissociative mechanism	(1) $1/2 O_2 + * \rightarrow O_{(ads)}$	(1) $1/2 O_2 + * \rightarrow O_{(ads)}$
	(2) $O_{(ads)} + H^+ + e^- \rightarrow OH_{(ads)}$	(2) $O_{(ads)} + H_2O \rightarrow OOH^- + H^+ + *$
	(3) $OH_{(ads)} + H^+ + e^- \rightarrow H_2O + *$	

Note: * represents a surface free site on catalyst

There is no unified conclusive mechanism for ORR [171]. Taking metal oxide catalysts into consideration, commonly reported are three hypothetical reaction routes of the ORR in alkaline electrolyte which are shown in Figure 3-1. The (a) ‘end-on’ adsorption route corresponds to the associative mechanism, and (b) ‘side-on’ adsorption route corresponds to

dissociative mechanism mentioned above. Route (c) is more like an intermediate state of route (a) and (b) where bidentate adsorption takes oxygen vacancies into consideration.

In route (a) (end-on adsorption), the starting state a1 is the OH covered surface; a2 results from O₂ adsorption on one metal site, displacing OH coverage; a3 is the protonation of a2, resulting an OOH group; finally, O-O bond on OOH group breaks and protonates to form an OH group, returning to the original state. Route (a) is exemplified on the rutiles IrO₂, RuO₂, the pyrochlores Pb₂Ru_{2-x}Pb_xO_{7-y} and the perovskites Sr_{1-x}Nb_xO₃ [172].

In route (b), side-on adsorption, the state of b1 presents the same with a1, while O₂ is adsorbed on two neighboring metal sites, which is followed by O-O bond and formation of metal dimer b3; then b3 is protonated to finish the catalytic cycle. Li-doped NiO and perovskite La_{0.5}Sr_{0.5}CoO₃ are reported to undergo route (b) [173, 174].

In route (c), the surface presents oxygen vacancies. One oxygen of the O₂ molecule fills the vacancy, the other one displaces the OH⁻ surface group, resulting in c2 as a superoxide, which is followed by protonation to be c3. Then the bridging oxygen is protonated to form c4, after discharge and releasing OH, vacancies are recovered [171]. This process was proposed to explain the mechanism of ORR on SrCoO_{3-δ} perovskite oxides [175, 176].

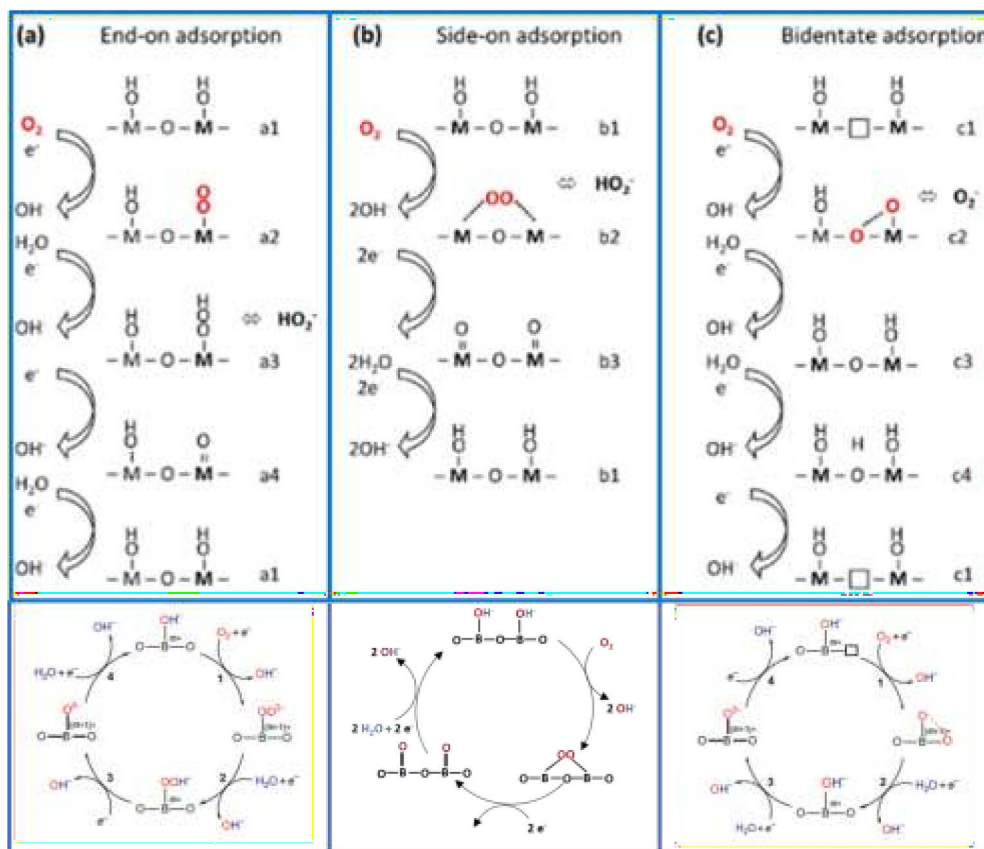


Figure 3-1 : Hypothetical proposals for electrolytic reduction of oxygen to hydroxide in alkaline media. Prototypical O₂ adsorption in (a) end-on configuration, (b) side-on configuration and (c)

bidentate configuration with participation of a lattice oxygen vacancy [171]; the schematic below is corresponding to the above routes, route (a) corresponds to reference [177]

3.2. Catalysts for ORR and OER

In commercial primary zinc-air batteries and rechargeable zinc-air fuel cells, Pt/C and MnO₂ are the most applied catalysts for ORR. Pt-based catalyst has the problem of low stability in concentrated alkaline electrolyte; the catalytic activity of MnO₂ is relatively low [20]. Their performance is still to be improved.

Noble metal-based catalysts continue to improve in perspectives of price reduction and stability enhancement. Noble metal (Pt, Au, Ag, Pd and Ru) clusters, noble metal-transition metal alloys are investigated to have higher activity and better stability on ORR catalysis, as reviewed in [178-180]. Transition metal-based catalysts like metal alloys, oxides, hydro(oxy)oxides, perovskite, spinel oxides are developed to show good ORR, OER catalysis performance, or as bi-functional catalysts for both ORR and OER. Metal-free carbon-based catalysts are widely reported as well to have superior bi-functional performance applied in air electrodes [181, 182]. Metal/carbon hybrid catalysts combine the advantages of both metal-based and carbon-based catalyst, outstanding oxygen electrocatalysis [183-186].

3.2.1. Noble metal catalysts

Noble metals for OER reaction: Noble metals have been applied in a plethora of fields as catalysts. For ORR catalysis, Pt is the most reported and applied case. The intrinsic activity of Pt on ORR is usually studied on Pt single crystals. Their structures and sizes are deemed as the main factors influencing their catalytic activity. Structure is decided by the bonding geometry, resulting in different particle shapes and sizes, bounded by different facets, and thus having surface atoms with different reactivities (low or high coordinated), which are often termed as structure effect, electronic effect and ensemble effect as in [187, 188], they interfere with each other.

Overall, the effective approaches to improve the activity of catalysts for ORR or OER can be either to increase the number of active sites via support application, morphology control, or to increase the intrinsic activity via alloy or electronic structure tuning, as schematically shown in Figure 3-2.

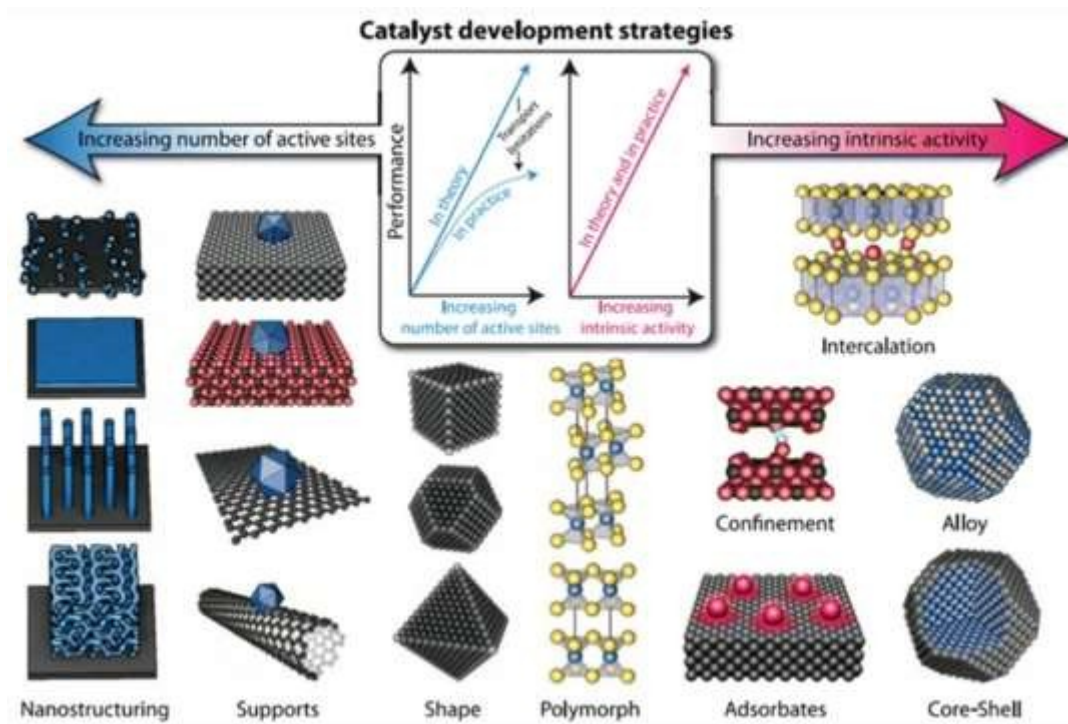


Figure 3-2 : The effective approaches to improve catalyst activity [27]

The high-index facets have higher activity than low-index facets because high-index facets are associated with multiple atomic steps, edges, and kinks [189-191]. Size effect of Pt on ORR catalysis usually studied using supported Pt catalyst is linked to the facet distribution and the structure sensitive adsorption, which can be explained from the standpoint of single crystal shape and size. When particle sizes decrease from 5 to 1 nm, facet {111} decreases a lot [188]. In a weakly adsorbed electrolyte, like dilute HClO₄ or KOH, facet {111} is more active. While in strongly adsorbed electrolyte, like diluted H₂SO₄, H₃PO₄, {100} facet is more active [187]. Concave Pt nanocubes were reported to have lower activity than the Pt/C catalyst for ORR catalysis because of their relatively larger size and therefore smaller portion of active Pt atoms on the surface [192]. Some authors reported that the specific activity of Pt/C is not dependent on particle size even in a range of 1 - 5 nm, which is not predictable from a point view of single crystal [193]. To explain the different conclusions, different reaction mechanisms or other decisive parameters on ORR catalytic activity were proposed, e.g., interparticle distance [193-195].

Non-precious supports or alloys are useful for price reduction and activity enhancement [196]. Bimetallic Pt alloys e.g., Pt-Ni and Pt-Co bulk alloys are reported to have higher activity towards ORR because Pt crystal is more prone to form Pt-OH which is less active than the bimetallic alloys. The second metal Ni or Co plays a protective rather a synergistic role [187].

But Pt-Pd binary superlattice was reported to have synergistic effect for ORR activity [197]. There are various types of Pt alloys synthesized to show good ORR catalytic activity, including Pt-transition metal binary, ternary, or quaternary alloys considering the compositions; porous alloys, nanowires, nanotubes, nanorods alloys considering their structures and morphologies [188]. Core-shell structured particles with Pt monolayer positioned at shell are widely studied. Core materials, compositions and structures have a large influence on the core-shell particles, e.g., Shao et al. [198] synthesized Pd-Cu@Pt, which showed higher ORR activity than Pd@Pt, Au(111)@Pt was two times more active than Au(100)@Pt and Au(110)@Pt due to the compressive strain in Au(111) facets which weakened the oxygen binding strength [199]. Similarly, AuNi_{0.5}Fe@Pt showed better performance compared with Au@Pt [200]. The good performance of such core-shell systems is attributed to the complex electronic effect and a structural effect, like compressive strain, ligand formation, surface roughness etc. [188].

It was reported that the ORR activity of the different oxidation states of Pd increased with its valence state: Pd⁰ < Pd²⁺ < perovskite-type ionic compound Pd^{3+/4+} [201]. Pt is not suitable for OER catalysis because at the higher potentials, OH species cover Pt surface to form Pt oxides which decrease its activity [202].

Ir, Ru oxides and alloys are better choices for OER catalysis [203]. Like Pt in ORR catalysis, Ir or Ru synthesized to form various structures from 0D to 3D morphologies (nanoclusters, nanowires, nanorods, nanotubes etc.) have enhanced activity for OER. This has been related both to electronic effect and structural effect, leading to change of bonding towards the intermediates formed during adsorption on the catalyst surface [203]. The single Ir^V atomic sites on the top atomic layer of IrO₂ transformed from Ir^{IV} are deemed to be preferable for the formation of OOH intermediates in the oxide-hydroxide-oxide path during OER process [204]. Tuning the composition often offers an electronic effect, as exemplified in [205] where doping Cu in IrO₂ could change the d-orbital occupation from low spin Ir(t_{2g}⁵e_g⁰) to partially filled e_g orbitals. Likewise, bimetallic, or multiple metallic alloys also have an activity enhancement. The active surface sites of the Ir alloys (Ir-Co, Ir-Ni, Ir-Fe, Ir-Cu) are agreed to be Ir at oxidized states. Similar to the electronic effect of Cu doped IrO₂, the Ir alloys are also prone to have a partially occupied e_g orbital, which optimizes the bonding strength toward the adsorption of intermediate species [206] which is also seen in the Ir-Cu nanoframes and Cu-Rh core-shells and Rh-Cu twinned nanorod frames [207].

Reducing the particle size of Ir to nanoclusters or single atoms would dramatically enhance the activity for OER. Zhang et al. [208] realized the incorporation of Ir nanoclusters and Ir single atoms into Co(OH)₂ nanosheets. With the two active sites of transformed Ir oxide

and CoOOH, it yielded comparable and even better OER performances than commercial IrO₂ in neutral and alkaline electrolyte. From the above, except for the size effect, the substrate-Ir interaction is also highlighted. Metal-support interaction studies have expanded to various forms of carbon materials which can adjust the loading content of noble metal, specific active sites (per surface area), electronic structure, corrosion resistance, charge transfer rate, etc. [203]. The Rh nanoclusters loading content can be reduced to 6.7 wt.% on support of single-walled carbon nanotubes [209]. It is indicated that the density of state of carbon materials is linked to their electronic polarization capability, and it is commonly sequenced as below: single-walled carbon nanotubes > multi-walled carbon nanotubes > graphene > carbon black, which is accordance to their electrocatalytic performance [210]. Surface physicochemical properties of catalysts is very important for the OER catalytic activity. Surface morphology sculpture techniques are applied to create high-index facets, islands, or nanodendrites from a template decoration approach, to form hollow structures from a template etching method [203]. Lu et al. [211] reported platinum-gold nanoparticles to be a good bi-functional catalyst, having surface Au and Pt atoms primarily responsible for ORR and OER.

As a conclusion, noble metals for ORR and OER catalysis are still on development as well as the determination of their catalytic mechanisms. Size effects accompanied with structural effects from the micro and macro perspectives are deeply and widely researched. A pool of noble metal-based catalysts is designed and synthesized according to specific electronic effects. New discoveries are always expected, more blameless and intrinsic principles should be unveiled. The perspective may also be projected to the bi-functional oxygen electrocatalysts, as is already reported in a few studies [212], that Pt-based catalyst may have good potential for both ORR and OER.

3.2.2. Carbon-based metal-free catalysts

In the field of oxygen electrocatalysis, metal-free catalysts have been pursued intensively, especially after the appearance of an outstanding work about a vertically aligned nitrogen-doped carbon nanotube (VA-NCNT) arrays which could exhibit 3-times higher activity than that of Pt/C and better cyclability applied in alkaline fuel cell owing to the high surface area, good electrical, mechanical properties, and superb thermal stability [213]. Subsequently, N-doped graphene and graphitic flakes [214-216], various heteroatom-doped carbon materials, e.g., B-doped CNTs [217] or graphene [218], S-doped graphene [219], P-doped graphite layers [220], I-doped graphene [221] and edge-halogenated (Cl, Br or I) graphene nanoplatelets [222]; binary or ternary doping of different heteroatoms into carbon

materials e.g., B, N co-doped VA-CNTs [223] or graphene [224], N, S-doped graphene [225], N, P-doped graphene [226], N, B, P-doped carbon [227] were widely investigated. Aside from this, clever structural design of carbon materials also makes a difference.

The commonly seen carbon materials including graphene, carbon black, CNTs, CNFs (carbon nanofibers), mesoporous carbon, or activated carbon, etc. usually have little activity towards the ORR. However, the electrocatalytic activity of the carbon materials can be enhanced by heteroatom doping which could greatly alter the electron distribution of dopants and adjacent C atoms via the delocalization of π electrons, and by C defect/vacancy which could also destroy the unity of π conjugation and influence the electronic structure of adjacent C atoms [228].

The ORR mechanism on N-doped carbon materials demonstrated that carbon atoms next to pyridinic N show Lewis basicity and the oxygen molecule is first adsorbed at such carbon atoms followed by protonation of the adsorbed O_2 as shown in Figure 3-3 [229].

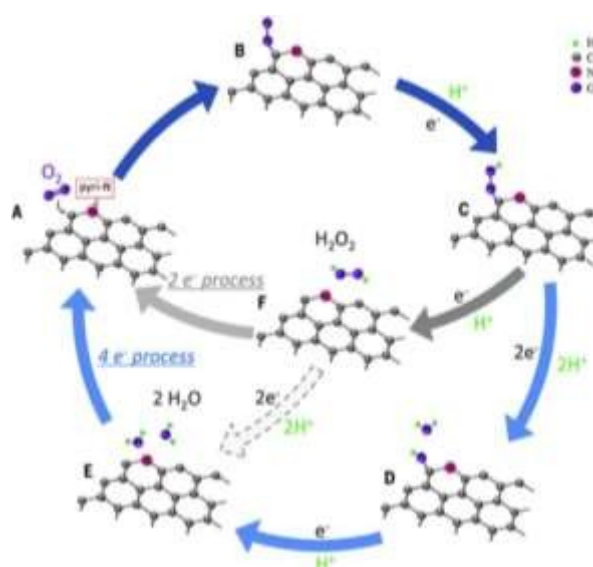


Figure 3-3: Schematic ORR mechanism on N-doped carbon materials [229]

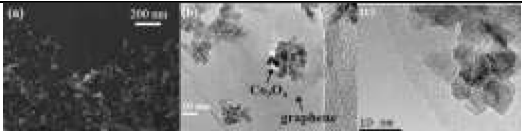
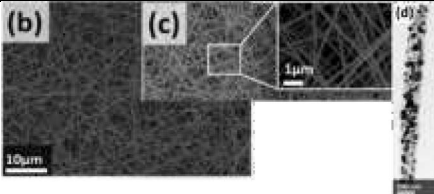
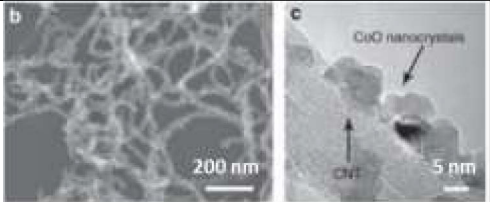
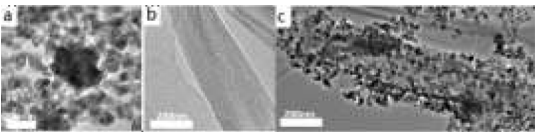
3.2.3. Metal/carbon hybrid catalysts

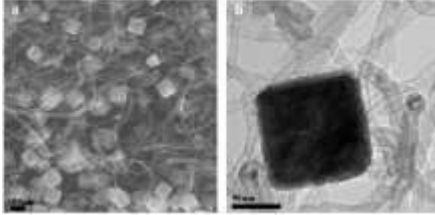
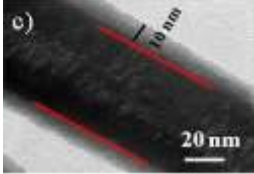
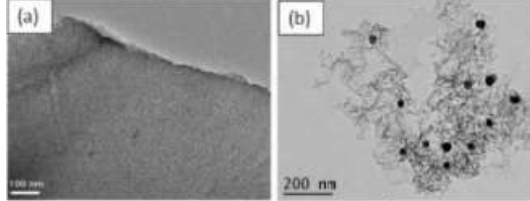
Though metal free catalysts are under a massive development, metal-based catalysts are generally more stable than carbon-based materials under strong oxidation atmosphere [230], the metal/carbon hybrid catalysts attract much attention. More correctly speaking, the hybrid catalysts all present synergistic effects, they function with multiple types of active sites via possible chemical bonding between the two different materials, usually synthesized from metal materials nucleation and growth on the nanocarbon materials [231]. Here, conventional

composite electrodes with catalysts and carbon materials of which the main contribution is the electronic conductivity enhancement by physical contact, rather the electronic structure tuning effect between the carbon materials and the metal catalysts, whereas they also make positive effect on the overall catalytic activity for ORR or OER [232-234]. Various forms of carbon (e.g., carbon black, graphene, carbon tubes, carbon fibers, and graphene) could be used to overcome the low electrical conductivity of the metal oxide-based catalysts. Up to now, noble metal, non-noble metal, metal oxides are variously hybridized with carbon materials in different structures [181], as simply listed in Table 3-3 as the representatives.

Transition metal nitrides or phosphides and the hybrid with carbon materials were also reported to have good ORR catalysis taking advantage of the great electronegativity difference between metals and N or P, e.g., Fe₂Ni₂N/Co@NCNT [235], cobalt phosphide embedded into a nitrogen, sulfur, phosphorus co-doped carbon matrix [236], Fe₃Pt/Ni₃FeN bifunctional catalyst [237], Co₂P–CoN double active centers confined in N-doped carbon nanotube Co₂P/CoN-in-NCNTs [238], carbon-supported M_xP_y (M = Ni, Co, W, Cr, and Mo) [239] etc.

Table 3-3 : Some metal/carbon hybrid catalysts for ORR or OER

Metal material	Carbon material	SEM or TEM image	Catalyst and Ref.
Co ₃ O ₄	N-doped graphene		Co ₃ O ₄ /N-rmGO [184]
FeCo bimetal	CNT		FeCo–CNT [240]
Co–Ni nanoparticles	Electrospun graphitic carbon nanofibers		Co–Ni/CNF [241]
CoO nanocrystals	N-CNT		CoO/N-CNT [242]
CoFe ₂ O ₄ (CFO) nanoparticles	Rod-like ordered mesoporous carbon		CFO/RC [243]

Cubic cobalt oxide	Multi-walled carbon nanotube		cCo ₃ O ₄ /MWCNTs [244]
BaMnO ₃ nanorods	C nanorods		BaMnO ₃ @5%C nanorod [245]
FeNi alloy	N-doped carbon		FeNi-NC [246]

3.2.4. Transition metal catalysts

As mentioned above the transition metals could on one hand play a role as an additive in noble metal-based catalysts for ORR or OER by tuning their special electronic and structural effects, where noble metals occupy the active sites. On the other hand, they can also function as active catalysts for ORR and OER themselves. Transition metals are widely used as catalysts in the form of oxides, either as single metal oxides (e.g., MnO_x, Co₃O₄) or as mixed oxides (perovskite oxides, spinel oxides etc.). Since most of the oxides used are late transition metals with filled e_g orbitals (Mn, Co, Ni...), they form basic oxides that must be used in alkaline electrolytes because they are not stable in acidic solutions which dissolve them [247]. The metal cations on catalyst surface are deemed as the active sites for ORR [248]. Besides, transition metal phosphates, chalcogenide materials have been also studied as oxygen electrocatalysts [249, 250]. Studies about ORR on oxides catalysts have been put forward since 1970s. Enormous efforts have been made to understand the mechanism of ORR and the main parameters influencing activity of the catalysts, empirical and intrinsic conclusions were obtained by the aid of technique advancement and multiple-angles insights. Some requirements have been proposed for ORR oxide electrocatalysts [171].

An electronic conductivity higher than 10³ Ω⁻¹ m⁻¹ is the first requirement for a good electrode. The electronic conductivity of perovskites varies for different transition metals. They can be insulating or metallic. D. B. Meadowcroft et al. [251] studied several different transition metal oxides including NiO, In₂O₃, SnO₂, CoO, LaCrO₃, LaCoO₃, PrCoO₃, SrMoO₃ for ORR activity, discovering that only cobaltite was active for ORR. Comparing the properties of

LaCrO₃ and LaCoO₃, it was concluded that both N and P-type conductivities were possible for oxygen adsorption. Bevan et al. [173] proposed that the paramagnetic property of the catalyst should be a requirement for good ORR activity, based on the ‘side-on’ adsorption model of the paramagnetic oxygen molecule. Lithium-doped NiO showed great catalytic activity towards ORR above its Neel temperature (in the paramagnetic state). However Larsson et al. [252] conducted a very systematic work on 26 different perovskite oxides with different magnetic moments, but they demonstrated that there was no significance relation between the magnetic property of the perovskites and their activity towards ORR. The important fact is only that they need to be conducting to optimize electron transport.

Instead of ‘side-on’ oxygen adsorption mechanism, ‘end-on’ type oxygen adsorption was proposed more reasonable in the case of perovskite oxides because of the intrinsic incompatibility between the crystal structure of perovskite oxides and oxygen molecule [253]. According to the ‘end-on’ oxygen adsorption, it was easily accepted that oxides with σ^* band formed by an e_g orbital of transition metal cation mixed with s- p_σ orbitals of O in M--O--M (M denote transition metal) would be better for their catalytic activity, owing to the easiness of e_g orbital interaction with oxygen. Based on the above, Matsumoto [247, 253, 254] supported qualitatively that the catalysts with σ^* band containing electrons was a decisive factor on the catalytic activity of perovskite oxides through a thorough study on LaNi_{1-x}M_xO₃, La_{1-x}Sr_xMnO₃, LaTiO₃, SrVO₃, SrRuO₃, and V_{0.2}Ti_{1.8}O₃ that varied with conducting band. Suntivich et al. [177] studied a series of perovskite oxides with various A sites and B sites, accompanied by different e_g , t_{2g} occupations. The relation between activity of the catalysts (around 4 orders of magnitude in intrinsic ORR activity) and their e_g filling presented a volcano shape as shown in Figure 3-4 (a). This ‘descriptor’ accords to a M-shape relationship between the activity and the d-electron numbers per B cation. This could be high spin d^4 such as Mn³⁺ ($3d^4$, $(t_{2g})^3(e_g)^1$ in octahedral field) or low spin d^7 such as Ni³⁺ ($3d^7$ configuration $(t_{2g})^6(e_g)^1$ in octahedral field). Meantime the effect of B-O covalency of the perovskite oxides on the catalytic activity was also investigated under the same e_g filling, it was found that the covalency or hybridization of the B-O bond also played a role that the perovskite oxide with higher hybridization of B-O bond produced higher catalytic activity for ORR, as shown in Figure 3-4(b). Analogue to the analysis for ORR, the OER activity also has a volcano-shape relationship with the e_g filling [255]. Suntivich et al. [256] further indicated a similar mechanism of ORR on transition metal oxides and noble metal Pt, the O₂/OH⁻ exchange model and the rate-determining step was governed by the O₂ binding strength.

Petrie et al. [257] studied the strain effect on oxygen electrocatalysis of LaNiO_3 thin film. Combining with DFT (density functional theory) calculation, they revealed that the strain could induce the orbital splitting and polarization as well as the surface asymmetry which was not like d-band center theory. Besides, as an analogy with d-band center of metal relative to Fermi Level (E_F), they proposed a new parameter e_g -center (E_{e_g}) which was determined by weighting the center of each state to its orbital occupancy at the surface, to describe the catalytic activity. They concluded that the compressive strain induced a lower E_{e_g} , which destabilized Ni-O chemisorption and increased bi-functional activity of LaNiO_3 for ORR and OER, as schematically explained in Figure 3-4 (c) and (d). Other DFT work was also applied to dig into the mechanism and the main factors of ORR or OER on perovskite oxides. The OH^* or O^* coverage on the surface of oxides were found to be relative to the surface stability, taking the coverage into account, a more correct method was found to model and calculate the ORR process on perovskite oxides [258].

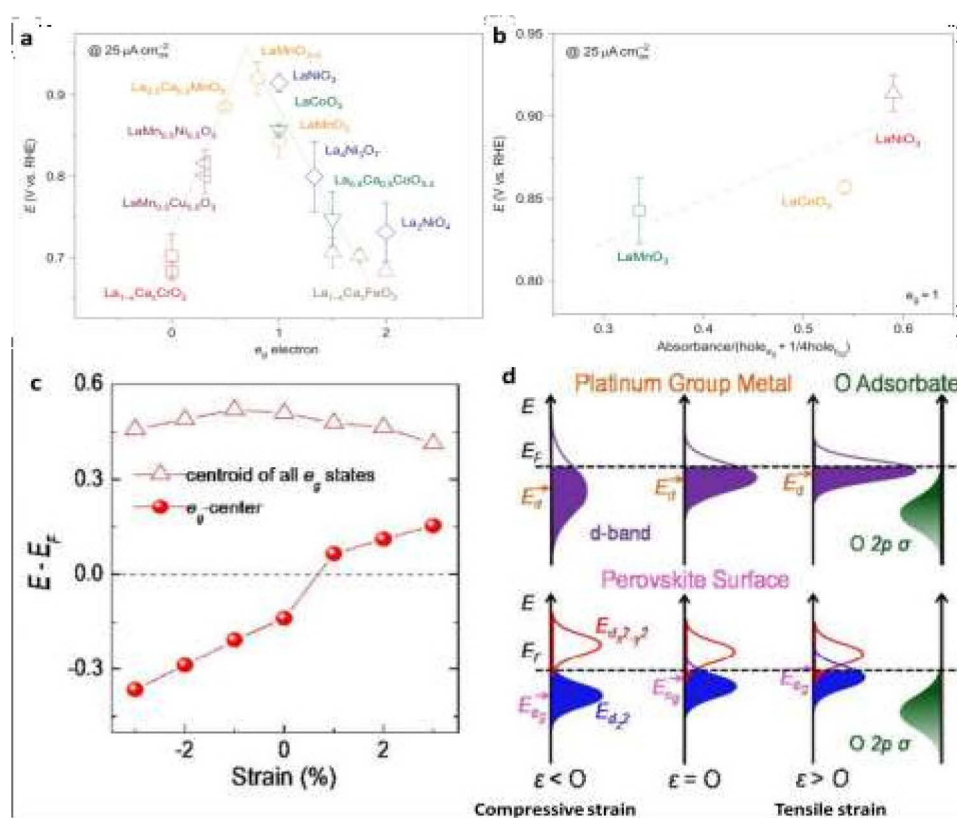


Figure 3-4 : (a) Potentials at $25 \mu\text{A cm}^{-2}$ as a function of e_g orbital in perovskite-based oxides; (b) Potentials at $25 \mu\text{A cm}^{-2}$ as a function of the B-O covalency, which is estimated by the normalized absorbance at e_g -filling = 1 [177]; (c) Position of the centroids calculated from DOS for the e_g states and the e_g -center (E_{e_g}) with respect to E_F as a function of strain; (d) Schematics relating this trend in perovskites to the d-band center (E_d) in Pt. While changes in bandwidth play a significant role in E_d shifts for Pt group metals, orbital splitting and polarization have a greater effect at the asymmetric surface of correlated perovskite oxides such as LaNiO_3 [257]

Transition metal alloys: Transition-metal selenides (M_xSe_y , $M = Fe, Co, Ni$) and their carbon hybrid catalysts are also widely used for electrocatalysis of OER and ORR [259]. Yang et al. [246] synthesized FeNi alloy and N co-doped carbon as the catalyst in oxygen electrode of a home-made Zn-air battery which displayed excellent charging and discharging polarization curves and robust cycle stability, superior to the 20% Pt/C+IrO₂-based one.

Single transition metal oxides: Among all the oxides, manganese and cobalt are most applied as the active sites for their valence variability. Their catalytic activity depends on chemical composition, crystallographic structure, oxidation state, morphology, and surface area from a macro view [260], while intrinsically, all is about electronic and structure effects.

Manganese oxides (MnO_x) were reported for ORR catalysis early in 1973 [261]. Up to now, MnO_2 , Mn_3O_4 , Mn_2O_3 , Mn_5O_8 , MnO , $MnOOH$ are all reported to have ORR catalysis activity in alkaline electrolyte [262-266]. Among them, $MnOOH$ was thought the most active, because all other structures would transform to $MnOOH$ during the catalytic reaction of ORR [267]. The difference of the catalytic activity of MnO_x for ORR in alkaline electrolyte was thought to be in the second step of O_2 reduction to OH^- , namely HO_2^- to OH^- . While for the first two-electron process from O_2 to HO_2^- , MnO_x showed no difference [268]. MnO_2 with different crystal structures vary in their activity for ORR catalysis, it was generally accepted with the following sequence: β - $MnO_2 < \lambda$ - $MnO_2 < \gamma$ - $MnO_2 < \alpha$ - $MnO_2 \approx \delta$ - MnO_2 [269]. There also existed a controversy about the position of δ - MnO_2 , possibly because of different synthesis processes yielding different surface areas and morphologies. The δ - MnO_2 phase prepared by a sol-gel method adopted in [270] showed highest activity among the different crystallographic structures, while in [271] hydrothermal process was applied, δ - MnO_2 presented lowest activity towards ORR. Besides, β - MnO_2 also presented a controversy in the work [262], where β - MnO_2 was testified to have higher activity than λ - MnO_2 as in Figure 3-5(e), this was possibly caused by the effect of morphology according to the authors. The α - MnO_2 nanowires presented higher activity than nanospheres and microparticles, their morphologies and activity performance comparison are shown as Figure 3-5(a), (b), (c) and (d). Other morphologies like nanosheet [272], nanotube [273], nanorod [108], nanoflake[274], nanoball [275], nanoflower [276], urchin-like [277], star-like [278], etc., were also tuned to obtain better activity than Pt/C. Some work concluded that the activity of them obeyed a general sequence as below: nanowire > nanorod > nanotube > nanoparticle > nanoflower [276]. Similar to crystallographic structures, there are also other works proposing different sequences or counterexamples [260]. The Mn_3O_4 nanoflakes with facets (001) exhibited greatly higher activity than Mn_3O_4 nanorods with exposed facets (101) on ORR catalysis [274]. It was also found that the Mn with higher

oxidative state in MnO_x showed higher activity for ORR catalysis. Tang et al. [279] synthesized MnO_x nanorods with different heat treatments to obtain MnO_x -350A (heating at 350 °C in air), MnO_x -650A (650 °C in air), and MnO_x -600N (600 °C in N_2). MnO_x -350A had higher Mn valence than the others (more of Mn^{3+} and Mn^{4+}), and MnO_x -600N had the lowest. The ORR catalytic activity increased with Mn valence state, as presented in Figure 3-5 (f), this could be explained from the step during ORR that Mn^{4+} (MnO_2) was reduced to Mn^{3+} , followed by electron transfer from Mn^{3+} (MnOOH) to oxygen and recovering Mn^{4+} [267, 280]. The Mn valence in MnO_x could also be tuned by the electrochemical approach; imposing negative potential caused lower valence and applying positive potential brought higher valence.

From the above, composition, crystallographic structure, morphology could all be the factors that influence the activity of MnO_x catalysts. But most of these works never take into consideration of the different stoichiometries (and the resulting electronic conductivities), the different crystallographic sites exposed to the surface as well as the different specific areas of the catalysts.

There is a similar case with nickel-based oxides where the control of the potential could change the oxidation state and the concentration of trivalent nickel [173]. Cobalt is another widely used transition metal in ORR catalysis. CoO and Co_3O_4 were reported as bi-functional catalysts, especially CoO deposited onto N-doped carbon [281-283]. Spinel-type Co_3O_4 is more synthesized as ORR catalyst. There are Co^{2+} and Co^{3+} in Co_3O_4 , and Co^{2+} is deemed the active part for ORR catalysis due to its preference for O_2 adsorption [284]. There are also different morphologies of Co_3O_4 , to which their properties are related intimately. Co_3O_4 with the morphologies of core-shell [285], nanosheet [286], nanotube [287], nanoflower [288], nanofiber [289], nanofilm [290], nanosphere [291] etc. are seen in the previous works. CoO and MnO_2 composite catalysts supported on reduced graphite oxide ($\text{CoO}/\text{MnO}_2/\text{RGO}$) with a synergistic effect from both CoO and MnO_2 , exhibited comparable performance with that of Pt/C [292], as is seen in Figure 3-5 (g).

A synergistic effect was also achieved from the combination of N-doped carbon shell and metallic Co species GCN-Co@CoO [184, 293]. N-doped carbon materials with different morphologies are commonly integrated with transition metal oxides, tuning their electronic structure, resulting in enhanced catalytic activity; or acting as a metal-free catalyst.

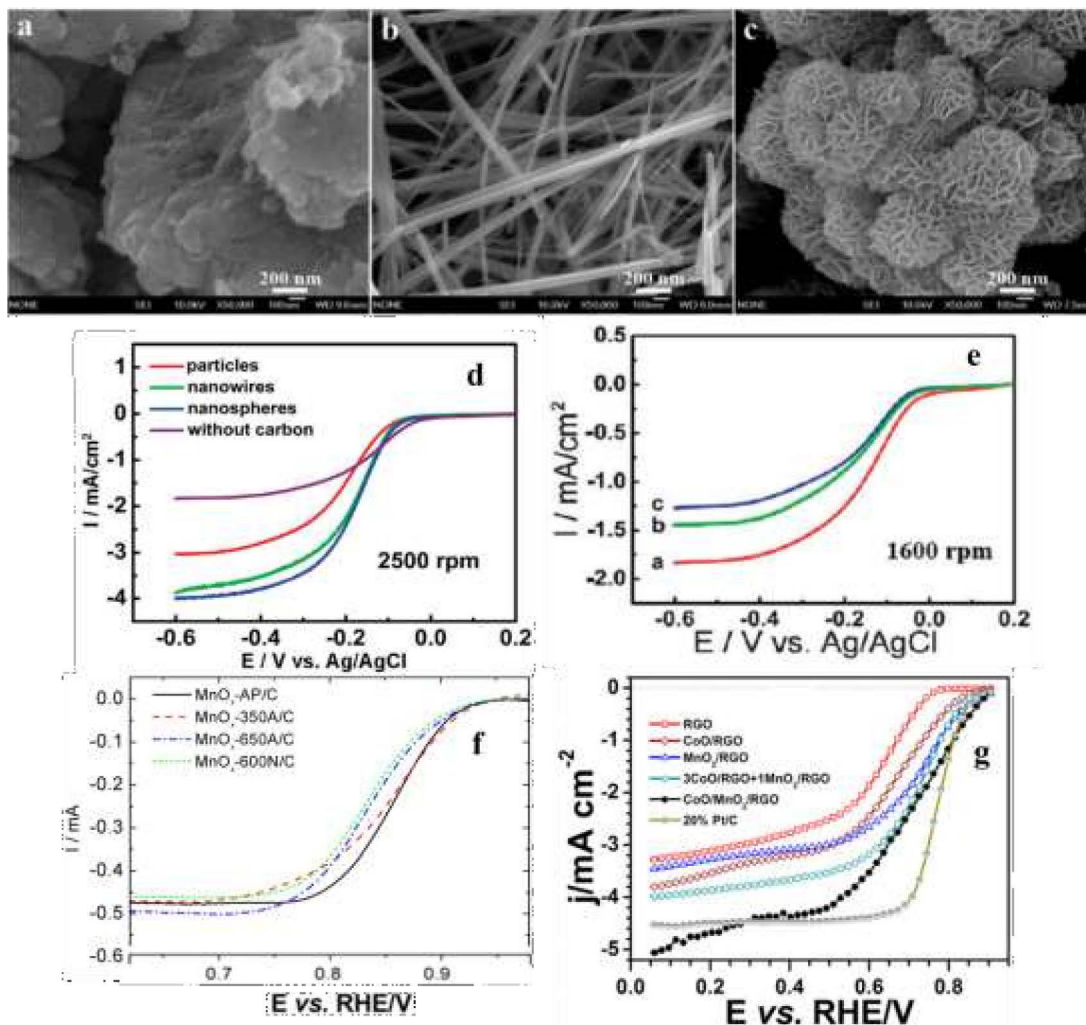


Figure 3-5 : SEM of different morphologies of α - MnO_2 (a) microparticles (b) nanowires (c) nanospheres; (d) comparison between polarization curves of catalysts supported on carbon with the above three morphologies at the rotation rate of 2500 rpm; (e) polarization curves of catalysts with different crystallographic structures: α - MnO_2 (red), β - MnO_2 (green), and λ - MnO_2 (blue) at the rotation rate of 1600 rpm in electrolyte: O_2 -saturated 0.1 M NaOH solution [262] (f) polarization curves of MnO_x nanorods with different Mn valences under the condition of the scan rate of 10 mV s^{-1} , and the rotating rate is 1600 rpm in electrolyte: O_2 -saturated 1 M NaOH solution [279]; (g) polarization curves of different composite catalysts of CoO and MnO_2 C at a rotating rate of 1600 rpm and a scan rate of 5 mV s^{-1} in O_2 -saturated 0.1 M KOH solution [292].

Ni-based [294], Fe-based [295], La-based [296], Ce-based [297], Cu-based [298], Mo-based [299], Ti-based [300], V-based [301] oxides are also reported to have activity for ORR catalysis, while usually inferior to Mn-based and Co-based catalysts. Nickel (Ni^{3+} , $3d^7$) shows a high activity for ORR catalysis [173]. Their activities appear better in multinary oxides or associated with carbon materials than in their single oxides. Ni-based, V-based oxides are more applied as catalysts for OER than ORR or as bi-functional catalysts because they are stable in a wide potential range [257, 302, 303].

Perovskite oxides: Perovskite oxides are extensively studied as oxygen catalysts in air electrode, having a great potential for application. They have the common formula of ABO_3 ,

where generally, the A site cation is an alkaline earth or rare-earth ion, and B site cation is a transition metal. A or B could be substituted by other elements to form $A_{1-x}A'_xB_{1-y}B'_yO_3$.

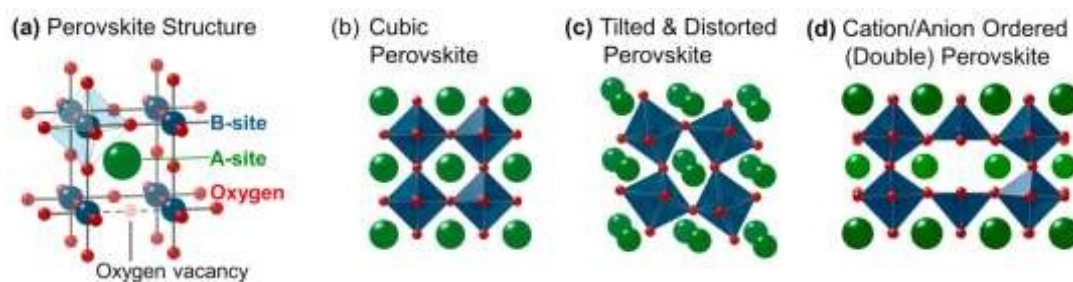


Figure 3-6 : (a) Schematic unit cell of perovskite oxide, (b) cubic perovskite structure (c) distorted structure, (d) double perovskite structure [171]

The ideal crystal structure of perovskite oxides is cubic with the $Pm\bar{3}m$ space group, where the A cation is in the center of the cube in dodecahedral coordination and the B cation is in octahedral coordination toward oxygen. To define the domain of stability of the perovskite structure, a tolerance factor, t is given:

$$\text{Equation 3-1: } t = \frac{r_A + r_O}{\sqrt{2}(r_B + r_O)} = 1$$

where r_A , r_B , and r_O are the radii of the respective ions. The ideal cubic perovskite is obtained when $0.9 < t < 1$. Under this value it becomes distorted to rhombohedral or orthorhombic symmetry [304, 305]. The radius of the cations A is around 1 to 1.7 Å, and it is around 0.6 Å for B cations [306]. The double perovskite oxides may form because of the more than 50% substitution of B-site, thus an ordering of two types of B cations may be present [307]. It can be also because of the large difference in ionic radius between the A-site and B-site ions, resulting an ordering of A-site cations along the c direction, e.g., $\text{LnBaCo}_2\text{O}_{5+\delta}$ [308]. The flexibility of the structure in turn makes A or/and B site doping possible, resulting in structure distortion, accompanied with change of B-O bond angle, and obviously modifying the hybridization of electronic orbitals, aiming to obtain preferable properties for ORR.

A-site effects: Sun et al. [309] studied three A-doped LaMnO_3 ($\text{La}_{0.7}\text{Ca}_{0.3}\text{MnO}_3$, $\text{La}_{0.7}\text{Sr}_{0.3}\text{MnO}_3$, and $\text{La}_{0.7}\text{Ba}_{0.3}\text{MnO}_3$) with radius of the doped A cations larger than La^{3+} . This doping gave rise to a deviation of the hybridization between orbits of O 2p and Mn 3d from the “head collision” mode. While it could involve the B-O-B bond angle increasing to 180° , accompanied by enhanced B-O orbital overlap which was deemed as the driving force to facilitate the $\text{O}^{2-}/\text{OH}^-$ exchange (surface hydroxide displacement), namely the rate-determining step of ORR on perovskite oxides. This increase of B-O hybridization could simultaneously be promoted via a decrease of charge transfer gap between O 2p and Mn 3d states resulting from

the shift of e_g center to the Fermi Level. The bigger the radius of the doping cation is, the larger the electronic conductivity and the higher the efficiency of ORR catalysis.

Hyodo et al. [310] investigated the catalytic activity for ORR on a series of $AMnO_3$ perovskite oxides catalysts with different A sites in alkaline solution. The ORR activities of the catalysts were measured with a prepared gas-diffusion electrode, and their activity sequence from high to low in the aspect of the A site was: $La > Pr > Nd > Sm > Gd > Y > Dy > Yb$. It was indicated that the activity increased with the radius of A site cationic ions. They also studied the effect of A site substitution on the activity of catalyst $Pr_{1-x}Ca_xMnO_3$ with alike gas-diffusion electron [311]. The activities followed the sequence that $Pr_{0.8}Ca_{0.2}MnO_3 > Pr_{0.8}Sr_{0.2}MnO_3 > Pr_{0.8}Ba_{0.2}MnO_3 > PrMnO_3$.

Hu et al. [312] prepared $La_{1-x}Ca_xMnO_3$ ($x = 0, 0.1, 0.2, 0.3, 0.4, 0.5$) perovskite-graphene composites for ORR catalysis. When $x = 0.4$ the Ca-doped catalyst showed the highest activity with achievable equilibrium between the increase of active sites due to the surface enrichment of Mn^{4+}/Mn^{3+} in the oxides and the decrease of the randomization degree of crystal oxygen vacancy distribution with increase of Ca-doping ratio. Hammouche et al. [313] also studied Ca-doping effect but on cobalt-based perovskite oxides $La_{1-x}Ca_xCoO_3$ ($x = 0, 0.2, 0.4, 0.45, 0.6$). Likely, it was observed that the maximum activity was reached by $La_{0.6}Ca_{0.4}CoO_3$. This doping level usually corresponds to the best conducting properties of the material. It was qualitatively explained that the highest surface area and the most surface composition of Co in $La_{0.6}Ca_{0.4}CoO_3$ contributed to its high activity.

The most extensively studied materials are the La-based perovskite with strontium substitution because of the similar atom size between lanthanum and strontium that there is no big structure distortion after doping of strontium [260]. The divalent Sr^{2+} substitution to trivalent La^{3+} induces vacancies in the electronic structure which improves the electron transfer and oxygen mobilization [62]. Pavone et al. [314] applied First-principle quantum mechanical calculations to analyze the electronic structure and oxygen defect formation of $La_{1-x}Sr_xMnO_3$ (LSMO, $x=0, 0.25, 0.5$). It was revealed that strontium doping in LSMO leads to holes formation in the electronic structure and the material turns from insulator to metal. Also there is a partial oxidation of Mn ions from a formal state of manganese $Mn(3+)$ to $Mn(4+)$. Mn^{4+} ion is smaller than Mn^{3+} . This causes a decrease in LSMO unit cell volume with increasing Sr content. The oxygen defect formation energy also decreases with Sr doping increase. For the more part of experimental work, Tulloch et al. [315] synthesized $La_{1-x}Sr_xMnO_3$ ($x = 0, 0.2, 0.4, 0.6, 0.8, 1$) and measured their activity for ORR on RDE in 1 M KOH. $La_{0.4}Sr_{0.6}MnO_3$ showed the best performance among them as presented in Figure 3-7(a) owing to a four-electron

reduction process, a minimum in crystallite size and a maximum in BET surface area. Stoerzinger et al. [316] compared the reductive activities of the epitaxial $\text{La}_{1-x}\text{Sr}_x\text{MnO}_3$ ($x = 0, 0.10, 0.20, 0.33, 0.50, 0.70, 1.00$) grown by pulsed laser deposition on Nb-doped SrTiO_3 with different surface orientations. Their activities are shown in Figure 3-7(b), $\text{La}_{0.67}\text{Sr}_{0.33}\text{MnO}_3$ exhibited the optimal performance, resulting from a moderate amount of Sr^{2+} substitution of La^{3+} , and introducing both Mn^{4+} and ligand hole character, which further decreased the in-plane resistivity and increased the ORR activity. Zhao et al. [317] synthesized $\text{La}_{1-x}\text{Sr}_x\text{MnO}_3$ ($x = 0, 0.2, 0.6$), and $\text{La}_{0.4}\text{Sr}_{0.6}\text{MnO}_3$ showed the highest current density and exhibited excellent ORR activity, as seen in Figure 3-7(d). Oxygen vacancies on the oxide surface generated by Sr-doping was deemed the primary reason for the enhancement of ORR activity, and secondly, the increase of specific surface area from Sr substitution increased the contact between catalyst and carbon, further the electronic conductivity and activity. There are enormous studies concerning $\text{La}_{1-x}\text{Sr}_x\text{MnO}_3$ [318].

Zhu et al. [319] increased the ORR activity of LaFeO_3 by generating different levels of A-site deficiency. They reported that $\text{La}_{0.95}\text{FeO}_{3-\delta}$ was the most active one, attributed from the creation of oxygen vacancies and Fe^{4+} species on the perovskite surface, demonstrated by XPS characterization. Xue et al. [320] synthesized A-site defected $(\text{La}_{1-x}\text{Sr}_x)_{0.98}\text{MnO}_3$ and applied it in Al-air battery, achieving a superior power density. It was indicated that the deficiency would tune the Mn cation valence and increase oxygen adsorption capacity of perovskites, therefore increase the ORR activity. Besides, the effective results from A-site deficiency have been widely obtained, e.g., $\text{La}_{0.4}\text{Sr}_{0.4}\text{Sc}_{0.9}\text{Ni}_{0.1}\text{O}_{3-\delta}$ [321], $\text{Sr}_{1-x}\text{Sc}_{0.175}\text{Nb}_{0.025}\text{Co}_{0.8}\text{O}_{3-\delta}$ [322], $\text{Sr}_{2-x}\text{Fe}_{1.4}\text{Ni}_{0.1}\text{Mo}_{0.5}\text{O}_{6-\delta}$ [323], $\text{La}_{0.54}\text{Sr}_{0.4}\text{Fe}_{0.2}\text{Co}_{0.8}\text{O}_{3-\delta}$ [324], $\text{Sr}_{0.95}\text{Ag}_{0.05}\text{Nb}_{0.1}\text{Co}_{0.9}\text{O}_{3-\delta}$ [325], $\text{Ba}_{0.9}\text{Co}_{0.5}\text{Fe}_{0.4}\text{Nb}_{0.1}\text{O}_{3-\delta}$ [326], $\text{La}_{0.7}(\text{Sr}_{0.3-x}\text{Pd}_x)\text{MnO}_3$ [327].

Bak et al. [328] confirmed that the formation of a Ruddlesden–Popper-type two-dimensional faults in the LaNiO_3 oxide which is a distorted structure from the octahedral structure, was favored by La excess. It made a positive effect of LaNiO_3 on catalytic activity enhancement. Xu et al. [329] synthesized A-site excessive $(\text{La}_{0.8}\text{Sr}_{0.2})_{1+x}\text{MnO}_3$ ($x = 0, 0.05, \text{ and } 0.1$) for ORR/OER bi-functional catalyst. Their activities are presented as Figure 3-7(a) and (b) for ORR and OER, respectively. The catalyst with $x = 0.05$ exhibited both higher catalytic activity and better structural stability than the other two. It was suggested from the DFT calculation that the transition metal d-band center and oxygen p-band center both approaching the Fermi level was the main reason for the enhanced electrochemical activity as shown in Figure 3-7(c) and (d).

From the above, both A-site deficiency and excess (B-site deficiency) in $\text{La}_{0.8}\text{Sr}_{0.2}\text{MnO}_3$ can enhance the bi-functional performance, which seems illogical. Miao et al. [330] retried a series of La_xMnO_3 ($x = 0.85 - 1.15$) to recheck the effect of La-deficiency and excess. In their work, La-deficiency rather than La-excess was denounced to be effective for both ORR and OER activity. This enhancement could be attributed to its proper Mn cation valence, large amount of oxygen vacancies, upper shift of d-band center and strong adsorption capacity to oxygenated species. Similar work about the positive effect of A-site excess has gradually been explored recently, e.g., $\text{Pr}_{1+x}\text{Ba}_{1-x}\text{Co}_2\text{O}_{6-\delta}$ [331], $\text{Gd}_{1.05}\text{Ba}_{1.05}\text{Co}_2\text{O}_{5+\delta}$ [332], $(\text{Bi}_{0.4}\text{Sr}_{0.6})_{1.1}\text{Co}_{0.3}\text{Fe}_{0.7}\text{O}_{3-\delta}$ [333].

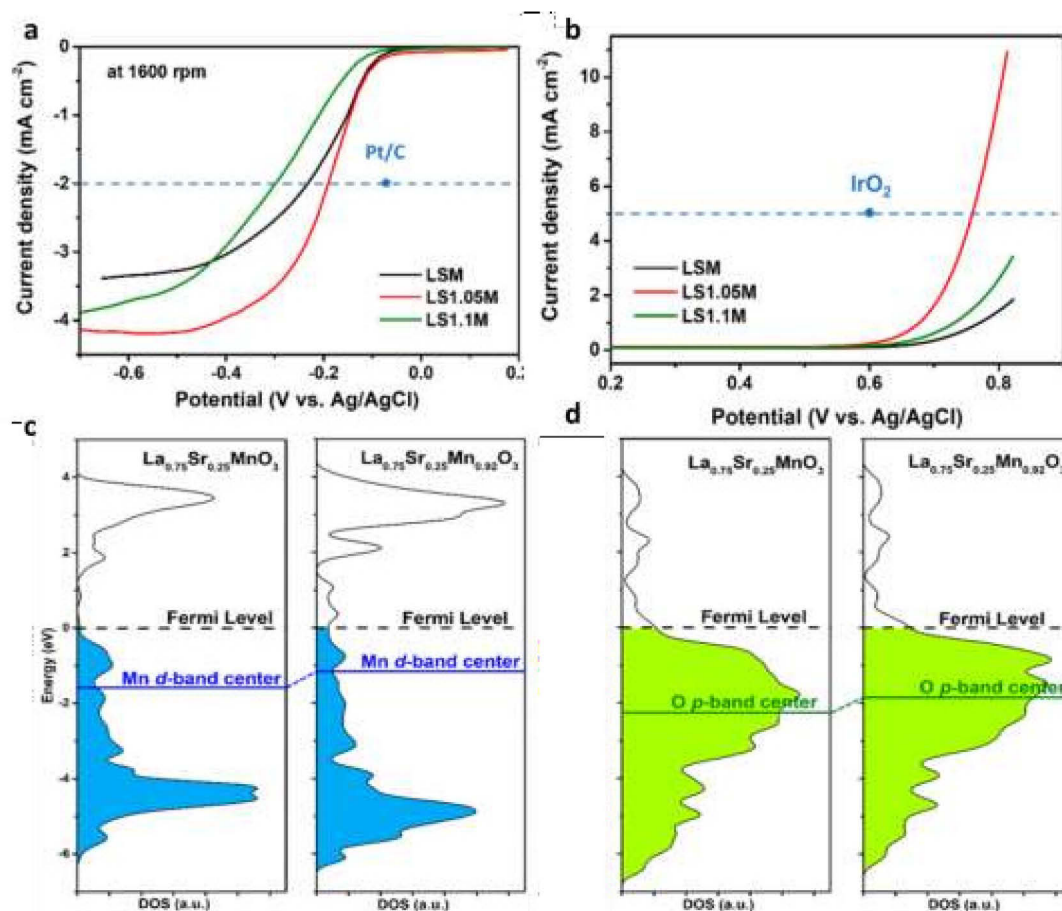


Figure 3-7 : catalytic activity of $(\text{La}_{0.8}\text{Sr}_{0.2})_{1+x}\text{MnO}_3$ (a) towards ORR compared to Pt/C; (b) towards OER compared to IrO_2 ; (c) Mn d-band center; (d) O p-band center of $(\text{La}_{0.8}\text{Sr}_{0.2})_{1.05}\text{MnO}_3$ relative to Fermi level [329]

B-site effects: There are tremendous studies about B-site doped perovskite oxide for oxygen electrocatalysis, including all the reported ORR catalysts with two or more transition metals in B-site. Compared to perovskite oxide catalysts with A-site deficiency or excess, those with B-site deficiency or excess are seldom reported, only a few in the application of SOFC, because B-site deficiencies or excess is energetically unfavorable and may easily cause the

formation of impurity phases, which gives rise to a resistance for charge transfer and, thus a reduction in catalytic performance, though it was suggested the introduction of B-site cation deficiency improved the oxygen mobility [334].

La-based perovskite oxides with La in the A site have been extensively studied for its role on ORR catalysis. With different transition metals, the catalytic activity of the La-based perovskite oxides varies with a sequence as below:



Noteworthy is that the sequence obtained from experiments is different from that obtained from the theoretical calculations, because the activation barrier is neglected in the computation work, and experimental materials are not quite defined for the effective surface area and oxygen stoichiometry [335]. Substitution of Ni in the B site changes the activity of each catalyst with different extents, which may change the sequence to the following:

$\text{LaNiO}_3 < \text{LaNi}_{0.5}\text{Fe}_{0.5}\text{O}_3 \approx \text{LaNi}_{0.5}\text{Co}_{0.5}\text{O}_3 \approx \text{LaNi}_{0.5}\text{Cr}_{0.5}\text{O}_3 < \text{LaNi}_{0.5}\text{Mn}_{0.5}\text{O}_3$ as demonstrated in Figure 3-8. There is no important differences between the different substitutions but they all show an increase of activity as compared to pure LaNiO_3 [336].

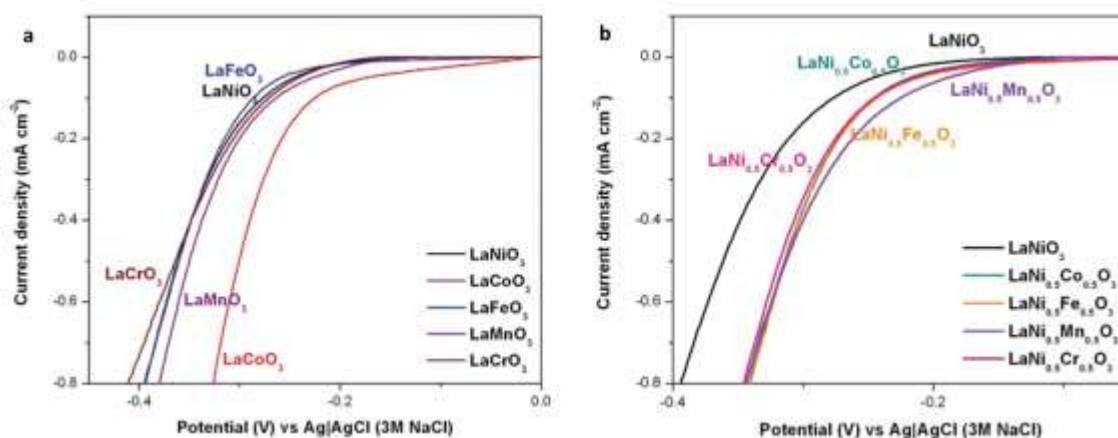


Figure 3-8 : Polarization curves of (a) LaNiO_3 , LaCoO_3 , LaFeO_3 , LaMnO_3 , and LaCrO_3 and (b) $\text{LaNi}_{0.5}\text{Co}_{0.5}\text{O}_3$, $\text{LaNi}_{0.5}\text{Fe}_{0.5}\text{O}_3$, $\text{LaNi}_{0.5}\text{Mn}_{0.5}\text{O}_3$, and $\text{LaNi}_{0.5}\text{Cr}_{0.5}\text{O}_3$ (all in O_2 -saturated 0.1 M KOH electrolyte at 20 mV s^{-1} of scan rate) [336]

Oxygen deficiency or vacancy effect: Perovskite oxides with oxygen deficiency was also reported to have good potential for bi-functional catalyst [337]. The oxygen vacancies can act as acceptors or donors that contributes to the charge transfer between the adsorbate and adsorbent. Therefore, there is a simultaneous filling and creation of lattice oxygen vacancies in oxygen-cation deficient perovskite oxides, in this way, the intrinsic ORR catalytic activity is affected [260]. In the above mentioned ORR mechanism concerning of oxygen vacancies, the oxygen vacancies may govern the physical parameters of the ionic diffusion rates and reflect

the potential electronic structure of the perovskite-type catalysts, as the high activity of $\text{La}_{1-x}\text{Sr}_x\text{CoO}_{3-\delta}$ could be rationalized from the standpoint of the electronic structure and participation of lattice oxygen in the reactive mechanism [260]. The $\text{La}_{0.67}\text{Sr}_{0.33}\text{MnO}_3$ epitaxial thin films was reported to exhibit ORR current not limited by oxygen transport using rotating electrode. The energy of oxygen vacancy formation was also found to be inversely proportional to the position of the O p-band center relative to Fermi level, i.e., the lower the p-band relative to the Fermi level, the higher the energy of oxygen vacancy formation, which was demonstrated by the study on thin-film iron and cobalt perovskite oxides $\text{La}_{0.5}\text{Sr}_{0.5}\text{FeO}_{3-\delta}$ (LSF), $\text{La}_{0.5}\text{Ca}_{0.5}\text{FeO}_{3-\delta}$ (LCF), $\text{La}_{0.5}\text{Ba}_{0.5}\text{FeO}_{3-\delta}$ (LBF) and $\text{La}_{0.6}\text{Sr}_{0.4}\text{Co}_{0.2}\text{Fe}_{0.8}\text{O}_{3-\delta}$ (LSCF) [338].

Morphology effect: Overall, the intrinsic activity of the perovskite oxide catalysts for ORR is commonly believed to be dependent on the e_g filling, the metal-oxygen bond, and the localization of the metal 3d-band center and oxygen 2p-band center relative to their Fermi Levels. The activity enhancement from substitution or doping, the deficiency of A or B-site metal, of oxygen could mostly be explained from the above three points of view. The extrinsic activity enhancement could be realized by morphology control, to design synthesis route enabling to increase the surface area and expose more active sites.

Surface tuning also makes great influence on catalytic activity of the perovskite oxides for ORR or OER. Cheng et al. [339] utilized atomic layer deposition (ALD) to control atomic level of A or B cations the composition at the atomic level on the surface of Sr doped perovskite oxides LaFeO_3 (LSF), LaMnO_3 (LSM), and LaCoO_3 (LSC), schemed in Figure 3-9. They revealed A-site termination on LSF and LSM made an enhancement of the catalytic activity towards ORR, while not evident on LSC. In contrast, B-site terminated surface decreased the catalytic activity. The activity increase might be ascribed from the oxygen vacancies formation because of A-site termination, and oxygen vacancies were deemed as the main active sites.



Figure 3-9 : Schematic showing the different ALD-modified surfaces [339]

3.2.5. Bi-functional catalysts

Transition-metal oxides exhibit different oxidation states because of their partially filled d orbitals, facilitating the movement of electrons and oxygen-ions through oxygen vacancies. This enables them to be excellent candidates as bifunctional catalysts for oxygen electrode reactions [177]. Generally, the carbon-based catalysts cannot stand the highly oxidative potential range for OER, at least higher than 1.229 V, because carbon could be eroded at 0.207 V vs standard hydrogen electrode (SHE) [230]. The ORR mechanism has been already described above. So, the mechanism for OER will be introduced here.

In 1977, Tseung et al. [340] studied the effect of a series of semiconducting oxides on oxygen evolution, proposing a correlation between the potential of the oxides redox couple (lower oxide/higher oxide couple) and the minimum potential for OER. Trasatti et al. [341] then synthesized a series of catalysts including rutile, spinel, and perovskite oxides, showing good OER performance. He established a volcano-shape relationship between the enthalpy of oxidation and OER overpotential shown in Figure 3-10.

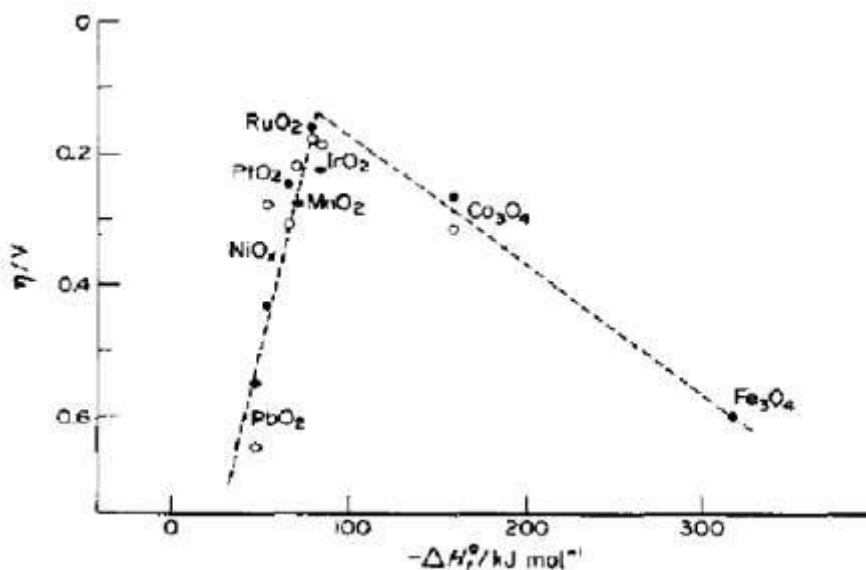


Figure 3-10: Electrocatalytic activity in O_2 evolution at various oxide electrodes as a function of the enthalpy; hollow circle: in alkaline electrolyte and solid circle in acidic electrolyte [341]

Further, the enthalpy of $M(OH)_3$ formation was found to be inversely relative to the current density at constant OER overpotential and subsequently desorption of OH^* intermediates was predicted as the rate-determining step by Bockris and Otagawa [342]. Later, different mechanisms were proposed. Rossmeisl et al. [335, 343] indicated that only after the surface coverage attained a proper value which was dependent on the catalyst material, the HOO^* formation would occur. These authors identified a scaling relationship between the binding/adsorption energy of HO^* or HOO^* and O^* on metal or metal oxides surface via DFT study. So, a single descriptor $\Delta G_{O}^{0*} - \Delta G_{OH}^{0*}$ was proposed for the activity of OER. In this study, the theoretical overpotential is independent on the pH. In Goodenough's work [344], the oxide surface is based on a model that the binding of water and the oxide surface would be affected by the pH of the electrolyte and come to an equilibrium with it. They investigated the catalyst particles of $Pb_2Ir_2O_{7-y}$, $Pb_2Ru_2O_{7-y}$, RuO_2 , IrO_2 and $Sr_{1-x}NbO_{3-\delta}$, utilizing two methods to obtain the information about their surface protonation in electrolytes with different pH: measuring the mean surface charge density versus pH, and CV of the surface reactions in different pH. They concluded that the protonation of the oxide surface had a great influence on the mechanism of both ORR and OER. Generally, in acid electrolytes (specifically in the pH range lower than the point of zero-zeta potential), the oxide surface was fully protonated, and the ORR was blocked, while in alkaline electrolyte (more specifically in the pH range higher than the point of zero-zeta potential), the ORR was active, and mechanisms for ORR and OER were similar to those proposed by Rossmeisl. The above mechanism is also known as the “acid-

base mechanism” [345]. It was also demonstrated in a dimer form [346]. Analogous to the above mentioned ‘side-on’ or association mechanism of ORR, the “direct-coupling mechanism” concerns double centers in the case of OER, which was evidenced by both experimental and computational work [347, 348]. They are reverse to each other. The three mechanisms are schemed in Figure 3-11.

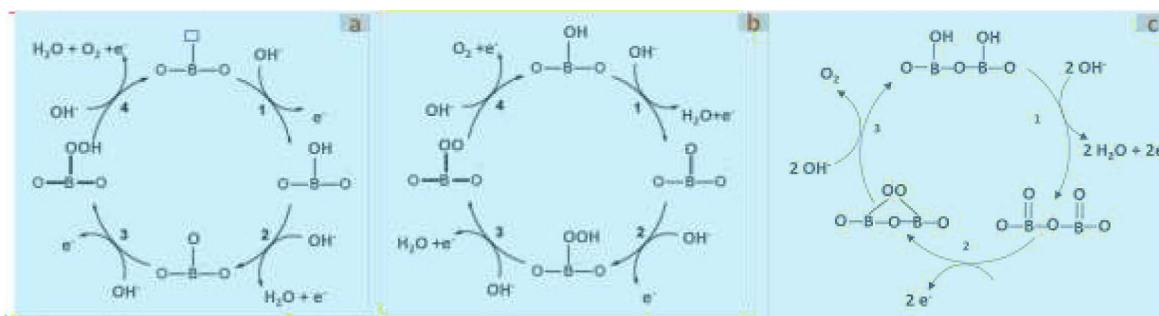


Figure 3-11 : Proposed mechanisms of OER on metal or metal oxide surface (a) by Rossmeisl et al.; (b) by Goodenough et al. (acid-base mechanism); (c) direct-coupling mechanism

Like the strategies for improving the activity of catalysts for ORR, the same theories can be implanted to OER. Catalysts with higher ORR activity and a good electrical conductivity are also likely to act as active OER catalysts. However, there are many catalysts which have a good activity for OER, but not for ORR [230]. Based on the design principle related to e_g filling, $\text{Ba}_{0.5}\text{Sr}_{0.5}\text{Co}_{0.8}\text{Fe}_{0.2}\text{O}_{3-\delta}$ (BSCF) was predicted and proved to have a good OER activity with at least one order of magnitude higher than the commercial IrO_2 catalysts [255]. The positive effect of the cubic $\text{Ba}_{0.5}\text{Sr}_{0.5}\text{Co}_{0.6}\text{Fe}_{0.4}\text{O}_3$ (BSCF82) structure on the OER activity was reported partially owing to the amorphous surface information during OER process, which induced leaching of A-site metal, thus higher surface area and higher activity during OER process [349]. This effect was also seen in the cases of $\text{Ba}_{0.5}\text{Sr}_{0.5}\text{Co}_{0.6}\text{Fe}_{0.4}\text{O}_{3-\delta}$ (BSCF64) and $\text{SrCo}_{0.8}\text{Fe}_{0.2}\text{O}_{3-\delta}$ (SCF82). All of them had the similarly high-positioned O p-band center. The high O p-band center was estimated to be relative to the high oxygen vacancy concentration and high lattice oxygen mobility. It was not seen in the catalysts e.g., $\text{La}_{0.6}\text{Sr}_{0.4}\text{CoO}_{3-\delta}$ (LSC46), LaCoO_3 (LCO), and LaMnO_3 (LMO) with low O p-band center. The related O p-band centers relative to Fermi Level are shown in Figure 3-12(b). Another similar amorphization-enhanced OER activity was reported about Sn vacancies produced by Ar plasma on SnCoFe perovskite hydroxide [350]. Grimaud et al. [351] further reported the series of Co-based double perovskite $(\text{Ln}_{0.5}\text{Ba}_{0.5})\text{CoO}_{3-\delta}$ (also written in $\text{LnBaCo}_2\text{O}_{5+\delta}$, $\text{Ln} = \text{Pr, Sm, Gd and Ho}$) which maintained stable structure during OER, but also exhibited higher activity than BSCF, as demonstrated in Figure 3-12(c). The high possibility of e_g filling of unity supported its high activity. Besides,

the computed O p-band center relative to the Fermi level and the parameters derived from it were suggested to be appropriate alternatives for descriptors of the OER activity and stability of oxides. The O p-band center relative to Fermi Level of the double perovskite oxides could be indicated by the oxidation state of the Co which was also related to the oxygen content and the Ln, as shown in Figure 3-12(d) and (e). Figure 3-12(e) also shows the change of the O p-band center with the fully relaxed or constrained stoichiometric double perovskite oxides. The difference of the relaxed or constrained stoichiometric double perovskite was resulted from A-site and B-site ionic radius mismatch which generated distortion and rotation of Co-O octahedra, modifying the Co-O bond length and Co 3d– O 2p orbital hybridization [352]. The oxidation state of Co, or the Co valency in perovskite oxides reflects the Co-O hybridization, that the higher valency is, the higher hybridization is. The increase of the Co oxidation state may be ascribed to the increased possibility of charge transfer between the metal 3d band and the O 2p band [353].

The Co-based perovskite oxides exemplified above the role of oxygen vacancies, the A-site metals, and their derived Co oxidation states from O p-band center versus Fermi Level, the surface amorphization, etc. Too low the O p-band center causes low hybridization of B-O bond, while too high p-band center may result in structure instability, and no further increase of OER activity, as the comparison between BSCF82 ($\text{Ba}_{0.5}\text{Sr}_{0.5}\text{Co}_{0.8}\text{Fe}_{0.2}\text{O}_{3-\delta}$) and $(\text{Pr}_{0.5}\text{Ba}_{0.5})\text{CoO}_{3-\delta}$. So, appropriate O p-band center is necessary for high OER activity.

The correlation between oxygen deficiency and OER high activity is widely proved with various metal oxides. The hybrid or composite metal/carbon catalysts also occupy their place in oxygen electrocatalysis with improved activity [354, 355]. Metal-free bi-functional catalysts were also reported [356]. Besides, there are other kinds of bi-functional catalysts, e.g., layered double hydroxides [357], metal–organic frameworks [358], sulfides [359], phosphates [360], etc.

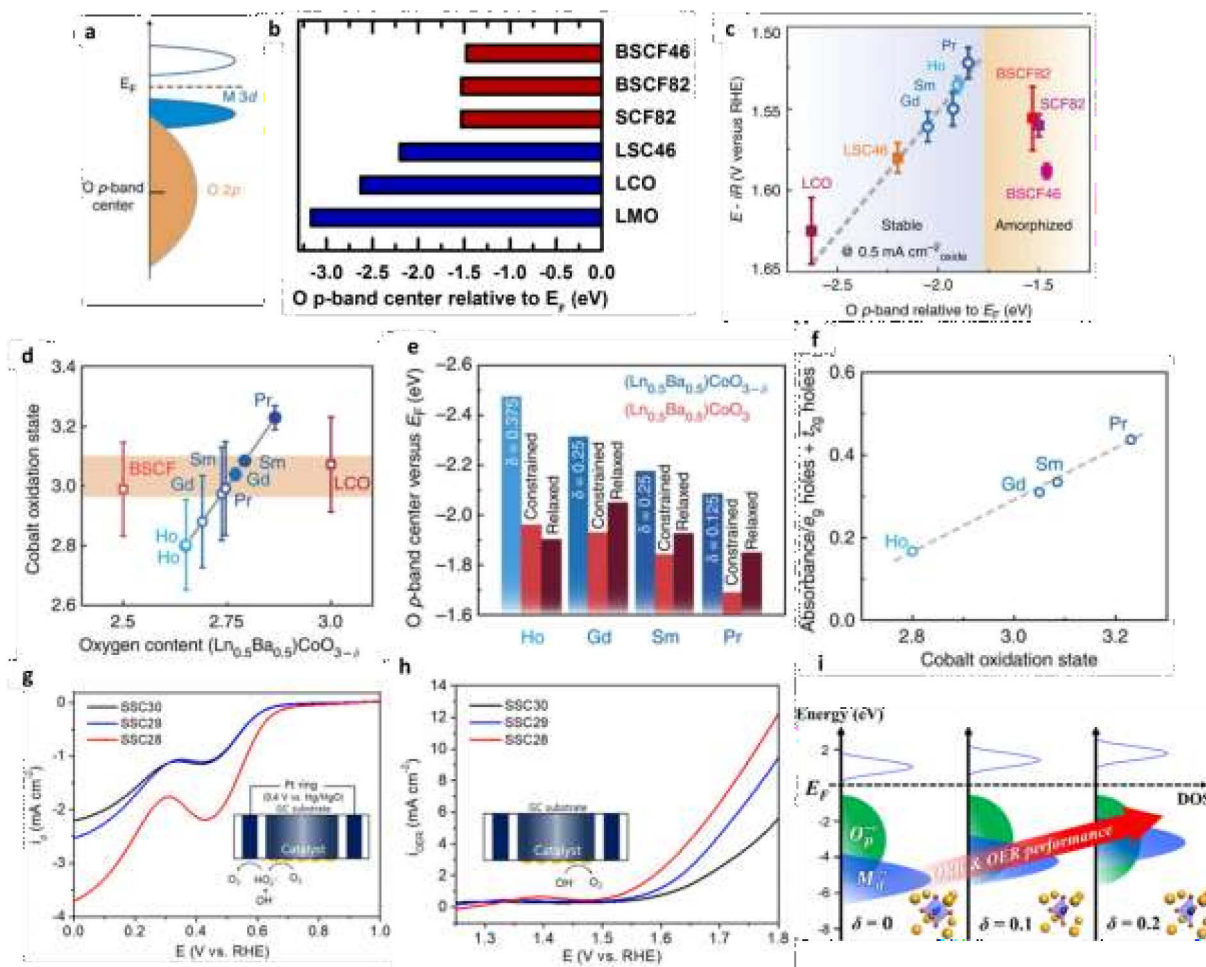


Figure 3-12 : (a) Schematic representation of the O p-band for transition metal oxides; (b) the comparison of the O p-band center relative to Fermi Level (E_F) of different perovskite oxides [349]; (c) evolution of the i_R -corrected potential at 0.5 mA cm^{-2} oxide versus the O p-band center relative to E_F (eV); (d) Co oxidation state variation with the oxygen content and A-site materials; (e) The computed O p-band center versus the Fermi level for the nonstoichiometric $(\text{Ln}_{0.5}\text{Ba}_{0.5})\text{CoO}_{3-\delta}$ double perovskites (having δ constrained to the values obtained from chemical titration) and stoichiometric $(\text{Ln}_{0.5}\text{Ba}_{0.5})\text{CoO}_3$ in the constrained or relaxed structure; (f) Integrated intensities of the O K-edge pre-edge region normalized to oxygen content per formula unit and the nominal number of empty cobalt 3d states in both e_g and t_{2g} symmetry[351]; (g) ORR (h) OER activity of $\text{Sm}_{0.5}\text{Sr}_{0.5}\text{CoO}_{3-\delta}$ (SSC, $\delta = 0, 0.1, \text{ and } 0.2$) in O_2 -saturated 0.1 M KOH at a scan rate of 10 mV s^{-1} and a rotation rate of 1600 rpm ; (i) relation between metal d-band center lift and ORR/OER performance [337]

3.2.6. Conclusion on the literature survey

Noble metals are probably good for ORR, but they are expensive and not stable in alkaline solutions. Carbon-based materials are new but are not stable at high potential. The oxides are cheaper and stable at higher potential. However, the activity is difficult to control, and sometimes the papers found in literatures give controversial results. There are many parameters relating the activity of the catalyst, e.g., surface area, electronic conductivity, surface state, crystal structure, and the solid state defects etc.

It is difficult to control the oxidation state and the stoichiometry of simple oxides such as cobalt or manganese oxides during their synthesis and during their electrochemical properties. The electronic conductivity is also hard to control. Thus, they do not give reproducible results in electrocatalysis. The properties may also change during the electrochemical reactions.

The electronic states and conductivity of multinary oxides such as perovskites appear easier to control. As an example, in the ABO_3 structure, we can make aliovalent substitution in the A-site (Sr^{2+} for La^{3+}), which can change the filling of the d-orbitals of the B cation without disordering the B-site. This will easily transform the material from insulator to metal. These metals offer a cheap alternative to precious metals and their oxide-containing surface is well adapted to adsorb oxygen.

The literature emphasizes the role of the partial filling of e_g orbitals in the ORR activity. This is mostly obtained with late transition metal in +3 oxidation state such as Mn ($3d^4$), Fe ($3d^5$), Co ($3d^6$), Ni ($3d^7$). These oxides are all stable in alkaline electrolyte.

From these articles, the most studied and maybe the most promising materials are $LaMnO_3$, $LaCoO_3$, and $LaNiO_3$. Especially, manganese ($3d^4$, high spin $t_{2g}^3 e_g^1$) and nickel ($3d^7$ low spin, $t_{2g}^6 e_g^1$) are interesting because they are cheap (as compared to cobalt) and they easily give good conducting phases upon doping (manganese in $La_{1-x}Sr_xMnO_3$, LSMO) or without doping (nickel in $LaNiO_3$).

Our synthesis of nickel perovskites with high specific area by solution techniques were not so successful and reproducible because we could not obtain single phase materials. So, we choose LSMO system because it is cheap and not toxic as compared to cobalt. Moreover, its synthesis is well-known to perform, so that we can use reproducible powders to study the formulation of inks and electrodes assembly.

3.3. ORR or OER catalytic characterization

ORR and OER are structure-sensitive reactions, which means catalyst structure makes a big difference to the catalytic activity [187]. To obtain the quantitative performance of ORR catalysts, we have extensively studied their properties with a three-electrode system using a rotating disk as the working electrode. Despite detecting all the involved intermediate products is beyond current techniques, rotating disk electrode (RDE) can fulfill partial quantification work about kinetic study of ORR.

To perform the measurement, a slurry containing catalyst, carbon, and binder is drop-deposited on the tip of the electrode. After the solvent is evaporated, a catalytic layer within

100 nm of thickness is formed and attached on the electrode. The main role of the carbon material mixed with catalyst is to enhance the conductivity and disperse the catalyst, while it also has a catalytic effect on ORR [361].

$\text{La}_{0.8}\text{Sr}_{0.2}\text{CoO}_3$ alone is reported to have no activity for ORR, while with carbon, it is active [362]. The effect of carbon as an additive in the catalyst layer for ORR catalysis was studied and it was believed that carbon preferentially reduced O_2 to HO_2^- which was consecutively reduced to OH^- on the metal oxide catalyst [363]. Carbon may also influence the stability of the catalysts due to its easiness to be oxidized at oxidative potential range [171]. But its major role is to bring a good conductivity to the electrode.

Typically, there are three regions on the ORR polarization curves as seen in Figure 3-13. The ORR polarization curves show a kinetic-controlled region at the onset of reduction processes, a diffusion-controlled region at voltages lower than 0.5 V, a diffusion-kinetic combined region in between [284].

The kinetic-controlled zone shows the potential for the onset and the limitation of the reduction of oxygen. It is characteristic of the activity the catalyst. It is mostly related to the intrinsic properties of the catalyst surface. The potential at a constant current density or the current density at a constant potential in the mixed kinetic-diffusion controlled region is usually the metric for the catalytic activity of the catalyst for ORR [284].

The diffusion-controlled zone is characteristic of the concentration of oxygen species at the vicinity of the catalyst. It is related to the dissolution of oxygen (with or without oxygen bubbling, in the presence of pure oxygen or mixed with nitrogen in air), the convection of the solution to the electrode (with or without rotation), the diffusion of oxygen into the porosity of the electrode. The limiting current thus gives an information on the extrinsic properties such as the quality of the electrode assembly, its porosity and permeation properties. The most correct way to get the real catalyst activity is to be normalized to the number of active sites. While in practical cases, normalization to surface area or mass is applied instead [284].

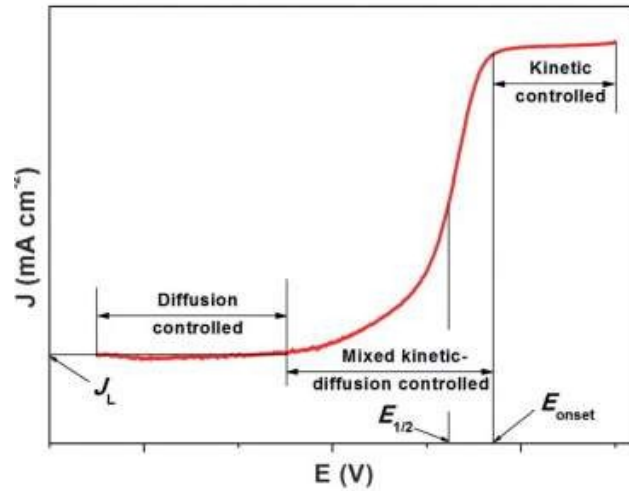


Figure 3-13 : Typical polarization curve of ORR [284]

Because oxygen has a very limited dissolution in water, the reaction is limited by the transport of oxygen to the electrode. The current measured is affected by the mass transport current controlled by the rotation rate.

The Levich equation below is a well-known method to have the mass transport correction.

$$\text{Equation 3-2 : } i^{-1} = i_m^{-1} + i_k^{-1}$$

where i is the measured current (density), i_m is the mass transport current (density), and i_k is the kinetic current (density). i_m is also called Levich current, which can be calculated by Equation 3-3 as a function of the disk rotating rate and some physical properties of the electrolyte, when using a rotating disk electrode (RDE).

$$\text{Equation 3-3 : } i_m = 0.62nFAD_0^{2/3}\nu^{-1/6}C_0\omega^{1/2}$$

where n is the number of moles of electrons transferred in the reaction, F is the Faraday constant (C/mol), A is the electrode area (cm²), D_0 is the diffusion coefficient of oxygen in the electrolyte (cm² s⁻¹), ν is the kinematic viscosity (cm² s⁻¹) of the electrolyte, C_0 is the concentration of oxygen in electrolyte, and ω is the rotating rate of electrode. Normally except for ω , the other parameters are constant, so, the mass transport current is proportionate to $\omega^{1/2}$. By varying the rotating rate, i_m is easily obtained, then the i_k [364]. We need to emphasize that A is the geometric area of the electrode which is not the effective surface area of catalyst because in the Levich conditions, the current is limited by the convective flow of oxygen species to the electrode.

Some work aimed to exclude the effects from carbon materials or binders, the single crystals are synthesized as a thin film on the disk to get a more fundamental insight [365, 366]. Some representative works relating to the activity measurement with different disk materials and types of catalyst on the disk are listed in Table 3-4.

Table 3-4 : Some representative references on ORR catalytic activity measurement concerning different RDE materials and catalyst types on disk

Catalyst	Disk and ring material	Carbon	Binder	Type	Attach	Catalyst load	Ref
Mn _y O _x /C	Disk: Pyrolytic graphite Ring: gold	Vulcan XC-72 (integrated in catalyst)	Nafion solution (5 wt.% in isopropyl alcohol)	Thin film of composite	Drop-deposition	40 μg cm ⁻²	[280]
LaNiO ₃ /LaAlO ₃ (001)	Disk: glassy carbon	-	-	Thin film on single crystal substrate	Conductive paste	-	[257]
Pt (111)	Disk: glassy carbon	-	-	Thin film of single crystal	Sputtering on disk	-	[257]
LaCu _{0.5} Mn _{0.5} O ₃	Disk: glassy carbon	Nitric acid treated acetylene black	Na ⁺ -exchanged Nafion solution with tetrahydrofuran	Thin film of composite	Drop-deposition	250 μg _{oxide} cm ⁻² _{disk}	[364]
Pt/C (46 w.t.% Pt)	Disk: glassy carbon	Vulcan XC-72 (integrated in catalyst)	Nafion® solution (5 wt.%, Fluka)	Thin film	Drop-deposition of catalyst and Nafion separately	5 μg _{Pt} cm ⁻² _{disk}	[364, 367]
La _{1-x} Sr _x MnO ₃	Disk: glassy carbon	Vulcan-XC72 carbon	5 wt% Nafion solutions	Thin film of composite	Drop-deposition		[317]
La _{1-x} Sr _x MnO ₃	Disk: glassy carbon	-	Nafion® 117 solution (Fluka)	Thin film of composite	Drop-deposition	108.7 ± 2.0 μg cm ⁻²	[315]
La _{1-x} Sr _x MnO ₃ /SrTiO ₃	-	-	-	Thin film of single crystal	-	-	[316]
La _{1-x} Ca _x MnO ₃ -graphene	Disk: glassy carbon; Ring: Pt	Acetylene black	PTFE			57 μg·cm ⁻²	[312]
FeNi alloy and N co-doped carbon	Disk: glassy carbon	-	Nafion solution (5 wt %)	Thin film of composite	Drop-deposition	~0.2 mg cm ⁻²	[246]
Nitrogen-doped single-walled carbon nanotubes (NCNTs)	Disk: glassy carbon	-	Nafion solution (5 %)	Thin film of NCNTs cast on Nafion	Attach	-	[214]

3.4. Synthesis methods for perovskite oxides

There is a wide range of methods to prepare single metal oxides or multinary oxides such as perovskites, spinel garnet oxides, etc. Conventional methods include solid reactions or solution-based synthesis such sol-gel or coprecipitation. The choice of the method as well as each procedure used during the synthesis (heating time, atmosphere, cooling rate...) may change the properties of the final powder with different degrees (microstructure, specific surface area, oxidation state, homogeneity of doping, surface states).

Solid state reaction is an energy-extensive process, where grinding and mixing of powders of oxides, carbonates or salts is followed by long-time high-temperature sintering process to obtain ions diffusion and form the new phase. Coprecipitation method consists in mixing two solutions containing soluble cations and the precipitating agent, respectively. The common precipitating agents are ammonium carbonate and ammonium citrate. Inorganic salts, organic salts, or alkoxides are the choices for preparing solution with cations to be precipitated. Precipitation reactions happen quickly. After filtrating, rinsing, and drying the precipitate, a homogeneous mixture of cations at the microscopic level or even at the “molecular” level is obtained. The reaction is not diffusion limited and theoretically only related to local ordering and decomposition of the precipitating reagents. Thus, a coprecipitate usually crystallizes at much lower temperatures than that with solid state reaction method for a shorter duration. It usually leads to smaller particles and their sintering can be avoided. Sol-gel method involves the formation through hydrolysis and condensation of homogeneous metal oxides or hydroxides without the presence of a precipitant. Calcination should not be necessary to eliminate the precipitant although thermal treatment is necessary to obtain crystallization and eliminate the last hydroxides. There are also the Pechini techniques, where complexing polymers (based on citric acid and ethylene glycol) traps all cations close to each other. This technique is the most versatile for synthesis of multinary oxides such as perovskites. The derivative techniques are also commonly termed as combustion method or amorphous method [368]. Solution containing metal cations chelate with an organic complexing or chelating agent, normally organic acids (such as EDTA, citric acid, malic acid, glycine, carboxylate azides, urea, oxalyl dihydrazide) which also polymerize in the metal cations-complexing agent system. The complex reaction and polymerization process take a few hours before the solution becomes gel. Then drying and sintering process is similar with that of coprecipitation method. Usually, the quantification of complexation agent to metal salts equal or a little above their stoichiometric value gives better

crystallized phases. Too much or less complexation agent would result in carbonaceous impurities or heterogeneous materials.

In addition to the three conventional methods, there are hydrothermal, reverse micelle synthesis, spray and freeze drying, spray pyrolysis, microwave assisted synthesis and sintering, combustion synthesis and physical vapor deposition, molten salt treatment method, sonochemical method [369, 370]. Among all these methods, the physicochemical properties of the metal salts and the conditions of calcination count the most to the properties of final powders.

Synthesis routes have influence on the catalytic performance of the perovskite oxides. Generally, the particle sizes are 1 - 20 μm from solid reaction method, while from sol-gel method or coprecipitation method, the particle sizes are in a scale of tens to hundreds of nanometers. Different synthesis routes produce different surface structures. In [371], solid state synthesis, drip pyrolysis, citrate route, sol-gel, carbonate coprecipitation, and oxalate coprecipitation have been adopted to synthesize $\text{La}_{1-x}\text{Sr}_x\text{MnO}_3$. Their performance as a catalyst in cathode of SOFC (solid oxide fuel cell) was compared on a fixed bed reactor and CO was the fuel. Materials obtained from carbonate coprecipitation were reported to have highest catalytic activity in this work. Acetate salts compared to nitrate salts used as starting material to prepare perovskite oxide via solution routes were advantageous to increase the surface area of the final powder [372].

The A-site deficiency or stoichiometry is normally realized from the control of the quantity of starting materials. It also depends on the lattice energy and the relative chemical bond. Oxygen deficiency is always accompanied by A-site deficiency [373]. The formation energy of oxygen deficiency/vacancy is dependent on the position of O 2p-band center relative to the Fermi level, and A-site deficiency has a positive effect on that. For an intentional control of oxygen deficiency, low oxygen environment is usually needed during the heat treatment of perovskite oxides synthesis. Formation of oxygen vacancies is endothermic; an elevated temperature and a longer time will favor for oxygen deficiency [374]. Oxygen deficiency could also be introduced electrochemically by applying a negative potential. While generally, there is no ascertained method to have oxygen deficiency/vacancy. Here are listed some approaches for making oxygen deficiency/vacancy in Table 3-5, especially from the comparison with the corresponding highly crystallized particles.

Table 3-5 : Oxygen deficiency/vacancy generation approaches

Catalyst	Synthesis route	Ref
(d)MnO ₂	<ul style="list-style-type: none"> • 50 mL (0.1 M) MnSO₄·5H₂O+50 mL (0.1 M) K₂S₂O₈ mixed • 25 mL (1.2 M) NaOH added • Stirring for 1 h, and ageing for 1 h • Gathering precipitates and freeze drying 	[375]
(c)MnO ₂	<ul style="list-style-type: none"> • Suspension transferred into Teflon-lined autoclaves, and heated at 160 °C for 24 h 	[375]
(c)β-MnO ₂	<ul style="list-style-type: none"> • 30 mL (0.1 M) MnSO₄· and 30 mL (0.6 M) KMnO₄ solution • KMnO₄ dropped into MnSO₄ solution with stirring • Mixture transferred into Teflon-lined autoclaves, heated to 140 °C at a rate of 4 °C min⁻¹ and maintained at this temperature for 12 h while continuously stirring 	[339]
(d)β-MnO ₂	<ul style="list-style-type: none"> • Heat treatment of (c)β-MnO₂, e.g., at 350 °C for 2 h in Ar 	[339]
(c)CaMnO ₃	<ul style="list-style-type: none"> • MnCO₃ (1 mmol) + CaCO₃ (1 mmol) in 10.5 mL (0.5 M) dilute HNO₃ • 5.25 mL (0.25 M) (NH₄)₂CO₃ dripped and stirring for 30 min, ageing for 3 h • Precipitates centrifuged, washed, vacuum-dried, and calcined at 900 °C in air for 5 h 	[365]
(d)CaMnO ₃	<ul style="list-style-type: none"> • Heat treatment in a H₂/Ar (5%/95%) forming gas 	[365]
(c)La _{0.67} Sr _{0.33} MnO ₃	<ul style="list-style-type: none"> • Pulsed laser deposition of La_{0.67}Sr_{0.33}MnO₃ epitaxial thin films on substrate (100) 0.5 wt % Nb-doped SrTiO₃ 	[365]
(d)La _{0.67} Sr _{0.33} MnO ₃	<ul style="list-style-type: none"> • Applying potential on the film electrode 	[365]

Note: (d) means with oxygen deficiency; (c) means highly crystallized, red point is the step different between the two synthesis routes, and the black point is the same step which is listed only once.

In this work, the strontium doping lanthanum manganese oxide have been synthesized via two different methods, a polymeric citrate solution process and a carbonate coprecipitation process. After synthesis and characterization of the powders, electrochemical studies have been conducted with a rotating disk electrode. We focused on the strontium substitution effect in La₁₋

$x\text{Sr}_x\text{MnO}_3$ system because as a conclusion of the literature study its activity is correct, and manganese is cheap and non-toxic.

3.5. Experimental study

The experiments for this part have two parts, first is the perovskite synthesis and its physical characterization by XRD and BET, and second is the electrochemical characterization by cyclic voltammetry.

Two synthesis routes have been applied to synthesize $\text{La}_{1-x}\text{Sr}_x\text{MnO}_3$, citrate solution process and coprecipitation process. Lanthanum acetate sesquihydrate (Alfa Aesar), strontium acetate (Aldrich), manganese acetate tetrahydrate (Sigma-Aldrich) and citric acid (Sigma-Aldrich) are used for the citrate solution process. Lanthanum nitrate hexahydrate (Alfa Aesar), strontium nitrate (Prolabo), manganese nitrate tetrahydrate (CL chem-lab), ammonium bicarbonate (Alfa Aesar) and ammonium hydroxide (25 wt.%, Acros organics) are used for the coprecipitation process.

XVC-72 (Carbot) and Nafion (20 wt.% in lower aliphatic alcohols/ H_2O mix, Sigma-Aldrich) are treated before ready to use. The VXC-72 is treated with nitric acid and Nafion solution is treated via K^+ exchange with 0.3 M KOH (Sigma-Aldrich) solution.

3.5.1. $\text{La}_{1-x}\text{Sr}_x\text{MnO}_3$ (LSMO) synthesis

Normally metal nitrates are commonly used to prepare the aqueous precursor solution in both synthesis processes mentioned above, because they cost less and dissolve more easily. While in this work, acetates instead of nitrates are used in citrate solution process to avoid explosion caused by nitrates with organics during calcination under high temperature.

In the citrate solution process, the acetates of the corresponding cations are dissolved stoichiometrically in deionized water to get 40 mL solution with the concentration of 0.25 M Mn^{3+} , $(1-x) * 0.25 \text{ M La}^{3+}$, and $x * 0.25 \text{ M Sr}^{2+}$. Another 2 M 10 mL equivalent moles of citric acid is presented. Then, the citric acid solution is rapidly poured into the acetate solution. Immediately a white precipitate appears. Then 5 mL of ammonium hydroxide (25 wt. %) is progressively added into the precipitated suspension until the precipitate dissolves again. The aqueous solution is then put in an oven at 80 °C for 24 h to evaporate water until a transparent gel form. Then the temperature is increased to 150 °C. The gel foams and becomes a spongy beige solid. This solid is ground and calcined either in air or in flowing oxygen separately, with a heating rate of 150 °C h^{-1} up to the desired temperature where it stays for 4 hours.

In the carbonate coprecipitation method, nitrates are dissolved stoichiometrically to get 20 mL solution with the concentration of 0.5 M Mn^{3+} , $0.5 * (1-x)$ M La^{3+} , and $0.5 * x$ M Sr^{2+} . Surplus ammonium bicarbonate (60 mL 0.5 M) is dissolved in deionized water with equivalent moles of ammonium. Then the ammonium carbonate solution is rapidly added into the nitrate solution, white precipitate appears. After reaction and ageing for 30 mins, the precipitate is filtrated, washed, and collected. The filtrated precipitate is dried in oven at 150 °C overnight when the white precipitate turns gray. Then it is ground and calcined in oxygen atmosphere at 500 °C, 700 °C, 900 °C, and 1100 °C.

3.5.2. Physical characterization of $\text{La}_{1-x}\text{Sr}_x\text{MnO}_3$

The LSMOs are characterized with X-Ray Diffraction (XRD), Brunauer-Emmett-Teller (BET) and Scanning Electron Microscope (SEM). The structure of the as-prepared perovskites is tested at 45 kV and 40 mA using a PANalytical powder diffractometer with $\text{Cu K}\alpha$ ($\lambda=1.54056 \text{ \AA}$) in the 2 theta (θ) range from 5° to 80°, with a scan rate of $2.5^\circ \text{ min}^{-1}$. BET is conducted on a Belsorp MAX, nitrogen gas is used as the probe gas, which is a standard approach and allows measurement of the surface areas as low as $0.01 \text{ m}^2 \text{ g}^{-1}$. Morphology of the LSMOs is characterized on a Proxima 100-Micromecha machine in a field emission gun scanning electron microscope (FEG-SEM ZEISS LEO1530) operating at 20kV, accompanied by a PRINCETON GAMMA TECH PGT x-ray PRISM Digital Spectrometer.

Le Bail refinements on the XRD patterns are carried out using the opensource software Fullprof [376]. During refinements, general parameters, such as the scale factor, background parameters, sample displacement, and peak shape are optimized.

Powder XRD patterns of $\text{La}_{1-x}\text{Sr}_x\text{MnO}_3$ synthesized from three different processes (coprecipitation method calcined in oxygen, citrate solution process calcined in oxygen or air) are shown in the following parts. The effects of substitution of strontium, the calcination temperature, the synthesis process, and the calcination atmosphere will be compared and discussed in detail taking some of the patterns as examples.

3.5.2.1. Effect of synthesis temperature

The precursors are calcined at different temperatures. Figure 3-14 shows the example of $\text{La}_{0.7}\text{Sr}_{0.3}\text{MnO}_3$ calcined at different temperatures for the coprecipitated carbonates (a), and the citrate calcined in oxygen (b) or air (c).

When calcined at 500 °C, there is no crystallized phase formed both in the coprecipitation process or in the citrate solution process. The fact that an amorphous material

is obtained instead of different crystalline oxides indicates a good mixing of the different elements by the solution method that prevents phase separation and crystallization of simple oxides. The citrate method yields the pure perovskite starting from 700°C.

For the carbonate coprecipitation method, the material obtained at 700°C still presents a multiphase system and the perovskite only appears as the major material above 900°C. The peak position is the same, but the peak shape becomes sharper with increasing temperature of calcination, which indicate the particles are better crystallized with larger diffraction domains.

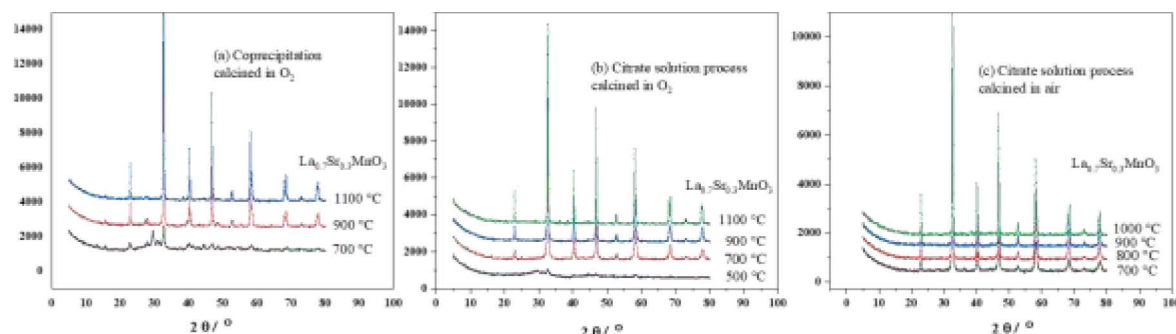


Figure 3-14 : XRD patterns of $\text{La}_{0.7}\text{Sr}_{0.3}\text{MnO}_3$ calcined at different temperatures, (a) by coprecipitation method calcined in O_2 (b) by citrate solution process calcined in O_2 (c) by citrate solution process calcined in air

3.5.2.2. Effect of substitution/doping of strontium

It is easy to see in Figure 3-15(a) that phases obtained at 900°C from carbonate coprecipitation process are multiphases while the citrate process with calcination either in oxygen or air results in a pure phase shown as Figure 3-15(b) and (c). We may have lost some manganese upon filtering the carbonates precipitate. This is not possible to lose some elements in the citrate method because there is no filtering step.

As shown in Figure 3-15 (b) and (c), with varied strontium substitution ratio, the patterns change a little concerning the peak position and peak shape, where undoped stoichiometric LaMnO_3 should adopt an orthorhombic structure, that transforms to rhombohedral with strontium doping [314, 377]. This is due to the Jahn-Teller distortion of the Mn^{3+} ($3d^4$) ion that transforms to the regular Mn^{4+} ($3d^3$) ion upon doping with strontium. In our case, a cubic structure appears at both low ($x = 0$) and high ($x = 0.5$) strontium doping ratio after calcination in oxygen. Thus, this difference with the literature may be related to the oxygen over-stoichiometry $\text{LaMnO}_{3+\delta}$ which changes the oxidation state of Mn^{3+} to Mn^{4+} similarly to strontium doping.

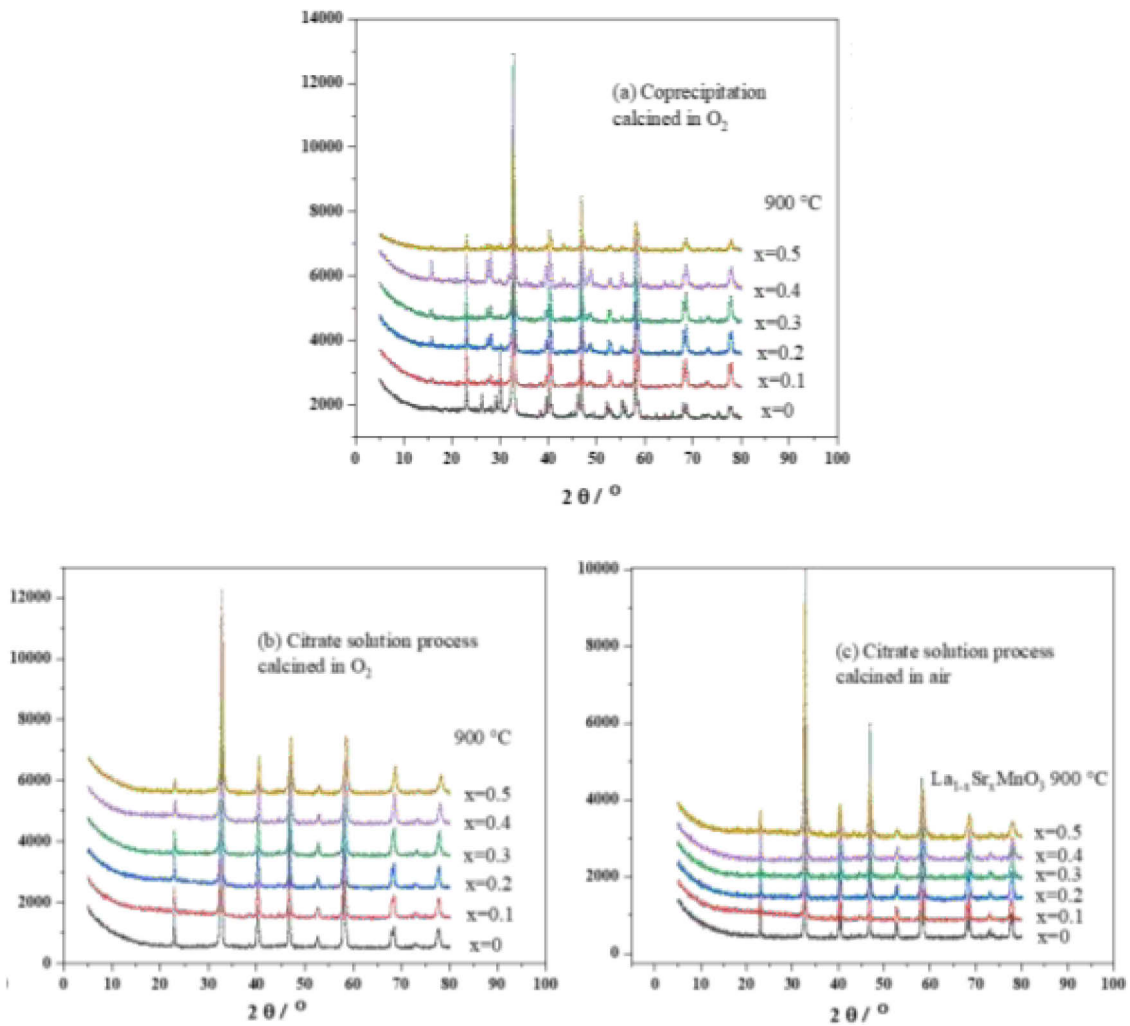


Figure 3-15 : XRD patterns of $\text{La}_{1-x}\text{Sr}_x\text{MnO}_3$ calcined at 900 °C, (a) by carbonate coprecipitation method calcined in O_2 (b) by citrate solution process calcined in O_2 (c) by citrate solution process calcined in air

To get a more correct information of the unit cell from the XRD patterns, the Le Bail refinement was adopted to verify the unit cell parameters. The rhombohedral structure was used as a reference structure for Le Bail refinement since a cubic structure would be a special case of rhombohedron either with $\alpha = 90^\circ$ (cubic P) or 60° (cubic F) anyway.

The diffraction profiles of LSMO obtained from citrate solution process either calcined in air or oxygen are analysed by Le Bail refinement using open-source software FullProf. The unit cell parameters can be obtained from the refinement as shown in Figure 3-16. The refinements are based on the rhombohedral structure, the main unit cell parameters are a , b , c ($a=b$). Unit cell volume and α_R are also calculated. Data from Hammouche's work [378] are compared with those from our work. Generally, LSMO synthesized from citrate solution process calcined in either air at 1000 °C or oxygen at 1100 °C are identical to the results from

Hammouche's work. LSMO calcined in oxygen at other temperatures have the similar tendency to Hammouche's work with the variance of strontium substitution ratio.

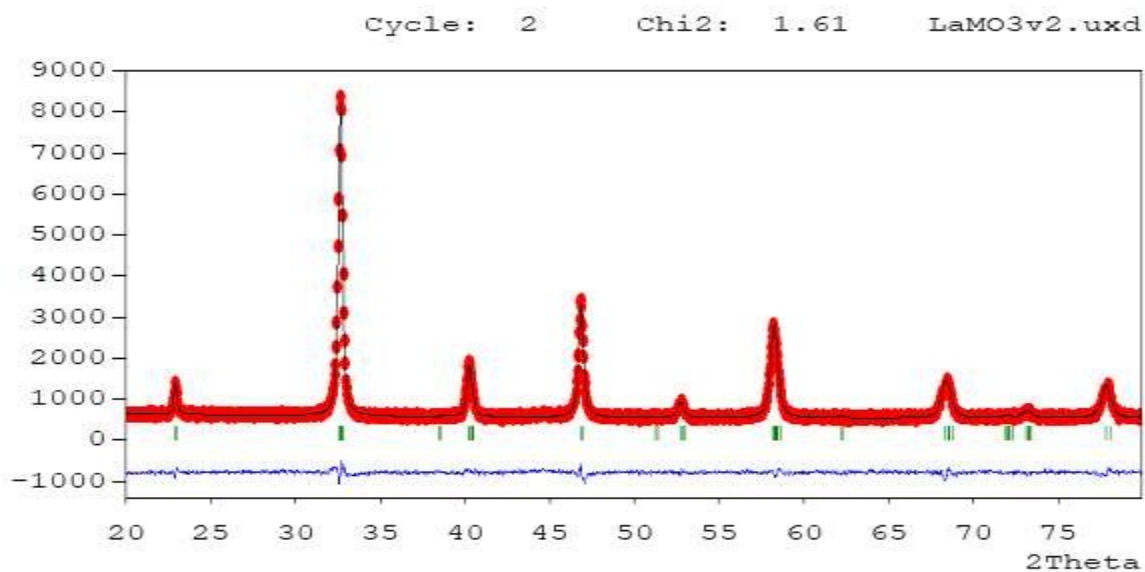
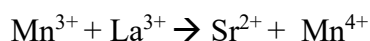


Figure 3-16 : The Le-Bail refinement of $\text{La}_{0.7}\text{Sr}_{0.3}\text{MnO}_3$ calcined at 900 °C in oxygen

LSMO calcined in air at 700 – 900 °C give irregular values while the changes are much more regular when calcined under oxygen. This indicates that the oxygen content is probably much better controlled under oxygen flow.

The change of angle tends towards 60° upon strontium doping (indicating a tendency to form a cubic structure). The cell volume decreases with the strontium doping although the Shannon and Prewitt ionic radius in XII coordination of La^{3+} and Sr^{2+} are respectively 1.32 Å and 1.44 Å. This probably indicates a higher oxidation state of Mn with the substitution of lanthanum by strontium.



Indeed, the cell parameter “a” of the structure relates to the distance of Mn-O-Mn because the tolerance factor of the perovskite is below 1. Indeed, in computational works [314], the unit cell volume is predicted to decrease with the increase of strontium doping.

The synthesis temperature influences the cell parameters when synthesis has been performed under oxygen. The lower synthesis temperatures lead to smaller cell volume. This may be explained by oxygen over-stoichiometry $\text{LaMnO}_{3+\delta}$. Note that the oxygen excess is related to the presence of cation vacancies in the unit cell and true chemical formula should be written $\text{La}_{3/3+\delta}\text{Mn}_{3/3+\delta}\text{O}_3$ equivalent to $\text{La}_{1-y}\text{Mn}_{1-y}\text{O}_3$ oxygen over-stoichiometry thus decreases the unit cell density first and like strontium oxidizes Mn^{3+} to Mn^{4+} .

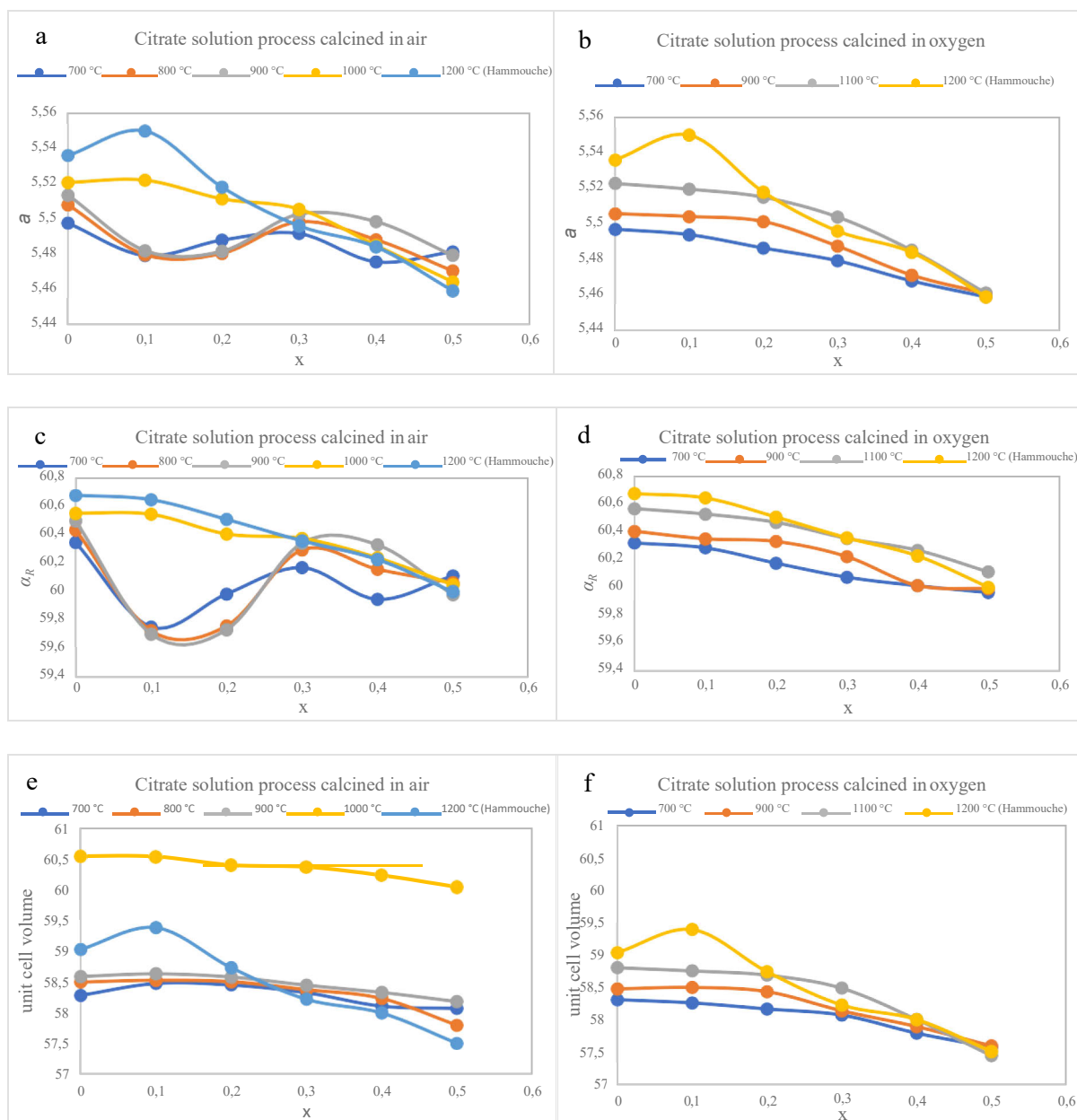


Figure 3-17 : Cell parameters of LSMO synthesized from citrate solution process (a, c, e) calcined in air (b, d, f) calcined in oxygen (some data are from Hammouche’s work)

Concerning the BET characterization, the calcination temperature has a big influence on the surface area of LSMOs. Taking LSMO0.3 synthesized from citrate solution process calcined in air as an example, the surface area of LSMO0.3 calcined at different temperatures as well as the nitric treated VXC-72 are listed in Table 3-6. Generally, in the selected calcination temperature range, the surface area decreases rapidly with increase of calcination temperature.

Table 3-6: Surface area of LSMO0.3 obtained from calcination at different temperatures in air

Temperature (°C)	700	800	900	1100
Surface area (m ² g ⁻¹)	23.8	19.7	8.78	0.921
Surface area of nitric acid treated VXC-72 is 232 m ² g ⁻¹				

SEM images show some LSMO particles are agglomerated into big blocks while some present as small particles. Figure 3-18 presents the SEM images of LSMOs with different calcination temperatures, LSMO calcined at 1100 °C exhibits more agglomerated blocks than that at 900 °C. Morphology has no big difference between LSMOs with different strontium doping as shown in Figure 3-19. While the morphology of LSMOs synthesized with different processes have evident different characteristic indicated in Figure 3-20. Particles from citrate solution processes contain honeycomb foam-like structure. The calcination in oxygen yields finer and more concentrated ‘honeycomb cells’. This foam morphology must originate from the gas generation in a molten system during the citrate process. This structure is not seen in those synthesized from the carbonate coprecipitation, where a dense structure is obtained instead.

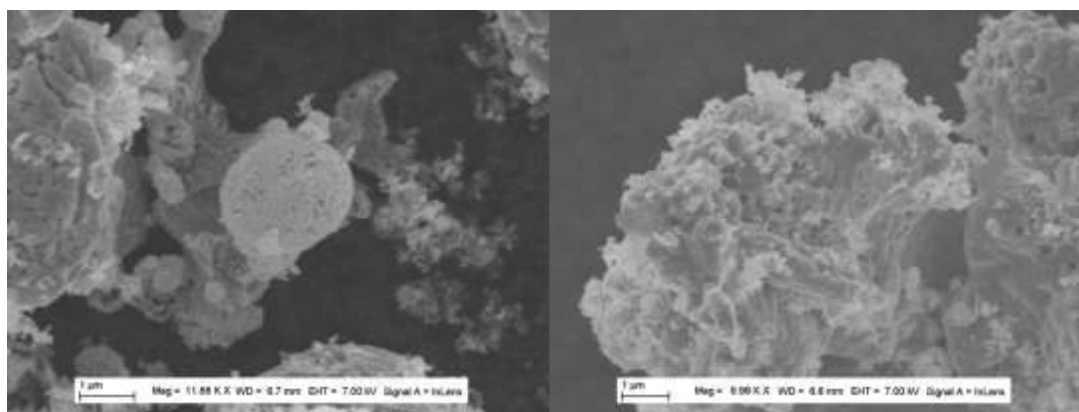


Figure 3-18: SEM images of LSMO0.3 synthesized from coprecipitation process calcined at 900 °C (left) and 1100 °C (right)

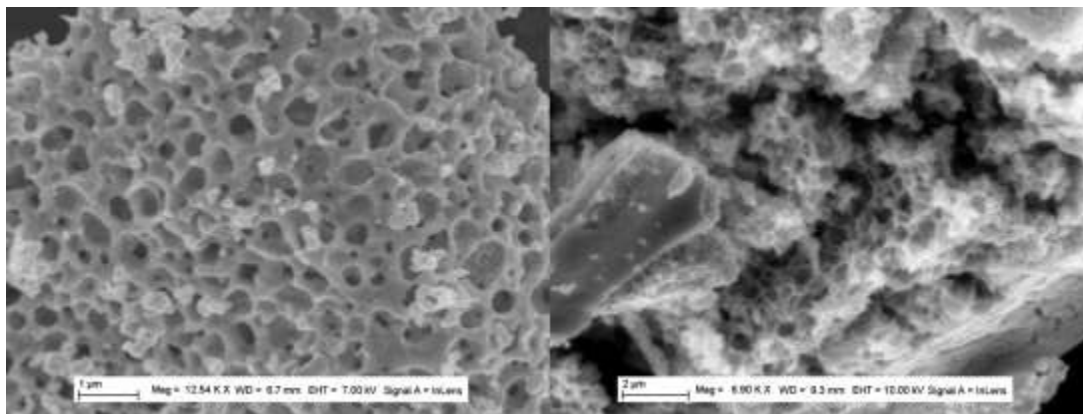


Figure 3-19: SEM images of LSMO synthesized from citrate solution process calcined in air calcined at 900 °C, LSMO0.3 (left) and LSMO0.2 (right)

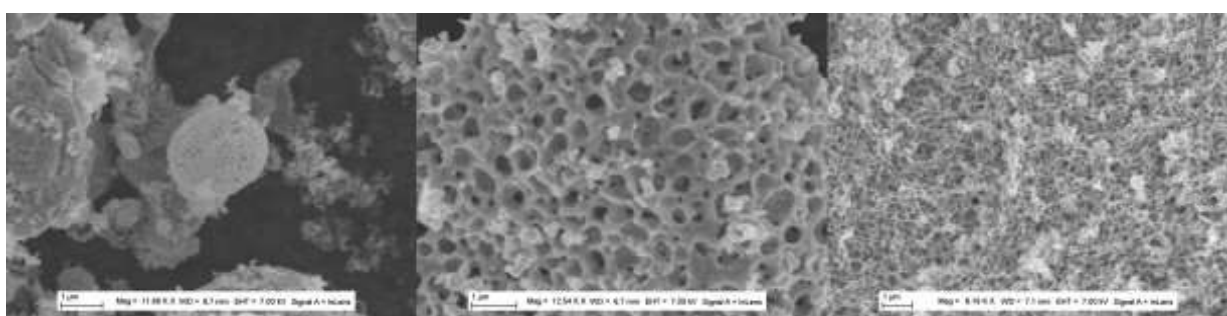


Figure 3-20: SEM images of LSMO synthesized from coprecipitation process (left), citrate solution process calcined in air (middle), calcined in oxygen (right) calcined at 900 °C

3.5.3. Electrochemical characterization of $\text{La}_{1-x}\text{Sr}_x\text{MnO}_3$

The electrochemical characterization of the catalyst $\text{La}_{1-x}\text{Sr}_x\text{MnO}_3$ has been done on inks of the catalyst formulated with conductive carbon and polymeric binder. We had a lot of difficulties to obtain reproducible results and we finally reproduced the protocol by Sunsivitch et al. [364] who used Nafion® (a perfluorosulfonic acidic membrane) as the binder for making electrodes. Then inks were deposited onto a rotating disk electrode and studied as a function of the rotation rate.

A typical preparation method is as follows:

A slurry containing catalyst, binder, and carbon material in the solvent is made. A drop of the slurry then is coated on the tip of RDE (Radiometer analytical) with a diameter of 3 mm and a surface area of 0.07 cm², after the solvent is evaporated, the active materials are attached on the disk firmly.

First, the carbon material is treated with nitric acid to increase its hydrophilicity. Its treatment is as below: 2 g of carbon black (VXC-72) is mixed with 20 mL nitric acid (1 M from VWR) using an electronic mixer for 5 min, then it is put in the oven at 80 °C for 4 hours.

Followed is the filtration of the mixture, and collection of the carbon black, then drying it overnight in the oven at 80 °C.

Because it is delivered in its acidic form, the catalysts risk a partial dissolution in contact with this acidic environment. 3 mL purchased Nafion solution (wt. 20%) is mixed with 2 mL 0.3 M KOH solution to neutralize it, similar way adopted from [364]. After shaking the mixture for a night on a shaker, the obtained solution is ready to use directly.

To make the slurry, 75 mg catalyst material, 15 mg of carbon black (nitric acid treated), and 15 mg Nafion (K^+ exchanged, dry mass, 125 μ L solution) are well mixed in 6 mL deionized water, followed of which, the mixture is sonicated for around 2 mins. Then 1 μ L of the slurry is dropped on the tip of glassy carbon electrode, after 10 mins drying in an oven at 60 °C, the electrode is ready to conduct cyclic voltammetry (CV) experiment.

A three-electrode system is applied; RDE is the working electrode, platinum electrode from Metrohm-Hach is used as counter electrode, and Ag/AgCl (3 M KCl) is the reference electrode (with a protective KCl filled guard against corrosion), 0.3 M KOH is the electrolyte. Potential scan ranges from -1 V to 0.5 V vs Ag/AgCl (3 M KCl) with a scan rate of 10 mV s⁻¹.

The scans were started first from the OCV towards negative potentials under oxygen bubbling. The samples showing the onset of a negative reduction current at the highest potential (less negative) should have the best catalytic activity for ORR.

3.5.3.1. Oxygen reduction effect of LSMO

To prove that the reaction involves an oxygen reduction, oxygen-nitrogen shift to the electrolyte has been adopted. $La_{0.7}Sr_{0.3}MnO_3$ synthesized from citrate solution process calcined in air is used as catalyst. As is shown in Figure 3-21, before the CV scan, oxygen is firstly bubbled into the electrolyte for 30 min to get saturated. As the potential scan starts, there appears a reductive peak with an onset potential of around -0.2 V vs Ag/AgCl (3 M KCl).

When the gas is shifted to nitrogen, the reductive current dramatically decreases, with more cycles of nitrogen bubbling, the reductive current goes lower to nearly flat. When oxygen is shifted back, the reductive current immediately reappears, though the current is not as high as the first scan with oxygen bubbling, due to lower oxygen concentration in the electrolyte. With further oxygen bubbling for 30 min, the current turns back closely to the first cycle obtained under oxygen. This indicates that the reduction current is linked to oxygen reduction. This indeed proves that we are actually studying oxygen reduction reactions.

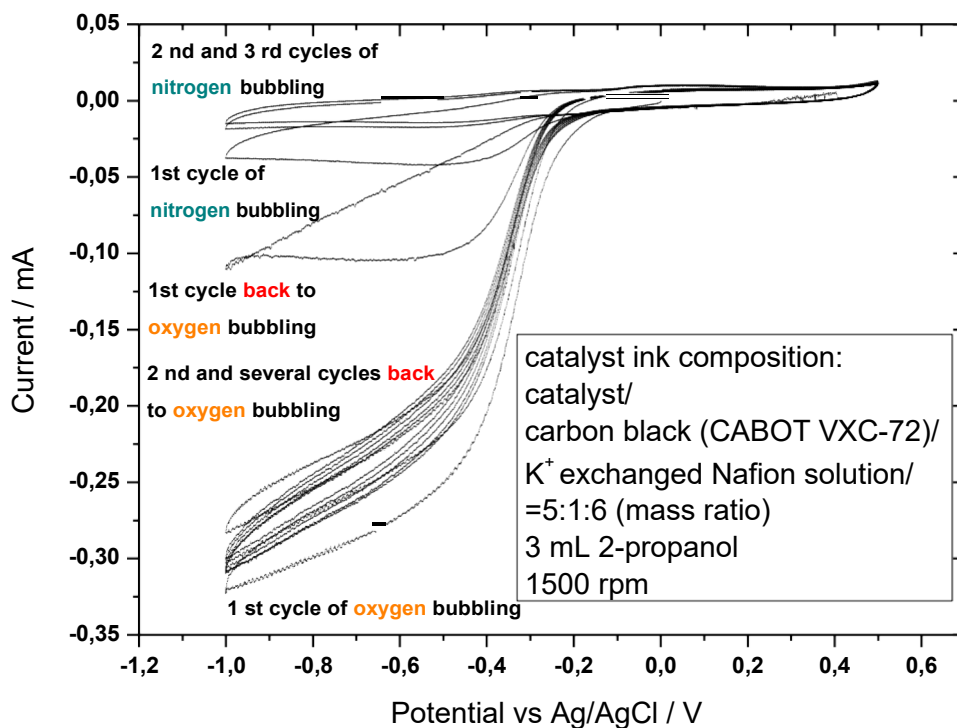


Figure 3-21 : CVs of $\text{La}_{0.7}\text{Sr}_{0.3}\text{MnO}_3$ in electrolyte with shifted oxygen-nitrogen-oxygen, at 1500 rpm

3.5.3.2. Effect of treatment of the ink

From many trials of this experiment, we found that the ink treatment is quite important to make sure that the CV experiments are reproducible and comparable.

In this case, mixing homogeneously using a motor ultraturax (XENOX MHX/E) and sonication by an ultrasonic processor UP100H (100W, 30kHz from Hielscher). The rotor ultraturax mixing duration is 5 mins to get a homogeneous state, and sonication is lasted for 2 mins where the particles in ink are well-broken and the solvent is not too hot to be evaporated. The inks are dropped on the disk electrode immediately after the sonication to avoid heterogeneity caused by further settlement.

To show the effect of sonication on the dispersion of catalyst, Figure 3-22 shows the cyclic voltammograms obtained using $10 \mu\text{L}$ of the same ink without and with sonication for 2 min. We can observe that the ink obtained from simple mixing shows a much larger capacitive effect than that after sonication.

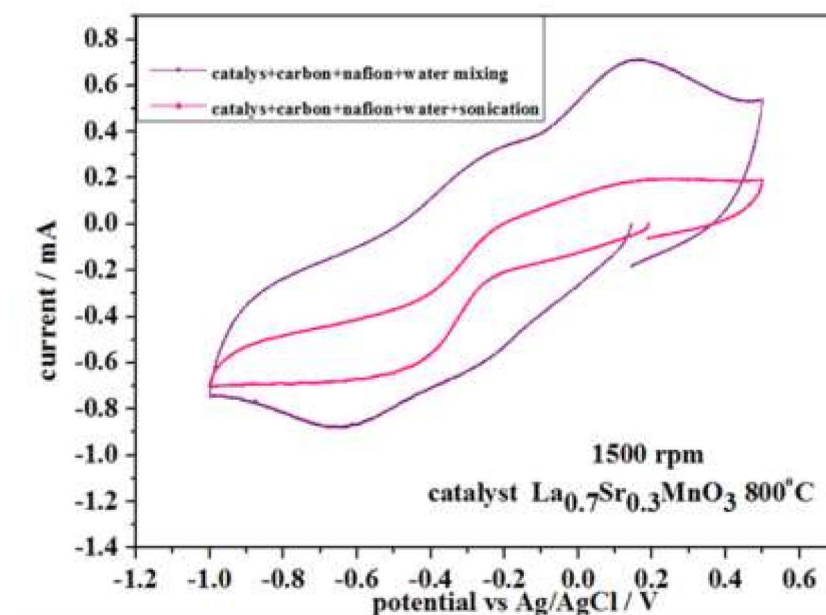


Figure 3-22: Cyclic voltammograms from inks with different mixing treatment, catalyst was $\text{La}_{0.7}\text{Sr}_{0.3}\text{MnO}_3$ calcined at $800\text{ }^\circ\text{C}$ in air synthesized from citrate solution process. Mixture of 75 mg catalyst material, 15 mg of carbon black (nitric acid treated), and 15 mg Nafion. All mixed with ultraturax for 5 min and sonicated for 2 min or not. Drop volume $10\text{ }\mu\text{L}$ deposited onto a glassy carbon rotating electrode

This shows the importance of two types of mixing distributive mixing (homogeneous mixture of carbon, polymer binder and catalyst) obtained by the ultraturax and dispersive (breaking the catalysts into smaller grains) obtained by sonication.

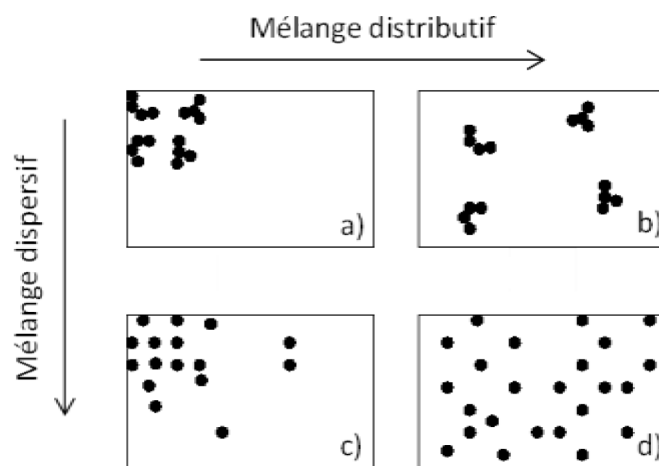


Figure 3-23: Illustration of the two types of mixing particles into a binder [379]

3.5.3.3. Reproducibility of the experiment

As shown for the effect of sonication, during repeating the experiments, we found that reproducibility is not easy to be ensured. Every parameter maybe sensitive to the final cyclic

voltammogram. After strictly controlling all the mixing, the composition of each material in the ink, the oxygen concentration in the electrolyte etc., we could finally obtain reproducible results.

As shown in Figure 3-24, the experiments are done either with the same ink, or with the inks containing the same materials. All the experiments are prepared at different times, namely four experiments separated by days or weeks. The catalyst $\text{La}_{0.7}\text{Sr}_{0.3}\text{MnO}_3$ (LSMO0.3) is obtained from citrate solution process calcined in air at $900\text{ }^\circ\text{C}$. The catalyst powders are kept in a plastic bottle sealed with parafilm, so the possible reactions between the powder and atmosphere components (water, CO_2 , oxygen) can be limited to maximum. Figure 3-24(a) shows the cyclic voltammograms of two experiments from the same ink. The ink for the repeated one is mixed for 3 mins before use. Figure 3-24(b) presents the repeating experiments from two inks prepared separately which are conducted in different days. Even though the cyclic voltammograms are not completely the same, in general the onset potentials for oxygen reduction in the experiments are nearly the same which is the most important for catalysts comparison.

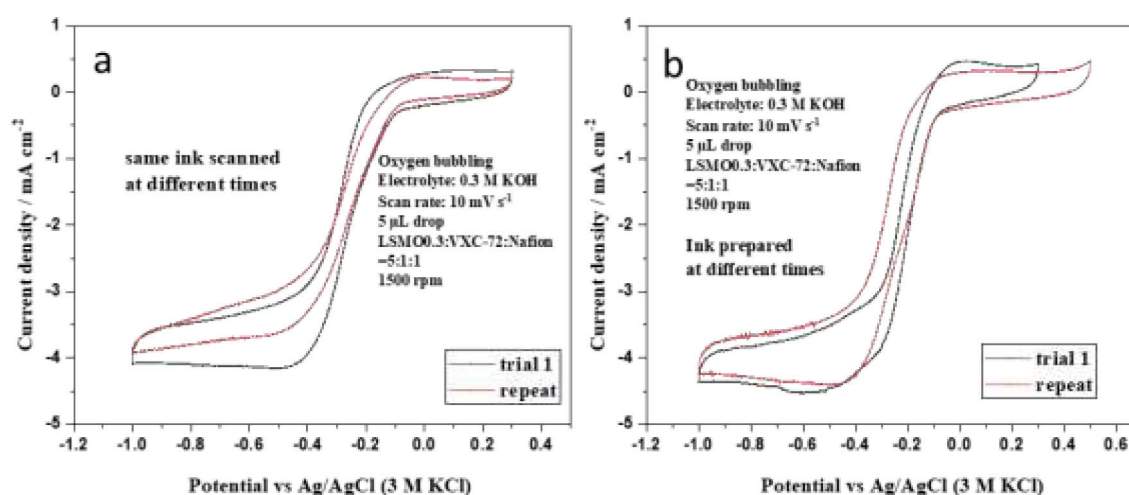


Figure 3-24 : Repeating experiments with (a) the same ink conducted at different times 1500 rpm with O_2 saturation in the electrolyte (b) and inks with same compositions prepared at different times

3.5.3.4. The first scan of the ink

We observe that the first scans of the cyclic voltametric experiments are quite different from the other scans which is very little discussed in articles. LSMO0.3 synthesized from citrate solution process under calcination at $900\text{ }^\circ\text{C}$ in air is used for the scans.

The ink is composed of 75 mg LSMO0.3, 15 mg VXC-72, 15 mg Nafion in 6 mL deionized water (5:1:1 in mass ratio), after mixing for 5 mins and sonication for 2 mins before use. Before reutilization of the ink, mixing for 3 mins is applied every time. The voltammetry

has been performed without rotation seen from Figure 3-25, there are two clear cathodic peaks during scan towards the negative potential, and two anodic peaks during the first positive scan in every scan in O₂ saturated electrolyte. Moreover, there is big difference between the first and the second scan (and following scans) about the first cathodic peak as Figure 3-25(b) shows. The sharp reduction peak slowly disappears in the second and following scans.

The first cathodic peak disappears anyway in N₂ saturated electrolyte observed from both Figure 3-25(a) and (b), which indicates that the first cathodic peak can be referred to oxygen reduction reaction. This transitory peak is probably linked to pre-adsorbed species on the dry ink.

The second cathodic peak is also different between the first scan and the others, either in N₂ or O₂ saturated electrolyte. Generally, after first scan, the second cathodic peak locates more positive, while with further scans, the potential location changes a little. The second cathodic peak is reported to correspond with the first anodic peak during the positive scan [380], they are Mn³⁺ reduction to Mn²⁺ and Mn²⁺ oxidation to Mn³⁺, respectively. It may also be attributed to the high oxygen coverage on the surface of the dry ink, which needs more overpotential for reduction. The second anodic peak seems not relative to the gas atmosphere in electrolyte, its position moves towards positive potentials with shift of atmosphere using the same electrode. It may be related to OH⁻ oxidized to HO₂⁻, while atmosphere is shifting, the progressive OH⁻ desorption from the electrode surface to the electrolyte, meantime the OH⁻ in the electrolyte also transports to the near surface of electrode, which makes the overpotential higher as well as a little higher current.

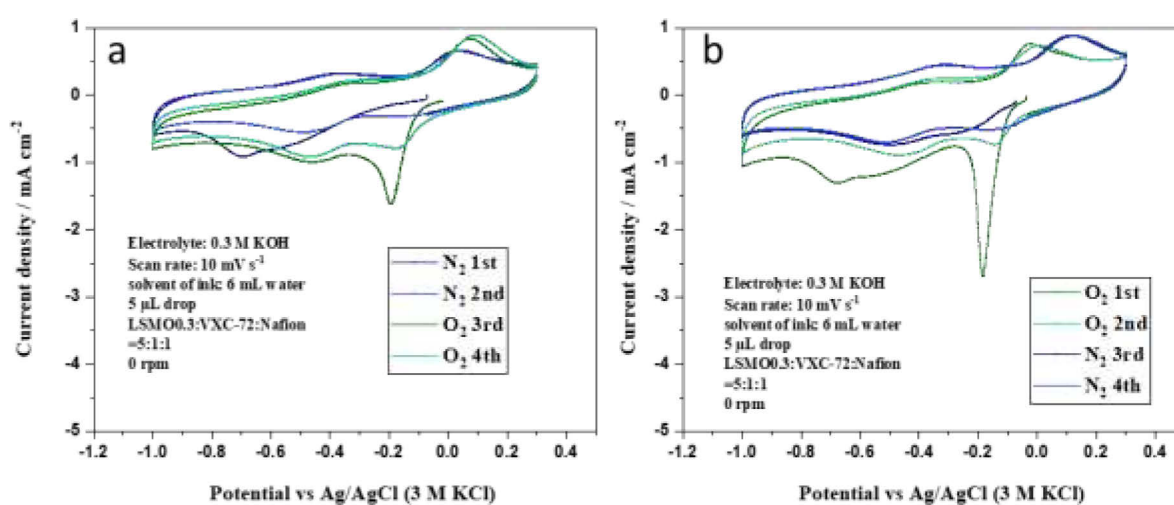


Figure 3-25 : Cyclic voltammograms of La_{0.7}Sr_{0.3}MnO₃ in electrolyte saturated with different gas (a) from N₂ to O₂; (b) from O₂ to N₂, without rotation

The first cathodic peak is related to oxygen reduction as rationalized above by the necessary presence of oxygen bubbling.

Concerning which component in the ink plays this role, other inks containing different components have been also studied as shown in Figure 3-26.

- Without VXC-72 in the ink, the first and second cathodic peak seem integrate into one broad peak. The onset potential is slightly more negative than that with VXC-72 in the ink.
- Without LSMO0.3 in the ink, there is only one sharp cathodic peak, corresponding to the first cathodic peak in the case with LSMO0.3 in the ink. While the onset potential is more negative, namely more overpotential, which also demonstrates that the VXC-72 alone has catalytic activity for oxygen reduction, though lower than LSMO0.3.
- The similar case is seen on bare glassy carbon which also has a weak oxygen reduction activity.
- As for the two anodic peaks, they are undoubtedly associated to the LSMO0.3 because they are not observed when it is not present.

So, the sharp reduction peak does not seem to be specific of the LSMO catalysts because it is observed with the carbon alone. But it changes in the presence of LSMO and there is a synergic effect of both carbon and LSMO. There may be also an impurity in the Nafion or in the solution which is irreversibly decomposed by the reduction.

To avoid this transitory effect, we exclusively used the data from the second scan.

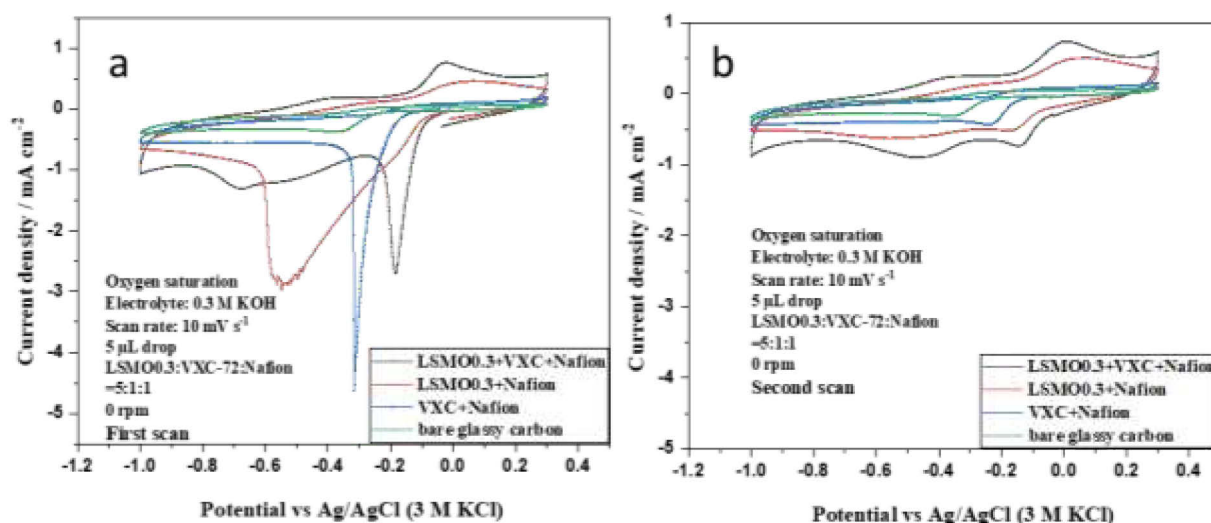


Figure 3-26 : First scan (a) and second scan (b) of cyclic voltammograms of inks with different components

3.5.3.5. Effect of the ink composition

The effects of carbon and catalyst are separately tested with the cyclic voltammetry method. Three inks are prepared:

- 75 mg LSMO+15 mg VXC-72+15 mg Nafion, i.e., the complete formulation
- 75 mg LSMO+15 mg Nafion, i.e., no carbon
- 15 mg VXC-72+15 mg Nafion, i.e., no catalyst

Figure 3-27(a) and (b) shows the three electrodes using the above-mentioned inks and the bare glassy carbon under N_2 and O_2 bubbling, respectively. The fluctuations are sometimes caused by the oxygen bubbling. Note that the experiments have been carried out without any rotation.

Under nitrogen, we can observe that glassy carbon and VXC-72 show a low capacitive effect. LSMO0.3 shows a large capacitive effect, and it is emphasized by the presence of carbon which probably brings a better conductivity. We may speak of pseudo-capacitive effect because it is superimposed with oxidation and reduction peaks. When VXC-72 is added, all the redox reactions on LSMO0.3 are also sharper, with evident redox peaks, which is owing to the conductivity increase by VXC-72.

Under oxygen, all samples show a reduction current below -0.2 V vs Ag/AgCl but the reduction current is much higher (more negative) with the catalyst alone and maximal with the mixture catalyst-carbon.

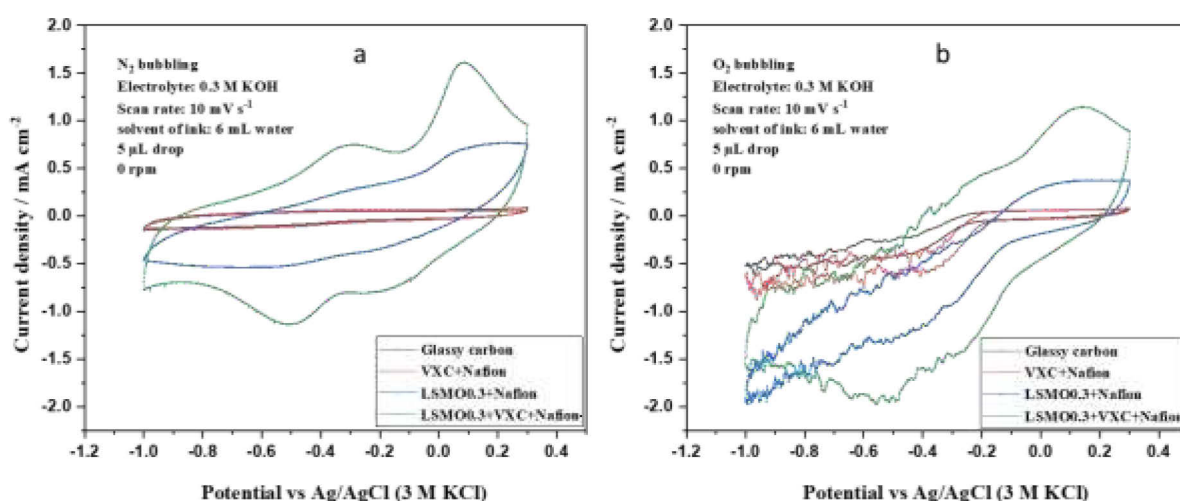


Figure 3-27: CV curves of different inks with different components in bubbling N_2 (a) and O_2 (b)

Figure 3-28 presents the effect of the convection generated from rotation of RDE. With enough oxygen transport to the electrode, the same conclusion can be obtained that the VXC-

72 has oxygen reductive catalytic activity, and LSMO0.3 presents higher activity from the more positive onset potential.

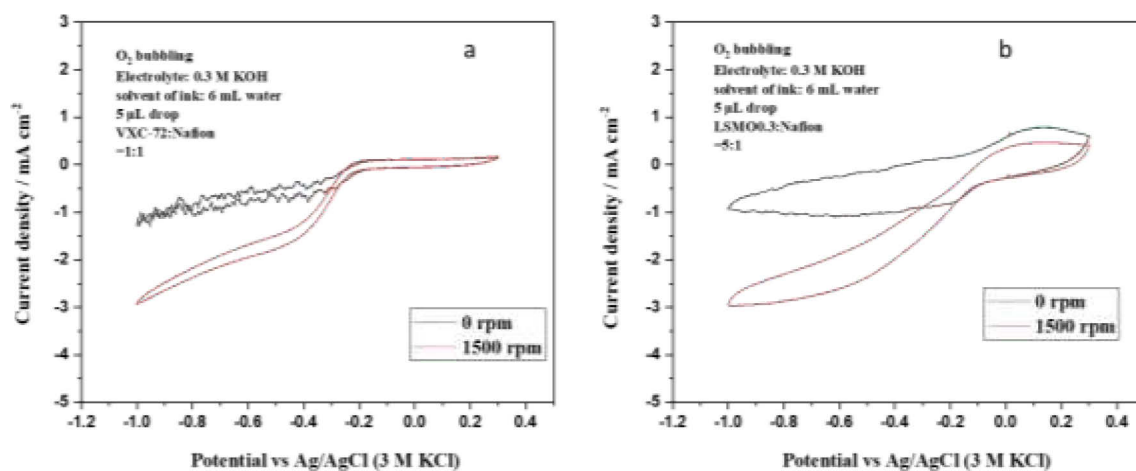


Figure 3-28: CV curves of different inks with different components (a) VXC-72+Nafion (b) LSMO0.3+Nafion in bubbling O₂ with different rotation rates

3.5.3.6. Effect of scan rate

The anodic peaks are not visible when scan rate is low under the rotation rate of 1500 rpm, while they are more clearly seen with higher scan rate ($> 20 \text{ mV s}^{-1}$) as seen from Figure 3-29. Thus, 10 mV s^{-1} is a proper scan rate for this series of CV studies.

Moreover, the current density measured at 0.2 V has a linear relationship with the scan rate, which accords to the capacitor characterization (Figure 3-30). Indeed, the current observed on a capacitor should be calculated as

$$\text{Equation 3-4: } I = C v$$

Where C is the capacity in Farads and v is the scan rate (in V s^{-1}).

We obtain for the sample a capacity of around 10 F cm^{-2} as indicated in Figure 3-30. This value is quite interesting as a matter of fact and although it was not our topics which should require a further study (change of electrolyte) for application to supercapacitors.

The capacitive effect is a problem for the study of the electrochemical reactions. Based on this, we decide to normalize the current density according to that measured at 0.2 V to eliminate the capacity contribution from the true faradaic contribution of the ORR reaction. Also, a scan rate of 10 mV s^{-1} was considered as a good choice to avoid too large capacity effect.

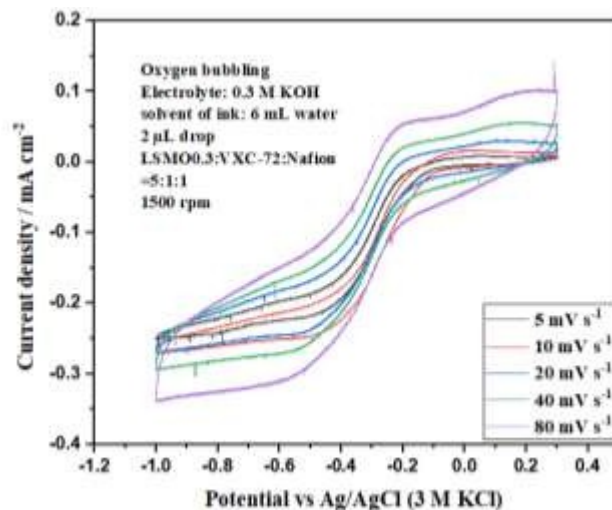


Figure 3-29 : CV curves of LSMO0.3 at different scan rates

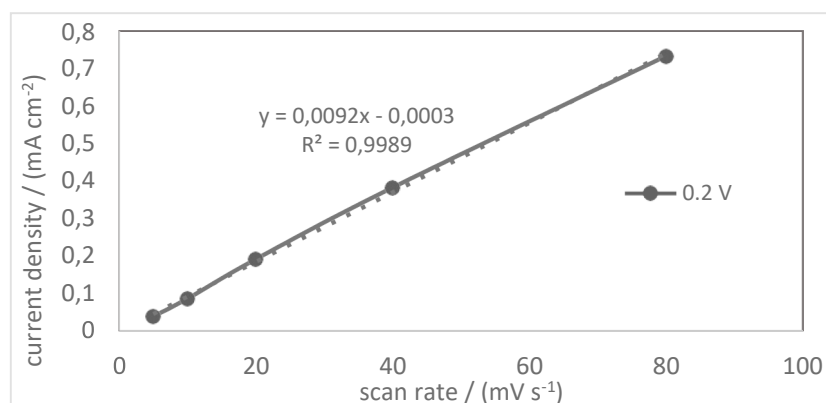


Figure 3-30 : Current density-scan rate relationship, current density is the medium of anodic and cathodic current density at 0.2 V

3.5.3.7. Analysis of the electrochemical behavior without rotation as a supercapacitor effect

Those readers who are only interested in ORR reactions can easily skip the following paragraph, because we are going to apply the methodology for studying supercapacitors. But this is a macroscopic approach which should be taken with caution because it does not differentiate properly redox reactions from capacitive effects.

The capacity measured with the LSMO-carbon-Nafion mixture is worth a study for supercapacitor applications. So, in the following part, we have studied the electrode in static mode (not rotation of the RDE) but with the approach that some use to study supercapacitors. This is interesting because many studies have studied supercapacitors made with oxides without paying much attention to redox reactions. This was associated to pseudo-capacitive effects. Of course, they study them under sealed conditions without oxygen bubbling. But some effects may be associated to some oxygen dissolved in the solutions.

The charges pass through the electrode are composed of three parts:

- the faradaic charges from electron-transfer redox reactions in the bulk electrode.
- the faradaic charges from electron-transfer through the surface atoms, also called as pseudo-capacitance.
- capacitive, i.e., non-faradaic charges from double-layer effect.

Considering all the components, the current passing through electrode can be expressed as below [381]:

$$\text{Equation 3-5: } i = av^b$$

where i is the measured current, v is the scan rate.

Normally, b value is between 0.5 to 1 which are from the pure redox reaction ($b = 0.5$) limited by diffusion of species regardless the reversibility of the reaction, and from the pure capacitance ($b = 1$), based on the two equations below:

For redox reaction:

$$\text{Equation 3-6: } i = nFACoD^{1/2}v^{1/2}(\alpha nF/RT)^{1/2}\pi^{1/2}\phi(E)$$

where Co is the surface concentration of the electrode material, α is the transfer coefficient, D is the chemical diffusion coefficient, n is the number of electrons involved in the electrode reaction, A is the surface area of the electrode materials, and $\phi(E)$, a function represents the normalized current for a totally irreversible system as indicated by the cyclic voltametric response, which is dependent on potential E , F , R , T have their normal meanings.

For the capacitance as Equation 3-4.

The value of b can explain the electrochemical system is more a battery or a capacitor, which can be obtained from the slope of $\log i \sim \log v$.

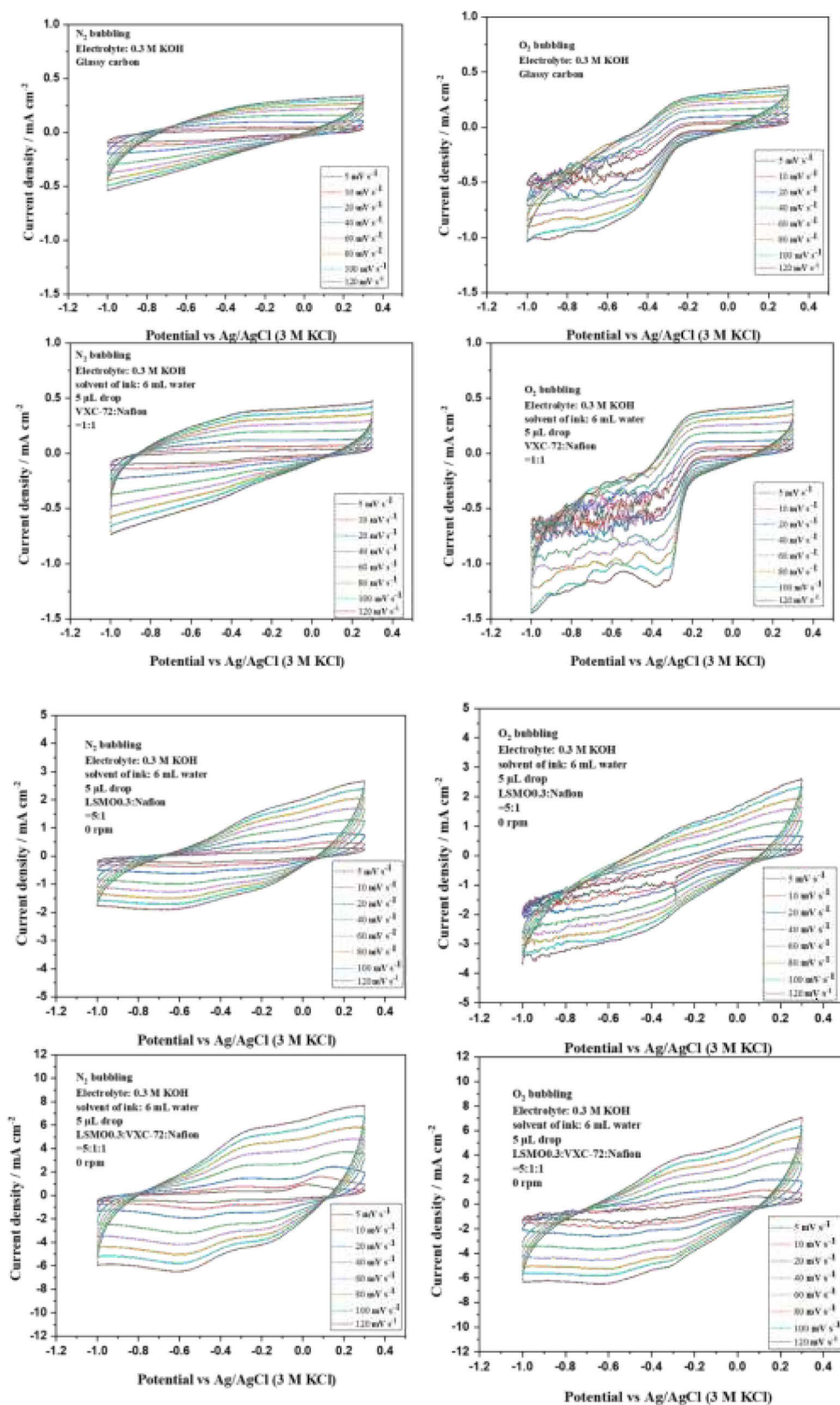


Figure 3-31: The CV curves from inks with different compositions under different scan rates and different gas bubbling; left column with N_2 and right for O_2

Figure 3-31 shows all the CV curves obtained from different components under different scan rates in either O₂ or N₂ atmosphere. The curves associated to nitrogen bubbling could be characteristic of materials for capacitors. Anodic and cathodic currents compensate each other. Those obtained with oxygen bubbling would not be acceptable because the anodic charge is much larger than the cathodic one as shown in Figure 3-32. This, of course, exhibits a non-reversible reaction.

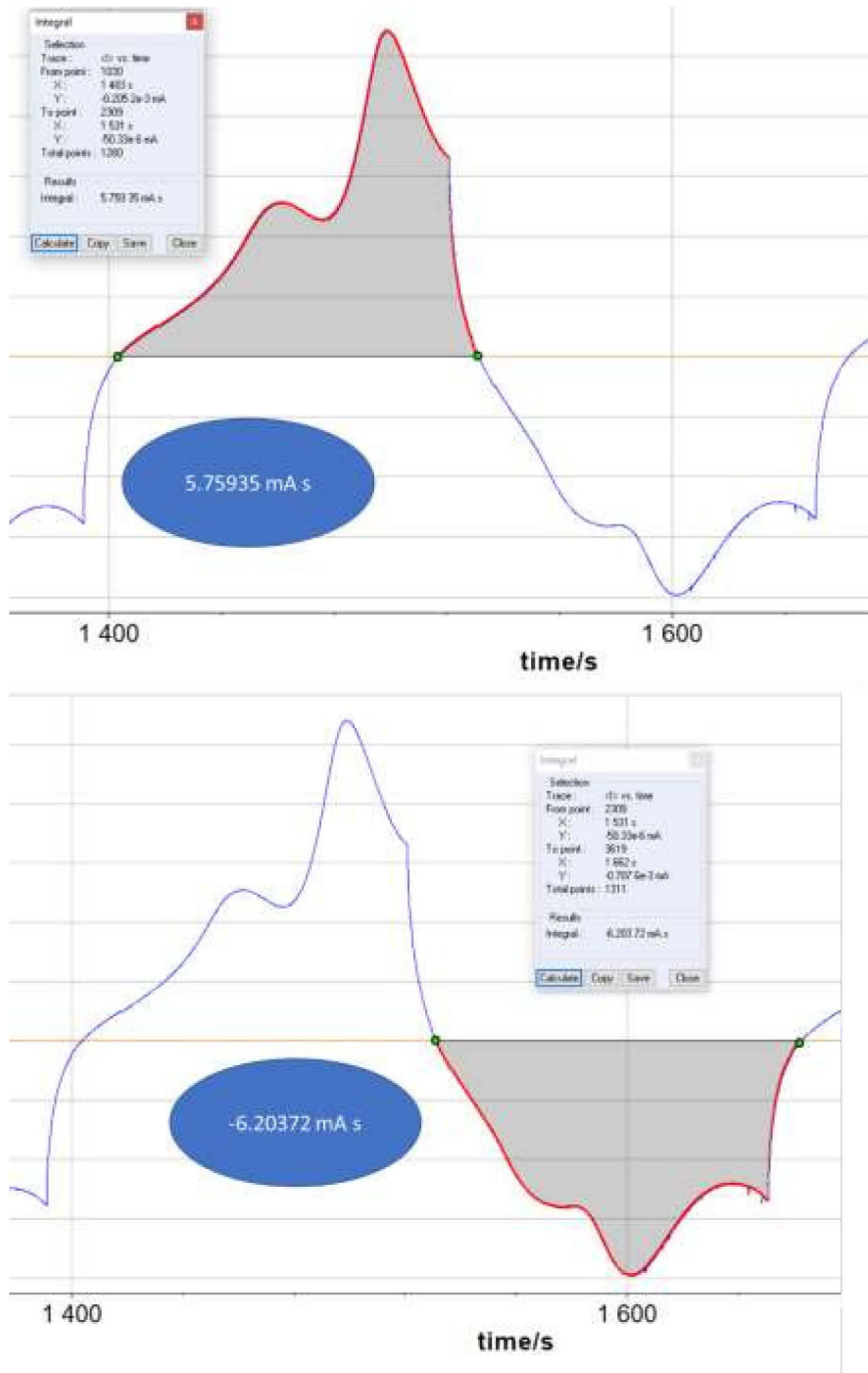


Figure 3-32 : Positive and negative charges in a CV cycle for LSMO+VXC-72+Nafion with N₂ bubbling

Anodic currents at potential of 0, 0.1, and 0.2 V are selected to plot $\log i \sim \log v$. For all the plots, the R-squared values are larger than 0.99, indicating very good linear relationship as shown in Figure 3-33 as an example. The detailed slopes are listed in Table 3-7. Among them, all follows a good linearity in all the applied scan rate range, except the cases with all the composition of LSMO + VXC-72 + Nafion which present much higher currents and two slopes in two smaller range of scan rates. In these cases, the scan rate has a bigger influence on the reactions or adsorption state on the electrode surface than the other cases with less components in the ink.

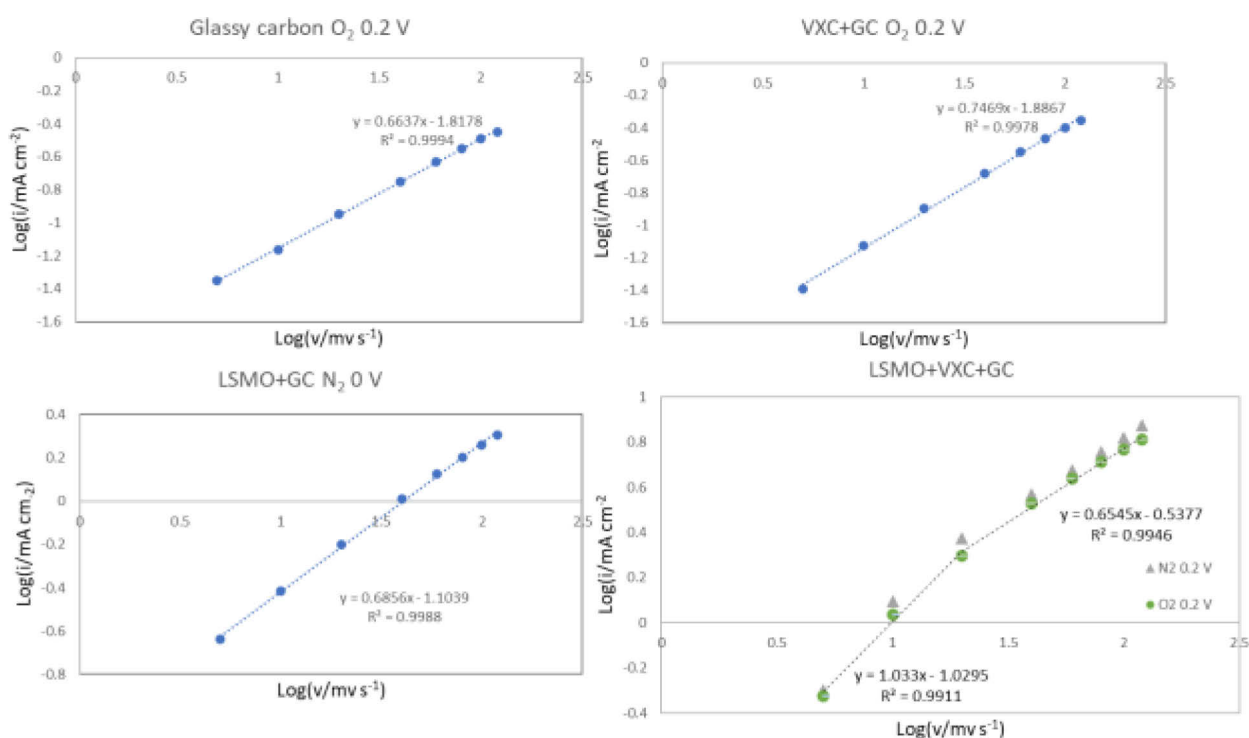


Figure 3-33: $\log i \sim \log v$ plots

As mentioned above, the slope b closer to 0.5 means the redox reaction dominates in the electrochemical process, approaching to 1 indicates capacitive effect is the main element. From Table 3-7, we can know that the bare glassy carbon and VXC-72 + Nafion show a b coefficient of 0.7 - 0.8. This should be a capacitive effect but limited by the diffusion of species in the electrolyte. A similar b parameter is seen in the case with LSMO + Nafion than that with VXC-72 + Nafion, which is also clearly seen in the CV curves above.

Specially for the case with all the components LSMO + VXC-72 + Nafion, the cyclic voltammetry shows bumps associated to redox reactions. And the $\log(i) - \log(v)$ plots show two regimes associated to low (5, 10, 20 mV s^{-1}) and high scan rates (20 – 120 mV s^{-1}). Not only the scan rate influences the slope, but the potential also plays a role. At 0 V, with low scan

rate, there exists mostly redox performance on the electrode when bubbling N₂, while it changes to capacitive when bubbling O₂; at high scan rate, the situation reverses, namely, the capacitive effect decreases with N₂ changing to O₂. Except for the condition at 0 V with N₂ bubbling, the others all present more reactive effect at high scan rates than at low scan rates. At 0.1 V, with O₂ introducing, the redox effect increases at both low and high scan rates. At 0.2 V, the electrode exhibits mostly a characteristic capacitor behavior either under N₂ or O₂ bubbling. This can also support the choice of the current at 0.2 V as a normalization standard. Moreover, 10 mV s⁻¹ selected as the scan rate for different perovskites comparison is reasonable. The capacitance decreases a little with O₂ bubbling at low scan rates, while the reactive effect decreases a little at high scan rates.

Table 3-7 : All the slopes of logi~logv plots

GC	0 V	0.1 V	0.2 V
N ₂	0.7324	0.7266	0.7313
O ₂	0.7102	0.6737	0.6637
VXC+GC			
N ₂	0.7668	0.7738	0.7469
O ₂	0.8278	0.7914	0.785
LSMO+GC			
N ₂	0.6848	0.6471	0.6878
O ₂	0.7131	0.7184	0.7714
LSMO+VXC+GC			
N ₂			
5 10 20 mV s ⁻¹	0.4315	0.8534	1.1125
20 40 60 80 100 120 mV s ⁻¹	0.7688	0.6196	0.6394
O ₂			
5 10 20 mV s ⁻¹	0.8768	0.8294	1.033
20 40 60 80 100 120 mV s ⁻¹	0.6712	0.5951	0.6545

3.5.3.8. Effect of rotating rate

The rotating rates are increased from 0 to 3000 rpm, and back to 400 rpm to check the reversibility and the loss of powder in Figure 3-34. Indeed, high rotation rate may bring to the

loss of powder from the ink deposit. But if the current returns to its original value, we may prove that this did not occur.

Indeed, there is always a loss of reactivity with more cycles on, seen from the onset potential change of oxygen reduction reaction. The ORR reduction curves show an expected increase of the reduction current as a function of the rotation of the disk electrode as shown in Figure 3-34. There is a plateau below -0.6 V which is related to the limitation of current by the convection of oxygen species. A true plateau is never achieved, and this may be due to a diffusion of species in the thickness of the electrode as well as some other redox reactions appearing at lower potentials.

We plotted the current at -0.7 V vs Ag-AgCl as a function of $\omega^{1/2}$. This is shown in Figure 3-35. A very good linear relationship is observed between i^{-1} and $\omega^{1/2}$ based on the Koutecký-Levich analysis, taken with Equation 3-3 : $i_m = 0.62nFAD_0^{2/3}v^{-1/6}C_0\omega^{1/2}$, (F is the faradic constant 96485 C mol⁻¹, D is the oxygen diffusion coefficient which is 2.1*10⁻⁵ cm² s⁻¹, v is the kinetic viscosity of electrolyte which is 0.01 cm² s⁻¹, and C is the concentration of oxygen in electrolyte which is 1.3*10⁻⁶ mol cm⁻³) shown in Figure 3-35, so that the electron transfer number n is calculated 3.96 based on Equation 3-2 and Equation 3-3. So, we verify:

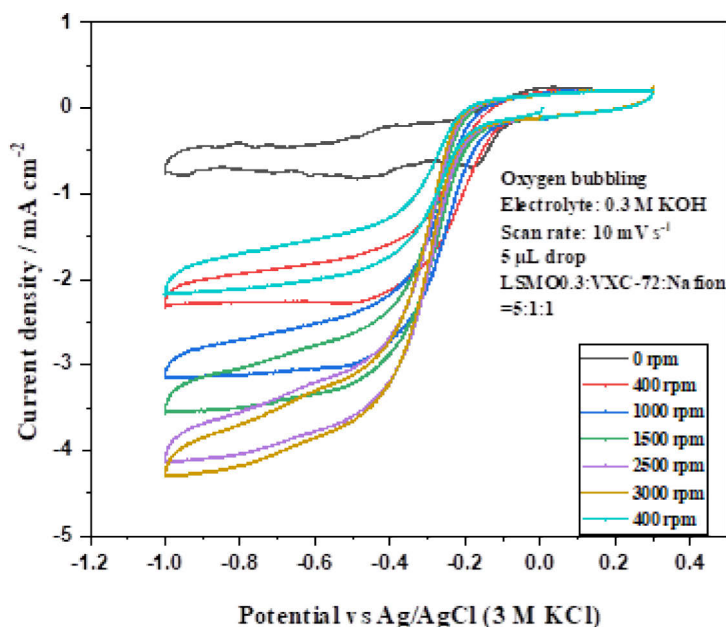


Figure 3-34 : CV curves at different rotation rates

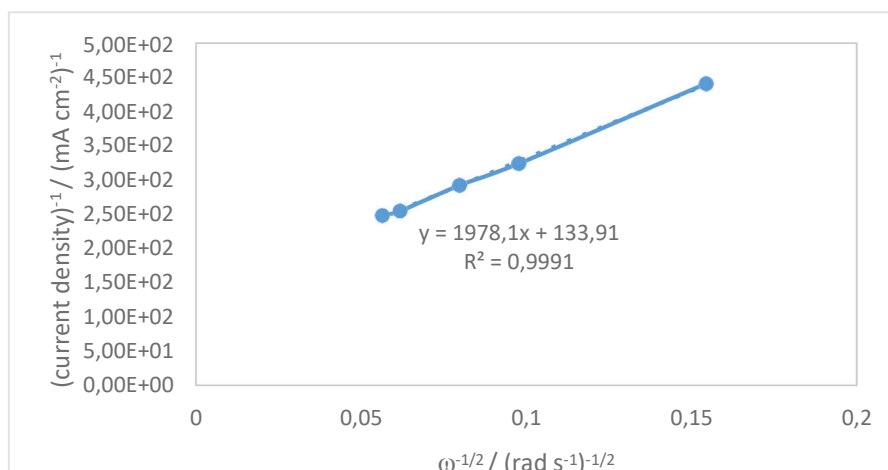


Figure 3-35 : Koutecký-Levich analysis of the CVs in Figure 3-34, current density is the one at potential of -0.7 V vs Ag/AgCl (3 M KCl)

As is indicated by Equation 3-3, the limiting current from ORR on RDE is proportional to oxygen concentration in the electrolyte. By bubbling pure oxygen (1 atm of oxygen) or air (0.2 atm of oxygen) into the electrolyte we should expect a ratio of 1/5 in the limiting current. This is indeed the case, Figure 3-36 further demonstrates that the limiting current density is clearly related to oxygen pressure. It is -4.5 mA cm^{-2} for oxygen gas and -1 mA cm^{-2} for air bubbling. This proves again that is an oxygen reduction reaction.

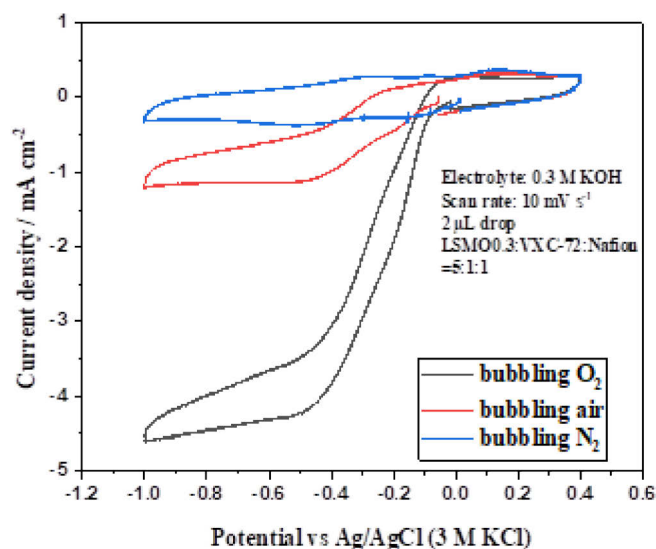


Figure 3-36 : CV curves under different concentrations of oxygen

3.5.3.9. Effect of drop volume

The optimized loading mass of catalyst on disk electrodes is commonly seen around $250 \mu\text{g cm}^{-2}$ in articles. While it is found that drop volume has a big influence on the cyclic voltammogram, especially for the limiting current plateau and the onset potential for oxygen

reduction reaction. This is expected because it relates to the geometrical area of the electrode. Pictures obtained on the electrodes in Figure 3-37 show that they have the same diameter with different thicknesses and coverages.

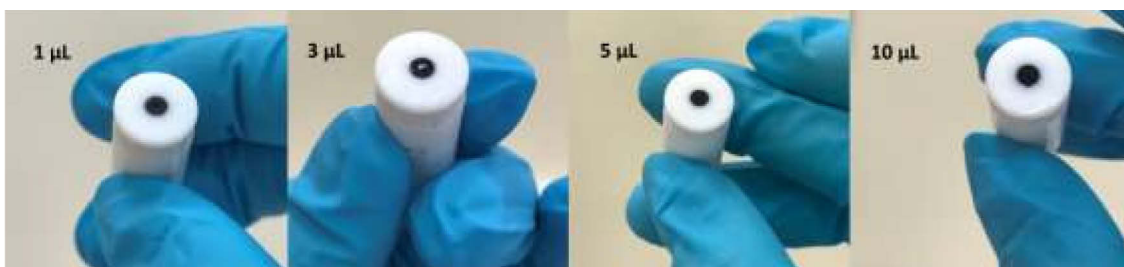


Figure 3-37: Pictures of the electrodes loaded with different drop volumes of ink

Therefore, we have studied the effect of the volume of the ink drop deposited onto the rotating disk electrode. Drop volumes between 1 μL and 10 μL were studied. These different loadings of ink on the disk show different capacitive effects exhibited in potential range of 0 - 0.3 V as presented in Figure 3-38(a). Generally, the higher the loading, the higher the capacitive current. They nearly show the same limiting current within 5 μL loading.

If we normalize the current ascribed to capacitive current based on the curve from 1 μL , we may investigate the effect of the redox reactions as indicated in Figure 3-38(b). All the curves nearly have the same onset potential. Taken into consideration the limiting current plateau, which indicating a complete diffusion-limited region, 3 μL or 5 μL are both favorable. because they yield a flat plateau of limiting current. The 10 μL drop does not give a flat plateau because it is probably too thick. Thus, we choose 5 μL for most of the studies because a better coverage of the ink on the glassy carbon disk whereas the 3 μL drop after drying is merely able to cover whole surface of disk.

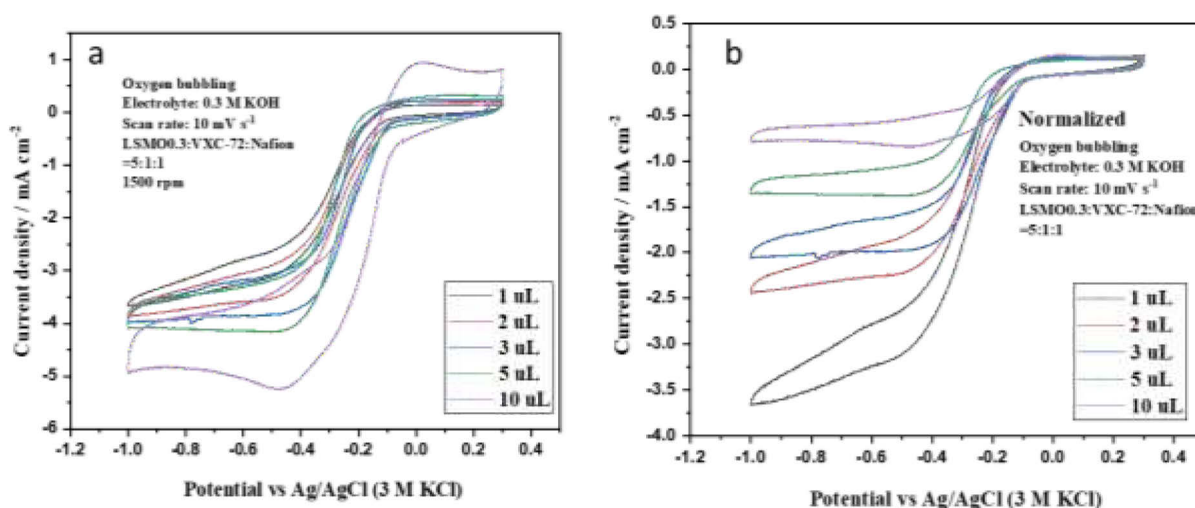


Figure 3-38 : (a) Original CV curves from inks with different drop volumes on the disk; (b) the corresponding normalized CV curves

3.5.3.10. Effect of different carbons and of formulations

As mentioned above, VXC-72 has a catalytic activity towards ORR and has a relatively strong adsorption ability. Other kinds of carbon materials have been also studied for comparison. Active carbon and graphite are treated with nitric acid the same way as VXC-72. The ink containing VXC-72 shows extraordinarily higher limiting current than the others, as well as a more positive onset potential from Figure 3-39. Curves located at 0 – 0.3 V are similar among these three carbon materials. This indicates a same capacitive effect.

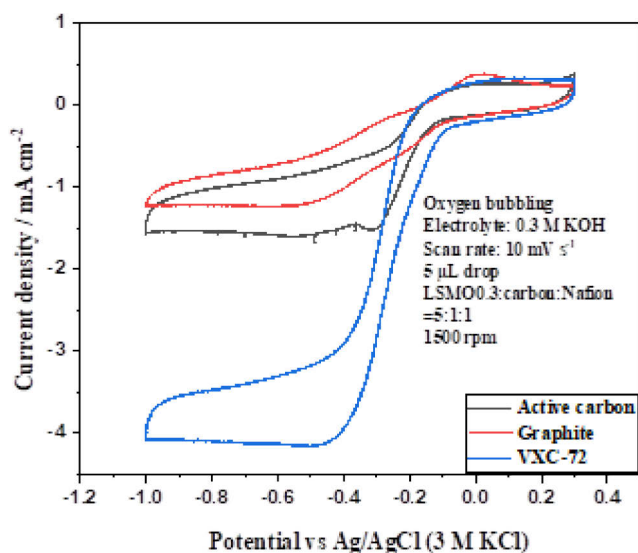


Figure 3-39 : CV curves of inks containing different types of carbon materials

Varying the content of VXC-72 or Nafion in the ink also generates an enormous difference as shown in Figure 3-40 and Figure 3-41. High loadings of VXC-72 or low loadings

of Nafion make the CV curves much “fatter” indicating a higher capacitive effect. Less VXC-72 content may contribute to lower electronic conductivity, which results in lower limiting current density and lower oxygen reduction activity. Too little Nafion is not enough to bind the materials well to the disk, and results in fluctuation in the CV curve.

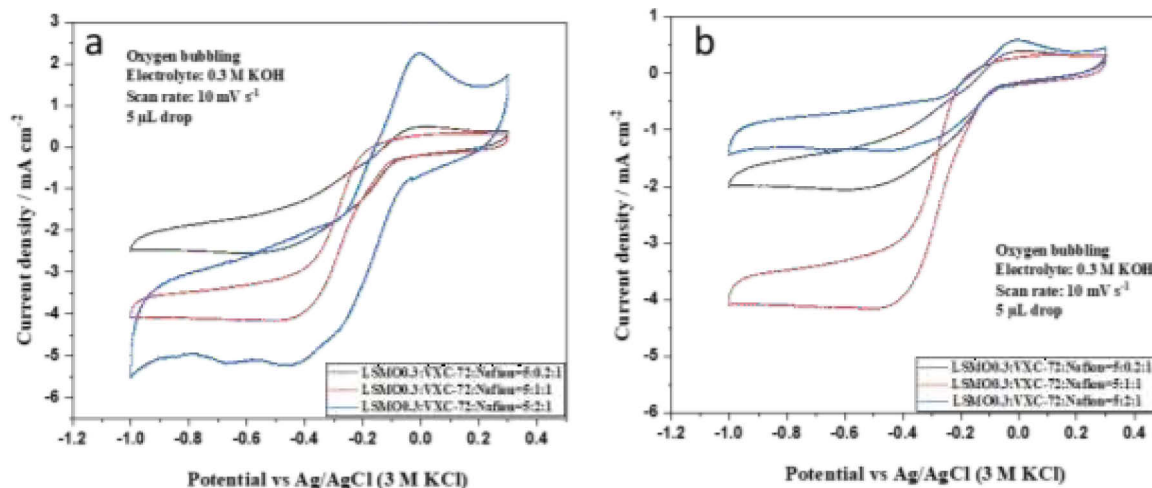


Figure 3-40 : (a) Original CV curves from inks with different quantities of VXC-72 in the ink; (b) the corresponding normalized CV curves

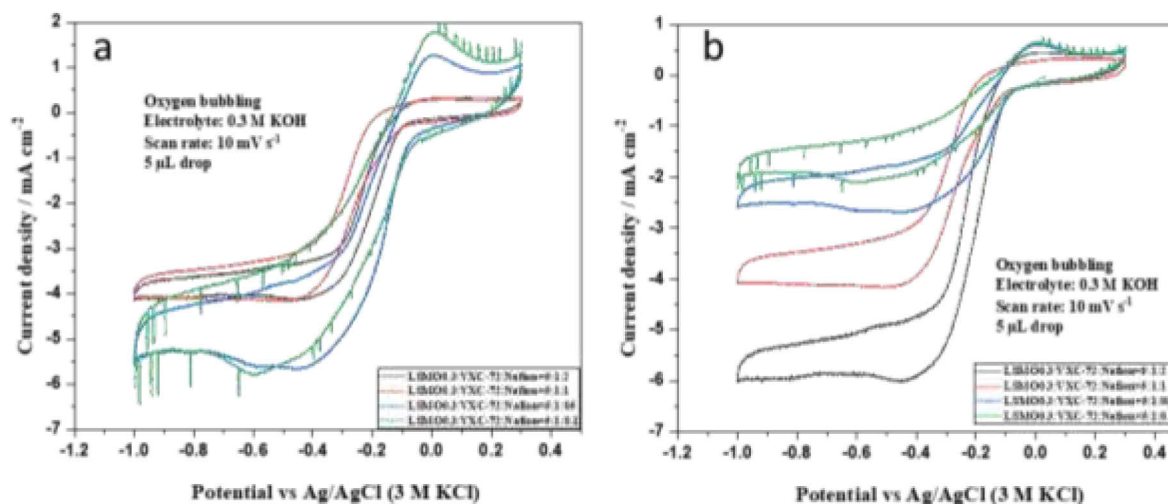


Figure 3-41 : (a) Original CV curves from inks with different quantities of Nafion in the ink; (b) the corresponding normalized CV curves

Based on the above, a formulation for ink composed of 75 mg LSMO, 15 mg VXC-72, 15 mg Nafion in 6 mL deionized water is preferable for comparison consideration.

3.5.3.11. Effect of synthesis route of the catalysts

Three processes are applied to synthesize LSMOs, including citrate solution process during which calcination is undergoing either in air or oxygen atmosphere, and carbonate

coprecipitation process calcination in oxygen. We now observe the onset of reduction current around -0.2 V. Taking LSMO0.3 calcined at 900 °C from three processes for comparison as presented in Figure 3-42. It shows that calcination in oxygen exhibits a little higher oxygen reduction activity than that in air, and citrate solution process shows the best performance.

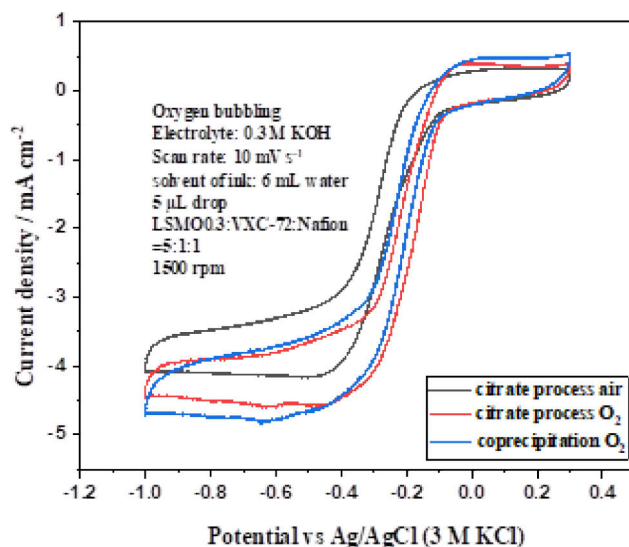


Figure 3-42 : CV curves of LSMO0.3 calcined from three processes

3.5.3.12. Effect of calcination temperature

As is mentioned above, higher capacitive effect generally shows more positive onset potential, which is also seen in Figure 3-43(a). After normalization the capacitive effect, we can compare the effect donated from electrochemical performance. LSMO0.3 synthesized from citrate solution process calcined in air at different temperatures are characterized by BET, for recalling, their surface areas are listed as below:

Table 3-8 : Surface area of LSMO0.3 obtained from calcination at different temperatures in air

Temperature (°C)	700	800	900	1100
Surface area (m ² g ⁻¹)	23.8	19.7	8.78	0.921
Surface area of nitric acid treated VXC-72 is 232 m ² g ⁻¹				

Calcination temperature has an evident effect on surface area. While compared to the surface area of VXC-72, they are much lower.

From Figure 3-43(a), the surface area between LSMO0.3 calcined at 800, 900, 1100°C does not bring about much difference in the aspects of capacitive effect. But a catalytic affect is associated also to the carbon area. We considered that the capacitive effect is due to the carbon only. So, we normalized the curves to the capacitive effect to be sure that all electrodes are related to the same surface of carbon.

After this normalization we can see that the best catalytic effect is observed for the sample obtained at 800°C because of its highest ORR onset potential as shown in Figure 3-43(c). This may be a compromise between the good crystallinity of the perovskite (as seen by the width of the X-ray diffraction peaks) and a high surface area as measured by BET).

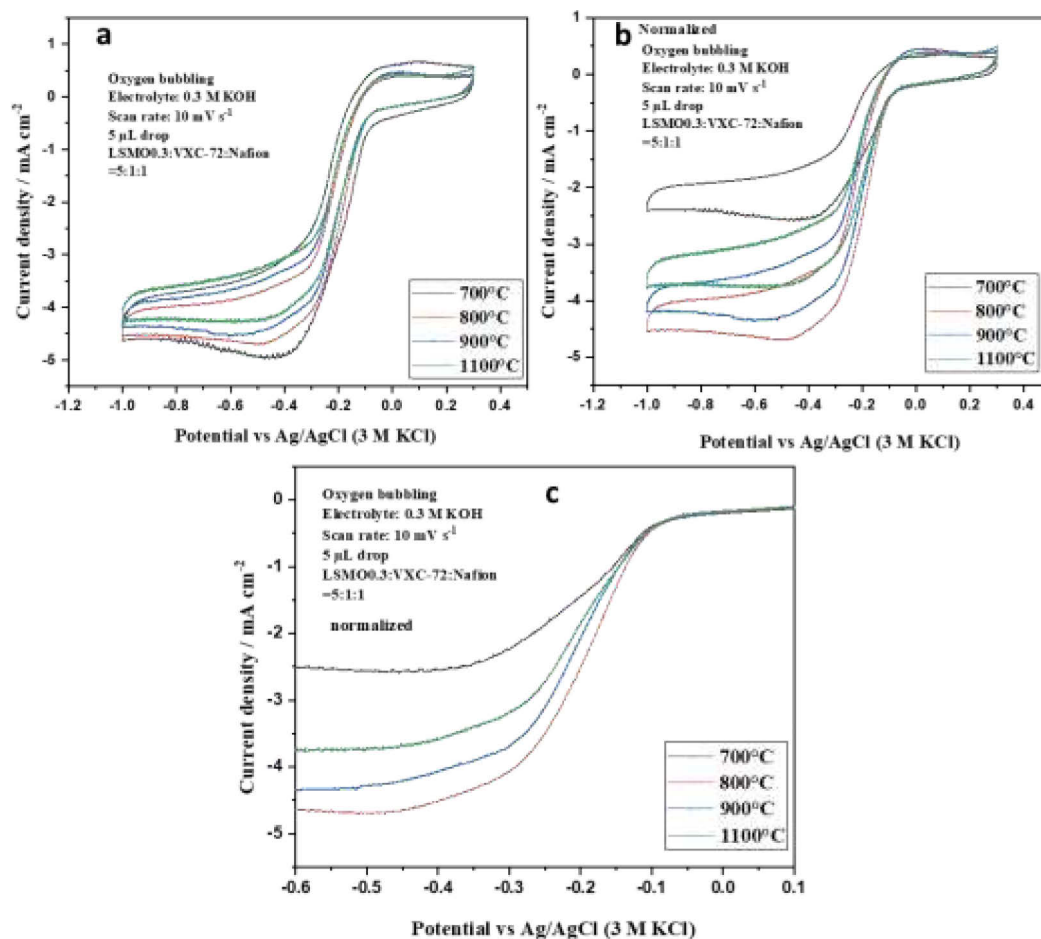


Figure 3-43 : (a) Original CV curves of LSMO_{0.3} synthesized from citrate solution process calcined in air at different temperatures; (b) the corresponding normalized CV curves; (c) the subsection of curve from negative scan in the range of -0.6 - 0.1 V

3.5.3.13. Effect of strontium doping

For this series of experiments, LSMOs with different strontium doping ratios from 0 to 0.5 are synthesized from citrate process and calcination at 900 °C in air at the same time. The mixture of 75 mg of LSMO, 15 mg VXC-72, 15 mg Nafion (125 μL Nafion solution) is dispersed in 6 mL deionized water. After mixing and sonication, 5 μL inks are dropped on the glassy carbon disk. The CV curves are obtained under O₂ bubbling and 1500 rpm.

Strontium doping brings about significant difference in capacitive effect as shown in Figure 3-44(a). After normalization of the capacitive effect, the difference of electroactivity between each other can be compared. They show around 0.1 V difference of the potential at

normalized current density of 0.75 mA cm^{-2} as presented in Figure 3-44(c). The compound with $x=0.3$, LSMO0.3 exhibits the highest activity. The performance between LSMO0.2 and LSMO0.4 is similar, so is among LSMO0, LSMO0.1, LSMO0.5.

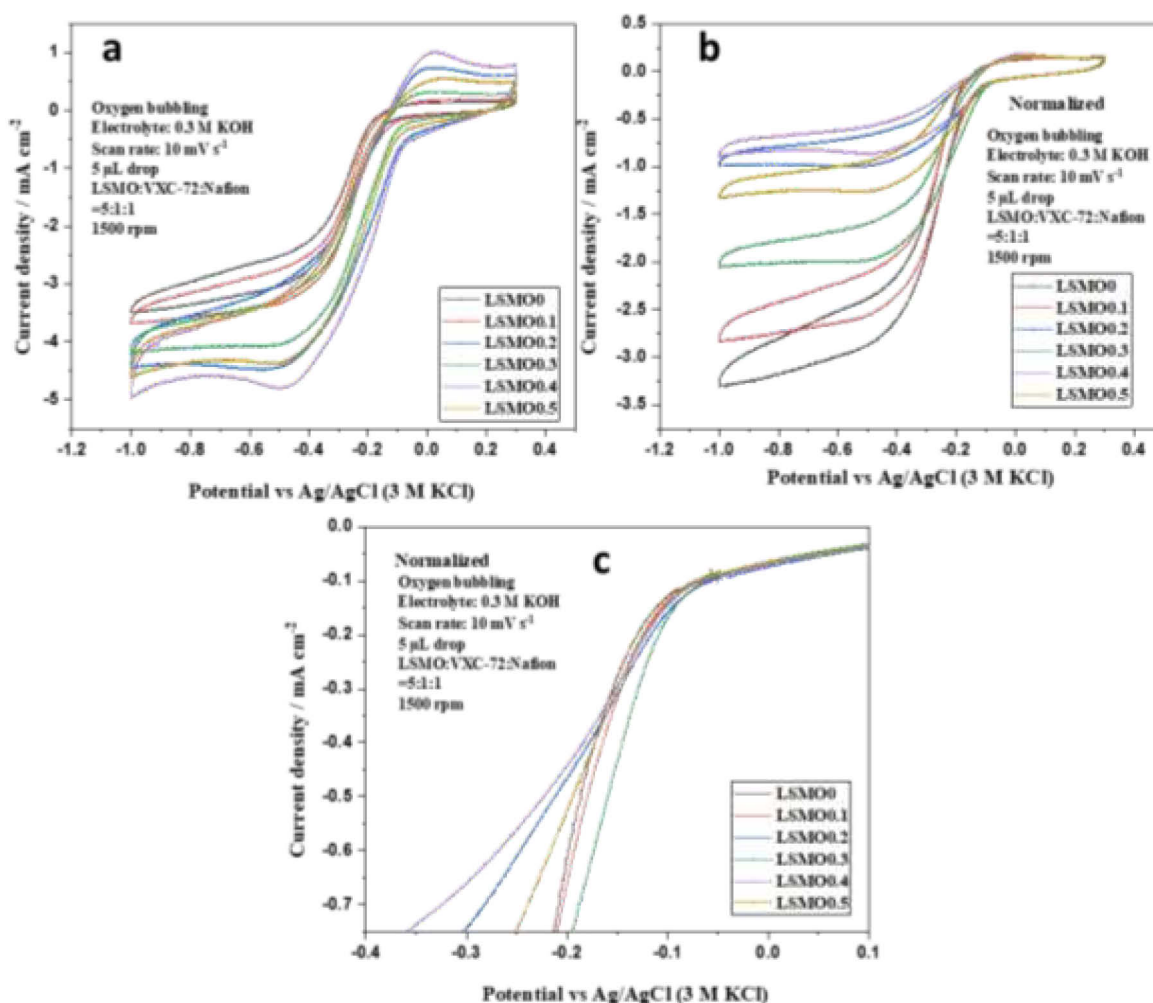


Figure 3-44 : (a) Original CV curves of LSMOs with different Sr doping synthesized from citrate solution process calcined in air at different temperatures; (b) the corresponding normalized CV curves; (c) the subsection of curve from negative scan in the range of -0.4 - 0.1 V

The Tafel slopes obtained from plot (logi-potential) in Figure 3-45 are around $-160 \pm 10 \text{ mV dec}^{-1}$, except for the case of LSMO0.3 which is -127 mV dec^{-1} . The slopes of the cases LSMO0, LSMO0.1, and LSMO0.5 are close, so are those of LSMO0.2 and LSMO0.4. Assumed that ORR has the same reaction mechanism on all the LMSOs, difference in Tafel slopes could therefore be concluded from different charge transfer coefficient α according to the simplified equation of Tafel slope $\frac{2.3RT}{\alpha nF}$, [382] The first electron transfer is the rate determining step which is also commonly accepted in articles.

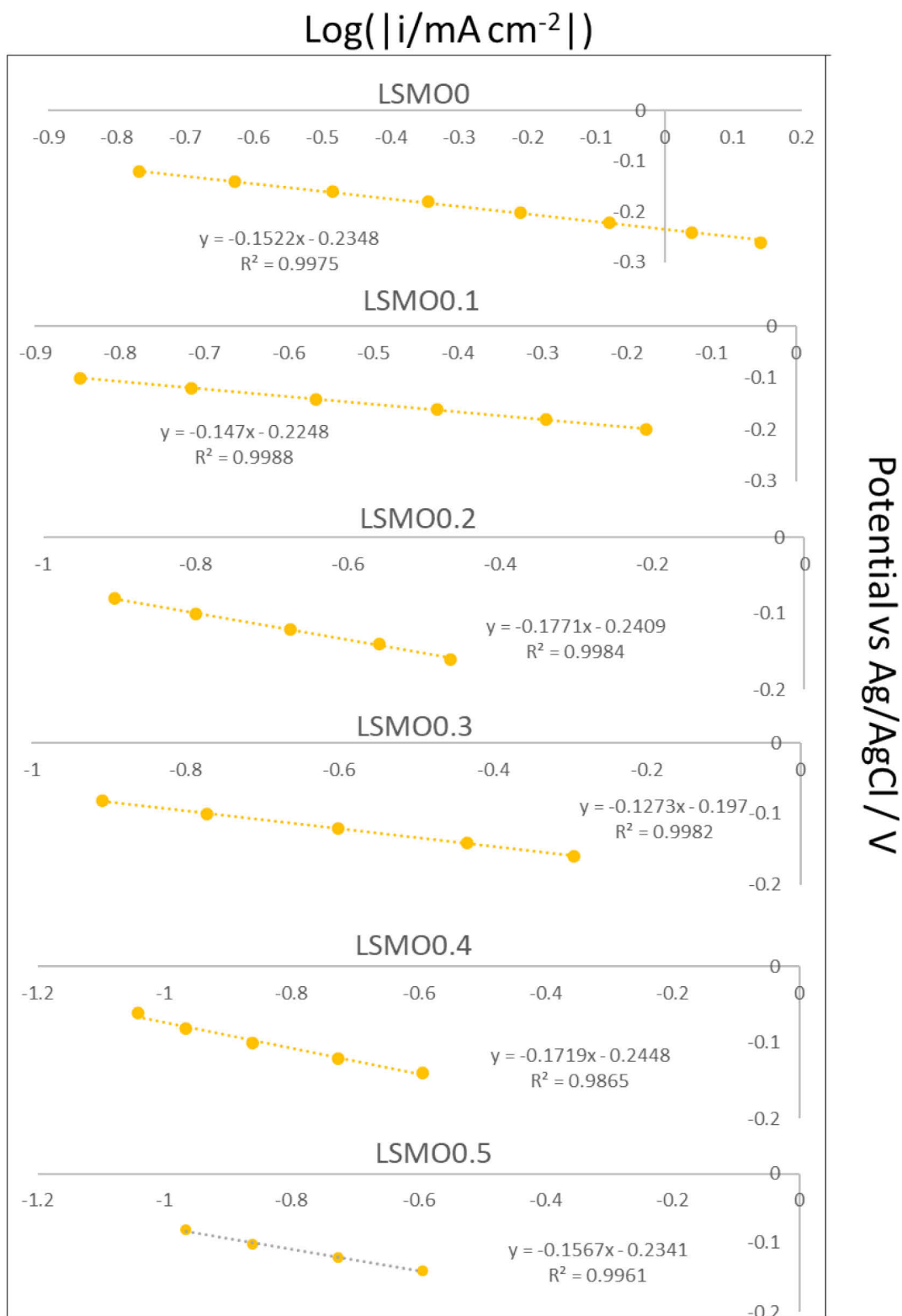


Figure 3-45 : Tafel slope comparison between LSMOs with different Sr doping based on CV curves from Figure 3-44

3.5.4. Conclusion

Based on the studies on LSMO characterization, it is concluded that ink-RDE characterization method is a very sensitive experiment. If not well controlled, the experimental error may be greater than the difference among them.

We optimized a method for mixing and formulating inks and obtained reproducible data.

For optimization of the ink formulation, an appropriate selection of carbon material, material composition, drop volume on the disk can be decided. Too much catalyst, or carbon material would increase the capacitive effect.

The first scans of the LSMO inks are different from the following scans because of the original adsorption state of the electrode. The scan rate of 10 mV s^{-1} and the way for normalizing the current density is rationalized. The capacitive effect and redox reaction effect both exist in the anodic current at potential of 0 - 0.2 V.

For the catalysts synthesized from different processes, the ones calcined in oxygen shows higher ORR activity than those calcined in air. Citrate solution process can obtain better crystallized structures and less impurities, which also contributes to its better performance for ORR activity. Calcination temperature generates evident difference in the surface area. Calcination at 800 - 900 °C appears as good compromise between good activity and good surface area.

For the doping content, Strontium doping with an atomic ratio of 0.3 to lanthanum (i.e., $\text{La}_{0.7}\text{Sr}_{0.3}\text{MnO}_3$) shows the best catalytic activity.

All these formulations studies made for rotating disk electrode and optimization of the analytical studies can be useful for the formulation of true membrane electrode assemblies that we are going to show in the next paragraph.

3.6. Air electrode and zinc-air battery assembly

In rechargeable batteries or fuel cells, air electrode is commonly composed of:

- 1) A catalyst layer containing catalyst particles for ORR and OER, carbon particles and ionomers. This layer must be hydrophilic to allow access of the electrolyte at the triple interface (ions-gas-electrode).
- 2) A gas diffusion layer (GDL) which is hydrophobic. This is a porous layer that allows the gases to access to the electrode but prevents the electrolyte to leak out and to soak the porosity.

- 3) A current collector that collects charges. It can also be a Nickel support (grid or foam) that will be active for OER reactions. In this case the Nickel grid is in the inside near the electrolyte of at least intermediate between the hydrophilic catalyst layer and the hydrophobic GDL, so that it is soaked in the electrolyte.

There are two-electrodes and three-electrodes configuration for zinc-air batteries or fuel cells, ORR and OER both take place on the air electrode during charge-discharge cycles. In three-electrodes configuration, ORR and OER are separately performed on different electrodes, which generally improves the problem of short cycle-life of two-electrodes configuration, though with the sacrifice of configuration and operation complexity.

Carbon materials are responsible for electron conducting and ionomers are for binding the materials and ionic conducting. The materials can be physically or chemically combined. The former cases are commonly seen in the conventional electrode formulation with metal oxides catalysts and the latter are usually seen in the carbon-based catalysts.

There are carbon based and metal based GDLs. The latter ones show better electrical conductivity and oxidative stability than the former. Carbon based GDLs face the disadvantage of oxidative corrosion attributed to intrinsic reductive property of carbon material, while metal substrates avoid this issue well by formation of the metal oxide or hydroxide, which are hard to be oxidized. Graphitization of carbon powders enhance its corrosion resistance [383].

In general, the suitable hydrophilicity or hydrophobicity of the material in the air electrode determines the catalytic activity and stability. Besides, conductivity is another requisite for air electrode. These conditions can be realized by adding hydrophobic polymers like Polytetrafluoroethylene (PTFE), polyvinylidene difluoride (PVDF) and/or fluorinated ethylene propylene (FEP) to GDL with impregnating method. Different kinds of hydrophobic agents and different quantities used will affect the degree of the hydrophobicity. Figure 3-46 presents the main polymers utilized as binder in lithium-air batteries.

PTFE is commonly used in air electrode formulation of its very good resistant to alkaline electrolytes, oxidation, and high hydrophobicity. Hydrophilic membranes can be obtained by mixing PVDF with carbons or oxides in lower concentration (10 - 30%) and hydrophobic performance in higher PVDF concentrations (30 - 70%) [384]. Many manufacturers realize membranes with gradients of hydrophobicity because it is easier to attach 5 layers with a small difference of composition than two rather different layers.

There are various methods to realize the integration of the layers, including mechanical and chemical attachment, e.g., pressing, direct coating and sputtering, hydrothermal treatment, electrodeposition, electrospinning, etc. The mechanical attachment outweighs in the respective

of convenient operation, though faces the problem of weak physical contact, which causes high interface electronic transfer resistance. Overall good integration of the layers should be ensured for the good contact between the layers and the porous structure.

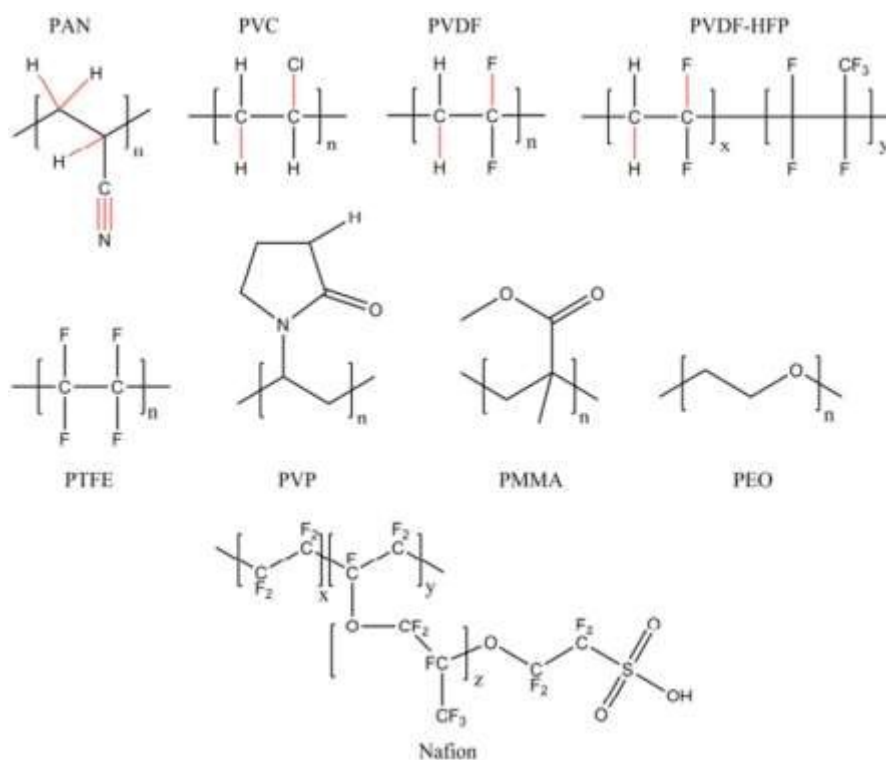


Figure 3-46 : The main binders applied in lithium-air batteries [385]

3.6.1. PTFE used as the binder used in air electrode

Lithium-ion batteries are the most popular commercialized batteries. PTFE and PVDF are widely used as binder in lithium-ion batteries [386, 387]. They are also effective to be applied for the zinc-air batteries, commonly used in academic studies. Table 3-9 is a simple collection of the application of PTFE in air electrode where PTFE can be used either in catalytic layer or GDL.

Table 3-9 : Air electrode formulations of alkaline metal-air rechargeable batteries

Catalytic layer	GDL	current collector	Attachment	Ref
PTFE (1%): acetylene black: catalyst = 10:40:50 wt.%	Purchased	Nickel foam	Pressure 4 MPa for 30s	[312]

Catalyst : Super P : 5% Nafion solution (5%) = 7 :7 :6	Activated carbon and PTFE	Nickel foam	Coating	[388]
PTFE (10%), catalyst and Vulcan XC 72	Carbon and PTFE	Nickel mesh	Rolling	[383]
PTFE (10%), catalyst and Vulcan XC 72	Carbon and PTFE	lead-plated copper screen	Rolling	[389]

3.6.2. PVDF-HFP used as the binder in air electrode

PVDF is conventionally used as binder in the lithium-ion batteries [390]. With the development of Li-O₂ batteries, it is widely used in Li-O₂ as well. While it is reported that PVDF would undergo degradation in Li-O₂ batteries resulting in the formation of LiF [391-393]. The fluorinated derivatives of PVDF, PVDF-HFP is also applied as binder in lithium-ion batteries, in electrode, electrolyte or separator [394-396]. As a copolymer of PVDF and HFP (hexafluoropropylene): the -PVDF group is quite crystallized, offering a good quality of mechanical strength, the -HFP group containing F atom with strong electronegativity, capable of enlarging the amorphous region in polymer matrix, facilitating for higher concentration of charge carriers, and capturing lithium ions to migrate within the disorder region, thus providing good ionic conductivity. It is investigated that the electrochemical behaviors of PVDF-HFP electrodes achieved the best with a mass ratio of around 2.5 - 5% in the cathode of lithium-ion battery [390]. The HFP content in PVDF-HFP, the removal method of an ancillary plasticizer (propylene carbonate (PC), di-n-butyl phthalate (DBP)), are proved to have little influence on the discharge capacity and rate capability of positive electrode of lithium-ion battery. Porosity decrease is not a decisive factor that deteriorate the performance of electrode of lithium-ion batteries [394]. PVDF-HFP is also succeeded for application in cathode, electrolyte, or separator of Li-O₂ batteries and fuel cells due to the good air permeability and ionic conductivity [385, 397-399]. Table 3-10 lists some cases of PVDF-HFP or PVDF application as binder in cathode of Li-O₂/air batteries. Pan et al. [398] compared the performance of three electrodes using three binders, PVDF-HFP, PFTE, and Nafion, respectively, in the alkaline-acid direct ethylene glycol fuel cells. It was revealed that the cathodes with PVDF-HFP as binder showed the best performance either in the cycle test or the power density. It was indicated that the low ohmic resistance of PVDF-HFP from its intrinsic porous property was the key for enhancing the anodic reaction kinetics.

The application of PVDF-HFP is rarely reported in other metal-air batteries, especially applied as binder in the cathode. It was utilized as binder in the zinc electrode of a zinc-air solid rechargeable battery [400]. In the following work, we aim to have a research about the effect of PVDF-HFP as a binder in the air electrode of zinc-air battery from a functional and economic standpoint of view. To make a porous electrode, we apply DBP as a plasticizer and ether to extract it. Besides, air electrode using PTFE as binder will also be formulated and compared.

Table 3-10 : PVDF-HFP or PVDF as binder used in Li-O₂/air batteries

Catalytic layer	Current collector	Attachment	Ref
Carbon Super P: PVDF-HFP binder: α -MnO ₂ nanowire = 25:33:42 (mass ratio)	Aluminum mesh	Cast and dry at 120°C	[401, 402]
Ru/RuOx/ITO: PVDF-HFP = 85:15 (mass ratio), catalyst loading of 0.9±0.1 mg cm ⁻²	Carbon coated GDL	Deposition using a doctor blade technique	[403]
Active carbon materials composed of 13C (97%): PVDF (Kynar 2801) = 90:10 (mass ratio), catalyst loading of 1 mg cm ⁻²	Ni-mesh	Cast	[404]
Resorcinol-formaldehyde (RF) aerogel: α -MnO ₂ nanomaterials: PVDF = 64:16:20 (mass ratio), catalyst loading of 5 mg cm ⁻²	Ni metal foam	Electro-spraying	[405]
ZCO catalyst: SWCNTs: PVDF= 15:5:4 (mass ratio), catalyst loading of 0.6-0.8 mg cm ⁻²	Carbon paper (also served as GDL)	Coating	[393]

3.7. Zinc-air battery assembly

Two processes of formulation of the air electrode are presented. PTFE (dispersion 60% in deionized water, Sigma-Aldrich) and PVDF-HFP (Sigma-Aldrich, average Mw ~455000) are used as binder, respectively. Different quantities of binders are used in the hydrophilic

(catalytic layer) and hydrophobic layers (GDL), carbon black VXC-72 is another material in the components of the layers.

The battery setup is shown as Figure 3-47 which is a three-electrodes configuration. The winding Pt wire is the counter electrode, reference electrode is the Ag/AgCl (3 M KCl) electrode, electrolyte is the 7 M KOH-0.7 M ZnO-0.7 M LiOH solution (40 mL). The working electrode is the air electrode which is inserted in the bottom part of the setup and it is put between two nickel rings which is served as current collector. There is a small chamber under the air electrode where oxygen is introduced and flowed out. The air electrode is cut into a circle with a diameter of 3 cm. The potential is scanned in the range of -1-0.5 V or -0.5 - 0.5 V vs Ag/AgCl (3 M KCl) with a scan rate of 10 mV s⁻¹.

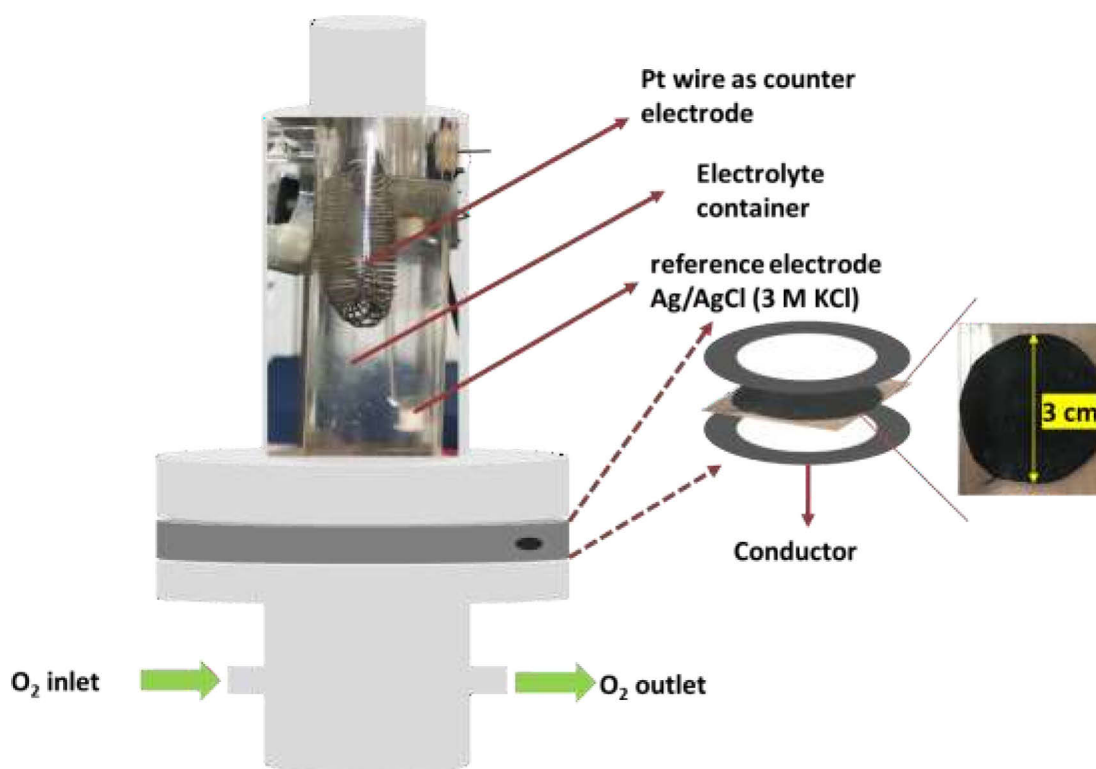


Figure 3-47 : Setup for air electrode installation

3.7.1. Air electrode formulation with PTFE as the binder

The PTFE used is a suspension dispersed in deionized water. For the hydrophobic layer, 2.5 g suspension, 2.5 g carbon black VXC-72 and some deionized water are mixed well using a magnetic mixer. For the hydrophilic layer, 1.0 g active carbon (Norit GSX, Alfa Aesar), 1.35 g MnO₂ which is the active material for the oxygen reactions, 1.75 g carbon black VXC-72, 0.9 g PTFE and some deionized water are mixed. Then the mixture undergoes centrifugation to separate and remove the water under the conditions of a rotation speed of 5000 rpm and a time duration of 10 mins. After removing the centrifuged water, the solid part is dried in oven at 140

°C. Then the dry solid obtained are rolled using stainless steel roller with some droplets of acetone to get two homogeneous layers as shown the insertion of Table 3-11 where compositions of the layers are also listed. The hydrophilicity is roughly tested by a drop of water and the permeability is tested by a drop of ethanol. Both layers have good permeability which is proved by rapid adsorption of ethanol on both layers. The contact angle of water on catalytic layer is less than 90° and on GDL is larger than 90°, which means the hydrophilicity is as expected.

Table 3-11 : Compositions in the two layers of air electrode using PTFE as binder

Layer	Components	Percentage /%	Mass/g	Total mass of paste	
Hydrophobic layer	PTFE	50	2.5	5	
	Carbon black	50	2.5		
Hydrophilic layer	Active carbon	20	1.0	5	
	MnO ₂	27	1.35		
	Carbon black	35	1.75		
	PTFE	18	0.9		

The two layers are separately put between two flat heavy metals, then they all are put in oven at 185 °C for 3 hours, after which, the layers are pressed under 10 tons of pressure using a presser to get thinner and stronger layers. The two layers are inserted in two pieces of nickel grid and the layers and the nickel grids are cut into the same round shape shown in Figure 3-48. The layers are then put between two flat heavy metals in the oven at 160 °C overnight before ready to conduct the cyclic voltammetry experiment, the final thickness of the air electrode is 0.5 mm.

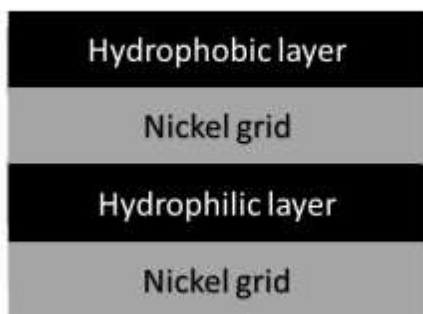


Figure 3-48 : Schematic of the layers (left) and the photo of the obtained air electrode (right)

3.7.2. Air electrode formulation with PVDF-HFP as the binder

The PVDF-HFP pellets are firstly dissolved in acetone to get a solution with a mass to volume ratio of 15% (m/V). Plasticizer DBP is accompanied to generate pores in the layers formulated with binder PVDF-HFP. Different with PTFE suspension, PVDF-HFP acetone solution could be mixed with the carbon material and catalyst with the composition as listed in Table 3-12, to obtain a homogeneous ink. Then a doctor blade capable to adjust the thickness is used to make a uniform layer with thickness of 250 μm which is the maximum limit, though still much thinner than that formulated using PFTE as binder especially when the layer is dry in air and the thickness is around 140 μm .

Table 3-12 : Compositions in the two layers of air electrode using PVDF-HFP as binder

Layer	Components	Percentage/%	Mass/g
Hydrophobic layer	PVDF-HFP	54.13	0.708
	DBP	38.23	0.5
	VXC-72	7.64	0.1
Hydrophilic layer	MnO ₂	56.05	0.88
	VXC-72	5.99	0.094
	PVDF-HFP	15.03	0.236
	DBP	22.93	0.36



To enhance the mechanical strength of the electrode, ten pieces of the dry hydrophilic and hydrophobic layers are piled and put on two sides of the nickel foam, respectively, presented as Figure 3-49. Then followed is the heat-press treatment of the whole using an electronic iron for 5 s. The nickel foam is pretreated by firstly immersion in a dilute PVDF-HFP acetone solution (2 g PVDF-HFP dissolved in 100 mL acetone) and then heating in oven

at 400 °C for 5 minutes for better binding between both layers and the nickel foam. The combined layers and the nickel foam are cut together into a round shape similar to the above. Then electrode is immersed in ether for 2 minutes to extract the DBP in the layers. Detachment would happen after this operation; press would then be imposed to get the layer attached again. The final obtained air electrode has a thickness of 0.3 mm.

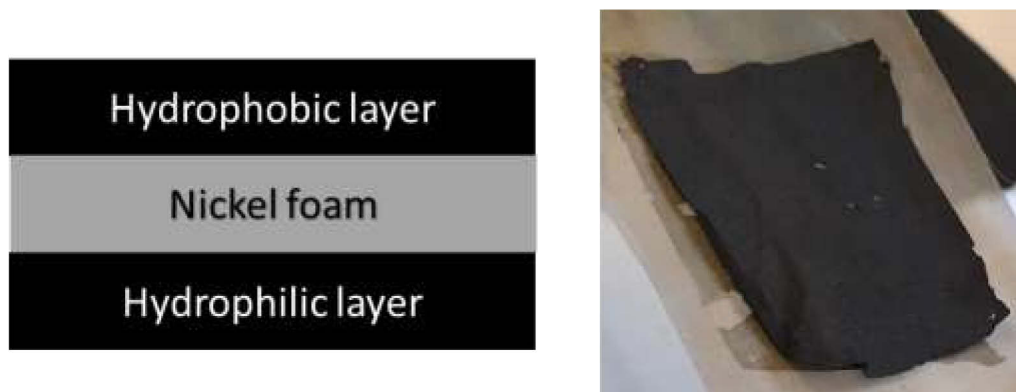


Figure 3-49 : Schematic of the layers (left) and the photo of the obtained air electrode (right)

3.7.3. Zinc-air battery setup

The static zinc-O₂ battery is also realized in the same setup as shown in Figure 3-50. Zinc electrode is a straight copper wire; air electrode is the one formulated with PVDF-HFP and the synthesized catalyst La_{0.7}Sr_{0.3}MnO₃; the electrolyte is 7 M KOH-0.7 M ZnO-0.7 M LiOH. Oxygen is introduced and flows out from the bottom part of the setup. The galvanostatic charge-discharge cycles with two-electrodes are conducted on the mode of galvanostatic cycling with potential limiting (GCPL) and coulombic efficiency determination (CED). The results are presented in Figure 3-51. Firstly, the battery is charged for zinc deposition on the copper wire at 5 mA for 30 mins, then several cycles of discharge-charge are set at different currents of 2, 5, 10, 20, 50 mA with a potential limitation between 0.5 - 2 V. When the applied current is at 2 and 5 mA, the battery undergoes well after 4 cycles of discharge-charge at each current. The overpotential is higher at higher current of 5 mA than at 2 mA. When the current increases to 10 mA, the discharge process breaks down a little, while the charge process works normally except with higher overpotential. Then at 20 mA, the battery is totally in failure that both discharge and charge processes reach the potential limits at the very beginning of the imposition of current of 20 mA.

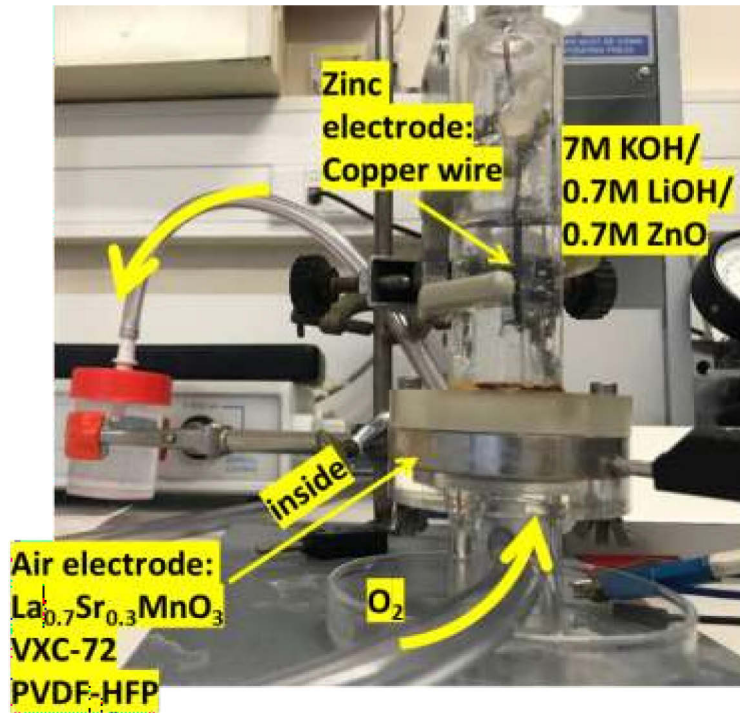


Figure 3-50 : Photo of the zinc-O₂ battery

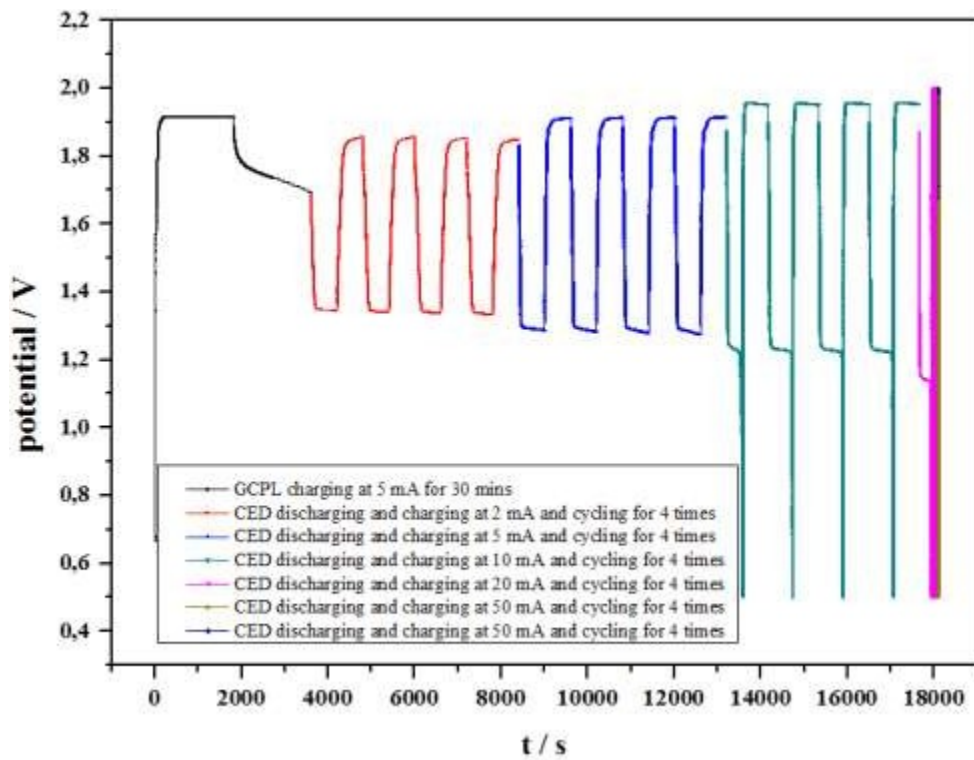


Figure 3-51 : Galvanostatic discharge-charge cycles at different currents

3.8. Conclusion

In this chapter, the catalysts and the catalytic mechanism proposed for ORR and OER are firstly introduced, then perovskite oxides as catalysts are emphasized. There are large amounts of reported perovskites performing superior activity towards ORR or OER, characterized by linear sweeping voltammetry (LSV) while not many conducting cyclic voltammetry (CV) included. In this work, a well-known perovskite $\text{La}_{1-x}\text{Sr}_x\text{MnO}_3$ (LSMO) is synthesized with different routes, calcination temperatures and atmosphere. They are characterized by XRD, SEM, BET to get the phase profile, morphology, and specific surface area.

Generally, much pure phases are obtained from citrate solution route above 500 °C. Calcination temperature has a big influence on the specific surface area, which is basically decrease with temperature in the range studied (700 - 1100 °C). The morphology of the LSMOs synthesized from citrate solution route are similar, and different from that from that obtained from coprecipitation route.

Cyclic voltammetry is emphasized to characterize the electrochemical performance of LSMOs, especially the ORR catalysis. An ink formulation was optimized for this study and could allow the comparison between LSMOs calcined at different temperatures and with different strontium doping ratios.

LSMOs alone shows good ORR catalytic activity. But the conduction introduced by carbon additives largely increases the redox effect of LSMOs. Among different strontium doping ratios, the one with an atomic ratio of 0.3 to lanthanum (i.e., $\text{La}_{0.7}\text{Sr}_{0.3}\text{MnO}_3$) shows the best catalytic activity.

Two trials of fabrication air electrodes with two kinds of binders are presented, for the convenience of thickness control, the fabrication with PVDF-HFP is preferable. As for the battery assembly, it also has potential for application as binder in metal-air batteries. While the overall performance should be further developed, especially from the engineering standard point of view.

Chapter 4 Overall conclusion and perspective

4.1. Overall conclusion

This essay deals with the conventional issues involved in zinc-air battery, spread into two main parts: zinc electrode and air electrode.

Detailed literature surveys about the zinc electrode are as follows: the mechanism of zinc dissolution from perspective of the intermediate dissoluble species, and the passivated film formation; the mechanism of zinc dendrite initiation and growth from both experimental and modelling work; the problems existed in zinc electrode performance; the common trials for suppressing the problems; several experimental zinc-air flow battery demonstrations. Through the earlier studies about the fundamental issues of zinc electrode, namely the related mechanisms, it is found that the theoretical accordance is often hard to achieve by all. And the later studies are more located to the application improvement based on a variety of different electrode forms including zinc plates, zinc powder pastes, etc. Either for the theory or the application aimed research, different materials or setups are important in the view of experimental design for better observation, variables controlling, or of adjusting to flexibility for application.

In the study for zinc electrode, zinc dendrite growth and hydrogen evolution are the main related problems. The effects of compositions in electrolyte including LiOH and a large range of different concentrations of ZnO are studied. The hydrodynamic condition of electrolyte is also emphasized, accompanied by the current imposed on zinc electrode. Under those systematic considerations, zinc deposition-dissolution process is researched in detail with two homemade setups targeting the static and flowing cases, respectively. Zinc plates with different sizes are used in these two setups.

- One in a static condition, so that only the diffusion is ensured, the slight convective effect could be only from hydrogen evolution.

- One in the flow case with a setup size which is even suitable for industrial application.

The evolution of zinc deposition-dissolution is observed in-situ using a microscope. The galvanostatic cycles are mainly conducted to process the zinc deposition-dissolution via a potentiostat.

The results show that the component LiOH in electrolyte 7 M KOH-0.7 M ZnO-0.7 M LiOH has no evident effect either on the zinc deposition process observed under a microscope, or the corresponding response from chronopotentiometry experiment. Higher current density imposed on the electrode and electrolyte with lower zincate concentration will cause more dendrite in a shorter time. The morphology of zinc dendrite is also sharper in electrolytes with low zincate concentration. While hydrogen evolution occurs more easily at lower current density and in electrolyte with lower zincate concentration. The occurrence of hydrogen evolution is more dependent on the potential. The evolved hydrogen either adsorbed on the electrode or desorbed from electrode plays a role in morphology change of electrode surface, from the perspective of surface area decrease and local convection introduction, respectively. Flowing electrolyte can effectively depress the zinc dendrite growth, but hydrogen evolution also aggravates with flowing electrolyte. The rate of deposition and dissolution of zinc which is indicated by the area increase and decrease shown in the pictures taken by the assembled camera, is found to be linear with time.

For the air electrode, the mechanisms for oxygen electrocatalysis are introduced in detail. The proposed 'descriptors' are also expanded. For this surface sensitive reaction, electronic effect, structure effect, and morphology effect can have a great impact on the catalytic activity. Through controlling the growth of single-crystal catalyst to expose different facets or sizes, alloying with other metals to adjusting the electronic effect as well reducing the cost, new materials designing and improving etc., a variety of oxygen catalysts have been reported. Among them, perovskite oxides especially lanthanum manganese oxides and the strontium doped ones are widely studied owing to their good activity based on the e_g filling near to 1.

For activity characterization of the catalysts, the onset potential for ORR in linear sweep voltammetry curve, or the potential at a given current is commonly even uniquely used as the comparative metric. Whereas few paid attentions on the cyclic voltammogram. As in our case, the cyclic voltammograms result in difference not only between the onset potential for ORR, but also between the shape of the curves which may indicate some other reactions occurring on the surface of electrode or indicate the pseudocapacitive effects with different catalysts. And these differences may further decide the onset potential to some extent. This work deals mostly

with the cyclic voltammetry results, and a normalization method is proposed for the comparison of different catalysts.

Firstly, a systematic catalyst synthesis work has been done. LSMOs are synthesized from three routes, citrate solution process calcined in air or oxygen, and coprecipitation process calcined in oxygen. The related physical properties are characterized with XRD, BET and SEM. Powders obtained from citrate solution process either calcined in air or oxygen are easier to have crystallized phases than those from coprecipitation process. The morphology between solution route and precipitation route is different, the former presents more holes on surface, while the latter is denser block-like. Calcination temperature makes a big difference on the BET surface area.

Then detailed investigations of catalytic activity of LSMOs are conducted including the ink preparation, ink composition optimization and comparison between different LSMOs. We stressed the importance of the formulation and mixing method to obtain reproducible results. We observed that the catalyst properties are amplified by the addition of carbons which yields a better electronic conductivity. The contribution of capacitive effect and redox effect to the measured current is quantified. The normalization is based on the current at a potential where near pure-capacitive effect is detected. Among LSMOs, strontium doping ratio of 0.3 exhibits the best performance.

Further step to application in a battery, two air electrode formulations with LSMO0.3 as the catalytic material, VXC-72 as carbon material and PTFE or PVDF-HFP as binder material are fabricated. Accompanied with a copper wire as the collector at the zinc electrode, a whole zinc-air battery is installed starting in a discharged state with zinc oxide dissolved in an alkaline KOH electrolyte.

We formulated hydrophobic and hydrophilic electrodes with PVDF. Under galvanostatic cycling, the battery works well under low current, while becomes inactive under high current. The air electrode is yet to be improved.

4.2. Perspectives

This work combines engineering and fundamental research, many interesting phenomena have been recovered which will become the future work. Even though at beginning a zinc-air flow battery was the target and we also have tried to install the flow setup, time could be less spared on this before we tried our best to understand the cyclic voltammograms.

Also, the short time allowed for this PhD and the difficulties associated to the period of COVID made experiments very difficult. We compensated with a large literature survey.

It is highly recommended using cyclic voltammetry to compare catalysts for ORR catalysis rather than only linear sweep voltammetry. Reproducibility of the experiments should be emphasized, and CV is a better way than LSV to show the reproducibility. A more convincing and universal method for ORR catalytic activity characterization is still suspended. Not only the effective surface area that commonly mentioned in articles is important, the effect from the accompanied redox reactions is also necessary to be taken into consideration, regarding characterizing the activity of perovskite oxides for ORR catalysis.

The air electrode formulation suitable for zinc-air battery assembly should consider both performance and cost. Using PVDF-HFP as binder could be very interesting, which is undergoing in the lab. For zinc-air flow battery realization, there remains more engineering problems, especially for preventing leakage at the air electrode assembly.

Reference

- [1] Dunn, B., H. Kamath, and J.-M. Tarascon, Electrical Energy Storage for the Grid: A Battery of Choices. *Science*, 2011. **334**(6058): p. 928.
- [2] IEA. market analysis and forecast from 2019 to 2024. 2018 [cited 2020 08.27]; Available from: <https://www.iea.org/data-and-statistics/charts/renewable-capacity-growth-by-country-region-2018-2024>.
- [3] Khodadoost Arani, A.A., G. B. Gharehpetian, and M. Abedi, Review on Energy Storage Systems Control Methods in Microgrids. *International Journal of Electrical Power & Energy Systems*, 2019. **107**: p. 745-757.
- [4] 2019 [cited 2020 08.27]; Available from: <https://www.energy.gov/sites/prod/files/2019/07/f64/2018-OTT-Energy-Storage-Spotlight.pdf>.
- [5] Ibrahim, H., A. Ilinca, and J. Perron, Energy storage systems—Characteristics and comparisons. *Renewable and Sustainable Energy Reviews*, 2008. **12**(5): p. 1221-1250.
- [6] Zhang, C., et al., Energy storage system: Current studies on batteries and power condition system. *Renewable and Sustainable Energy Reviews*, 2018. **82**: p. 3091-3106.
- [7] Kent, R., Energy Management in Plastics Processing: Strategies, Targets, Techniques, and Tools. 2018: Elsevier.
- [8] Sufyan, M., et al., Sizing and applications of battery energy storage technologies in smart grid system: A review. *Journal of Renewable and Sustainable Energy*, 2019. **11**(1): p. 014105.
- [9] Laslett, D., Can high levels of renewable energy be cost effective using battery storage? Cost of renewable energy scenarios for an isolated electric grid in Western Australia. *Renew. Energy Environ. Sustain.*, 2020. **5**.
- [10] IEA. Battery storage is (almost) ready to play the flexibility game. 2019 [cited 2020 08.27]; Available from: <https://www.iea.org/commentaries/battery-storage-is-almost-ready-to-play-the-flexibility-game>.
- [11] Yang, Y., et al., Battery energy storage system size determination in renewable energy systems: A review. *Renewable and Sustainable Energy Reviews*, 2018. **91**: p. 109-125.
- [12] IEA. Technology mix in storage installations excluding pumped hydro, 2011-2016. 2019 [cited 2020 08.27]; Available from: <https://www.iea.org/data-and-statistics/charts/technology-mix-in-storage-installations-excluding-pumped-hydro-2011-2016>.
- [13] May, G.J., A. Davidson, and B. Monahov, Lead batteries for utility energy storage: A review. *Journal of Energy Storage*, 2018. **15**: p. 145-157.
- [14] Divya, K.C. and J. Østergaard, Battery energy storage technology for powersystems—An overview. *Electric Power Systems Research*, 2009. **79**(4): p. 511-520.
- [15] Ziegler, M.S., et al., Storage Requirements and Costs of Shaping Renewable Energy Toward Grid Decarbonization. *Joule*, 2019. **3**(9): p. 2134-2153.
- [16] Chau, K.T., Y.S. Wong, and C.C. Chan, An overview of energy sources for electric vehicles. *Energy Conversion and Management*, 1999. **40**(10): p. 1021-1039.
- [17] Rahman, M.A., X. Wang, and C. Wen, High Energy Density Metal-Air Batteries: A Review. *Journal of The Electrochemical Society*, 2013. **160**(10): p. A1759-A1771.
- [18] Gorman, S.F., Development and operation of an electrically rechargeable zinc-air flow battery. 2017, University of Southampton.

- [19] Chen, X., et al., Recent Advances in Materials and Design of Electrochemically Rechargeable Zinc–Air Batteries. *Small*, 2018. **14**(44): p. 1801929.
- [20] Li, Y. and J. Lu, Metal–Air Batteries: Will They Be the Future Electrochemical Energy Storage Device of Choice? *ACS Energy Letters*, 2017. **2**(6): p. 1370-1377.
- [21] Zheng, J.P., et al., Theoretical Energy Density of Li–Air Batteries. *Journal of The Electrochemical Society*, 2008. **155**(6): p. A432.
- [22] Jörissen, L., Bifunctional oxygen/air electrodes. *Journal of Power Sources*, 2006. **155**(1): p. 23-32.
- [23] Abraham, K.M. and Z. Jiang, A Polymer Electrolyte - Based Rechargeable Lithium/Oxygen Battery. *Journal of The Electrochemical Society*, 1996. **143**(1): p. 1-5.
- [24] Xu, K., Nonaqueous Liquid Electrolytes for Lithium-Based Rechargeable Batteries. *Chemical Reviews*, 2004. **104**(10): p. 4303-4418.
- [25] Bryantsev, V.S., et al., Predicting Solvent Stability in Aprotic Electrolyte Li–Air Batteries: Nucleophilic Substitution by the Superoxide Anion Radical ($O_2^{\bullet-}$). *The Journal of Physical Chemistry A*, 2011. **115**(44): p. 12399-12409.
- [26] Visco, S.J., et al., Protected active metal electrode and battery cell structures with non-aqueous interlayer architecture. 2007, Google Patents.
- [27] Cheng, F. and J. Chen, Metal–air batteries: from oxygen reduction electrochemistry to cathode catalysts. *Chemical Society Reviews*, 2012. **41**(6): p. 2172-2192.
- [28] Wang, Y., P. He, and H. Zhou, A lithium–air capacitor–battery based on a hybrid electrolyte. *Energy & Environmental Science*, 2011. **4**(12): p. 4994-4999.
- [29] Yoo, E. and H. Zhou, Li–Air Rechargeable Battery Based on Metal-free Graphene Nanosheet Catalysts. *ACS Nano*, 2011. **5**(4): p. 3020-3026.
- [30] Peng, S.-H., H.-C. Lu, and S. Jessie Lue, Formation of Nanocrystalline Cobalt Oxide-Decorated Graphene for Secondary Lithium-Air Battery and Its Catalytic Performance in Concentrated Alkaline Solutions. *Nanomaterials*, 2020. **10**(6).
- [31] Kumar, B., et al., A Solid-State, Rechargeable, Long Cycle Life Lithium–Air Battery. *Journal of The Electrochemical Society*, 2010. **157**(1): p. A50.
- [32] Kumar, B. and J. Kumar, Cathodes for Solid-State Lithium–Oxygen Cells: Roles of Nasion Glass-Ceramics. *Journal of The Electrochemical Society*, 2010. **157**(5): p. A611.
- [33] Caramia, V. and B. Bozzini, Materials science aspects of zinc–air batteries: a review. *Materials for Renewable and Sustainable Energy*, 2014. **3**(2): p. 28.
- [34] Mainar, A.R., et al., An overview of progress in electrolytes for secondary zinc-air batteries and other storage systems based on zinc. *Journal of Energy Storage*, 2018. **15**: p. 304-328.
- [35] Su, C.-Y., et al., Atomic Modulation of FeCo–Nitrogen–Carbon Bifunctional Oxygen Electrodes for Rechargeable and Flexible All-Solid-State Zinc–Air Battery. *Advanced Energy Materials*, 2017. **7**(13): p. 1602420.
- [36] Yang, C.-C. and S.-J. Lin, Improvement of high-rate capability of alkaline Zn–MnO₂ battery. *Journal of Power Sources*, 2002. **112**(1): p. 174-183.
- [37] Zhang, X.G., Fibrous zinc anodes for high power batteries. *Journal of Power Sources*, 2006. **163**(1): p. 591-597.
- [38] Fu, J., et al., Electrically Rechargeable Zinc–Air Batteries: Progress, Challenges, and Perspectives. *Advanced Materials*, 2017. **29**(7): p. 1604685.
- [39] Ma, Y., et al., Performance of Mg–14Li–1Al–0.1Ce as anode for Mg-air battery. *Journal of Power Sources*, 2011. **196**(4): p. 2346-2350.
- [40] Liang, Y., et al., Rechargeable Mg Batteries with Graphene-like MoS₂ Cathode and Ultrasmall Mg Nanoparticle Anode. *Advanced Materials*, 2011. **23**(5): p. 640-643.

- [41] Zhang, T., Z. Tao, and J. Chen, Magnesium–air batteries: from principle to application. *Materials Horizons*, 2014. **1**(2): p. 196-206.
- [42] Sathyanarayana, S. and N. Munichandraiah, A new magnesium — air cell for long-life applications. *Journal of Applied Electrochemistry*, 1981. **11**(1): p. 33-39.
- [43] Yang, S. and H. Knickle, Design and analysis of aluminum/air battery system for electric vehicles. *Journal of Power Sources*, 2002. **112**(1): p. 162-173.
- [44] Liu, Y., et al., A comprehensive review on recent progress in aluminum–air batteries. 2017. **2**(3): p. 246-277.
- [45] Beck, F. and P. Rüetschi, Rechargeable batteries with aqueous electrolytes. *Electrochimica Acta*, 2000. **45**(15): p. 2467-2482.
- [46] Xu, M., et al., Rechargeable Zn-air batteries: Progress in electrolyte development and cell configuration advancement. *Journal of Power Sources*, 2015. **283**: p. 358-371.
- [47] Zhao, X., et al., Ultrafine SmMn₂O₅- δ electrocatalysts with modest oxygen deficiency for highly-efficient pH-neutral magnesium-air batteries. *Journal of Power Sources*, 2020. **449**: p. 227482.
- [48] Wen, H., et al., High energy efficiency and high power density aluminum-air flow battery. *International Journal of Energy Research*, 2020. **44**(9): p. 7568-7579.
- [49] Zhang, L., et al., Study of zinc electrodes for single flow zinc/nickel battery application. *Journal of Power Sources*, 2008. **179**(1): p. 381-387.
- [50] Li, Z., et al., Deep-Breathing Honeycomb-like Co-Nx-C Nanopolyhedron Bifunctional Oxygen Electrocatalysts for Rechargeable Zn-Air Batteries. *iScience*, 2020. **23**(8): p. 101404.
- [51] Hilder, M., B. Winther-Jensen, and N.B. Clark, The effect of binder and electrolyte on the performance of thin zinc-air battery. *Electrochimica Acta*, 2012. **69**: p. 308-314.
- [52] R. Mainar, A., et al., Alkaline aqueous electrolytes for secondary zinc–air batteries: an overview. *International Journal of Energy Research*, 2016. **40**(8): p. 1032-1049.
- [53] Jindra, J., J. Mrha, and M. Musilová, Zinc-air cell with neutral electrolyte. *Journal of Applied Electrochemistry*, 1973. **3**(4): p. 297-301.
- [54] Thomas Goh, F.W., et al., A Near-Neutral Chloride Electrolyte for Electrically Rechargeable Zinc-Air Batteries. *Journal of The Electrochemical Society*, 2014. **161**(14): p. A2080-A2086.
- [55] Sumboja, A., et al., Durable rechargeable zinc-air batteries with neutral electrolyte and manganese oxide catalyst. *Journal of Power Sources*, 2016. **332**: p. 330-336.
- [56] Kumar, G.G. and S. Sampath, Electrochemical Characterization of a Zinc-Based Gel-Polymer Electrolyte and Its Application in Rechargeable Batteries. *Journal of The Electrochemical Society*, 2003. **150**(5): p. A608.
- [57] Dewi, E.L., et al., Cationic polysulfonium membrane as separator in zinc–air cell. *Journal of Power Sources*, 2003. **115**(1): p. 149-152.
- [58] Li, Y. and H. Dai, Recent advances in zinc–air batteries. *Chemical Society Reviews*, 2014. **43**(15): p. 5257-5275.
- [59] Khor, A., et al., Review of zinc-based hybrid flow batteries: From fundamentals to applications. *Materials Today Energy*, 2018. **8**: p. 80-108.
- [60] Leung, P.K., et al., Membrane-less hybrid flow battery based on low-cost elements. *Journal of Power Sources*, 2017. **341**: p. 36-45.
- [61] Thomas, S., et al., Self-repairing oxides to protect zinc: Review, discussion and prospects. *Corrosion Science*, 2013. **69**: p. 11-22.
- [62] Zhu, H., P. Zhang, and S. Dai, Recent Advances of Lanthanum-Based Perovskite Oxides for Catalysis. *ACS Catalysis*, 2015. **5**(11): p. 6370-6385.

- [63] Higgins, D., et al., Activated and nitrogen-doped exfoliated graphene as air electrodes for metal–air battery applications. *Journal of Materials Chemistry A*, 2013. **1**(7): p. 2639-2645.
- [64] Lin, C., et al., Solid-State Rechargeable Zinc–Air Battery with Long Shelf Life Based on Nanoengineered Polymer Electrolyte. *ChemSusChem*, 2018. **11**(18): p. 3215-3224.
- [65] Ji, D., et al., Hierarchical catalytic electrodes of cobalt-embedded carbon nanotube/carbon flakes arrays for flexible solid-state zinc-air batteries. *Carbon*, 2019. **142**: p. 379-387.
- [66] Parker, J.F., et al., Rechargeable nickel–3D zinc batteries: An energy-dense, safer alternative to lithium-ion. *Science*, 2017. **356**(6336): p. 415.
- [67] Bass, K., et al., Methods for the reduction of shape change and dendritic growth in zinc-based secondary cells. *Journal of Power Sources*, 1991. **35**(3): p. 333-351.
- [68] Spendelow, J.S. and A. Wieckowski, Electrocatalysis of oxygen reduction and small alcohol oxidation in alkaline media. *Physical Chemistry Chemical Physics*, 2007. **9**(21): p. 2654-2675.
- [69] Li, Y., et al., Advanced zinc-air batteries based on high-performance hybrid electrocatalysts. *Nature Communications*, 2013. **4**(1): p. 1805.
- [70] Lee, D.U., et al., Recent progress and perspectives on bi-functional oxygen electrocatalysts for advanced rechargeable metal–air batteries. *Journal of Materials Chemistry A*, 2016. **4**(19): p. 7107-7134.
- [71] Patel, S. Fluidic Energy’s First Zinc-Air Battery Storage Systems Reach Five Year Milestone, Setting Performance Records and Paving the Way for Renewables Adoption. 2017 [cited 2020 08.27]; Available from: <https://www.powermag.com/press-releases/fluidic-energys-first-zinc-air-battery-storage-systems-reach-five-year-milestone-setting-performance-records-and-paving-the-way-for-renewables-adoption/>.
- [72] Sapkota, P. and H. Kim, Zinc–air fuel cell, a potential candidate for alternative energy. *Journal of Industrial and Engineering Chemistry*, 2009. **15**(4): p. 445-450.
- [73] Dirkse, T.P. and N.A. Hampson, The Zn(II)/Zn exchange reaction in KOH solution—I. Exchange current density measurements using the galvanostatic method. *Electrochimica Acta*, 1972. **17**(1): p. 135-141.
- [74] Dirkse, T.P. and N.A. Hampson, The Zn(II)/Zn exchange reaction in KOH solution—II. exchange current density measurements using the double-impulse method. *Electrochimica Acta*, 1972. **17**(3): p. 383-386.
- [75] Dirkse, T.P. and N.A. Hampson, The Zn(II)/Zn exchange reaction in KOH solution—III. Exchange current measurements using the potentiostatic method. *Electrochimica Acta*, 1972. **17**(6): p. 1113-1119.
- [76] Bockris, J.O.M., Z. Nagy, and A. Damjanovic, On the Deposition and Dissolution of Zinc in Alkaline Solutions. *Journal of The Electrochemical Society*, 1972. **119**(3): p. 285.
- [77] Hendrikx, J., et al., The electrodeposition and dissolution of zinc and amalgamated zinc in alkaline solutions. *Electrochimica Acta*, 1984. **29**(1): p. 81-89.
- [78] Muralidharan, V.S. and K.S. Rajagopalan, Kinetics and mechanism of corrosion of zinc in sodium hydroxide solutions by steady-state and transient methods. *Journal of Electroanalytical Chemistry and Interfacial Electrochemistry*, 1978. **94**(1): p. 21-36.
- [79] Chang, Y.C. and G. Prentice, A Model for the Anodic Dissolution of Zinc in Alkaline Electrolyte: Kinetics of Initial Dissolution. *Journal of The Electrochemical Society*, 1984. **131**(7): p. 1465-1468.
- [80] Chang, Y.C. and G. Prentice, Anodic Dissolution of Zinc Electrodes in Alkaline Electrolyte: Mass Transport Effects. *Journal of The Electrochemical Society*, 1985. **132**(2): p. 375-378.

- [81] Mokaddem, M., P. Volovitch, and K. Ogle, The anodic dissolution of zinc and zinc alloys in alkaline solution. I. Oxide formation on electrogalvanized steel. *Electrochimica Acta*, 2010. **55**(27): p. 7867-7875.
- [82] Bockelmann, M., et al., Electrochemical characterization and mathematical modeling of zinc passivation in alkaline solutions: A review. *Electrochimica Acta*, 2017. **237**: p. 276-298.
- [83] Sharma, S.K. and M.D. Reed, Raman study of zincate ions in concentrated alkaline solutions. *Journal of Inorganic and Nuclear Chemistry*, 1976. **38**(11): p. 1971-1972.
- [84] Cachet, C., B. Saidani, and R. Wiart, The Behavior of Zinc Electrode in Alkaline Electrolytes: II . A Kinetic Analysis of Anodic Dissolution. *Journal of The Electrochemical Society*, 1992. **139**(3): p. 644-654.
- [85] Cachet, C., U. Ströder, and R. Wiart, The kinetics of zinc electrode in alkaline zincate electrolytes. *Electrochimica Acta*, 1982. **27**(7): p. 903-908.
- [86] Cachet, C., B. Saïdani, and R. Wiart, The Behavior of Zinc Electrode in Alkaline Electrolytes: I . A Kinetic Analysis of Cathodic Deposition. *Journal of The Electrochemical Society*, 1991. **138**(3): p. 678-687.
- [87] Wang, K., et al., Dendrite growth in the recharging process of zinc–air batteries. *Journal of Materials Chemistry A*, 2015. **3**(45): p. 22648-22655.
- [88] Bockris, J.O.M., Z. Nagy, and D. Drazic, On the Morphology of Zinc Electrodeposition from Alkaline Solutions. *Journal of The Electrochemical Society*, 1973. **120**(1): p. 30.
- [89] Diggle, J.W., A.R. Despic, and J.O.M. Bockris, The Mechanism of the Dendritic Electrocrystallization of Zinc. *Journal of The Electrochemical Society*, 1969. **116**(11): p. 1503.
- [90] Cheng, J., et al., Preliminary study of single flow zinc–nickel battery. *Electrochemistry Communications*, 2007. **9**(11): p. 2639-2642.
- [91] Moshitev, R. V. and P. Zlatilova, Kinetics of growth of zinc dendrite precursors in zincate solutions. *Journal of Applied Electrochemistry*, 1978. **8**(3): p. 213-222.
- [92] Huber, K., Anodic Formation of Coatings on Magnesium, Zinc, and Cadmium. *Journal of The Electrochemical Society*, 1953. **100**(8): p. 376.
- [93] Huber, K., Studien zur Chemie und zur Struktur anodisch erzeugter Niederschläge und Deckschichten. 3. Mitteilung. Über die Farbe anodisch erzeugter Zinkoxydschichten. *Helvetica Chimica Acta*, 1944. **27**(1): p. 1443-1455.
- [94] Hull, M.N., J.E. Ellison, and J.E. Toni, The Anodic Behavior of Zinc Electrodes in Potassium Hydroxide Electrolytes. *Journal of The Electrochemical Society*, 1970. **117**(2): p. 192.
- [95] Yang, H., et al., Improved discharge capacity and suppressed surface passivation of zinc anode in dilute alkaline solution using surfactant additives. *Journal of Power Sources*, 2004. **128**(1): p. 97-101.
- [96] Powers, R.W. and M.W. Breiter, The Anodic Dissolution and Passivation of Zinc in Concentrated Potassium Hydroxide Solutions. *Journal of The Electrochemical Society*, 1969. **116**(6): p. 719.
- [97] McKubre, M.C.H. and D.D. Macdonald, The Dissolution and Passivation of Zinc in Concentrated Aqueous Hydroxide. *Journal of The Electrochemical Society*, 1981. **128**(3): p. 524-530.
- [98] Jung, C.-Y., et al., Computational analysis of the zinc utilization in the primary zinc-air batteries. *Energy*, 2016. **102**: p. 694-704.
- [99] Lee, C.W., et al., Novel electrochemical behavior of zinc anodes in zinc/air batteries in the presence of additives. *Journal of Power Sources*, 2006. **159**(2): p. 1474-1477.
- [100] Shivkumar, R., G. Paruthimal Kalaigan, and T. Vasudevan, Effect of additives on zinc electrodes in alkaline battery systems. *Journal of Power Sources*, 1995. **55**(1): p. 53-62.

- [101] Thomas, S., et al., Corrosion of Zinc as a Function of pH. *Corrosion*, 2012. **68**(1): p. 015009-1-015009-9.
- [102] Stamm, J., et al., Modeling nucleation and growth of zinc oxide during discharge of primary zinc-air batteries. *Journal of Power Sources*, 2017. **360**: p. 136-149.
- [103] Zhao, Z., et al., Challenges in Zinc Electrodes for Alkaline Zinc–Air Batteries: Obstacles to Commercialization. *ACS Energy Letters*, 2019. **4**(9): p. 2259-2270.
- [104] Riede, J.-C., T. Turek, and U. Kunz, Critical zinc ion concentration on the electrode surface determines dendritic zinc growth during charging a zinc air battery. *Electrochimica Acta*, 2018. **269**: p. 217-224.
- [105] Yuan, Z., et al., Negatively charged nanoporous membrane for a dendrite-free alkaline zinc-based flow battery with long cycle life. *Nature Communications*, 2018. **9**(1): p. 3731.
- [106] Garcia, G., E. Ventosa, and W. Schuhmann, Complete Prevention of Dendrite Formation in Zn Metal Anodes by Means of Pulsed Charging Protocols. *ACS Applied Materials & Interfaces*, 2017. **9**(22): p. 18691-18698.
- [107] Banik, S.J. and R. Akolkar, Suppressing Dendritic Growth during Alkaline Zinc Electrodeposition using Polyethylenimine Additive. *Electrochimica Acta*, 2015. **179**: p. 475-481.
- [108] Wen, Y.-h., et al., The inhibition of the spongy electrocrystallization of zinc from doped flowing alkaline zincate solutions. *Journal of Power Sources*, 2009. **193**(2): p. 890-894.
- [109] Wongrujipairoj, K., et al., Suppression of zinc anode corrosion for printed flexible zinc-air battery. *physica status solidi (b)*, 2017. **254**(2): p. 1600442.
- [110] Yi, J., et al., Challenges, mitigation strategies and perspectives in development of zinc-electrode materials and fabrication for rechargeable zinc–air batteries. *Energy & Environmental Science*, 2018. **11**(11): p. 3075-3095.
- [111] Wen, Y.-H., et al., Preliminary study on zinc–air battery using zinc regeneration electrolysis with propanol oxidation as a counter electrode reaction. *Journal of Power Sources*, 2009. **188**(1): p. 301-307.
- [112] Liu, K., et al., Effects of dodecyltrimethylammonium bromide surfactant on both corrosion and passivation behaviors of zinc electrodes in alkaline solution. *Materials Chemistry and Physics*, 2017. **199**: p. 73-78.
- [113] Deyab, M.A., Application of nonionic surfactant as a corrosion inhibitor for zinc in alkaline battery solution. *Journal of Power Sources*, 2015. **292**: p. 66-71.
- [114] Fashu, S., et al., Effect of EDTA and NH₄Cl additives on electrodeposition of Zn–Ni films from choline chloride-based ionic liquid. *Transactions of Nonferrous Metals Society of China*, 2015. **25**(6): p. 2054-2064.
- [115] Hou, Z., et al., Surfactant widens the electrochemical window of an aqueous electrolyte for better rechargeable aqueous sodium/zinc battery. *Journal of Materials Chemistry A*, 2017. **5**(2): p. 730-738.
- [116] Sharma, Y., et al., Triethanolamine as an additive to the anode to improve the rechargeability of alkaline manganese dioxide batteries. *Journal of Power Sources*, 2001. **94**(1): p. 129-131.
- [117] Torrent-Burgués, J. and E. Guaus, Effect of tartaric acid in the electrodeposition of zinc. *Journal of Applied Electrochemistry*, 2007. **37**(5): p. 643-651.
- [118] Yano, M., et al., Effect of additives in zinc alloy powder on suppressing hydrogen evolution. *Journal of Power Sources*, 1998. **74**(1): p. 129-134.
- [119] Li, B., et al., Ambipolar zinc-polyiodide electrolyte for a high-energy density aqueous redox flow battery. *Nature Communications*, 2015. **6**(1): p. 6303.
- [120] Hosseini, S., et al., Ethanol as an electrolyte additive for alkaline zinc-air flow batteries. *Scientific Reports*, 2018. **8**(1): p. 11273.

- [121] Wang, J.M., et al., Effects of bismuth ion and tetrabutylammonium bromide on the dendritic growth of zinc in alkaline zincate solutions. *Journal of Power Sources*, 2001. **102**(1): p. 139-143.
- [122] Diggle, J.W. and A. Damjanovic, The Inhibition of the Dendritic Electrocrystallization of Zinc from Doped Alkaline Zincate Solutions. *Journal of The Electrochemical Society*, 1972. **119**(12): p. 1649.
- [123] Xie, C., et al., A Long Cycle Life, Self-Healing Zinc–Iodine Flow Battery with High Power Density. *Angewandte Chemie International Edition*, 2018. **57**(35): p. 11171-11176.
- [124] Zhang, C., et al., Study of the performance of secondary alkaline pasted zinc electrodes. *Journal of Applied Electrochemistry*, 2001. **31**(9): p. 1049-1054.
- [125] Zheng, Y., et al., Effects of barium on the performance of secondary alkaline zinc electrode. *Materials Chemistry and Physics*, 2004. **84**(1): p. 99-106.
- [126] Yin, Y., et al., Dendrite-Free Zinc Deposition Induced by Tin-Modified Multifunctional 3D Host for Stable Zinc-Based Flow Battery. *Advanced Materials*, 2020. **32**(6): p. 1906803.
- [127] Shivkumar, R., G.P. Kalaignan, and T. Vasudevan, Studies with porous zinc electrodes with additives for secondary alkaline batteries. *Journal of Power Sources*, 1998. **75**(1): p. 90-100.
- [128] Hosseini, S., et al., Discharge Performance of Zinc-Air Flow Batteries Under the Effects of Sodium Dodecyl Sulfate and Pluronic F-127. *Scientific Reports*, 2018. **8**(1): p. 14909.
- [129] Winsberg, J., et al., Poly(TEMPO)/Zinc Hybrid-Flow Battery: A Novel, “Green,” High Voltage, and Safe Energy Storage System. *Advanced Materials*, 2016. **28**(11): p. 2238-2243.
- [130] Ito, Y., et al., Zinc morphology in zinc–nickel flow assisted batteries and impact on performance. *Journal of Power Sources*, 2011. **196**(4): p. 2340-2345.
- [131] Cheng, Y., et al., A long-life hybrid zinc flow battery achieved by dual redox couples at cathode. *Nano Energy*, 2019. **63**: p. 103822.
- [132] Xie, C., et al., A Low-Cost Neutral Zinc–Iron Flow Battery with High Energy Density for Stationary Energy Storage. *Angewandte Chemie International Edition*, 2017. **56**(47): p. 14953-14957.
- [133] Fukami, K., et al., General Mechanism for the Synchronization of Electrochemical Oscillations and Self-Organized Dendrite Electrodeposition of Metals with Ordered 2D and 3D Microstructures. *The Journal of Physical Chemistry C*, 2007. **111**(3): p. 1150-1160.
- [134] Ito, Y., et al., Gas evolution in a flow-assisted zinc–nickel oxide battery. *Journal of Power Sources*, 2011. **196**(15): p. 6583-6587.
- [135] Park, M., et al., A High Voltage Aqueous Zinc–Organic Hybrid Flow Battery. *Advanced Energy Materials*, 2019. **9**(25): p. 1900694.
- [136] Zhang, L., et al., A High-Energy-Density Redox Flow Battery based on Zinc/Polyhalide Chemistry. *ChemSusChem*, 2012. **5**(5): p. 867-869.
- [137] Li, X., et al., Ion exchange membranes for vanadium redox flow battery (VRB) applications. *Energy & Environmental Science*, 2011. **4**(4): p. 1147-1160.
- [138] Amunátegui, B., et al., Electrochemical energy storage for renewable energy integration: zinc-air flow batteries. *Journal of Applied Electrochemistry*, 2018. **48**(6): p. 627-637.
- [139] Wang, K., et al., Advanced rechargeable zinc-air battery with parameter optimization. *Applied Energy*, 2018. **225**: p. 848-856.
- [140] Pan, J., et al., Preliminary study of alkaline single flowing Zn–O₂ battery. *Electrochemistry Communications*, 2009. **11**(11): p. 2191-2194.

- [141] Bockelmann, M., U. Kunz, and T. Turek, Electrically rechargeable zinc-oxygen flow battery with high power density. *Electrochemistry Communications*, 2016. **69**: p. 24-27.
- [142] Pichler, B., et al., The impact of operating conditions on component and electrode development for zinc-air flow batteries. *Journal of Applied Electrochemistry*, 2018. **48**(9): p. 1043-1056.
- [143] Cheng, Y., et al., Efficient unitary oxygen electrode for air-based flow batteries. *Nano Energy*, 2018. **47**: p. 361-367.
- [144] McLarnon, F.R. and E.J. Cairns, The Secondary Alkaline Zinc Electrode. *Journal of The Electrochemical Society*, 1991. **138**(2): p. 645-656.
- [145] Chang, T.S., Y.Y. Wang, and C.C. Wan, Structural effect of the zinc electrode on its discharge performance. *Journal of Power Sources*, 1983. **10**(2): p. 167-177.
- [146] Turney, D.E., et al., Rechargeable Zinc Alkaline Anodes for Long-Cycle Energy Storage. *Chemistry of Materials*, 2017. **29**(11): p. 4819-4832.
- [147] Arouete, S., K.F. Blurton, and H.G. Oswin, Controlled Current Deposition of Zinc from Alkaline Solution. *Journal of The Electrochemical Society*, 1969. **116**(2): p. 166.
- [148] Mayers, M.Z., J.W. Kaminski, and T.F. Miller, Suppression of Dendrite Formation via Pulse Charging in Rechargeable Lithium Metal Batteries. *The Journal of Physical Chemistry C*, 2012. **116**(50): p. 26214-26221.
- [149] Wang, R.Y., D.W. Kirk, and G.X. Zhang, Effects of Deposition Conditions on the Morphology of Zinc Deposits from Alkaline Zincate Solutions. *Journal of The Electrochemical Society*, 2006. **153**(5): p. C357.
- [150] Naybour, R.D., The Effect of Electrolyte Flow on the Morphology of Zinc Electrodeposited from Aqueous Alkaline Solution Containing Zincate Ions. *Journal of The Electrochemical Society*, 1969. **116**(4): p. 520.
- [151] Zhu, J., Y. Zhou, and C. Gao, Influence of surfactants on electrochemical behavior of zinc electrodes in alkaline solution. *Journal of Power Sources*, 1998. **72**(2): p. 231-235.
- [152] Chu, M.G., J. McBreen, and G. Adzic, Substrate Effects on Zinc Deposition from Zincate Solutions: I. Deposition on Cu, Au, Cd and Zn. *Journal of The Electrochemical Society*, 1981. **128**(11): p. 2281-2286.
- [153] Naybour, R.D., Morphologies of zinc electrodeposited from zinc-saturated aqueous alkaline solution. *Electrochimica Acta*, 1968. **13**(4): p. 763-769.
- [154] Justinijanović, I.N. and A.R. Despić, Some observations on the properties of zinc electrodeposited from alkaline zincate solutions. *Electrochimica Acta*, 1973. **18**(10): p. 709-717.
- [155] Rogers, G.T. and K.J. Taylor, A rotating disc electrode study of the electrodeposition of zinc from alkaline zincate solutions. *Journal of Electroanalytical Chemistry and Interfacial Electrochemistry*, 1984. **167**(1): p. 251-264.
- [156] Dirkse, T.P. and R. Timmer, The Corrosion of Zinc in KOH Solutions. *Journal of The Electrochemical Society*, 1969. **116**(2): p. 162.
- [157] Rüetschi, P., Solubility and Diffusion of Hydrogen in Strong Electrolytes and the Generation and Consumption of Hydrogen in Sealed Primary Batteries. *Journal of The Electrochemical Society*, 1967. **114**(4): p. 301.
- [158] Einerhand, R.E.F., W.H.M. Visscher, and E. Barendrecht, Hydrogen production during zinc deposition from alkaline zincate solutions. *Journal of Applied Electrochemistry*, 1988. **18**(6): p. 799-806.
- [159] Lee, C.W., et al., Effect of additives on the electrochemical behaviour of zinc anodes for zinc/air fuel cells. *Journal of Power Sources*, 2006. **160**(1): p. 161-164.
- [160] Wang, R.Y., D.W. Kirk, and G.X. Zhang, Characterization and Growth Mechanism of Filamentous Zinc Electrodeposits. *ECS Transactions*, 2019. **2**(16): p. 19-27.

- [161] Ito, Y., et al., An indicator of zinc morphology transition in flowing alkaline electrolyte. *Journal of Power Sources*, 2012. **211**: p. 119-128.
- [162] Yang, H.S., et al., Critical rate of electrolyte circulation for preventing zinc dendrite formation in a zinc–bromine redox flow battery. *Journal of Power Sources*, 2016. **325**: p. 446-452.
- [163] Rogers, G. and K. Taylor, A rotating disc electrode study of the electrodeposition of zinc from alkaline zincate solutions. *Journal of Electroanalytical Chemistry and Interfacial Electrochemistry*, 1984. **167**(1-2): p. 251-264.
- [164] Einerhand, R., W. Visscher, and E. Barendrecht, Hydrogen production during zinc deposition from alkaline zincate solutions. *Journal of Applied Electrochemistry*, 1988. **18**(6): p. 799-806.
- [165] Dundálek, J., et al., Zinc electrodeposition from flowing alkaline zincate solutions: Role of hydrogen evolution reaction. *Journal of Power Sources*, 2017. **372**: p. 221-226.
- [166] Schmitt, T., et al., Zinc electrode shape-change in secondary air batteries: A 2D modeling approach. *Journal of Power Sources*, 2019. **432**: p. 119-132.
- [167] Brissot, C., et al., Dendritic growth mechanisms in lithium/polymer cells. *Journal of Power Sources*, 1999. **81-82**: p. 925-929.
- [168] Chen, C.P. and J. Jorne, The Dynamics of Morphological Instability during Electrodeposition. *Journal of The Electrochemical Society*, 1991. **138**(11): p. 3305-3311.
- [169] Li, Y., et al., Recent Progresses in Oxygen Reduction Reaction Electrocatalysts for Electrochemical Energy Applications. *Electrochemical Energy Reviews*, 2019. **2**(4): p. 518-538.
- [170] Wang, D.-W. and D. Su, Heterogeneous nanocarbon materials for oxygen reduction reaction. *Energy & Environmental Science*, 2014. **7**(2): p. 576-591.
- [171] Risch, M.J.C., Perovskite electrocatalysts for the oxygen reduction reaction in alkaline media. 2017. **7**(5): p. 154.
- [172] Goodenough, J.B. and B.L. Cushing, Oxide-based ORR catalysts, in *Handbook of Fuel Cells*.
- [173] Bevan, H.L. and A.C.C. Tseung, The electrochemical reduction of oxygen on high surface area lithium doped nickel oxides. *Electrochimica Acta*, 1974. **19**(5): p. 201-206.
- [174] Hibbert, D.B. and A.C.C. Tseung, Homomolecular Oxygen Exchange and the Electrochemical Reduction of Oxygen on Semiconducting Oxides. *Journal of The Electrochemical Society*, 1978. **125**(1): p. 74-78.
- [175] Mefford, J.T., et al., Water electrolysis on $\text{La}_{1-x}\text{Sr}_x\text{CoO}_{3-\delta}$ perovskite electrocatalysts. *Nature Communications*, 2016. **7**(1): p. 11053.
- [176] Grimaud, A., et al., Anionic redox processes for electrochemical devices. *Nature Materials*, 2016. **15**(2): p. 121-126.
- [177] Suntivich, J., et al., Design principles for oxygen-reduction activity on perovskite oxide catalysts for fuel cells and metal–air batteries. *Nature Chemistry*, 2011. **3**(7): p. 546-550.
- [178] Tang, Z., W. Wu, and K. Wang, Oxygen Reduction Reaction Catalyzed by Noble Metal Clusters. *Catalysts*, 2018. **8**(2).
- [179] Nosheen, F., et al., Noble Metal Based Alloy Nanoframes: Syntheses and Applications in Fuel Cells. 2019. **7**(456).
- [180] Sui, S., et al., A comprehensive review of Pt electrocatalysts for the oxygen reduction reaction: Nanostructure, activity, mechanism and carbon support in PEM fuel cells. *Journal of Materials Chemistry A*, 2017. **5**(5): p. 1808-1825.

- [181] Wang, Y.-J., et al., A Review of Carbon-Composited Materials as Air-Electrode Bifunctional Electrocatalysts for Metal–Air Batteries. *Electrochemical Energy Reviews*, 2018. **1**(1): p. 1-34.
- [182] Hu, C. and L. Dai, Carbon-Based Metal-Free Catalysts for Electrocatalysis beyond the ORR. *Angewandte Chemie International Edition*, 2016. **55**(39): p. 11736-11758.
- [183] Park, H.W., et al., Oxygen Reduction Reaction Using MnO₂Nanotubes/Nitrogen-Doped Exfoliated Graphene Hybrid Catalyst for Li-O₂Battery Applications. *Journal of The Electrochemical Society*, 2012. **160**(2): p. A344-A350.
- [184] Liang, Y., et al., Co₃O₄ nanocrystals on graphene as a synergistic catalyst for oxygen reduction reaction. *Nature Materials*, 2011. **10**(10): p. 780-786.
- [185] Wang, H., et al., Co_{1-x}S–Graphene Hybrid: A High-Performance Metal Chalcogenide Electrocatalyst for Oxygen Reduction. *Angewandte Chemie International Edition*, 2011. **50**(46): p. 10969-10972.
- [186] Wang, X.-R., et al., Identifying the Key Role of Pyridinic-N–Co Bonding in Synergistic Electrocatalysis for Reversible ORR/OER. *Advanced Materials*, 2018. **30**(23): p. 1800005.
- [187] Marković, N.M., et al., Oxygen Reduction Reaction on Pt and Pt Bimetallic Surfaces: A Selective Review. *Fuel Cells*, 2001. **1**(2): p. 105-116.
- [188] Shao, M., et al., Recent Advances in Electrocatalysts for Oxygen Reduction Reaction. *Chemical Reviews*, 2016. **116**(6): p. 3594-3657.
- [189] Xu, X., et al., Synthesis of Pt–Ni Alloy Nanocrystals with High-Index Facets and Enhanced Electrocatalytic Properties. *Angewandte Chemie International Edition*, 2014. **53**(46): p. 12522-12527.
- [190] Xie, S., et al., Catalysis on faceted noble-metal nanocrystals: both shape and size matter. *Current Opinion in Chemical Engineering*, 2013. **2**(2): p. 142-150.
- [191] Yu, T., et al., Platinum Concave Nanocubes with High-Index Facets and Their Enhanced Activity for Oxygen Reduction Reaction. *Angewandte Chemie International Edition*, 2011. **50**(12): p. 2773-2777.
- [192] Zhang, H., M. Jin, and Y. Xia, Noble-Metal Nanocrystals with Concave Surfaces: Synthesis and Applications. *Angewandte Chemie International Edition*, 2012. **51**(31): p. 7656-7673.
- [193] Nesselberger, M., et al., The Particle Size Effect on the Oxygen Reduction Reaction Activity of Pt Catalysts: Influence of Electrolyte and Relation to Single Crystal Models. *Journal of the American Chemical Society*, 2011. **133**(43): p. 17428-17433.
- [194] Bett, J., et al., Platinum crystallite size considerations for electrocatalytic oxygen reduction—I. *Electrochimica Acta*, 1973. **18**(5): p. 343-348.
- [195] Nesselberger, M., et al., The effect of particle proximity on the oxygen reduction rate of size-selected platinum clusters. *Nature Materials*, 2013. **12**(10): p. 919-924.
- [196] Roundtable, N.R.C.C.S. Critical Materials in Catalysis. in *The Role of the Chemical Sciences in Finding Alternatives to Critical Resources: A Workshop Summary*. 2012. National Academies Press (US).
- [197] Kang, Y., et al., Design of Pt–Pd Binary Superlattices Exploiting Shape Effects and Synergistic Effects for Oxygen Reduction Reactions. *Journal of the American Chemical Society*, 2013. **135**(1): p. 42-45.
- [198] Shao, M., et al., Pt Monolayer on Porous Pd–Cu Alloys as Oxygen Reduction Electrocatalysts. *Journal of the American Chemical Society*, 2010. **132**(27): p. 9253-9255.
- [199] Shao, M., et al., Enhanced Oxygen Reduction Activity of Platinum Monolayer on Gold Nanoparticles. *The Journal of Physical Chemistry Letters*, 2011. **2**(2): p. 67-72.

- [200] Gong, K., D. Su, and R.R. Adzic, Platinum-Monolayer Shell on AuNi_{0.5}Fe Nanoparticle Core Electrocatalyst with High Activity and Stability for the Oxygen Reduction Reaction. *Journal of the American Chemical Society*, 2010. **132**(41): p. 14364-14366.
- [201] Zhu, Y., et al., Boosting Oxygen Reduction Reaction Activity of Palladium by Stabilizing Its Unusual Oxidation States in Perovskite. *Chemistry of Materials*, 2015. **27**(8): p. 3048-3054.
- [202] Chen, M., et al., Nanocarbon/oxide composite catalysts for bifunctional oxygen reduction and evolution in reversible alkaline fuel cells: A mini review. *Journal of Power Sources*, 2018. **375**: p. 277-290.
- [203] Shi, Q., et al., Robust noble metal-based electrocatalysts for oxygen evolution reaction. *Chemical Society Reviews*, 2019. **48**(12): p. 3181-3192.
- [204] Sanchez Casalongue, H.G., et al., In Situ Observation of Surface Species on Iridium Oxide Nanoparticles during the Oxygen Evolution Reaction. *Angewandte Chemie International Edition*, 2014. **53**(28): p. 7169-7172.
- [205] Sun, W., et al., An efficiently tuned d-orbital occupation of IrO₂ by doping with Cu for enhancing the oxygen evolution reaction activity. *Chemical Science*, 2015. **6**(8): p. 4993-4999.
- [206] Pei, J., et al., Ir–Cu nanoframes: one-pot synthesis and efficient electrocatalysts for oxygen evolution reaction. *Chemical Communications*, 2016. **52**(19): p. 3793-3796.
- [207] Park, J., et al., RhCu 3D Nanoframe as a Highly Active Electrocatalyst for Oxygen Evolution Reaction under Alkaline Condition. *Advanced Science*, 2016. **3**(4): p. 1500252.
- [208] Huang, J., et al., CoOOH Nanosheets with High Mass Activity for Water Oxidation. *Angewandte Chemie International Edition*, 2015. **54**(30): p. 8722-8727.
- [209] Zhang, W., et al., Single-Walled Carbon Nanotube Induced Optimized Electron Polarization of Rhodium Nanocrystals To Develop an Interface Catalyst for Highly Efficient Electrocatalysis. *ACS Catalysis*, 2018. **8**(9): p. 8092-8099.
- [210] Wilder, J.W.G., et al., Electronic structure of atomically resolved carbon nanotubes. *Nature*, 1998. **391**(6662): p. 59-62.
- [211] Lu, Y.-C., et al., Platinum–Gold Nanoparticles: A Highly Active Bifunctional Electrocatalyst for Rechargeable Lithium–Air Batteries. *Journal of the American Chemical Society*, 2010. **132**(35): p. 12170-12171.
- [212] Sun, Y., et al., Ultrathin PtPd-Based Nanorings with Abundant Step Atoms Enhance Oxygen Catalysis. *Advanced Materials*, 2018. **30**(38): p. 1802136.
- [213] Gong, K., et al., Nitrogen-doped carbon nanotube arrays with high electrocatalytic activity for oxygen reduction. *science*, 2009. **323**(5915): p. 760-764.
- [214] Yu, D., Q. Zhang, and L. Dai, Highly Efficient Metal-Free Growth of Nitrogen-Doped Single-Walled Carbon Nanotubes on Plasma-Etched Substrates for Oxygen Reduction. *Journal of the American Chemical Society*, 2010. **132**(43): p. 15127-15129.
- [215] Ma, R., et al., Novel synthesis of N-doped graphene as an efficient electrocatalyst towards oxygen reduction. *Nano Research*, 2016. **9**(3): p. 808-819.
- [216] Gu, D., et al., Facile synthesis of N-doped graphene-like carbon nanoflakes as efficient and stable electrocatalysts for the oxygen reduction reaction. *Nano-micro letters*, 2018. **10**(2): p. 1-12.
- [217] Yang, L., et al., Boron - doped carbon nanotubes as metal - free electrocatalysts for the oxygen reduction reaction. *Angewandte Chemie International Edition*, 2011. **50**(31): p. 7132-7135.
- [218] Sheng, Z.-H., et al., Synthesis of boron doped graphene for oxygen reduction reaction in fuel cells. *Journal of Materials Chemistry*, 2012. **22**(2): p. 390-395.

- [219] Ma, Z., et al., Sulfur - Doped Graphene Derived from Cycled Lithium–Sulfur Batteries as a Metal - Free Electrocatalyst for the Oxygen Reduction Reaction. *Angewandte Chemie International Edition*, 2015. **54**(6): p. 1888-1892.
- [220] Liu, Z.W., et al., Phosphorus - doped graphite layers with high electrocatalytic activity for the O₂ reduction in an alkaline medium. *Angewandte Chemie International Edition*, 2011. **50**(14): p. 3257-3261.
- [221] Yao, Z., et al., Catalyst-free synthesis of iodine-doped graphene via a facile thermal annealing process and its use for electrocatalytic oxygen reduction in an alkaline medium. *Chemical Communications*, 2012. **48**(7): p. 1027-1029.
- [222] Jeon, I.-Y., et al., Facile, scalable synthesis of edge-halogenated graphene nanoplatelets as efficient metal-free electrocatalysts for oxygen reduction reaction. *Scientific Reports*, 2013. **3**(1): p. 1810.
- [223] Wang, S., et al., Vertically Aligned BCN Nanotubes as Efficient Metal-Free Electrocatalysts for the Oxygen Reduction Reaction: A Synergetic Effect by Co-Doping with Boron and Nitrogen. *Angewandte Chemie International Edition*, 2011. **50**(49): p. 11756-11760.
- [224] Xue, Y., et al., Three-dimensional B,N-doped graphene foam as a metal-free catalyst for oxygen reduction reaction. *Physical Chemistry Chemical Physics*, 2013. **15**(29): p. 12220-12226.
- [225] Wang, X., et al., One-pot synthesis of nitrogen and sulfur co-doped graphene as efficient metal-free electrocatalysts for the oxygen reduction reaction. *Chemical Communications*, 2014. **50**(37): p. 4839-4842.
- [226] Ma, R., et al., Ionic liquid-assisted synthesis of dual-doped graphene as efficient electrocatalysts for oxygen reduction. *Carbon*, 2016. **102**: p. 58-65.
- [227] Choi, C.H., S.H. Park, and S.I. Woo, Binary and Ternary Doping of Nitrogen, Boron, and Phosphorus into Carbon for Enhancing Electrochemical Oxygen Reduction Activity. *ACS Nano*, 2012. **6**(8): p. 7084-7091.
- [228] Ma, R., et al., A review of oxygen reduction mechanisms for metal-free carbon-based electrocatalysts. *npj Computational Materials*, 2019. **5**(1): p. 78.
- [229] Guo, D., et al., Active sites of nitrogen-doped carbon materials for oxygen reduction reaction clarified using model catalysts. *Science*, 2016. **351**(6271): p. 361.
- [230] Gupta, S., et al., Bifunctional Perovskite Oxide Catalysts for Oxygen Reduction and Evolution in Alkaline Media. *Chemistry – An Asian Journal*, 2016. **11**(1): p. 10-21.
- [231] Wang, H. and H. Dai, Strongly coupled inorganic–nano-carbon hybrid materials for energy storage. *Chemical Society Reviews*, 2013. **42**(7): p. 3088-3113.
- [232] Yan, Z., et al., Rapid low-temperature synthesis of perovskite/carbon nanocomposites as superior electrocatalysts for oxygen reduction in Zn-air batteries. *Nano Research*, 2018. **11**(6): p. 3282-3293.
- [233] Hardin, W.G., et al., Tuning the Electrocatalytic Activity of Perovskites through Active Site Variation and Support Interactions. *Chemistry of Materials*, 2014. **26**(11): p. 3368-3376.
- [234] Safakas, A., G. Bampos, and S. Bebelis, Oxygen reduction reaction on La_{0.8}Sr_{0.2}CoxFe_{1-x}O_{3-δ} perovskite/carbon black electrocatalysts in alkaline medium. *Applied Catalysis B: Environmental*, 2019. **244**: p. 225-232.
- [235] Wu, M., et al., Ultra-long life rechargeable zinc-air battery based on high-performance trimetallic nitride and NCNT hybrid bifunctional electrocatalysts. *Nano Energy*, 2019. **61**: p. 86-95.

- [236] Ahn, S.H. and A. Manthiram, Cobalt Phosphide Coupled with Heteroatom-Doped Nanocarbon Hybrid Electrocatalysts for Efficient, Long-Life Rechargeable Zinc–Air Batteries. *Small*, 2017. **13**(40): p. 1702068.
- [237] Cui, Z., et al., Ni₃FeN-Supported Fe₃Pt Intermetallic Nanoalloy as a High-Performance Bifunctional Catalyst for Metal–Air Batteries. *Angewandte Chemie International Edition*, 2017. **56**(33): p. 9901-9905.
- [238] Guo, Y., et al., Co₂P–CoN Double Active Centers Confined in N-Doped Carbon Nanotube: Heterostructural Engineering for Trifunctional Catalysis toward HER, ORR, OER, and Zn–Air Batteries Driven Water Splitting. *Advanced Functional Materials*, 2018. **28**(51): p. 1805641.
- [239] Parra-Puerto, A., et al., Supported Transition Metal Phosphides: Activity Survey for HER, ORR, OER, and Corrosion Resistance in Acid and Alkaline Electrolytes. *ACS Catalysis*, 2019. **9**(12): p. 11515-11529.
- [240] Kwak, W.-J., et al., Iron–cobalt bimetal decorated carbon nanotubes as cost-effective cathode catalysts for Li–O₂ batteries. *Journal of Materials Chemistry A*, 2016. **4**(18): p. 7020-7026.
- [241] Huang, J., et al., Electrospun graphitic carbon nanofibers with in-situ encapsulated Co–Ni nanoparticles as freestanding electrodes for Li–O₂ batteries. *Carbon*, 2016. **100**: p. 329-336.
- [242] Gao, R., et al., Carbon-Dotted Defective CoO with Oxygen Vacancies: A Synergetic Design of Bifunctional Cathode Catalyst for Li–O₂ Batteries. *ACS Catalysis*, 2016. **6**(1): p. 400-406.
- [243] Li, P., et al., In situ growth of spinel CoFe₂O₄ nanoparticles on rod-like ordered mesoporous carbon for bifunctional electrocatalysis of both oxygen reduction and oxygen evolution. *Journal of Materials Chemistry A*, 2015. **3**(30): p. 15598-15606.
- [244] Liu, Y., et al., Cubic spinel cobalt oxide/multi-walled carbon nanotube composites as an efficient bifunctional electrocatalyst for oxygen reaction. *Electrochemistry Communications*, 2013. **34**: p. 125-129.
- [245] Xu, Y., et al., Carbon-Coated Perovskite BaMnO₃ Porous Nanorods with Enhanced Electrocatalytic Performance for Oxygen Reduction and Oxygen Evolution. *Electrochimica Acta*, 2015. **174**: p. 551-556.
- [246] Yang, L., et al., Biomass-derived FeNi alloy and nitrogen-codoped porous carbons as highly efficient oxygen reduction and evolution bifunctional electrocatalysts for rechargeable Zn-air battery. *Energy Storage Materials*, 2018. **12**: p. 277-283.
- [247] Matsumoto, Y., H. Yoneyama, and H. Tamura, Electrochemical properties of lanthanum nickel oxide. *Journal of Electroanalytical Chemistry and Interfacial Electrochemistry*, 1977. **80**(1): p. 115-121.
- [248] Compton, R., *Electrode Kinetics: Reactions*. Comprehensive Chemical Kinetics, Volume 27. 1987: Elsevier Science & Technology.
- [249] Gao, M.-R., J. Jiang, and S.-H. Yu, Solution-Based Synthesis and Design of Late Transition Metal Chalcogenide Materials for Oxygen Reduction Reaction (ORR). *Small*, 2012. **8**(1): p. 13-27.
- [250] Zhan, Y., et al., Activity of Transition-Metal (Manganese, Iron, Cobalt, and Nickel) Phosphates for Oxygen Electrocatalysis in Alkaline Solution. *ChemCatChem*, 2016. **8**(2): p. 372-379.
- [251] Meadowcroft, D.B., Low-cost Oxygen Electrode Material. *Nature*, 1970. **226**(5248): p. 847-848.
- [252] Larsson, R. and L.Y. Johansson, On the catalytic properties of mixed oxides for the electrochemical reduction of oxygen. *Journal of Power Sources*, 1990. **32**(3): p. 253-260.

- [253] Matsumoto, Y., H. Yoneyama, and H. Tamura, Catalytic activity for electrochemical reduction of oxygen of lanthanum nickel oxide and related oxides. *Journal of Electroanalytical Chemistry and Interfacial Electrochemistry*, 1977. **79**(2): p. 319-326.
- [254] Matsumoto, Y., H. Yoneyama, and H. Tamura, Influence of the nature of the conduction band of transition metal oxides on catalytic activity for oxygen reduction. *Journal of Electroanalytical Chemistry and Interfacial Electrochemistry*, 1977. **83**(2): p. 237-243.
- [255] Suntivich, J., et al., A Perovskite Oxide Optimized for Oxygen Evolution Catalysis from Molecular Orbital Principles. *Science*, 2011. **334**(6061): p. 1383.
- [256] Suntivich, J. and Y. Shao-Horn, Trend in Oxygen Reduction Reaction on Transition Metal Oxide Surfaces. *ECS Transactions*, 2013. **58**(1): p. 715-726.
- [257] Petrie, J.R., et al., Enhanced Bifunctional Oxygen Catalysis in Strained LaNiO₃ Perovskites. *Journal of the American Chemical Society*, 2016. **138**(8): p. 2488-2491.
- [258] Lee, Y.-L., et al., Ab initio GGA+U study of oxygen evolution and oxygen reduction electrocatalysis on the (001) surfaces of lanthanum transition metal perovskites LaBO₃ (B = Cr, Mn, Fe, Co and Ni). *Physical Chemistry Chemical Physics*, 2015. **17**(33): p. 21643-21663.
- [259] Zhou, H., et al., Applications of MxSe_y (M = Fe, Co, Ni) and Their Composites in Electrochemical Energy Storage and Conversion. *Nano-Micro Letters*, 2019. **11**(1): p. 40.
- [260] Xue, Y., et al., Transition metal oxide-based oxygen reduction reaction electrocatalysts for energy conversion systems with aqueous electrolytes. *Journal of Materials Chemistry A*, 2018. **6**(23): p. 10595-10626.
- [261] Żółtowski, P., D.M. Dražić, and L. Vorkapić, Carbon-air electrode with regenerative short time overload capacity: Part 1. Effect of manganese dioxide. *Journal of Applied Electrochemistry*, 1973. **3**(4): p. 271-283.
- [262] Cheng, F., et al., MnO₂-Based Nanostructures as Catalysts for Electrochemical Oxygen Reduction in Alkaline Media. *Chemistry of Materials*, 2010. **22**(3): p. 898-905.
- [263] Huang, D., et al., Mn₃O₄/Carbon Nanotube Nanocomposites as Electrocatalysts for the Oxygen Reduction Reaction in Alkaline Solution. *ChemElectroChem*, 2014. **1**(9): p. 1531-1536.
- [264] Wang, W., et al., Porous Mn₂O₃: A Low-Cost Electrocatalyst for Oxygen Reduction Reaction in Alkaline Media with Comparable Activity to Pt/C. *Chemistry – A European Journal*, 2016. **22**(29): p. 9909-9913.
- [265] Wu, Q., et al., A novel octahedral MnO/ RGO composite prepared by thermal decomposition as a noble-metal free electrocatalyst for ORR. *Journal of Materials Science*, 2017. **52**(11): p. 6656-6669.
- [266] Sun, W., A. Hsu, and R. Chen, Carbon-supported tetragonal MnOOH catalysts for oxygen reduction reaction in alkaline media. *Journal of Power Sources*, 2011. **196**(2): p. 627-635.
- [267] Zhang, T., et al., Efficiently Enhancing Oxygen Reduction Electrocatalytic Activity of MnO₂ Using Facile Hydrogenation. *Advanced Energy Materials*, 2015. **5**(1): p. 1400654.
- [268] Mao, L., et al., Mechanistic study of the reduction of oxygen in air electrode with manganese oxides as electrocatalysts. *Electrochimica Acta*, 2003. **48**(8): p. 1015-1021.
- [269] Lima, F.H.B., M.L. Calegari, and E.A. Ticianelli, Electrocatalytic activity of dispersed platinum and silver alloys and manganese oxides for the oxygen reduction in alkaline electrolyte. *Russian Journal of Electrochemistry*, 2006. **42**(12): p. 1283-1290.
- [270] Lima, F.H.B., M.L. Calegari, and E.A. Ticianelli, Investigations of the catalytic properties of manganese oxides for the oxygen reduction reaction in alkaline media. *Journal of Electroanalytical Chemistry*, 2006. **590**(2): p. 152-160.

- [271] Meng, Y., et al., Structure–Property Relationship of Bifunctional MnO₂ Nanostructures: Highly Efficient, Ultra-Stable Electrochemical Water Oxidation and Oxygen Reduction Reaction Catalysts Identified in Alkaline Media. *Journal of the American Chemical Society*, 2014. **136**(32): p. 11452-11464.
- [272] Truong, T.T., et al., Morphological and Crystalline Evolution of Nanostructured MnO₂ and Its Application in Lithium–Air Batteries. *ACS Nano*, 2012. **6**(9): p. 8067-8077.
- [273] Li, T., et al., Tubular Monolayer Superlattices of Hollow Mn₃O₄ Nanocrystals and Their Oxygen Reduction Activity. *Journal of the American Chemical Society*, 2017. **139**(35): p. 12133-12136.
- [274] Liu, J., et al., Activating Mn₃O₄ by Morphology Tailoring for Oxygen Reduction Reaction. *Electrochimica Acta*, 2016. **205**: p. 38-44.
- [275] Wu, M.C., et al., Carbonized tubular polypyrrole with a high activity for the Br₂/Br⁻ redox reaction in zinc-bromine flow batteries. *Electrochimica Acta*, 2018. **284**: p. 569-576.
- [276] Selvakumar, K., et al., Physiochemical Investigation of Shape-Designed MnO₂ Nanostructures and Their Influence on Oxygen Reduction Reaction Activity in Alkaline Solution. *The Journal of Physical Chemistry C*, 2015. **119**(12): p. 6604-6618.
- [277] Zhao, S., et al., Hydrothermal synthesis of urchin-like MnO₂ nanostructures and its electrochemical character for supercapacitor. *Applied Surface Science*, 2015. **351**: p. 862-868.
- [278] Cheng, G., et al., Phase controllable synthesis of three-dimensional star-like MnO₂ hierarchical architectures as highly efficient and stable oxygen reduction electrocatalysts. *Journal of Materials Chemistry A*, 2016. **4**(42): p. 16462-16468.
- [279] Tang, Q., et al., Effect of Surface Manganese Valence of Manganese Oxides on the Activity of the Oxygen Reduction Reaction in Alkaline Media. *ACS Catalysis*, 2014. **4**(2): p. 457-463.
- [280] Lima, F.H.B., M.L. Calegari, and E.A. Ticianelli, Electrocatalytic activity of manganese oxides prepared by thermal decomposition for oxygen reduction. *Electrochimica Acta*, 2007. **52**(11): p. 3732-3738.
- [281] Zhang, X., et al., Co/CoO nanoparticles immobilized on Co–N-doped carbon as trifunctional electrocatalysts for oxygen reduction, oxygen evolution and hydrogen evolution reactions. *Chemical Communications*, 2016. **52**(35): p. 5946-5949.
- [282] Niu, Y., et al., One-pot synthesis of Co/N-doped mesoporous graphene with embedded Co/CoO_x nanoparticles for efficient oxygen reduction reaction. *Nanoscale*, 2017. **9**(29): p. 10233-10239.
- [283] Liu, T., et al., CoO nanoparticles embedded in three-dimensional nitrogen/sulfur co-doped carbon nanofiber networks as a bifunctional catalyst for oxygen reduction/evolution reactions. *Carbon*, 2016. **106**: p. 84-92.
- [284] Xia, W., et al., Earth-Abundant Nanomaterials for Oxygen Reduction. *Angewandte Chemie International Edition*, 2016. **55**(8): p. 2650-2676.
- [285] Zhang, J., et al., Facile synthesis of hierarchical porous Co₃O₄ nanoboxes as efficient cathode catalysts for Li–O₂ batteries. *Journal of Materials Chemistry A*, 2016. **4**(17): p. 6350-6356.
- [286] Wang, J., et al., Boosting the Electrocatalytic Activity of Co₃O₄ Nanosheets for a Li–O₂ Battery through Modulating Inner Oxygen Vacancy and Exterior Co³⁺/Co²⁺ Ratio. *ACS Catalysis*, 2017. **7**(10): p. 6533-6541.
- [287] Liu, L., et al., A 3D hierarchical porous Co₃O₄ nanotube network as an efficient cathode for rechargeable lithium–oxygen batteries. *Journal of Materials Chemistry A*, 2017. **5**(28): p. 14673-14681.

- [288] Leng, L., et al., Pd nanoparticles decorating flower-like Co₃O₄ nanowire clusters to form an efficient, carbon/binder-free cathode for Li–O₂ batteries. *Journal of Materials Chemistry A*, 2015. **3**(30): p. 15626-15632.
- [289] He, Y., et al., Ultrathin Co₃O₄ nanofilm as an efficient bifunctional catalyst for oxygen evolution and reduction reaction in rechargeable zinc–air batteries. *Nanoscale*, 2017. **9**(25): p. 8623-8630.
- [290] Zhao, Q., et al., Spinels: Controlled Preparation, Oxygen Reduction/Evolution Reaction Application, and Beyond. *Chemical Reviews*, 2017. **117**(15): p. 10121-10211.
- [291] Guan, C., et al., Hollow Co₃O₄ Nanosphere Embedded in Carbon Arrays for Stable and Flexible Solid-State Zinc–Air Batteries. *Advanced Materials*, 2017. **29**(44): p. 1704117.
- [292] Huang, W., et al., Reduced Graphene Oxide Supported CoO/MnO₂ Electrocatalysts from Layered Double Hydroxides for Oxygen Reduction Reaction. *Electrochimica Acta*, 2015. **173**: p. 575-580.
- [293] Tan, L., et al., Core@Shelled Co/CoO Embedded Nitrogen-Doped Carbon Nanosheets Coupled Graphene as Efficient Cathode Catalysts for Enhanced Oxygen Reduction Reaction in Microbial Fuel Cells. *ACS Sustainable Chemistry & Engineering*, 2019. **7**(6): p. 6335-6344.
- [294] Cui, Z., et al., Engineering hybrid between nickel oxide and nickel cobaltate to achieve exceptionally high activity for oxygen reduction reaction. *Journal of Power Sources*, 2014. **272**: p. 808-815.
- [295] Wu, Z.-S., et al., 3D Nitrogen-Doped Graphene Aerogel-Supported Fe₃O₄ Nanoparticles as Efficient Electrocatalysts for the Oxygen Reduction Reaction. *Journal of the American Chemical Society*, 2012. **134**(22): p. 9082-9085.
- [296] Xu, N., et al., Morphology controlled La₂O₃/Co₃O₄/MnO₂–CNTs hybrid nanocomposites with durable bi-functional air electrode in high-performance zinc–air energy storage. *Applied Energy*, 2016. **175**: p. 495-504.
- [297] Sun, S., et al., Electrocatalytic activity of silver decorated ceria microspheres for the oxygen reduction reaction and their application in aluminium–air batteries. *Chemical Communications*, 2017. **53**(56): p. 7921-7924.
- [298] Kuang, M., et al., Cu, Co-Embedded N-Enriched Mesoporous Carbon for Efficient Oxygen Reduction and Hydrogen Evolution Reactions. *Advanced Energy Materials*, 2017. **7**(17): p. 1700193.
- [299] Raghuveer, V., A. Manthiram, and A.J. Bard, Pd–Co–Mo Electrocatalyst for the Oxygen Reduction Reaction in Proton Exchange Membrane Fuel Cells. *The Journal of Physical Chemistry B*, 2005. **109**(48): p. 22909-22912.
- [300] Kim, J.-H., et al., Catalytic activity of titanium oxide for oxygen reduction reaction as a non-platinum catalyst for PEFC. *Electrochimica Acta*, 2007. **52**(7): p. 2492-2497.
- [301] Martins, M., et al., Mn₂O₃-MO (MO = ZrO₂, V₂O₅, WO₃) supported PtNi nanoparticles: Designing stable and efficient electrocatalysts for oxygen reduction and borohydride oxidation. *Microporous and Mesoporous Materials*, 2019. **273**: p. 286-293.
- [302] Shen, F.-C., et al., CoV₂O₆–V₂O₅ Coupled with Porous N-Doped Reduced Graphene Oxide Composite as a Highly Efficient Electrocatalyst for Oxygen Evolution. *ACS Energy Letters*, 2017. **2**(6): p. 1327-1333.
- [303] Sun, J., et al., Molecular engineering of Ni–/Co–porphyrin multilayers on reduced graphene oxide sheets as bifunctional catalysts for oxygen evolution and oxygen reduction reactions. *Chemical Science*, 2016. **7**(9): p. 5640-5646.
- [304] Zhu, J., et al., Perovskite Oxides: Preparation, Characterizations, and Applications in Heterogeneous Catalysis. *ACS Catalysis*, 2014. **4**(9): p. 2917-2940.
- [305] Megaw, H.D., Crystal structure of double oxides of the perovskite type. *Proceedings of the Physical Society*, 1946. **58**(2): p. 133-152.

- [306] Royer, S., et al., Perovskites as Substitutes of Noble Metals for Heterogeneous Catalysis: Dream or Reality. *Chemical Reviews*, 2014. **114**(20): p. 10292-10368.
- [307] Chen, X., et al., Rare earth double perovskites: a fertile soil in the field of perovskite oxides. *Inorganic Chemistry Frontiers*, 2019. **6**(9): p. 2226-2238.
- [308] Maignan, A., et al., Structural and Magnetic Studies of Ordered Oxygen-Deficient Perovskites $\text{LnBaCo}_2\text{O}_{5+\delta}$, Closely Related to the “112” Structure. *Journal of Solid State Chemistry*, 1999. **142**(2): p. 247-260.
- [309] Sun, Y., et al., Unfolding B–O–B Bonds for an Enhanced ORR Performance in ABO₃-Type Perovskites. *Small*, 2019. **15**(29): p. 1803513.
- [310] Hyodo, T., et al., Catalytic Activities of Rare - Earth Manganites for Cathodic Reduction of Oxygen in Alkaline Solution. *Journal of The Electrochemical Society*, 1996. **143**(11): p. L266-L267.
- [311] Hyodo, T., et al., Praseodymium-calcium manganites ($\text{Pr}_{1-x}\text{Ca}_x\text{MnO}_3$) as electrode catalyst for oxygen reduction in alkaline solution. 1997.
- [312] Hu, J., et al., Preparation of $\text{La}_{1-x}\text{Ca}_x\text{MnO}_3$ perovskite–graphene composites as oxygen reduction reaction electrocatalyst in alkaline medium. *Journal of Power Sources*, 2014. **269**: p. 144-151.
- [313] Hammouche, A., et al., Influential factors on oxygen reduction at $\text{La}_{1-x}\text{Ca}_x\text{CoO}_3$ electrodes in alkaline electrolyte. *Journal of Power Sources*, 2006. **153**(2): p. 239-244.
- [314] Pavone, M., et al., First-Principles Study of Lanthanum Strontium Manganite: Insights into Electronic Structure and Oxygen Vacancy Formation. *The Journal of Physical Chemistry C*, 2014. **118**(25): p. 13346-13356.
- [315] Tulloch, J. and S.W. Donne, Activity of perovskite $\text{La}_{1-x}\text{Sr}_x\text{MnO}_3$ catalysts towards oxygen reduction in alkaline electrolytes. *Journal of Power Sources*, 2009. **188**(2): p. 359-366.
- [316] Stoerzinger, K.A., et al., Highly Active Epitaxial $\text{La}_{1-x}\text{Sr}_x\text{MnO}_3$ Surfaces for the Oxygen Reduction Reaction: Role of Charge Transfer. *The Journal of Physical Chemistry Letters*, 2015. **6**(8): p. 1435-1440.
- [317] Zhao, Y., et al., Strontium-doped perovskite oxide $\text{La}_{1-x}\text{Sr}_x\text{MnO}_3$ ($x=0, 0.2, 0.6$) as a highly efficient electrocatalyst for nonaqueous Li-O₂ batteries. *Electrochimica Acta*, 2017. **232**: p. 296-302.
- [318] Zhang, Y., et al., Enhanced Catalytic Activity of LaMnO_3 by A-Site Substitution as Air Electrode of Zn–Air Batteries with Attractive Durability. *Energy & Fuels*, 2020. **34**(8): p. 10170-10177.
- [319] Zhu, Y., et al., Enhancing Electrocatalytic Activity of Perovskite Oxides by Tuning Cation Deficiency for Oxygen Reduction and Evolution Reactions. *Chemistry of Materials*, 2016. **28**(6): p. 1691-1697.
- [320] Xue, Y., et al., $(\text{La}_{1-x}\text{Sr}_x)_{0.98}\text{MnO}_3$ perovskite with A-site deficiencies toward oxygen reduction reaction in aluminum-air batteries. *Journal of Power Sources*, 2017. **342**: p. 192-201.
- [321] Gao, Y., et al., From material design to mechanism study: Nanoscale Ni exsolution on a highly active A-site deficient anode material for solid oxide fuel cells. *Nano Energy*, 2016. **27**: p. 499-508.
- [322] Chen, G., et al., Evaluation of A-site deficient $\text{Sr}_{1-x}\text{Sc}_{0.175}\text{Nb}_{0.025}\text{Co}_{0.8}\text{O}_{3-\delta}$ ($x=0, 0.02, 0.05$ and 0.1) perovskite cathodes for intermediate-temperature solid oxide fuel cells. *Ceramics International*, 2016. **42**(11): p. 12894-12900.
- [323] Feng, J., et al., Development and performance of anode material based on A-site deficient $\text{Sr}_{2-x}\text{Fe}_{1.4}\text{Ni}_{0.1}\text{Mo}_{0.5}\text{O}_{6-\delta}$ perovskites for solid oxide fuel cells. *Electrochimica Acta*, 2016. **215**: p. 592-599.

- [324] Ghosh, K.B., et al., La_{0.54}Sr_{0.4}Fe_{0.2}Co_{0.8}O_{3-δ}@Co_{0.01}Ce_{0.79}Gd_{0.2}O_{2-δ} functional cathode material for solid oxide fuel cell application. *International Journal of Hydrogen Energy*, 2017. **42**(4): p. 2327-2337.
- [325] Zhu, Y., et al., Promotion of Oxygen Reduction by Exsolved Silver Nanoparticles on a Perovskite Scaffold for Low-Temperature Solid Oxide Fuel Cells. *Nano Letters*, 2016. **16**(1): p. 512-518.
- [326] Jin, C., et al., A novel bifunctional catalyst of Ba_{0.9}Co_{0.5}Fe_{0.4}Nb_{0.1}O_{3-δ} perovskite for lithium-air battery. *International Journal of Hydrogen Energy*, 2014. **39**(6): p. 2526-2530.
- [327] Xue, Y., et al., La_{0.7}(Sr_{0.3-x}Pdx)MnO₃ as a highly efficient electrocatalyst for oxygen reduction reaction in aluminum air battery. *Electrochimica Acta*, 2017. **230**: p. 418-427.
- [328] Bak, J., et al., Formation of Two-Dimensional Homologous Faults and Oxygen Electrocatalytic Activities in a Perovskite Nickelate. *Nano Letters*, 2017. **17**(5): p. 3126-3132.
- [329] Xu, W., et al., A-site Excessive (La_{0.8}Sr_{0.2})_{1+x}MnO₃ Perovskite Oxides for Bifunctional Oxygen Catalyst in Alkaline Media. *ACS Catalysis*, 2019. **9**(6): p. 5074-5083.
- [330] Miao, H., et al., A-site deficient/excessive effects of LaMnO₃ perovskite as bifunctional oxygen catalyst for zinc-air batteries. *Electrochimica Acta*, 2020. **333**: p. 135566.
- [331] Bangwal, A.S., et al., Compositional effect on oxygen reduction reaction in Pr excess double perovskite Pr_{1+x}Ba_{1-x}Co₂O_{6-δ} cathode materials. *International Journal of Hydrogen Energy*, 2020. **45**(43): p. 23378-23390.
- [332] Yang, Y., et al., A new A-site excessive strategy to improve performance of layered perovskite cathode for intermediate-temperature solid oxide fuel cells. *Electrochimica Acta*, 2017. **231**: p. 686-693.
- [333] Khaerudini, D.S., et al., Evaluation of (Bi_{0.4}Sr_{0.6})_xCo_{0.3}Fe_{0.7}O_{3-δ} (x = 0.7, 0.8, 0.9, 1.0, 1.1) perovskite-type oxide as potential cathode for intermediate-temperature solid oxide fuel cells. *International Journal of Hydrogen Energy*, 2015. **40**(34): p. 11011-11021.
- [334] Kuai, X., et al., Boosting the Activity of BaCo_{0.4}Fe_{0.4}Zr_{0.1}Y_{0.1}O_{3-δ} Perovskite for Oxygen Reduction Reactions at Low-to-Intermediate Temperatures through Tuning B-Site Cation Deficiency. *Advanced Energy Materials*, 2019. **9**(38): p. 1902384.
- [335] Man, I.C., et al., Universality in Oxygen Evolution Electrocatalysis on Oxide Surfaces. *ChemCatChem*, 2011. **3**(7): p. 1159-1165.
- [336] Sunarso, J., et al., Oxygen Reduction Reaction Activity of La-Based Perovskite Oxides in Alkaline Medium: A Thin-Film Rotating Ring-Disk Electrode Study. *The Journal of Physical Chemistry C*, 2012. **116**(9): p. 5827-5834.
- [337] Lee, H., et al., Enhancing Bifunctional Electrocatalytic Activities via Metal d-Band Center Lift Induced by Oxygen Vacancy on the Subsurface of Perovskites. *ACS Catalysis*, 2020. **10**(8): p. 4664-4670.
- [338] Mueller, D.N., et al., Redox activity of surface oxygen anions in oxygen-deficient perovskite oxides during electrochemical reactions. *Nature Communications*, 2015. **6**(1): p. 6097.
- [339] Cheng, Y., et al., Enhancing Oxygen Exchange Activity by Tailoring Perovskite Surfaces. *The Journal of Physical Chemistry Letters*, 2019. **10**(14): p. 4082-4088.
- [340] Tseung, A.C.C. and S. Jasem, Oxygen evolution on semiconducting oxides. *Electrochimica Acta*, 1977. **22**(1): p. 31-34.
- [341] Trasatti, S., Electrocatalysis in the anodic evolution of oxygen and chlorine. *Electrochimica Acta*, 1984. **29**(11): p. 1503-1512.

- [342] Bockris, J.O.M. and T. Otagawa, The Electrocatalysis of Oxygen Evolution on Perovskites. *Journal of The Electrochemical Society*, 1984. **131**(2): p. 290-302.
- [343] Rossmesl, J., A. Logadottir, and J.K. Nørskov, Electrolysis of water on (oxidized) metal surfaces. *Chemical Physics*, 2005. **319**(1): p. 178-184.
- [344] Goodenough, J.B., R. Manoharan, and M. Paranthaman, Surface protonation and electrochemical activity of oxides in aqueous solution. *Journal of the American Chemical Society*, 1990. **112**(6): p. 2076-2082.
- [345] Wang, L.-P., Q. Wu, and T. Van Voorhis, Acid–Base Mechanism for Ruthenium Water Oxidation Catalysts. *Inorganic Chemistry*, 2010. **49**(10): p. 4543-4553.
- [346] Mavros, M.G., et al., What Can Density Functional Theory Tell Us about Artificial Catalytic Water Splitting? *Inorganic Chemistry*, 2014. **53**(13): p. 6386-6397.
- [347] Surendranath, Y., M.W. Kanan, and D.G. Nocera, Mechanistic Studies of the Oxygen Evolution Reaction by a Cobalt-Phosphate Catalyst at Neutral pH. *Journal of the American Chemical Society*, 2010. **132**(46): p. 16501-16509.
- [348] Wang, L.-P. and T. Van Voorhis, Direct-Coupling O₂ Bond Forming a Pathway in Cobalt Oxide Water Oxidation Catalysts. *The Journal of Physical Chemistry Letters*, 2011. **2**(17): p. 2200-2204.
- [349] May, K.J., et al., Influence of Oxygen Evolution during Water Oxidation on the Surface of Perovskite Oxide Catalysts. *The Journal of Physical Chemistry Letters*, 2012. **3**(22): p. 3264-3270.
- [350] Chen, D., et al., Preferential Cation Vacancies in Perovskite Hydroxide for the Oxygen Evolution Reaction. *Angewandte Chemie International Edition*, 2018. **57**(28): p. 8691-8696.
- [351] Grimaud, A., et al., Double perovskites as a family of highly active catalysts for oxygen evolution in alkaline solution. *Nature Communications*, 2013. **4**(1): p. 2439.
- [352] Rondinelli, J.M., S.J. May, and J.W. Freeland, Control of octahedral connectivity in perovskite oxide heterostructures: An emerging route to multifunctional materials discovery. *MRS Bulletin*, 2012. **37**(3): p. 261-270.
- [353] Goodenough, J.B.J.P.R., Theory of the role of covalence in the perovskite-type manganites [La, M (II)] Mn O₃. 1955. **100**(2): p. 564.
- [354] Mohamed, R., et al., Understanding the Influence of Carbon on the Oxygen Reduction and Evolution Activities of BSCF/Carbon Composite Electrodes in Alkaline Electrolyte. *ECS Transactions*, 2014. **58**(36): p. 9-18.
- [355] Liu, T., et al., Pyridinic-N-dominated carbon frameworks with porous tungsten trioxide nano-lamellae as a promising bi-functional catalyst for Li–oxygen batteries. *Nanoscale*, 2018. **10**(33): p. 15763-15770.
- [356] Yang, L., et al., Carbon-Based Metal-Free ORR Electrocatalysts for Fuel Cells: Past, Present, and Future. *Advanced Materials*, 2019. **31**(13): p. 1804799.
- [357] Wang, T., et al., Scalable preparation and stabilization of atomic-thick CoNi layered double hydroxide nanosheets for bifunctional oxygen electrocatalysis and rechargeable zinc-air batteries. *Energy Storage Materials*, 2019. **16**: p. 24-30.
- [358] Pourfarzad, H., M. Shabani-Nooshabadi, and M.R. Ganjali, Novel bi-functional electrocatalysts based on the electrochemical synthesized bimetallicmetal organic frameworks: Towards high energy advanced reversible zinc–air batteries. *Journal of Power Sources*, 2020. **451**: p. 227768.
- [359] Chen, L., et al., Cobalt sulfide/N,S-codoped defect-rich carbon nanotubes hybrid as an excellent bi-functional oxygen electrocatalyst. *Nanotechnology*, 2018. **30**(7): p. 075402.
- [360] Ahamad, T., et al., Synthesis and characterization cobalt phosphate embedded with N doped carbon for water splitting ORR and OER. *Journal of King Saud University - Science*, 2020. **32**(6): p. 2826-2830.

- [361] Poux, T., et al., Dual role of carbon in the catalytic layers of perovskite/carbon composites for the electrocatalytic oxygen reduction reaction. *Catalysis Today*, 2012. **189**(1): p. 83-92.
- [362] Miyahara, Y., et al., Influence of Surface Orientation on the Catalytic Activities of La_{0.8}Sr_{0.2}CoO₃ Crystal Electrodes for Oxygen Reduction and Evolution Reactions. *ChemElectroChem*, 2016. **3**(2): p. 214-217.
- [363] Poux, T., et al., Electrocatalytic oxygen reduction reaction on perovskite oxides: series versus direct pathway. *Chemphyschem*, 2014. **15**(10): p. 2108-20.
- [364] Suntivich, J., et al., Electrocatalytic Measurement Methodology of Oxide Catalysts Using a Thin-Film Rotating Disk Electrode. *Journal of The Electrochemical Society*, 2010. **157**(8): p. B1263.
- [365] Kan, D., et al., Overpotential-Induced Introduction of Oxygen Vacancy in La_{0.67}Sr_{0.33}MnO₃ Surface and Its Impact on Oxygen Reduction Reaction Catalytic Activity in Alkaline Solution. *The Journal of Physical Chemistry C*, 2016. **120**(11): p. 6006-6010.
- [366] Miyahara, Y., et al., Catalytic Roles of Perovskite Oxides in Electrochemical Oxygen Reactions in Alkaline Media. *Journal of The Electrochemical Society*, 2014. **161**(6): p. F694-F697.
- [367] Paulus, U.A., et al., Oxygen reduction on a high-surface area Pt/Vulcan carbon catalyst: a thin-film rotating ring-disk electrode study. *Journal of Electroanalytical Chemistry*, 2001. **495**(2): p. 134-145.
- [368] Pederson, L.R., et al., Combustion synthesis of YBa₂Cu₃O_{7-x}: glycine/metal nitrate method. *Materials Letters*, 1991. **10**(9): p. 437-443.
- [369] Athayde, D.D., et al., Review of perovskite ceramic synthesis and membrane preparation methods. *Ceramics International*, 2016. **42**(6): p. 6555-6571.
- [370] Zeng, S., et al., A review on photocatalytic CO₂ reduction using perovskite oxide nanomaterials. *Nanotechnology*, 2018. **29**(5): p. 052001.
- [371] Bell, R.J., G.J. Millar, and J. Drennan, Influence of synthesis route on the catalytic properties of La_{1-x}Sr_xMnO₃. *Solid State Ionics*, 2000. **131**(3): p. 211-220.
- [372] Gordes, P., et al., Synthesis of perovskite-type compounds by drip pyrolysis. *Journal of Materials Science*, 1995. **30**(4): p. 1053-1058.
- [373] Wang, H., et al., Cation Deficiency Tuning of LaCoO₃ Perovskite as Bifunctional Oxygen Electrocatalyst. *ChemCatChem*, 2020. **12**(10): p. 2768-2775.
- [374] Sun, C., et al., A formation mechanism of oxygen vacancies in a MnO₂ monolayer: a DFT + U study. *Physical Chemistry Chemical Physics*, 2011. **13**(23): p. 11325-11328.
- [375] Xiong, T., et al., Defect Engineering of Oxygen-Deficient Manganese Oxide to Achieve High-Performing Aqueous Zinc Ion Battery. *Advanced Energy Materials*, 2019. **9**(14): p. 1803815.
- [376] Rodríguez-Carvajal, J., et al., Electronic Crystallization in a Lithium Battery Material: Columnar Ordering of Electrons and Holes in the Spinel LiMn_2O_4 . *Physical Review Letters*, 1998. **81**(21): p. 4660-4663.
- [377] Jiang, S.P., Development of lanthanum strontium manganite perovskite cathode materials of solid oxide fuel cells: a review. *Journal of Materials Science*, 2008. **43**(21): p. 6799-6833.
- [378] Hammouche, A., E. Siebert, and A. Hammou, Crystallographic, thermal and electrochemical properties of the system La_{1-x}Sr_xMnO₃ for high temperature solid electrolyte fuel cells. *Materials Research Bulletin*, 1989. **24**(3): p. 367-380.
- [379] Agassant, J.-F., et al., Mise en forme des polymères: Approche thermomécanique de la plasturgie. 2014: Lavoisier-Tech & Doc.

- [380] Chen, X.J., K.A. Khor, and S.H. Chan, Electrochemical behavior of La(Sr)MnO₃ electrode under cathodic and anodic polarization. *Solid State Ionics*, 2004. **167**(3): p. 379-387.
- [381] Brezesinski, T., et al., Templated Nanocrystal-Based Porous TiO₂ Films for Next-Generation Electrochemical Capacitors. *Journal of the American Chemical Society*, 2009. **131**(5): p. 1802-1809.
- [382] Petrii, O.A., et al., Life of the Tafel equation: Current understanding and prospects for the second century. *Electrochimica Acta*, 2007. **52**(11): p. 3493-3504.
- [383] Müller, S., K. Striebel, and O. Haas, La_{0.6}Ca_{0.4}CoO₃: a stable and powerful catalyst for bifunctional air electrodes. *Electrochimica Acta*, 1994. **39**(11): p. 1661-1668.
- [384] Neburchilov, V., et al., A review on air cathodes for zinc–air fuel cells. *Journal of Power Sources*, 2010. **195**(5): p. 1271-1291.
- [385] Amanchukwu, C.V., et al., Understanding the Chemical Stability of Polymers for Lithium–Air Batteries. *Chemistry of Materials*, 2015. **27**(2): p. 550-561.
- [386] Manickam, M. and M. Takata, Effect of cathode binder on capacity retention and cycle life in transition metal phosphate of a rechargeable lithium battery. *Electrochimica Acta*, 2003. **48**(8): p. 957-963.
- [387] Megahed, S. and W. Ebner, Lithium-ion battery for electronic applications. *Journal of Power Sources*, 1995. **54**(1): p. 155-162.
- [388] Bian, J., et al., Mg Doped Perovskite LaNiO₃ Nanofibers as an Efficient Bifunctional Catalyst for Rechargeable Zinc–Air Batteries. *ACS Applied Energy Materials*, 2019. **2**(1): p. 923-931.
- [389] Müller, S., F. Holzer, and O. Haas, Optimized zinc electrode for the rechargeable zinc–air battery. *Journal of Applied Electrochemistry*, 1998. **28**(9): p. 895-898.
- [390] Jeschull, F., et al., On the Electrochemical Properties and Interphase Composition of Graphite: PVdF–HFP Electrodes in Dependence of Binder Content. *Journal of The Electrochemical Society*, 2017. **164**(7): p. A1765-A1772.
- [391] Papp, J.K., et al., Poly(vinylidene fluoride) (PVDF) Binder Degradation in Li–O₂ Batteries: A Consideration for the Characterization of Lithium Superoxide. *The Journal of Physical Chemistry Letters*, 2017. **8**(6): p. 1169-1174.
- [392] Nasybulin, E., et al., Stability of polymer binders in Li–O₂ batteries. *Journal of Power Sources*, 2013. **243**: p. 899-907.
- [393] Liu, B., et al., In Situ-Grown ZnCo₂O₄ on Single-Walled Carbon Nanotubes as Air Electrode Materials for Rechargeable Lithium–Oxygen Batteries. *ChemSusChem*, 2015. **8**(21): p. 3697-3703.
- [394] Du Pasquier, A., et al., Microstructure effects in plasticized electrodes based on PVDF–HFP for plastic Li-ion batteries. *Journal of Power Sources*, 2001. **97-98**: p. 758-761.
- [395] Pu, W., et al., Preparation of PVDF–HFP microporous membrane for Li-ion batteries by phase inversion. *Journal of Membrane Science*, 2006. **272**(1): p. 11-14.
- [396] Jeong, H.-S., E.-S. Choi, and S.-Y. Lee, Composition ratio-dependent structural evolution of SiO₂/poly(vinylidene fluoride-hexafluoropropylene)-coated poly(ethylene terephthalate) nonwoven composite separators for lithium-ion batteries. *Electrochimica Acta*, 2012. **86**: p. 317-322.
- [397] Zhang, D., et al., Novel composite polymer electrolyte for lithium air batteries. *Journal of Power Sources*, 2010. **195**(4): p. 1202-1206.
- [398] Pan, Z., Y. Bi, and L. An, A cost-effective and chemically stable electrode binder for alkaline-acid direct ethylene glycol fuel cells. *Applied Energy*, 2020. **258**: p. 114060.
- [399] Stabler, S.M. and R. Amin-Sanayei, Particulate polymer binder composite. 2018, Google Patents.

- [400] Fu, J., et al., Flexible High-Energy Polymer-Electrolyte-Based Rechargeable Zinc–Air Batteries. *Advanced Materials*, 2015. **27**(37): p. 5617-5622.
- [401] Younesi, R., et al., Li–O₂ Battery Degradation by Lithium Peroxide (Li₂O₂): A Model Study. *Chemistry of Materials*, 2013. **25**(1): p. 77-84.
- [402] Younesi, R., et al., Ether Based Electrolyte, LiB(CN)₄ Salt and Binder Degradation in the Li–O₂ Battery Studied by Hard X-ray Photoelectron Spectroscopy (HAXPES). *The Journal of Physical Chemistry C*, 2012. **116**(35): p. 18597-18604.
- [403] Vankova, S., et al., Influence of Binders and Solvents on Stability of Ru/RuO_x Nanoparticles on ITO Nanocrystals as Li–O₂ Battery Cathodes. *ChemSusChem*, 2017. **10**(3): p. 575-586.
- [404] Bae, Y., et al., Enhanced Stability of Coated Carbon Electrode for Li-O₂ Batteries and Its Limitations. *Advanced Energy Materials*, 2018. **8**(16): p. 1702661.
- [405] Park, M.-S., et al., Morphological Modification of γ -MnO₂ Catalyst for Use in Li/Air Batteries. *Journal of Nanoscience and Nanotechnology*, 2013. **13**(5): p. 3611-3616.

RÉSUMÉ

La batterie zinc-air devient une alternative potentielle à la batterie lithium-ion en raison de son avantage en termes de ressources, de sa densité d'énergie théorique élevée et de son faible potentiel de risque pour la sécurité. Ce travail met l'accent sur les problèmes conventionnels impliquant à la fois l'électrode à zinc et à air, visant à l'application.

Pour l'électrode de zinc, deux configurations maison sont utilisées pour étudier la croissance des dendrites de zinc et l'évolution de l'hydrogène pendant le dépôt avec un électrolyte statique et en flux, respectivement. On trouve qu'une concentration élevée de zincate dans un électrolyte avec 7 M KOH ($> 0,4$ M ZnO) et la présence de circulation de l'électrolyte sont préférables pour réduire la croissance des dendrites. Cependant l'électrolyte en circulation générerait plus de dégagement d'hydrogène. Pour l'électrode à air, une étude de voltampèremètre cyclique détaillée de l'activité catalytique de pérovskites de lanthane- manganèse dopés au strontium (LSMO) vis-à-vis de la réaction de réduction de l'oxygène est menée. Une nouvelle méthodologie est proposée pour la comparaison de l'activité catalytique des LSMO. L'assemblage de la batterie zinc-air est également testé en formulant les électrodes avec un polymère PVDF-HFP prometteur dans les applications d'électrode à air.

MOTS CLÉS

Electrode de zinc, électrode à air, électrocatalyse, réaction de réduction de l'oxygène (ORR), oxyde de lanthane strontium manganèse (LSMO), voltamètre cyclique

ABSTRACT

Zinc-air battery is becoming a potential alternative for lithium-ion battery owing to its resource stock advantage, high theoretical energy density, and low potential of safety risk. This work emphasizes the conventional issues involving both zinc and air electrode, aiming to application.

For the zinc electrode, two homemade setups are used to study the zinc dendrite growth and hydrogen evolution during deposition with static and flowing electrolyte, respectively. It is found that high zincate concentration in electrolyte with 7 M KOH (>0.4 M ZnO) and flowing electrolyte are preferable for depressing dendrite growth. While flowing electrolyte would generate more hydrogen evolution. For the air electrode, a detailed cyclic voltametric investigation of the catalytic activity of lanthanum strontium manganese oxides (LSMO) towards oxygen reduction reaction is conducted. A new current normalization method is proposed for comparison of catalytic activity of the LSMOs. Zinc-air battery assembly is also tested, while remaining to be improved. Nevertheless, cost-effective PVDF-HFP is found to be a promising binder for air electrode formulation.

KEYWORDS

Zinc electrode, air electrode, oxygen reduction reaction (ORR), lanthanum strontium manganese oxide (LSMO), cyclic voltammetry